3D TRANSDIMENSIONAL SEISMIC TOMOGRAPHY OF THE EARTH'S INNER CORE USING BODY WAVES AND NORMAL MODES

HENRY TRISTAN GARRETT BRETT

UTRECHT STUDIES IN EARTH SCIENCES
NO. 268

Members of the dissertation committee:

Prof. dr. Vernon Cormier
Department of Physics
University of Connecticut, USA

Prof. dr. Peter Shearer
Institute of Geophysics and Planetary Physics
Scripps Institution of Oceanography , USA

Prof. dr. Christine Thomas
Institut für Geophysik
University of Münster, Germany

Prof. dr. Jeannot Trampert
Department of Earth Sciences
Utrecht University, The Netherlands

Prof. dr. Jeroen Tromp
Department of Geosciences
University of Princeton, USA

ISBN: 978-90-6266-637-9
DOI: https://doi.org/10.33540/1658

The facilities of IRIS Data Services, and specifically the IRIS Data Management Center, were used for access to waveforms, related metadata, and/or derived products used in this study.

3D TRANSDIMENSIONAL SEISMIC TOMOGRAPHY

OF THE EARTH'S INNER CORE

USING BODY WAVES AND NORMAL MODES

3D TRANSDIMENSIONALE SEISMISCHE TOMOGRAPHIE

VAN DE BINNENKERN

MET BODY WAVES EN NORMAL MODES
(met een samenvatting in het Nederlands)

Proefschrift

ter verkrijging van de graad van doctor aan de Universiteit Utrecht op gezag van de rector magnificus, Prof. Dr. H.R.B.M. Kummeling, ingevolge het besluit van het college voor promoties in het openbaar te verdedigen op maandag 20 februari 2023 te 4.15 uur

door

Henry Tristan Garrett Brett

geboren op 25 februari 1995 te Belfast, Noord Ierland

Promotor: Prof. dr. A.F. Deuss

Copromotor: Dr. R.P. Hawkins

This thesis was accomplished with financial support from the European Research Council (ERC) under the European Union's Horizon 2020 research and innovation programme (grant agreement No 681535 - ATUNE) and a Vici award number 016.160.310/526 from the Netherlands organization for scientific research (NWO).

For Esther Allers
"Did you know that..."

Contents

Summary

Since the discovery of the inner core almost 100 years ago, the seismological community has found that the inner core contains significant heterogeneity in its elastic structure. This observation is significant and in many ways unexpected; we believe the inner core to be (relatively) chemically homogeneous consisting primarily of iron and nickel and certainly not containing the thermal and chemical heterogeneity we see in the Earth's crust and mantle. Yet, despite this assumption, we observe that seismic waves which pass through the inner core travel faster in a north-south direction than an east-west direction and that the spectra of whole Earth oscillations are anomalously split in a way which is consistent with the same velocity difference. This difference in velocity between two directions through the inner core is called anisotropy, and from mineral physics we have reason to believe that this anisotropy is caused by the alignment of iron crystals which are themselves anisotropic at inner core temperatures and pressures. However, this is not the end of the story, as many unanswered questions remain; What causes these iron crystals to align into an anisotropic fabric? Why are some regions of the inner core anisotropic and others not? Does the anisotropy and its strength vary with depth? To help answer these questions, we have to constrain the magnitude of the anisotropy and the location of anisotropy in the inner core. The primary goal of this thesis is to constrain, as well as possible, the elastic structure of the inner core.

To achieve our aim we first expand upon the body wave dataset by adding new observations of paths which travel almost parallel to Earth's axis of rotation, giving us improved sensitivity to velocity in the north-south direction in the inner core. We combine our new data with other body wave datasets to produce a 3D seismic tomographic model of the inner core. This model utilised a transdimensional Markov chain Monte Carlo methodology which not only determines the best fitting anisotropy structure in the inner core, but also the uncertainties in our model and it does not require any prior assumptions on the parameterization of the inner core. The advantage of this method is significant, especially because the relatively poor sampling

of the inner core means that prior assumptions on the parameterization may significantly affect the final model. In the transdimensional approach the parameterization is a part of the inversion. In our new transdimensional model we confirmed many previous observations, including an isotropic layer of $\sim$ 100 km thickness at the top of the inner core and that the inner core is split broadly into a western region and an eastern region. However, with the new data and methodology we are now able to make new robust observations, such as seeing for the first time that the western anisotropic zone is isolated to the northern hemisphere and that the inner most inner core exists but primarily in the eastern region. These observations are significant as it provides new insight into the mechanisms of inner core formation and dynamics, and we discuss the potential implications for inner core geodynamics.

However, body waves represent only one possible type of data we can use to investigate the inner core and it is important in deep Earth research to bring together as many sources of information as possible. Thus we then also added whole Earth oscillations and measure 18 normal modes sensitive to the inner core. We used a splitting function approximation and utilise a grid search methodology to constrain the uncertainties in the measurement. The data were then used to produce a preliminary 1D transdimensional model of inner core anisotropy using polynomial basis functions and find a model which agrees reasonably well with the spherical average of compressional anisotropy from the body wave model.

Finally, we describe a new method to combine the body waves and the normal modes into a single 3D transdimensional model. We show promising preliminary results from this methodology with a model which fits both the body waves and the normal mode data well, reproducing the main structures of our 3D body wave only model. Combining the body waves with the normal modes comes with caveats. We are not able to fit all of our mode measurements, and therefore we have not utilised all inner core sensitive normal modes that have been measured. Furthermore combining the two types of data results in multiple regions where the slowest direction is not perpendicular to Earth's axis of rotation. Previous authors have attributed an anomalous slow direction in the inner core to a inner most inner core. The complexity we recover in this anomaly confirms the difficulty in imaging the inner most inner core. Given the preliminary results, we feel confident that this is the right approach and should be extended in the future.

Samenvatting

De binnenkern van de aarde is bijna honderd jaar geleden ontdekt en sindsdien heeft de seismologische gemeenschap aangetoond dat deze aanzienlijke variatie in elastische structuur bevat. Dat is een belangrijke en enigszins onverwachte observatie: de binnenkern wordt namelijk beschouwd als (relatief) chemisch homogeen, voornamelijk bestaand uit ijzer en nikkel, met veel minder variatie in temperatuur en compositie dan we in de korst en de mantel zien. En toch observeren we dat seismische golven door de binnenkern sneller reizen in noord-zuidelijke richting dan in oost-westelijke richting. Ook zien we dat frequentiespectra van normal modes, de eigentrillingen van de aarde, gesplit zijn en dat deze splitting overeenkomt met dezelfde verschillen in seismische snelheid in de binnenkern. Dit fenomeen, waarbij de snelheid van seismische golven afhangt van de richting door het medium, wordt anisotropie genoemd. Onderzoek uit de mineraalfysica laat zien dat ijzerkristallen anisoptroop zijn onder de hoge druk en temperatuur die heersen in de binnenkern. De geobserveerde anisotropie in de binnenkern zou dan veroorzaakt kunnen worden door het op grote schaal en in dezelfde richting oriënteren van deze anisotrope ijzerkristallen. Maar daar is niet alles mee gezegd, want er zijn nog veel openstaande vragen: wat veroorzaakt de grootschalige oriëntatie van ijzerkristallen? Waarom zijn sommige delen van de binnenkern anisotroop en andere niet? Zijn er dieptevariaties in de sterkte en het voorkomen van anisotropie in de binnenkern? Binnenkernanisotropie moet beter in kaart worden gebracht om deze vragen te kunnen beantwoorden. Het hoofddoel van dit proefschrift is dan ook het zo goed mogelijk bepalen van de elastische structuur van de binnenkern.

Om te beginnen breiden we de bestaande body-wave dataset uit door observaties toe te voegen van golven met paden die bijna parallel lopen aan de rotatie-as van de aarde. Hiermee verbeteren we de gevoeligheid voor de snelheid in noord-zuidelijke richting in de binnenkern. Vervolgens combineren we onze nieuwe data met bestaande body-wave datasets om een 3-D seismisch tomografiemodel van de binnenkern te maken. Hiervoor gebruiken we een trans-dimensionale Markov chain Monte Carlo methode die de optimale anisotropiestructuur vindt om onze data te verklaren. De

voordelen van deze methode zijn dat ook de onzekerheden van de modelparameters worden bepaald en dat er geen aannames hoeven te worden gedaan over de parametrisatie van de binnenkern, omdat de parametrisatie onderdeel is van de inversie. Deze voordelen zijn aanzienlijk, met name omdat de slechte dekking van de binnenkern door de body-wave data betekent dat vooraf vastgestelde aannames over de parametrisatie van de binnenkern een grote invloed zouden hebben op het uiteindelijke model. Ons nieuwe, trans-dimensionale model bevestigt veel voorgaande observaties, waaronder het bestaan van een isotrope laag van 100 kilometer dikte bovenin de binnenkern en de grove verdeling van de binnenkern in een anisotrope westelijke helft en een isotrope oostelijke helft. Daarnaast zijn we met onze nieuwe dataset en methode in staat om een aantal nieuwe, robuuste observaties te doen. We zien voor het eerst dat de westelijke anisotrope zone beperkt is tot de noordelijke hemisfeer en dat de binnenste binnenkern zich voornamelijk in de oostelijke zone van de binnenkern bevindt. Dit zijn belangrijke observaties, omdat ze nieuwe inzichten bieden in de mechanismen die verantwoordelijk zijn voor de formatie en dynamiek van de binnenkern. We bespreken de potentiële implicaties van onze resultaten voor de geodynamica van de binnenkern in dit proefschrift.

Onderzoek naar de diepe aarde profiteert van het samenbrengen van zoveel mogelijk bronnen van informatie, waar body waves er maar één van zijn. Zodoende meten we ook 18 normal modes die gevoelig zijn voor de binnenkern, waarbij we gebruik maken van de splitting-functie benadering en we een grid-search methode toepassen om de meetonzekerheden te bepalen. Vervolgens gebruiken we deze metingen om een 1-D trans-dimensionaal model van binnenkernanisotropie te maken dat redelijk overeenkomt met de uitgemiddelde structuur van het body-wave model.

Ten slotte beschrijven we een nieuwe methode om observaties van body waves en normal modes te combineren tot een enkel 3-D trans-dimensionaal model. We laten veelbelovende, vroegtijdige resultaten zien van deze methode, waarmee we een model maken dat zowel de observaties van body waves als normal modes verklaart en tegelijkertijd de belangrijkste structuren van het 3-D body-wave model bevestigt. Ondanks dat niet al onze normal-mode metingen goed worden verklaard door dit gecombineerde model, en we hierdoor een aantal metingen buiten beschouwing laten, zijn we optimistisch dat onze methode veel potentie biedt voor de toekomst.

1
Prologue

The inner core lies at the centre of the Earth and at the centre of many Earth processes. Most importantly, the solidification of the inner core from the liquid outer core releases latent heat which helps drive the geodynamo generating Earth's magnetic field. The latent heat in turn provides a significant portion of the heat budget at the core mantle boundary (CMB) driving mantle convection and influencing tectonic processes visible at the surface of the Earth, including mantle upwellings and subducting slabs. In this way, it is important to think of the planet as a single system, and understanding the composition, structure and dynamics of the inner core is key to understanding how the Earth system functions as a whole.

However, the inner core of the Earth is arguably the most difficult region of our planet to study. The inner core lies $\sim$ 5150 km underneath the Earth's surface and yet it is easier to send probes millions of kilometers through space to study remote bodies of the solar system than it is to physically drill more than 10 km into the crust. That means we must resort to indirect sensing, such as seismology, to understand what is happening beneath our feet.

Oldham (1906) discovered the outer core through observing a P-wave shadow zone between 103° and 142° epicentral distance where no P-waves are observed. Gutenberg proposed that the outer core must be liquid after observing a S-wave shadow zone between from 103° to 180° epicentral distance where no S-waves were observed. However, it was Lehmann (1936) who observed P-waves arriving within this shadow zone and correctly concluded that this was due to reflections from a inner core which was most likely solid, although no direct evidence for the inner core's solidity existed at the time. Since Lehmann (1936) seismology has been key to studying the inner core. While other disciplines, such as mineral physics, provide valuable constraints on the physical properties of the inner core, or geodynamics, which attempts to understand the inner core's dynamic history, it is

only seismology which provides direct observations of the elastic properties of the inner core.

Initially seismometers were located sparsely around the world and with many different standards, but from 1962 onwards the first standardised global seismograph networks were installed. As the quality and quantity of seismometers increased and computational resources became more accessible the discipline of seismic tomography emerged. Seismic tomography as a field began in the mid 1970's where, typically, travel time data were used make 3D models of velocity variations in the crust and mantle (Aki and Lee, 1976). The field developed rapidly from then, where many groups produced mantle models in parallel using ever larger datasets. Some groups focused on imaging the mantle by using finite grids with P-wave arrival times (Dziewonski *et al.* (1977); Dziewonski (1984); Spakman *et al.* (1988); Hilst *et al.* (1997)) while others utilised a spherical harmonic parameterization to describe surface wave and normal mode observations (Woodhouse and Dziewonski (1984); Nataf *et al.* (1986); Li and Romanowicz (1996); Ritsema *et al.* (1999)). Waveform fitting methods attempt to go further than fitting travel time or phase information and to fit the whole waveform and take into account finite-frequency affects in 3D (Bamberger *et al.* (1982); Zhao *et al.* (2000); Dahlen *et al.* (2000); Nolet and Dahlen (2000)). Full waveform inversion (FWI) is computationally expensive and as such was limited to regional studies, but significant progress has been made in conducting global (FWI) and it is now possible to conduct full waveform inversion for the whole mantle (Lekić and Romanowicz (2011); Bozdağ *et al.* (2016); Thrastarson *et al.* (2022)).

However, while the mantle and the crust have been mapped extensively in 3D using a wealth of seismic observations, the inner core poses a unique challenge. Due to the inner core's depth any seismic observations of the inner core will be influenced by heterogeneity in the rest of the planet. Furthermore, the liquid outer core acts as a filter preventing shear waves travelling from the crust or mantle reaching the inner core. These two facts inherently make the inner core a relatively data sparse region of the Earth. This means that studies of the inner core have had to adopt different techniques to overcome such data limitations. In this thesis we aim to convince the reader that with the increase in reliable seismic data sensitive to the inner core and the use of Bayesian methodologies to constrain uncertainties in the data and model space, it is now possible to produce reliable and high resolution 3D seismic tomographic models. We will then use these models to observe exciting new features within the inner core with implications for our understanding of the deepest region of our planet.

1.1 Seismic observations of the inner core

The inner core is most commonly studied using travel times of compressional body waves. Usually, the compressional wave that travels through the mantle, outer core and inner core is measured alongside a reference phase which only traverses the mantle and outer core. These body waves are studied at short period (∼1Hz) and therefore are useful for finding small scale structures and regional variations within the inner core.

Poupinet *et al.* (1983) were the first to observe that compressional waves which travel in a north-south, or polar, direction in the inner core arrive approximately 3-5 seconds earlier than waves which travel in an east-west, or equatorial, direction through the inner core, (Figure 1.1). Morelli *et al.* (1986) proposed that this is explained by cylindrical anisotropy (also known as transverse isotropy) in the inner core. Seismic anisotropy arises when the velocity of a seismic wave travelling through a medium depends on its travel direction. Cylindrical anisotropy is a specific form of anisotropy in which the velocity along the symmetry axis is different from the velocity in the plane perpendicular to that axis. The symmetry axis in the inner core appears aligned to Earth's rotation axis. When using ray theory, body wave data are approximated as raypaths from which you can calculate the angle ζ, which is the angle between the inner core segment of the raypath and Earth's axis of rotation.

Woodhouse *et al.* (1986), corroborated the findings of Morelli *et al.* (1986) by showing that cylindrical anisotropy in the inner core is also consistent with observations of anomalously split normal modes. Normal modes are whole Earth oscillations which are excited after a large earthquake, they are long wavelength and most easily observed in the range of 0.0-10.0 mHz, unlike inner core sensitive body waves which are best observed between 0.5-2.0 Hz. This means that normal modes, can provide us with a independent observation of the inner core's elastic properties.

1.1.1 A heterogeneous inner core

Early studies of inner core anisotropy treated the inner core as homogeneous with the same velocity properties relative to a reference model throughout, which was justified considering the limited amount of data available. However, as data improved it became clear that the inner core exhibits significant lateral heterogeneity. Tanaka and Hamaguchi (1997) observed that polar paths travelling through the western part of the inner core arrived earlier than polar paths in the east (Figure 1.2). This hemispherical pattern has been confirmed by numerous studies since Tanaka and Hamaguchi

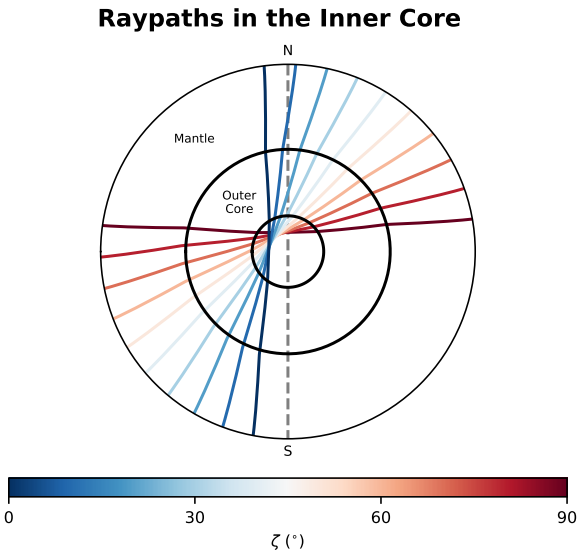

Figure 1.1 A cross section of the Earth showing 10 compressional wave raypaths with the colour corresponding to the angle ζ, between the inner core segment of the raypath and Earth's axis of rotation.

(1997) and it is now widely accepted that there is an 'eastern hemisphere' with minimal anisotropy and an anisotropic 'western hemisphere' (Creager (1999); Garcia and Souriau (2000); Sun and Song (2008a); Irving and Deuss (2011); Lythgoe *et al.* (2014)). Hemispheres in inner core anisotropy are also observed with normal modes by looking at cross coupling between inner core sensitive modes (Deuss *et al.*, 2010).

According to body waves anisotropy in the west is as high as 4-8% while anisotropy in the East is minimal, around ∼1% (Table 3.1). Differences between body wave studies may represent differences in the data used or the parameterization. For example, the quantity of reliable polar data varies greatly between studies, which will be the major topic of Chapter 3. The location of the hemisphere boundaries also varies significantly across previous studies, an issue we address in Chapter 4.

Anisotropy not only varies laterally but also strongly with depth in the inner core. Body wave data which is only sensitive to the top ∼100 km of the inner core show that there is minimal anisotropy here, but significant isotropic velocities differences exist between the hemispheres, with an isotropically fast eastern hemisphere (∼1-2%) and an isotropically slow western hemisphere (∼-0.5%) (Niu and Wen (2001); Waszek and Deuss

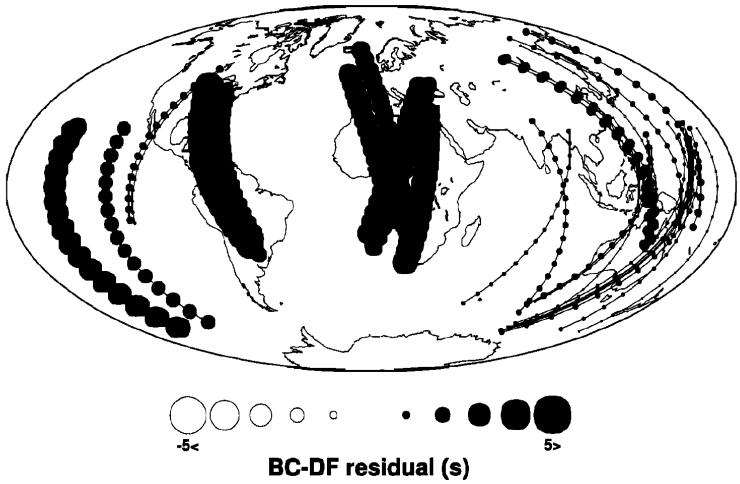

Figure 1.2 Polar raypaths from the dataset of Tanaka and Hamaguchi (1997), solid circles represent paths which arrived earlier (i.e. faster) than expected and hollow circles represent paths which arrived later (i.e. slower) than expected. A larger circle corresponds to a bigger anomaly. Figure taken from Tanaka and Hamaguchi (1997).

(2011); Burdick *et al.* (2019)). Anisotropy increases in the western hemisphere from approximately 100 km beneath the inner core boundary (ICB) until the centre of the inner core.

There is some evidence for an innermost inner core (IMIC), where the direction of slowest velocity, ζ_{slow}, is not in the equatorial plane or perpendicular to the symmetry axis (i.e. Earth's rotation axis), but at an angle of between $45° - 65°$ (Ishii and Dziewoński (2003); Beghein and Trampert (2003); Frost and Romanowicz (2019); Stephenson *et al.* (2020); Lima *et al.* (2022)). The existence of an IMIC is particularly difficult to verify as there is less data sensitive to the deep inner core than the outer inner core and the ζ_{slow} anomaly is subtle. However, there have now been multiple studies which have observed an IMIC and most consider the IMIC to be a sphere within the inner core with a radius between 300 and 690 km. In contrast Lythgoe *et al.* (2014) found that direct compressional body wave observations of an IMIC could also be fit through hemispherical variations and that the IMIC anomaly is a part of the eastern hemisphere.

1.2 Mineral physics & geodynamics

Interpreting seismic observations of the inner core requires an understanding of the composition, mineralogy and dynamic processes within the core. The inner core is made up of ∼90% iron and nickel and ∼ 10% lighter elements (Jephcoat and Olson (1987); Vocadlo and Price (2007)). Mineral physics tells us that the crystal structure of pure iron takes one of three forms: bcc (body centered cubic) at ambient conditions, transforming to fcc (face centered cubic) at higher temperatures and hcp (hexagonal close packed) at higher pressures. This information comes from two different sources: diamond anvil cell laboratory experiments and *ab initio* computer simulation. In diamond anvil cell experiments a sample of a material in question is exposed to high temperatures and pressures and then the crystal structure of the sample is inferred through X-ray diffraction (Boehler (1993); Tateno *et al.* (2010), see Hirose *et al.*, 2013 for a review). *Ab initio* calculations computationally model the atomic arrangement of the iron crystals using physical theory (Stixrude *et al.* (1997); Vočadlo *et al.* (2000)). While the most stable phase of iron at inner core temperatures and pressures is hcp (Stixrude and Cohen (1995); Hirose *et al.* (2013)), the differences in the free energies between hcp, bcc and fcc and the effect of light elements in the inner core mean the presence of fcc and bcc iron cannot be ruled out (Stixrude (2012); Martorell *et al.* (2015)).

These mineral physics considerations are important as hcp, fcc and bcc iron all exhibit anisotropy. They provide us with an explanation for the anisotropy we observe in seismology. Indeed, given the three different sources of evidence of anisotropy in the inner core: (i) body wave observations, (ii) normal mode observations and (iii) mineral physics experiments, I think it is unlikely that our observations of anisotropy in the inner core would be due to noise in our data or misinterpretation of mantle structure.

However, it is not enough for anisotropic crystals to be stable at inner core temperatures and pressures, there must be a process which aligns these crystals, as a random arrangement of anisotropic crystals would appear isotropic overall. Geodynamics attempts to understand the forces acting within the inner core and the dynamic evolution of the inner core with time which may provide mechanisms to align the iron crystals. There is a pattern in scientific studies of the inner core, where seismic observations of the inner core improve, mineral physicists refine experiments to find crystals with elastic parameters matching the seismic observations and geodynamicists attempt to reconstruct seismic observations with computational flow modelling.

Major open questions for geodynamic studies of the inner core include

finding the dominant cause of crystal alignment and the processes which lead to a hemispherical difference in the inner core. When it comes to crystal alignment this could either occur when iron crystals solidify locking in a preferred alignment or due to deformation within the inner core after solidification. In the solidification regime it has been proposed that crystals align with the magnetic field, due to the paramagnetic properties of iron (Karato, 1993), or that iron aligns with a prevalent heat flux due to increased heat extraction at the equator (Bergman, 1997). The solidification regime would result in strong anisotropy at the top of the inner core. Given that significant anisotropy in the inner core only starts 100 km below the ICB (Waszek and Deuss (2011); Burdick *et al.* (2019)) solidification regimes seem less likely (Alboussiere and Deguen, 2012).

Alternatively, crystal alignment could be achieved post solidification due to deformation within the inner core. Yoshida *et al.* (1996) suggested that preferential heat extraction at the equator of the inner core results in more crystallisation at the equator than the poles, causing gravitational instability and flow from the equator to the poles of the inner core. It would then be expected that the iron crystals would align with this flow (Figure 1.3). Similarly, Lorentz forces, if strong enough, could produce shear flow within the inner core (Karato (1999); Buffett and Wenk (2001)). The resulting flow would be in the opposite direction to Yoshida *et al.* (1996), with flow from the poles to the equator of the inner core, but still resulting in the same pattern of crystal alignment.

Hemispheres in the inner core have proved more difficult to explain with geodynamics. There are many processes in the Earth which posses symmetry relative to Earth's axis of rotation such as the Coriolis forces or the geomagnetic field etc, however, there are not many obvious causes for a hemispherical asymmetry. Broadly, two major mechanisms have been proposed to produce hemispherical structures in the inner core. Sumita and Olson (1999) and Aubert *et al.* (2008) propose that heat flux heterogeneity at the Core Mantle Boundary (CMB) result in long term patterns of flow within the outer core. This would occur due to the accumulation of cold slabs at the CMB which in turn would increase the heat gradient across the CMB locally. If this heat gradient could be maintained for at least 200 million years then it is possible this would induce a heterogeneous heat flux on the ICB. If this heat flux remained static for a long time this could lead to a difference in growth rate for the eastern and western hemispheres of the inner core, resulting in the hemispherical asymmetry (Figure 1.4). This mechanism has some unknowns however, as it is not clear how long we could expect heat fluxes to stay stable at the CMB, and the effect it would have

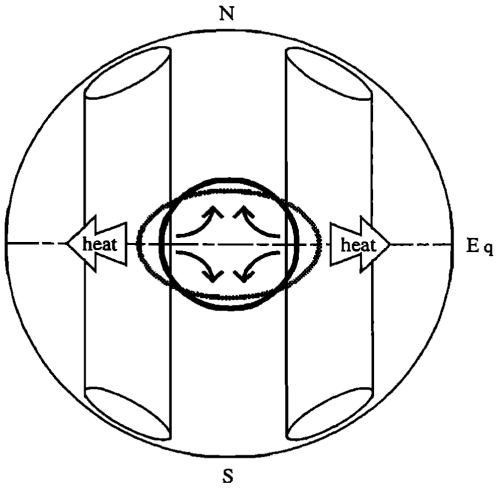

Figure 1.3 Cartoon illustrating the post solidification crystal alignment mechanism whereby the direction of flow in the inner core is driven by preferential heat extraction at the equator of the inner core. Figure taken from Yoshida *et al.* (1996).

on the rapidly convecting outer core.

Another mechanism proposes that the inner core itself is convecting due to thermal or compositional heterogeneity (Alboussiere *et al.* (2010); Deguen *et al.* (2018)). For a specific viscosity range the form of inner core convection becomes a translation, where the east of the inner core is melting and the west is crystallising. This would result in gravitational instability and as a consequence the inner core would translate to the east to maintain its centre of gravity (Figure 1.5). This translation would then result in a western hemisphere which was younger than the eastern hemisphere with different elastic properties.

1.3 Motivation & outline

I hope that this prologue has made it clear to the reader that the inner core is a fascinating yet challenging region of the Earth to study. Many open questions remain for inner core seismology, such as why does the magnitude of anisotropy observed in the inner core by normal modes and body waves differ? What is the exact shape of the hemispheres in the inner core? And is there an innermost inner core and if so what are its size, shape, and elastic properties? Innovative techniques are required to extract as much

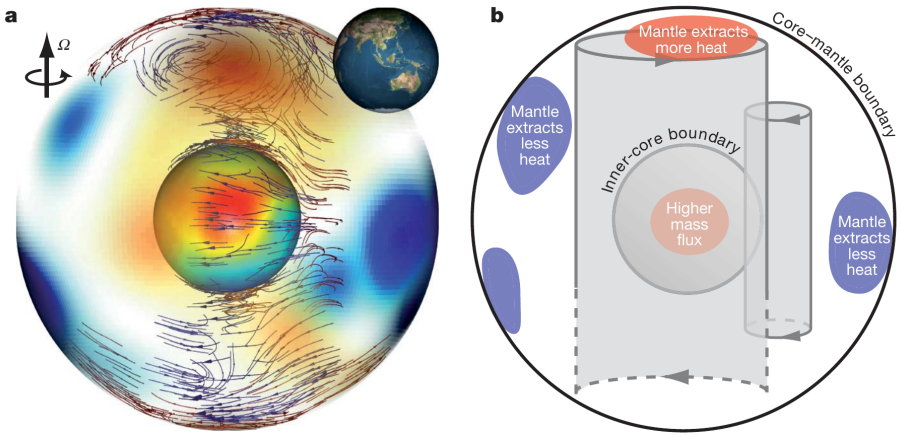

Figure 1.4 The influence of CMB heat flux heterogeneity on the solidification pattern of the inner core. Figure taken from Aubert *et al.* (2008).

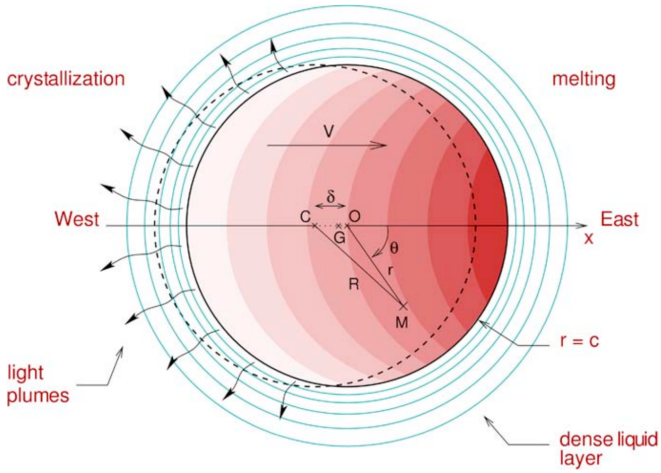

Figure 1.5 Showing translation from west to east in the inner core due to preferential crystalisation and how this could result in hemispherical asymmetry in the inner core. Figure taken from Alboussiere and Deguen (2012).

information from the seismic wavefield as possible, due to a relative lack of data and imperfect earthquake and seismometer distribution on the Earth's surface. Improved imaging of seismic anomalies within the inner core can provide new observations to inform geodynamic models of the inner core and mineral physics experiments.

To answer some of the open questions mentioned above, this thesis aims to improve body wave and normal mode observations of inner core anisotropy and to produce a high resolution probabilistic 3D tomographic model of inner core anisotropy, combining both types of data. This thesis is structured in such a way that data and model complexity increases with each chapter. We start from simple models using just body waves and end with a Bayesian transdimensional model jointly fitting normal modes and body waves. This systematic approach lends confidence to our final model and interpretations as the influence of each increase in complexity is clear.

Chapter 2 starts with a short primer on transverse isotropy and derive some fundamental equations for later chapters.

Chapter 3 focuses on increasing the body wave dataset with special attention on collecting more observations of ultra-polar raypaths ($\zeta < 20°$) making use of recently installed seismic stations in Antarctica. Using our newly collected data, we make initial estimates of inner core anisotropy and first order observations of its lateral and depth variations.

Chapter 4 combines our new differential travel time data with two already existing body wave datasets, giving us sensitivity to inner core anisotropy from the ICB to the centre of the inner core. We then apply a 3D transdimensional Markov Chain Monte Carlo (MCMC) methodology to produce a tomographic model of inner core isotropic and anisotropic compressional velocity variation. We then go on to interpret our model observing many new and interesting features of the inner core.

Chapter 5 introduces normal modes and we measure 18 self-coupled inner core sensitive normal modes using an up to date data set of spectra. We measure the inner core sensitive normal modes in a new way which explores the splitting function model space.

Chapter 6 takes the two normal mode zonal parameters which predominantly are sensitive to inner core anisotropy from our measured splitting functions to produce a 1D transdimensional model of inner core P-wave and S-wave anisotropy. We evaluate the agreement between the modes and the body waves by comparing our 1D normal mode model with the body wave model from Chapter 4.

In Chapter 7 we show preliminary results of a combined model of inner core anisotropy using both normal modes and body waves solving for

3D variations in P-wave anisotropy and show, with some caveats, that the normal modes and body waves agree on inner core structure.

In this thesis we show that the body waves and the normal modes both require anisotropy in the inner core. Furthermore, through higher resolution modelling we show that the normal modes and body waves agree on the overall magnitude of inner core anisotropy which was not the case with previous models of inner core anisotropy. This agreement is primarily achieved by resolving for the first time that the western anisotropic zone is isolated in the northern hemisphere, thus concentrating the high anisotropic zone in a smaller region and reducing the overall anisotropy of the inner core. We go on to conclude with our body wave data that the innermost inner core is isolated to the eastern hemisphere. We do all this using innovative Transdimensional MCMC modelling techniques which allow the parameterization of the model space to be defined by the data. In a data poor region like the inner core this allows us to extract as much information from the body wave and normal mode data as possible.

2

A short introduction to anisotropy in the inner core

This chapter is a primer on mathematical descriptions of anisotropy in the inner core. We assume that anisotropy in the inner core is best approximated by transverse isotropy where the symmetry axis is aligned with the Earth's rotation axis (also known as cylindrical anisotropy) which is described using the five Love parameters, A, C, L, F and N (Love, 1927). Since the first seismic observations of inner core anisotropy (Morelli *et al.* (1986); Woodhouse *et al.* (1986)) the Love parameters have been used to describe anisotropy with different combinations. In this thesis we use two different parameterizations for transverse isotropy, which we name the *body wave parameterization* for compressional wave anisotropy (utilised in Chapters 3-4) and the *normal mode parameterization* which incorporates both compressional and shear wave anisotropy (utilised in Chapters 6-7). We feel it is important to explicitly derive these two parameterizations from first principles to show how the two are related to each other and to highlight how they are simply abstractions of the formal general description of transverse isotropy. This chapter is intended as a reference for the reader to come back to in later chapters, while all other methods related to the model inversion or data processing will be explained in the corresponding chapter.

2.1 The body wave parameterization

In an anisotropic medium wave speed depends on the direction of travel through that medium. It is usually assumed that the inner core displays transverse anisotropy with a symmetry axis parallel to Earth's axis of rotation, this is also called cylindrical anisotropy. Here we will include a

short description of P-wave velocity from first principles in an transversely isotropic media. This derivation is largely based on the description from Song (1997).

We start with the case of plane wave propagation, which in a general elastic medium results in the following equation of motion (in Cartesian coordinates)

$$\rho \frac{\delta^2 u_i}{\delta^2 t} = \frac{\delta}{\delta x_j}(C_{ijkl} \frac{\delta u_k}{\delta x_l}) \tag{2.1}$$

where $i, j, k, l = 1, 2, 3$, where u is the displacement vector, C_{ijkl} is the stiffness matrix and ρ is density. For a plane wave $u_k(x_l, t) = A_k e^{i\omega(t - p_l x_l / c)}$ where A_k is the polarization vector, p_j is propagation direction, ω is angular frequency, t is time and c is phase velocity we have

$$B_{il} = c^2 A_i \tag{2.2}$$

where $B_{il} = C_{ijkl} p_j p_k / \rho$ which is the Christoffel matrix. Diagonalising the Christoffel matrix leads to the eigenvalues which give the phase velocities, c and the eigenvectors give the corresponding polarization directions. In general there are three real eigenvalues with three orthogonal eigenvectors, which in an isotropic media corresponds to one compressional P-wave, whose polarization vector coincides with the propagation direction, and two shear S-wave components. In an anisotropic medium the P eigenvector in general is not parallel to the propagation direction but in a weakly anisotropic media, such as the inner core this difference is minimal.

For a transversely isotropic medium, such as the inner core, we can describe the anisotropy with the five independent Love parameters, denoted as A, C, L, F and N (Love, 1927), which describe C_{ijkl}. These elastic parameters can be arranged into a matrix C_{mn} which is related to C_{ijkl} with the following index rules

$$\begin{aligned} m = i = j \text{ if } i = j \\ m = 9 - i - j \text{ if } i \neq j \\ n = k = l \text{ if } k = l \\ n = 9 - k - l \text{ if } k \neq l \end{aligned} \tag{2.3}$$

Taking the x_3 axis to be parallel to the axis of symmetry (in the case of the inner core, this would be the axis of rotation) we have:

$$C_{mn} = \begin{pmatrix} C_{11} & C_{11}-2C_{66} & C_{13} & 0 & 0 & 0 \\ C_{11}-2C_{66} & C_{11} & C_{13} & 0 & 0 & 0 \\ C_{13} & C_{13} & C_{33} & 0 & 0 & 0 \\ 0 & 0 & 0 & C_{44} & 0 & 0 \\ 0 & 0 & 0 & 0 & C_{44} & 0 \\ 0 & 0 & 0 & 0 & 0 & C_{66} \end{pmatrix} \tag{2.4}$$

$$C_{mn} = \begin{pmatrix} A & A-2N & F & 0 & 0 & 0 \\ A-2N & A & F & 0 & 0 & 0 \\ F & F & C & 0 & 0 & 0 \\ 0 & 0 & 0 & L & 0 & 0 \\ 0 & 0 & 0 & 0 & L & 0 \\ 0 & 0 & 0 & 0 & 0 & N \end{pmatrix} \tag{2.5}$$

Using the above C_{mn} matrices we can solve Equation 2.2 analytically and assuming the anisotropy is weak this provides us with the P-wave velocity in terms of the love coefficients

$$\begin{aligned} \rho V_p^2 =& \frac{1}{8}(3A+3C+4L+2F) + \frac{1}{2}(C-A)\cos(2\zeta) \\ &+ \frac{1}{8}(A+C-4L-2F)\cos(4\zeta) \end{aligned} \tag{2.6}$$

and the quasi S-wave velocities, whose particle motions are meridional and equatorial:

$$\rho S_{me}^2 = \frac{1}{8}(A+C+4L-2F) - \frac{1}{8}(A+C-4L-2F)\cos(4\zeta) \tag{2.7}$$

$$\rho S_{eq}^2 = \frac{1}{2}(L+N) + \frac{1}{2}(L-N)\cos(2\zeta) \tag{2.8}$$

where ζ is the angle between the propagation direction and the symmetry axis (Figure 2.1). The terms with $\cos(2\zeta)$ $\cos(4\zeta)$ are the anisotropy terms while the first term is independent of direction.

Focusing on P-wave anisotropy and considering only the perturbations for weak anisotropy, we can describe transverse isotropy in the common form:

$$\frac{\delta t}{t} = \frac{\delta V_p}{V_p} = a + b\cos^2(\zeta) + c\cos^4(\zeta) \tag{2.9}$$

where $\frac{\delta t}{t}$ is equivalent to the velocity anomaly $\frac{\delta v}{v}$ assuming low attenuation in the inner core, the equatorial velocity anomaly is given by a (also denoted

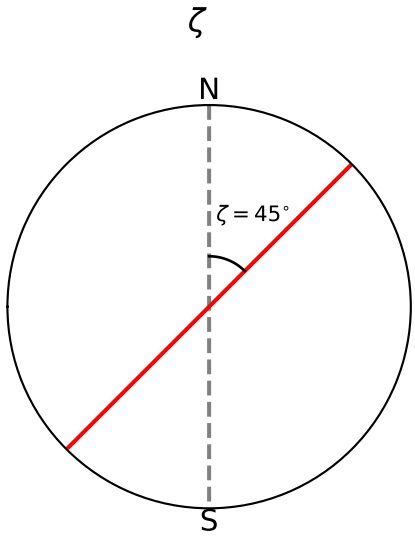

Figure 2.1 A cross section of the inner core, showing a raypath (the red line) passing through the inner core at an angle of $\zeta = 45°$ to Earth's axis of rotation.

as δV_{eq} in Chapters 4 and 7), b and c are related to components of the elastic tensor C_{mn}, by $b = (-A+2L+F)/A$ and $c = (A+C-4L-2F)/2A$ (Creager, 1992). The amount of anisotropy, δV_{ani}, is defined as the velocity difference between polar and equatorial raypaths, given by $b + c$. This measure of anisotropy is strictly for cylindrical anisotropy, and assumes that the slow and fast directions are perpendicular. From the model parameters a, b and c we calculate the isotropic velocity, or Voigt average velocity (Lythgoe *et al.*, 2014) commonly interpreted by mineral physicists;

$$\delta V_{iso} = a + \frac{b}{3} + \frac{c}{5} \tag{2.10}$$

Equation 2.9 reveals that the slowest velocity direction is not restricted to an angle of $\zeta = 90°$, but depends on combinations of b and c, thus can be any angle between $0 - 90°$. The slowest angle is obtained by differentiating Equation 2.9 and calculating its maximum value, following Lythgoe *et al.* (2014), which results in the following:

$$\zeta_{slow} = \cos^{-1} \sqrt{\frac{-b}{2c}} \tag{2.11}$$

Some variations in ζ_{slow} are statistically insignificant: it is possible to have a

large range of values of ζ_{slow} but with minimal absolute velocity differences between ζ_{slow} and $\zeta = 90°$. To only keep statistically significant values of ζ_{slow} we use a tolerance condition when calculating ζ_{slow} from our models of inner core anisotropy. The difference between ζ_{slow} velocity and the velocity at $\zeta = 90°$ must be greater than 0.5% relative to our reference model.

Alternatively, some authors use another form of Equation 2.9, where we replace $b = \epsilon - \sigma$, and $c = \sigma$:

$$\begin{aligned} \frac{\delta V_p}{V_p} &= a + (\epsilon - \sigma)\cos^2(\zeta) + \sigma\cos^4(\zeta) \\ \frac{\delta V_p}{V_p} &= a + \epsilon\cos^2(\zeta) - \sigma\sin^2(\zeta)\cos^2(\zeta) \end{aligned} \tag{2.12}$$

where $\epsilon = (C - A)/2A$ and $\sigma = (A + C - 4L - 2F)/2A$. Several inner core studies have used this alternative parameterization, including Morelli *et al.* (1986), Song (1997), Frost and Romanowicz (2019) and Lima *et al.* (2022).

2.2 The normal mode parameterization; α, β, γ

When using normal modes we parameterize anisotropy in the inner core differently to the body waves. Assuming that the axis of symmetry is parallel to Earth's axis of rotation, then only the zonal, c_{20} and c_{40} parameters of a normal mode splitting function would be affected by inner core anisotropy (Woodhouse *et al.* (1986); Tromp (1995)). This anisotropy can be described using three parameters α, β and γ, which are related to the Love parameters:

$$\begin{aligned} \alpha &= \frac{(C - A)}{A_0} \\ \beta &= \frac{(L - N)}{A_0} \\ \gamma &= \frac{(A - 2N - F)}{A_0} \end{aligned} \tag{2.13}$$

where $A_0 = \rho_0 v_{p0}^2$ is the reference value at the centre of the inner core, which we take from PREM (Dziewonski and Anderson, 1981). α describes the P-wave anisotropy, β describes the S-wave anisotropy and γ describes the anisotropy of waves not travelling parallel or perpendicular to the symmetry axis. In this way we do not model the inner core using absolute values of

A, C, L, F and N, but rather differences between them relative to our reference model.

The zonal parameters, c_{20} and c_{40}, of a normal mode splitting function can be calculated thus:

$$c_{s0} = \int_0^{ICB} \alpha(r)K_s^\alpha + \beta(r)K_s^\beta + \gamma(r)K_s^\gamma dr \tag{2.14}$$

where r is the radius, which we integrate from 0 to the inner core boundary, s is the spherical harmonic degree, c_{s0} is our measured splitting function value of c_{20} or c_{40} and K_s^α, K_s^β and K_s^γ are the sensitivity kernels of the c_{s0} coefficient to these model parameters which are calculated using normal mode theory (Tromp, 1995).

To calculate the fractional velocity of a P-wave in terms of α, β, γ and ζ relative to PREM, we start from Equation 2.9:

$$\frac{\delta V_p}{V_p} = \delta V_{eq} + b\cos^2(\zeta) + c\cos^4(\zeta) \tag{2.15}$$

we have renamed a to δV_{eq} to avoid confusion with α. From the definitions of α, β and γ it follows that:

$$b = 2\beta - \gamma \tag{2.16}$$

$$c = \frac{1}{2}\alpha - 2\beta + \gamma \tag{2.17}$$

and therefore the fractional differential travel time of a P-wave in terms of α, β, γ, δV_{eq} and ζ is:

$$\delta V_p(\zeta) = \delta V_{eq} + (2\beta - \gamma)\cos^2(\zeta) + (\frac{1}{2}\alpha - 2\beta + \gamma)\cos^4(\zeta) \tag{2.18}$$

or alternatively rearranging the equations to separate each of the parameters:

$$\frac{\delta V_p}{V_p} = \delta V_{eq} + \frac{1}{2}\alpha\cos^4(\zeta) + 2\beta[\cos^2(\zeta) - \cos^4(\zeta)] + \gamma[\cos^4(\zeta) - \cos^2(\zeta)] \tag{2.19}$$

This equation follows from Morelli *et al.* (1986) and can also be found in Beghein and Trampert (2003) (without the δV_{eq} term, as they did not take into account changes in equatorial velocity).

2.3 Conclusion

Ultimately, whether using a, b and c or α, β and γ we are attempting to simplify our description of transverse isotropy in such a way that we do not have to constrain all 5 of the Love parameters, A, C, L, F and N. When utilising normal mode data it is sensible to use α, β and γ as they have unique sensitivity to each parameter, while when using body wave data it is better to use a, b and c for the same reasons.

The difficulty comes when comparing models made using these two parameterizations or when trying to combine both types of data into a joint inversion. Combining the two types of data requires compromises, which we discuss at length in Chapter 7. In future work I would like to solve for models which utilise a more general description of transverse isotropy in the inner core, suitable for both normal modes and body waves and which would allow for the symmetry axis of the anisotropy to vary, and not remain fixed parallel to Earth's axis of rotation. This is still a work in progress and as such has not been incorporated into this thesis.

3

Inner core anisotropy measured using new ultra-polar PKIKP paths

We measure the seismic anisotropy of the inner core using PKPbc-PKPdf and PKPab-PKPdf differential travel times, as a function of the angle ζ between the Earth's rotation axis and the ray path in the inner core. Previous research relied heavily on body waves originating in the South Sandwich Islands (SSI) and traveling to seismic stations in Alaska to sample inner core velocities with low ζ (polar paths). These SSI polar paths are problematic because they have anomalous travel time anomalies, there are no ultra polar SSI paths with $\zeta < 20°$ and they only cover a small part of the inner core. Here we improve constraints on inner core anisotropy using recently installed seismic stations at high latitudes, especially in the Antarctic, allowing us to measure ultra polar paths with ζ ranging from $20° - 5°$. Our new data shows that the South Sandwich Island's polar events are fast but still within the range of velocities measured from raypaths originating elsewhere. We further investigate the effect of mantle structure on our data set finding that the SSI data is particularly affected by fast velocities underneath the SSI originating from the subducted South Georgia slab which is currently located just above the CMB. This fast velocity region results in mantle structure being misinterpreted as inner core structure and we correct for this using a P-wave tomographic model. We also analyse the effect of velocity changes on the raypaths within the inner

The research in this chapter was published as: Brett H., Deuss A., Inner core anisotropy measured using new ultra-polar PKIKP paths, *Geophysical Journal International*, **Volume 223**, Issue 2, November 2020, Pages 1230–1246, https://doi.org/10.1093/gji/ggaa348

core and find that faster velocities significantly change the raypath resulting in the ray travelling deeper into the inner core and spending more time in the inner core. To remove this effect we propose a simple but effective method to correct each event-station pair for the velocity dependent raypath changes in the inner core, producing a more reliable fractional travel time measurement. Combining the new ultra polar data with mantle and raypath corrections results in a more reliable inner core anisotropy measurement and an overall measured anisotropy of 1.9%-2.3% for the whole inner core. This is lower than previous body wave studies ($\sim$ 3% anisotropy) and in better agreement with the value of inner core anisotropy measured by normal modes ($\sim$ 2% anisotropy). We also identify regional variation of anisotropic structure in the top 500 km of the inner core which appears to be more complex than simple hemispherical variations. These regional variations are independent of the SSI data and are still present when these data are excluded. We also find a potential innermost inner core with a radius of 690 km and stronger anisotropy.

3.1 Introduction

Anisotropy was first observed in the inner core by Poupinet *et al.* (1983) and they found that the travel time of polar paths (raypaths with a $\zeta < 35°$ where ζ is the angle between the raypath and the Earth's axis of rotation) was shorter than for equatorial paths ($\zeta > 35°$). Morelli *et al.* (1986) quantified the inner core anisotropy explicitly, concluding that 1% cylindrical anisotropy with the fast direction aligned with Earth's rotation axis best explained the observed travel time residuals. In the same year Woodhouse *et al.* (1986) found that inner core anisotropy also explains observations of anomalous zonal splitting of Earth's free oscillations or normal modes.

The symmetry axis of anisotropy in the inner core has been a topic of research with early studies suggesting the axis is at an angle of 6°, relative to Earth's rotation axis (Shearer and Toy (1991); Creager (1992)); later research placed the axis of anisotropy between 4° and 10° (Su and Dziewonski (1995); Song (1996); Isse and Nakanishi (2002)). Irving and Deuss (2011) and more recently Frost and Romanowicz (2019) found that there was no evidence for a tilted anisotropy axis relative to the Earth's rotation axis.

There is also evidence for a heterogeneous distribution of inner core anisotropy into two hemispheres with different amounts of anisotropy (Tanaka and Hamaguchi (1997); Creager (1999); Garcia and Souriau (2000); Garcia (2002); Niu and Wen (2001); Wen and Niu (2002); Oreshin and Vinnik (2004); Yu and Wen (2006); Deuss *et al.* (2010); Irving and Deuss (2011);

Lythgoe *et al.* (2014)). A western hemisphere with slow isotropic velocity at shallow depths up to approximately 200km and strong anisotropy deeper in the inner core was recognised, along with an eastern hemisphere with a fast isotropic velocity at shallow depth and little or no anisotropy at larger depths. The boundaries between these hemispheres varies significantly between the different studies and the term hemisphere is misleading as the eastern hemisphere is often found to be almost half the size of the western hemisphere. Thus, some research has started calling the hemispheres the quasi-western and quasi-eastern hemispheres (Tanaka and Hamaguchi (1997); Irving and Deuss (2011)). Most evidence for hemispheres comes from body wave studies but normal modes have also observed the overall hemispherical pattern of anisotropy using cross coupled splitting function observations (Deuss *et al.*, 2010).

In addition to the lateral variations, there are also observed variations with depth. The uppermost 100 km of the inner core shows an isotropic slower layer in the west and a faster isotropic layer in the east (Niu and Wen (2001); Waszek and Deuss (2011)). Some studies have also found evidence for an innermost inner core with a radius varying between 300 and 750 km, and a fast symmetry axis of anisotropy being oriented in the pseudo equatorial plane and not showing hemispherical variations (Ishii *et al.* (2002a); Beghein and Trampert (2003); Ishii and Dziewoński (2003); Sun and Song (2008a)). The more recent body wave study by Lythgoe *et al.* (2014), however, does not observe an innermost inner core and proposes that observations of an innermost inner core are a result of averaging the hemispherical structure. Recent research by Frost and Romanowicz (2019) also shows that an innermost inner core is not required by their data but that if it did exist it would have a radius of 750 km and have an anisotropy axis quasi parallel to Earth's rotation axis.

Author	Year	Reference Phases	Overall Ani.	Hemispheres	Eastern Ani.	Western Ani.
Poupinet et al.	1983	P	-	-	-	-
Morelli et al.	1986	PKPbc, PKPab	1.0%	-	-	-
Shearer et al.	1988	PKPbc	3.0%	-	-	-
Shearer and Toy	1991	PKPbc	4.0%	-	-	-
Creager	1992	PKPbc	3.5%	-	-	-
Tanaka and Hamaguchi	1997	PKPbc	1.5%	yes	0.5%	2.4%
Creager	1999	PKPbc, PKPab	2.0%	yes	0.5%	2-4%
Garcia and Souriau	2000	PKPbc	3.0%	-	-	-
Garcia	2002	PKPbc, PKPab	3.0%	yes	-	-
Garcia et al.	2006	PKPbc, PKPab	-	yes	-	-
Sun and Song	2008	PKPbc, PKPab, PKPcd	2.0%	yes	0.5%	2.0%
Leykam et al.	2010	PKPbc, PKPab	0.7%	yes	0.1%	-
Irving and Deuss	2011	PKPbc, PKPab	3.5%	yes	1.4%	4.5%
Lythgoe et al.	2014	none	5%	yes	0.5-1.5%	3.5-8%
Frost and Romanowicz	2019	PKPbc, PKPab, PKIIKP-PKPdf2	3.5%	yes	-	-

Table 3.1 Summary of values of anisotropy from previous body wave studies, note that this list is not exhaustive. Some papers that propose hemispheres but don't explicitly state values of anisotropy, likewise some papers don't mention hemispheres at all, thus a lack of 'yes' under column 'Hemispheres' does not mean that those authors conclude that hemispheres don't exist. Some papers don't explicitly state their measured values of anisotropy and it has to be inferred. Papers which only used PKPcd as a reference phase and therefore focused on the upper most inner core have been left out.

Author	Year	Overall Ani.
Woodhouse et al.	1986	3.35%
Tromp	1993	2.1%
Durek and Romanowicz	1999	2.50%
Ishii et al.	2002	1.75%
Beghein and Trampert	2003	2.94
Mäkinen et al.	2014	1.75%

Table 3.2 Summary of values of anisotropy from normal mode studies of the inner core.

Table 3.1 summarizes previously published values of anisotropy and observations of hemispheres from body wave studies, while Table 3.2 does the same for normal mode studies for completeness. The value of inner core anisotropy found in previous body wave studies has an average value of 3% and ranges between 0.7% and 5%. The average value of anisotropy for normal modes from recent studies is 2% and lower than the measurements from body wave studies.

The main problem faced by studies which measure inner core anisotropy from body waves has been the dominance of raypaths going from earthquakes in the South Sandwich Islands (SSI) to seismic stations in Alaska in polar data ($\zeta < 35°$) and the lack of ultra-polar data ($\zeta < 20°$). The SSI to Alaska raypaths are problematic as they have a much stronger positive travel time anomaly than other polar raypaths (i.e. arrive earlier than expected). Due to the absence of ultra polar data, the anisotropy models have been extrapolated for $\zeta < 20°$ leading to anisotropy values of up to 5% for body waves (Table 3.1). The anisotropy from body waves has also been difficult to reconcile with much smaller normal mode anisotropy values of only 2%.

The source of the positive travel time anomaly from the SSI has been the subject of many previous studies. One of the earliest studies to draw attention to these raypaths was Romanowicz *et al.* (2003), who conducted corrections using mantle tomography models on the SSI to Alaska raypaths. They concluded that while some of the anomaly could be explained by mantle structure a significant source of the anomaly was necessary somewhere in the core. They proposed an 'outer core tangent cylinder' with a positive P-wave velocity anomaly of 1% as an explaination for the SSI anomaly. This cylindrical structure which is tangent to the inner core and parallel to Earth's axis of rotation was proposed by outer core geodynamical modelling (Hollerbach and Jones (1995); Olson *et al.* (1999)). Tkalčić (2010) took a

different approach and analysed PcP paths originating from the South Sandwich Islands. He found that these lower mantle phases with no sensitivity to the inner core, also exhibit strong positive travel time anomalies of the same order as that observed in the inner core. He concluded that the source of the travel time anomaly could be due to mantle structure beneath the South Sandwich Islands. Long *et al.* (2018) proposed that a lower mantle structure with a small size of only a few 100s of km underneath Alaska could explain the anomaly and would not show up easily on global tomographic models due to its small size. Most recently, the work of Frost *et al.* (2020), using array techniques in Alaska and 3D ray-tracing, shows that the Alaskan slab has a profound effect on the arrival times of the PKPdf phase, implying that the SSI anomaly is due to upper mantle affects on the Alaskan side of the SSI to Alaska raypaths.

The recent installation of new Antarctic seismic stations and a complete reanalysis of all suitable data available through the International Federation of Digital Seismograph Networks (FDSN) has made it possible to observe ultra polar paths and significantly increase the number of polar events which do not have an origin in the SSI region. In this chapter we will present a new large body wave data set of PKPdf-PKPbc and PKPdf-PKPab differential travel times with more polar and ultra-polar paths than previously published. The new data allows us to improve constraints on inner core anisotropy and to constrain the SSI anomaly. We also propose a simple method to correct differential travel time measurements for the fact that corresponding velocity anomalies lead to a shallower or deeper raypath in the inner core. In addition we also correct for the significant influence of heterogeneous mantle structure, as imaged through tomography, on our data. Combining the new data with raypath and mantle corrections greatly improves the longitudinal and depth resolution of the inner core and gives us greater insight into inner core structure. It also removes the need for using the South Sandwich Island ray paths and allows us to investigate anisotropy without using these data.

3.2 Methodology

3.2.1 Data collection and processing

We measure inner core anisotropy with compressional body waves, using the arrival time of the PKPdf phase (which travels through the mantle, outer core and inner core) in comparison to the arrival time of the PKPbc and PKPab phases (which only travel through the outer core and the mantle), see Figure 3.1 for their raypaths. Event-station pairs were collected for sta-

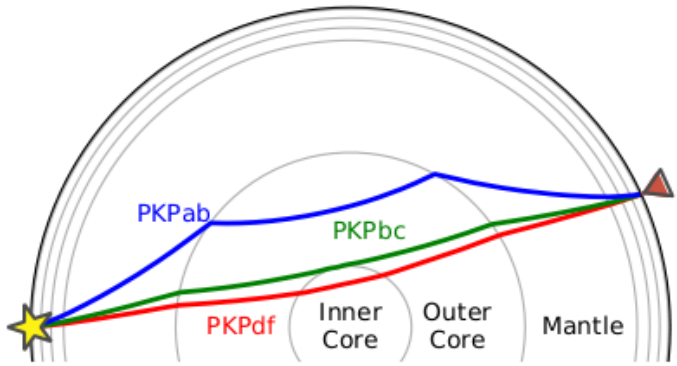

Figure 3.1 Raypaths of PKPdf (red),PKPab (blue) and PKPbc (green) phases through the Earth. Made using Obspy and TauP. The star represents the location of the source and the triangle is the location of the seismometer that measures the arrivals.

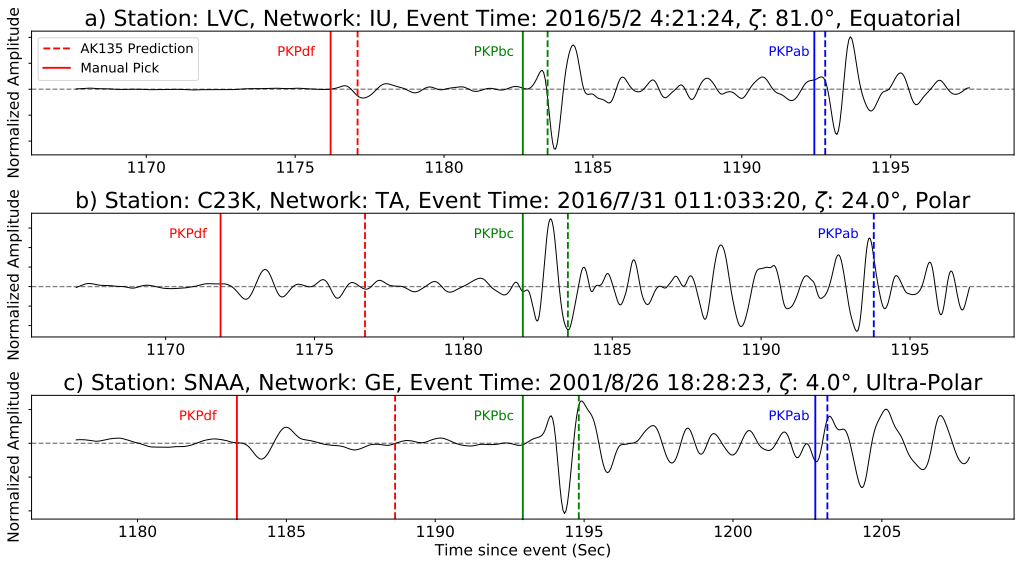

Figure 3.2 Three seismograms of different values of ζ showing PKPdf (red), PKPbc (green) and PKPab (blue) phases. The solid lines are the arrivals picked by hand while the dashed lines are the arrivals of each phase as predicted by AK135 (Kennett *et al.*, 1995) and is calculated using the TauP toolkit. (Crotwell *et al.*, 1999)

tions available through the FDSN recording between 1991 and 2019 with an epicentral distance between $146.5° - 178°$ and an event bodywave magnitude greater than $m_b = 5.0$. These seismograms are then bandpass filtered with two poles and corner frequencies at 0.5 and 2Hz. We inspected the vertical component seismograms for 188,257 event-station pairs by eye and from this selected a high quality data set of 2186 seismograms (a pass rate of 1.24%). The pass rate is so low due to the high attenuation of the PKPdf phase; this means that this phase is not visible above the noise threshold in the majority of seismograms.

We measure the travel time difference between PKPdf and PKPab or PKPbc, to minimize the effect of mantle structure and inaccuracies in event location and time (Creager, 1992). The difference in arrival times between these phases has been assumed to be caused by inner core structure alone. This assumption is based on the argument that the inner core (PKPdf) and outer core phases (PKPbc and PKPab) travel nearly the same path through the Earth, deviating only in the inner core. Looking at Figure 3.1 it can be seen this assumption is more valid for PKPbc than PKPab. We will investigate if this assumption is indeed correct in Section 3.3.2, and will show that especially for the South Sandwich Islands (SSI) this may not be the case. The PKPbc-PKPdf differential travel time is measured for epicentral distances between $146° - 155.5°$ while the PKPab-PKPdf differential travel time is measured for epicentral distances between $150° - 180°$. As a result, PKPbc-PKPdf is only sensitive to the upper 350 km of the inner core while the PKPab-PKPdf differential travel time is sensitive to up to 1100 km below the inner core boundary (allowing sampling of almost the entire volume of the inner core).

Using our measured arrival times, we calculate the differential travel time δt;

$$\delta t = (\mathrm{t_{PKPref}} - \mathrm{t_{PKPdf}})_{\mathrm{data}} - (\mathrm{t_{PKPref}} - \mathrm{t_{PKPdf}})_{\mathrm{AK135}} \tag{3.1}$$

Where $(\mathrm{t_{PKPref}} - \mathrm{t_{PKPdf}})_{\mathrm{data}}$ is the difference in arrival time between a reference phase (either bc or ab) and the PKPdf phase, as measured in the data. The second term, $(\mathrm{t_{PKPref}} - \mathrm{t_{PKPdf}})_{\mathrm{AK135}}$ is the difference in arrival time as predicted by the 1D model AK135 (Kennett *et al.*, 1995) and calculated using the TauP toolkit (Crotwell *et al.*, 1999). Differential travel times are corrected for ellipticity using the method of Dziewonski and Gilbert (1976).

We define the angle ζ between the raypath in the inner core and the Earth's rotation axis as:

$$\cos(\zeta) = \frac{\cos(\theta_o) - \cos(\theta_i)}{\sqrt{2 - 2\cos(\theta_o)\cos(\theta_i) - 2\sin(\theta_o)\sin(\theta_i)\cos(\phi_o - \phi i)}} \tag{3.2}$$

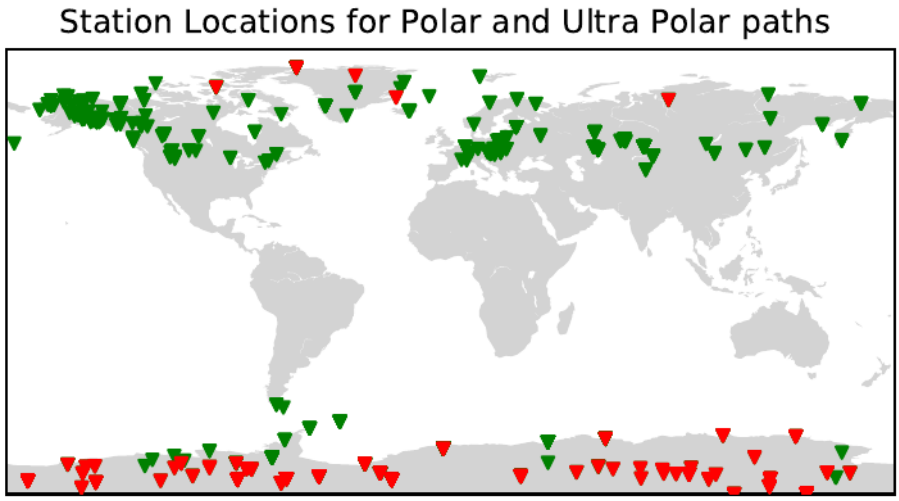

Figure 3.3 Map of the station locations used to measure polar data (green triangles) and ultra polar data (red triangles).

where θ_o and θ_i are the co-latitudes of where the ray leaves and enters the inner core while ϕ_o and ϕ_i are the longitudes (i.e. Irving and Deuss (2011)). The pierce point locations (where the PKPdf ray enters and leaves the inner core) are calculated using the AK135 model (Kennett *et al.*, 1995) and the TauP toolkit (Crotwell *et al.*, 1999) in combination with the python package 'Geographicslib'. If a raypath has $\zeta > 35°$, we call it a equatorial path, if it has $\zeta < 35°$ it is polar and if a raypath has $\zeta < 20°$ it is considered ultra-polar.

Figure 3.2 shows three example seismograms and the phase arrival times predicted by AK135 and our own picks. To measure the arrivals we pick the times of the onset of each phase, minimizing the effect of attenuation in the inner core which causes the PKPdf peak to be broadened relative to the PKPbc and PKPab arrivals. It can be seen that the PKPdf phase arrives approximately when predicted by AK135 on the equatorial seismogram (Figure 3.2a) but for the polar path (Figure 3.2b) and ultra polar path it arrives much earlier (Figure 3.2c). These travel time anomalies are evidence for anisotropy with the fast axis in the polar direction.

One of the key aims of this research is to significantly increase the currently available data sets of PKPdf-PKPbc and PKPdf-PKPab paths, particularly focusing on extending the observations of polar paths and earth-

ζ	ab & bc	Only bc	Only ab	Total
All ζ	742	821	623	2186
$\zeta > 35$	350	268	468	1086
$20 < \zeta < 35$	338	498	120	956
$\zeta < 20$	54	55	35	144

Table 3.3 Numbers of differential travel times collected for each phase and corresponding range of ζ. For some events both PKPab and PKPbc have been measured, for other events only one of the two phases has been measured. The "Total" column gives the total number of unique raypaths. i.e. $N_{ab\ \&\ bc} + N_{only\ ab} + N_{only\ bc}$

quakes not originating in the SSI. Our aim was largely achieved through the re-collection and re-analysis of all polar data available from the FDSN since 1991 and resulted in a data set of 2186 high quality seismograms of which 623 PKPbc (only), 821 PKPab (only), and 742 have both PKPab and PKPbc measurements (Table 3.3). 584 measurements are polar paths which do not originate in the SSI and of these 142 paths are ultra polar. This new polar data was largely collected from stations at high latitudes, especially the Antarctic; Figure 3.3 shows the locations of these stations. Leykam *et al.* (2010) were the first to recognise the potential of using these new high latitude seismic stations to better constrain inner core anisotropy. However, since Leykam *et al.* (2010) many more earthquakes have been recorded and yet more seismic stations installed at high latitudes allowing for a significant increase in ultra polar data. For example Leykam *et al.* (2010) measured 17 PKPdf-PKPab and PKPdf-PKPbc ultra polar paths in comparison to 144 in our study (Table 3.3). Revisiting this data is significant as our values of anisotropy for the inner core are much higher than those of Leykam *et al.* (2010) as a result of the increased data coverage. Data utilizing these new Antarctic seismic stations have also been used to investigate inner core anisotropy in the recent paper by Frost and Romanowicz (2019), however the dataset we present here has been collected independently and includes different event station pairs.

3.3 Results

3.3.1 Anisotropy

A medium is said to be anisotropic when seismic velocity is dependent on the direction of wave propagation through the medium. To accurately measure anisotropy, it is important to have differential travel time (δt) data with a good global coverage for all angles of ζ and spanning all longitudes. Figure

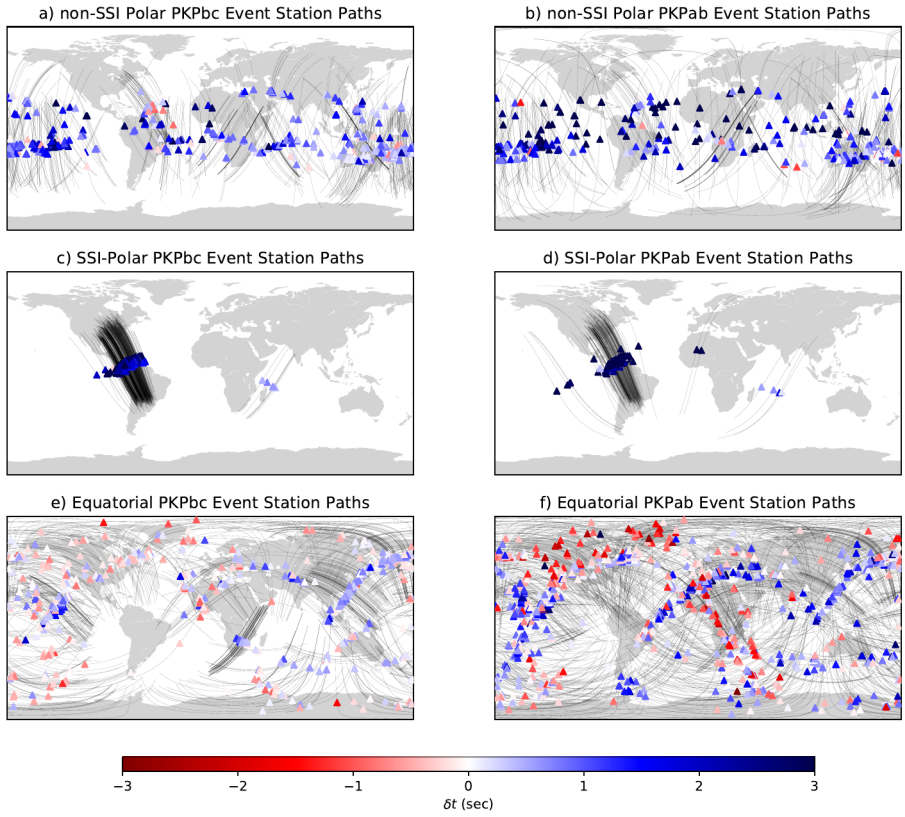

Figure 3.4 The global coverage of our data set with the left column being data with PKPbc as the reference phase and the right column with PKPab as a reference phase. a) and b) Raypath coverage within the inner core of polar data excluding the South Sandwich Islands, c) and d) Raypath coverage of polar South Sandwich Islands data and e) and f) Raypath coverage of equatorial data. The color of the triangles indicate the δt of each raypath and are plotted at the location of the turning point of the raypath.

3.4 shows the spatial sampling of our data set, and includes good even coverage of polar data which do not have an origin in the South Sandwich Islands (SSI) (Figure 3.4 a,b) due to our extensive use of stations in the Antarctic (Figure 3.3). Our data set represents a significant improvement in data coverage on previous research. Looking at the δt of all the paths it can be seen that polar paths have mostly positive δt (i.e. faster) than equatorial paths but that there are also examples of polar raypaths with negative δt (i.e. slower). There are more equatorial paths with negative δt than polar paths, but there are also regions of equatorial paths with positive δt (Figure 3.4 e,f). The polar paths for events originating in the SSI, have the strongest positive δt anomalies and high numbers of paths traveling to Alaska can be seen (Figure 3.4 c,d). These are the paths which have dominated inner core anisotropy measurements for so long due to their high number and strong positive anomaly; they are the reason why finding more polar and ultra polar data not originating in the SSI is important.

Figure 3.5 shows how $\frac{\delta t}{t}$ varies with ζ for our data set. $\frac{\delta t}{t}$ is the differential travel time δt calculated using Equation 3.1 normalized by the time spent in the inner core (t) as modelled using AK135. This normalization takes into account the different amount of time travelled by rays going deeper or shallower through the inner core. Raypaths with smaller values of ζ have a stronger positive travel time anomaly than equatorial paths with larger values of ζ, albeit with a large scatter (Figure 3.5 a,b). The SSI data clearly stand out when compared to other polar data, and unfortunately no ultra polar data exists for earthquakes originating in the SSI. Figure 3.6 shows the same figures without the SSI data further highlighting the influence of this data.

To measure anisotropy from our data we need to quantify the change in velocity as a function of ζ so that we can relate it to the relevant components of the elastic tensor. We model anisotropy using the same equation as in previous research (i.e. Creager (1992); Creager (1999); Irving and Deuss (2011); Lythgoe *et al.* (2014)):

$$\frac{\delta t}{t} = \frac{\delta v}{v} = a + b\cos^2(\zeta) + c\cos^4(\zeta) \tag{3.3}$$

where $\frac{\delta t}{t}$ is equivalent to the velocity anomaly $\frac{\delta v}{v}$ assuming low attenuation in the inner core, and a, b and c are related to the Love coefficients (Love, 1927) (Equation 3.3 is derived in Section 2.1, Equation 2.9). The equatorial velocity perturbation is given by a and $b + c$ describes the anisotropy (Creager, 1999). By fitting Equation 3.3 to our data set of measured $\frac{\delta t}{t}$, we determine the a, b and c parameters and relate these to velocity anisotropy.

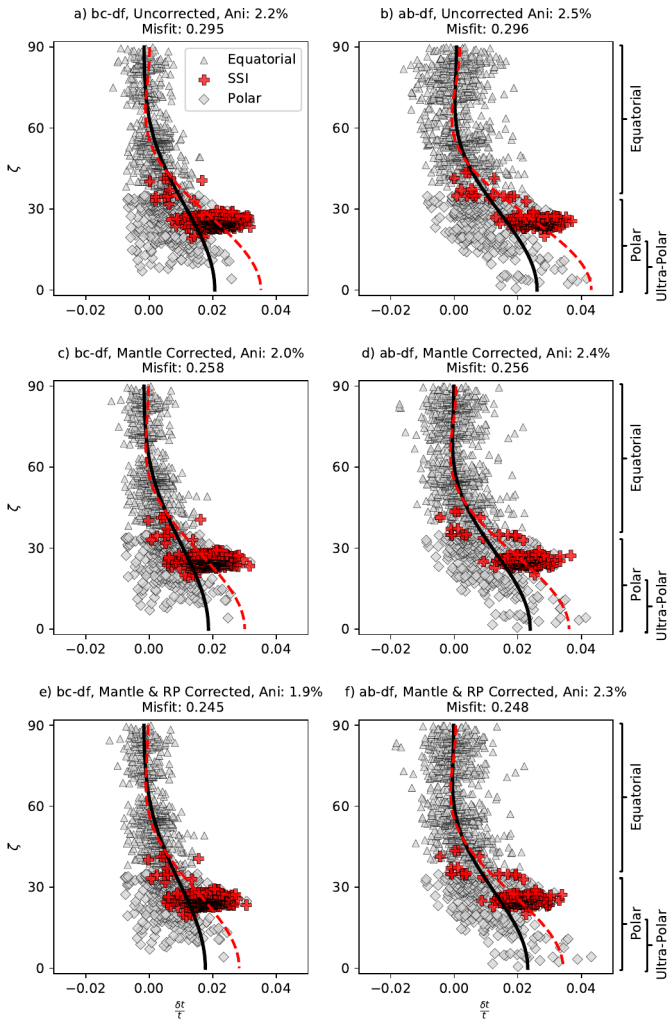

Figure 3.5 a) Variation of $\frac{\delta t}{t}$ as a function of ζ for a) PKPbc-PKPdf and b) PKPab-PKPdf. The black line is the function described by Equation 3.3 fitted to all data with a least squares norm. The red dashed line is the function described by Equation 3.3 fitted to equatorial and South Sandwich Islands data only. The triangles are equatorial data ($\zeta > 35°$), diamonds are polar data (not including South Sandwich Islands) and the crosses are the South Sandwich Islands data. c), d) variations of $\frac{\delta t}{t}$ against ζ applying mantle corrections using the UUP07 tomographic model. e), f) variation of $\frac{\delta t}{t}$ applying mantle and raypath corrections.

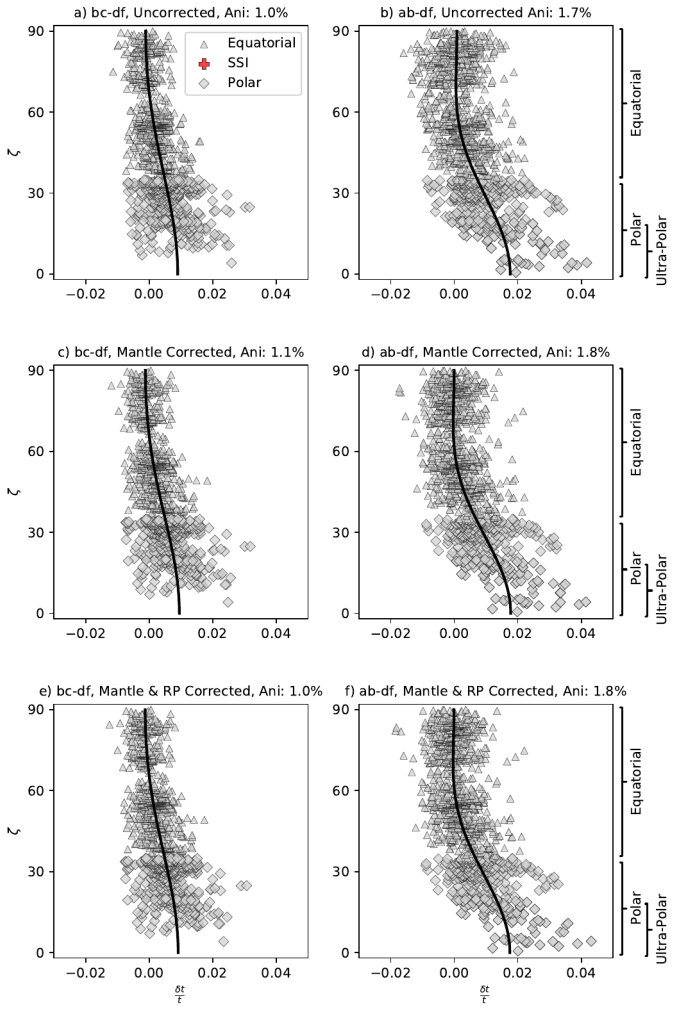

Figure 3.6 a) Variation of $\frac{\delta t}{t}$ as a function of ζ for a) PKPbc-PKPdf and b) PKPab-PKPdf with the SSI data removed. The black line is the function described by Equation 3.3 fitted to the data with a least squares norm. The triangles are equatorial data ($\zeta > 35°$), diamonds are polar data (not including South Sandwich Islands). c), d) variations of $\frac{\delta t}{t}$ against ζ applying mantle corrections using the UUP07 tomographic model. e), f) variation of $\frac{\delta t}{t}$ applying mantle and raypath corrections.

When we fit Equation 3.3 to our whole data set (including the SSI and our new ultra polar data) we get an average anisotropy for the inner core of 2.5% for PKPdf-PKPab and 2.2% for PKPdf-PKPbc. These values are lower than measurements from other body wave studies which normally find values of 3-4%. Our lower anisotropy values are a direct result of having more polar data and especially ultra polar data ($\zeta < 20°$). If we fit Equation 3.3 only to the equatorial data and data from the SSI, then we get a much larger anisotropy of 3.5% for PKPbc and 4.2% for PKPab. Without the ultra polar data, the anisotropy will be extrapolated from the SSI anomalies for $\zeta < 25°$ resulting in an overestimation of anisotropy. This is why raypaths travelling from the SSI to stations in Alaska became the focus of much debate (Tkalčić, 2015) and explaining the large positive velocity anomaly arising from the South Sandwich Island data is a key challenge in measuring inner core anisotropy.

3.3.2 The South Sandwich Islands

While the travel time anomalies $\frac{\delta t}{t}$ for the South Sandwich Islands (SSI) to Alaska raypaths are within the spread of other polar data, the source of the fast velocities is still an important question. After inspection of over 186,359 seismograms, we found that the SSI data had some of the clearest arrivals and were relatively easy to measure differential travel times. This leads to the conclusion that the observed PKPbc/ab-PKPdf measurements for the SSI are accurate, ruling out systematic measurement error. Thus there seems to be three possible explanations for the large SSI $\frac{\delta t}{t}$:

1. Mantle and outer core heterogeneity is affecting the arrival times of PKPdf/bc/ab phases unequally.

2. Our modelled raypaths are inaccurate.

3. The SSI $\frac{\delta t}{t}$ is an accurate measurement of the inner core and there is a large positive velocity anomaly along the SSI to Alaska raypaths.

Mantle heterogeneity

When we use differential arrival times to investigate inner core structure we assume that PKPdf and the reference phases PKPbc and PKPab sample the same structure in the mantle and that the outer core is laterally homogeneous. If this assumption is incorrect it would result in mantle structure being misinterpreted as inner core structure. Looking at Figure 3.1 it can be seen that there are large differences between the PKPab and PKPdf

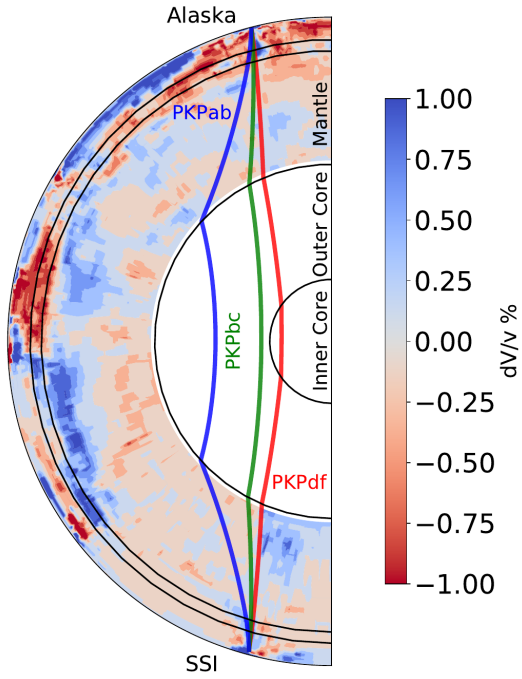

Figure 3.7 A cross section through the UUP07 model by Amaru (2007)

raypaths in the lower mantle and outer core while the raypaths travel much closer in the upper mantle. This is also reflected by the PKPbc raypaths but the differences are smaller. If mantle heterogeneity is indeed affecting the differential travel time measurements then it will most likely occur in the lower mantle because this is where the PKPbc and PKPdf raypaths differ most. However we cannot rule out upper mantle structure.

To investigate whether the PKPab, PKPbc and PKPdf phases sample different structure in the lower mantle we use the UUP07 mantle P-wave tomographic model from Amaru (2007). A cross section through the UUP07 model going from the SSI to Alaska (Figure 3.7) shows that underneath the SSI, there is a strong positive velocity anomaly interpreted to be the subducted South Georgia slab (Meer *et al.*, 2018). The PKPdf phase appears to just pass through this faster material underneath the SSI, while the PKPbc and PKPab phases do not. Thus, mantle structure does affect PKPbc, PKPab and PKPdf differently.

We correct for our whole data set for mantle structure using UUP07, including the SSI data and non-SSI data (Figure 3.5 c,d). This is done using

1D rays calculated for AK135 and then integrating the velocity anomaly from the tomographic model over the entire path of the ray. While taking into account 3D effects would be a more thorough approach, doing this for a global dataset and global tomographic model is not straightforward and considered as a subject for future study. Initially the effect appears minor, only reducing the anisotropy for PKPbc-PKPdf to 2% (Figure 3.5 a,c) and for PKPab-PKPdf to 2.4% (Figure 3.5 b,d). However, a closer look reveals that the SSI data is more strongly affected compared to the rest of the data. Furthermore the misfit (calculated using an L2 norm), shown in the title of each panel on Figure 3.5 is reduced in both the PKPbc and PKPab data by these corrections. Doubling or tripling the UUP07 corrections reduces the $\frac{\delta t}{t}$ anomaly from the SSI significantly, while the rest of the data experiences much lower $\frac{\delta t}{t}$ reductions (Figure 3.8). The choice of doubling or tripling the velocities in the UUP07 model is chosen only to get a first order estimate of the magnitude of the velocity anomalies necessary. Tripling UUP07 corrections moves the SSI measurement to be much more similar to the non-SSI data and brings them into better agreement. This can be seen by comparing the black and grey dashed lines in Figure 3.8 e) and f), which represent Equation 3.3 fitted to all the data (black line) and only the equatorial and SSI data respectively (grey dashed line). The PKPbc-PKPdf anisotropy reduces to 1.6% and the PKPab-PKPdf to 2.1% when UUP07 amplitudes are tripled. It may be an oversimplification to simply scale the amplitudes of UUP07, but it is well known from full waveform inversion studies that ray based travel time tomography significantly underestimates the amplitudes of velocity anomalies in the lower mantle. It can be seen on Figure 3.8 that doubling or tripling the tomographic velocity anomalies decreases the overall misfit of the bc-df data, but increases the misfit for the ab-df data. It is likely that such magnitude of change is reasonable for the SSI region, but a bad fit for the rest of the data. Further work is required to quantify and isolate this effect, so for the rest of the paper we shall primarily consider data with mantle corrections using the unscaled velocities from UUP07 (Amaru, 2007).

It is interesting to note that two recent papers, Long *et al.* (2018) and Frost *et al.* (2020), analysed the SSI to Alaska raypaths and also found that mantle structure was influencing the SSI data significantly. Long *et al.* (2018) showed that a small anomaly at the base of the mantle on the Alaskan side could cause the SSI travel time anomaly, while Frost *et al.* (2020) propose that the SSI data is affected by the slab underneath Alaska. While our mantle corrections do not find that the PKPdf, PKPbc and PKPab phases experience different velocities under Alaska we certainly do

not rule it out because we are using a global tomography model to correct our entire data set and not a high resolution local model under Alaska to specifically look at the SSI to Alaska raypaths. Indeed it seems possible that a combined influence from the Alaska and South Georgia slabs could be at the heart of the anomalous travel times and in the future it will be important to conduct full waveform tomography on the region covered by the SSI to Alaska raypaths.

In either scenario, present research does cast doubt on interpreting the SSI travel time anomalies as inner core structure because they may be severely affected by mantle structure.

Raypath corrections

The PKPdf raypath in the inner core changes significantly when the inner core velocity is varied by ±5% for an epicentral distance of 152° (the average of the SSI to Alaska paths), see Figure 3.9. Increasing the inner core velocity by 4% results in a raypath which travels 75 km deeper into the inner core. The corresponding inner core travel time, t, increases by 10 seconds (Figure 3.10b). Only raypaths with a small epicentral distance are severely affected, because at very large epicentral distances ($> 170°$) it is not possible to find a faster path through the inner core by travelling deeper. The raypaths from the SSI to Alaska have small epicentral distance, so they are most severely affected.

We propose a new method to determine $\frac{\delta t}{t}$, incorporating the change in t due to the velocity change. The traditional method of measuring fractional travel time, as described in Equation 3.1, involves measuring an observed value of differential travel time: PKPref-PKPdf (shown as the horizontal red dashed line in Figure 3.10a) and then finding the difference with the AK135 prediction (the blue dashed line) and dividing this by the inner core travel time as predicted by AK135. Instead, we find the uniform % change in AK135 inner core velocity (i.e. no scaling with depth) required to fit the observed differential arrival time δt and use that to calculate a new raypath and corresponding inner core travel time t_{corr} and use this new inner core travel time to calculate $\frac{\delta t}{t_{corr}}$ instead of $\frac{\delta t}{t_{AK135}}$. The newly calculated t_{corr} changes the differential travel time measurement $\frac{\delta t}{t_{corr}}$ by a maximum of 13.5% (Figure 3.5 e,f) which is enough to decrease the overall anisotropy measurement by 0.1% for both PKPab and PKPbc data sets to 1.9% and 2.3% respectively. This correction depends greatly on the magnitude of the δt measurement and the epicentral distance. The effect is greater for smaller epicentral distances and becomes insignificant for epicentral distances greater than 155°. It is interesting to note that the data

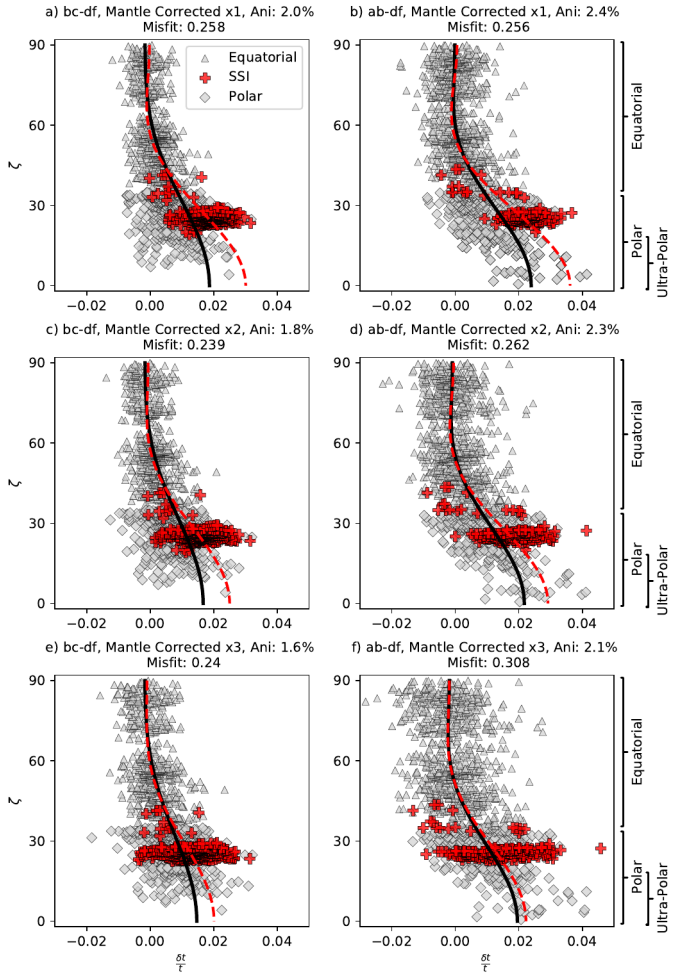

Figure 3.8 a) Variation of $\frac{\delta t}{t}$ as a function of ζ for a) PKPbc-PKPdf and b) PKPab-PKPdf with mantle corrections using the UUP07 model. The black line is Equation 3.3 fitted to all data with a least squares norm. The red dashed line is the function described by Equation 3.3 fitted to equatorial and South Sandwich Islands data only. The triangles are equatorial data ($\zeta > 35°$), diamonds are polar data (not including South Sandwich Islands) and the crosses are the South Sandwich Islands data. c), d) variations of $\frac{\delta t}{t}$ against ζ applying mantle corrections using the UUP07 tomographic model but with amplitudes x2. e), f) variation of $\frac{\delta t}{t}$ applying mantle corrections using the UUP07 tomographic model but with amplitudes x3.

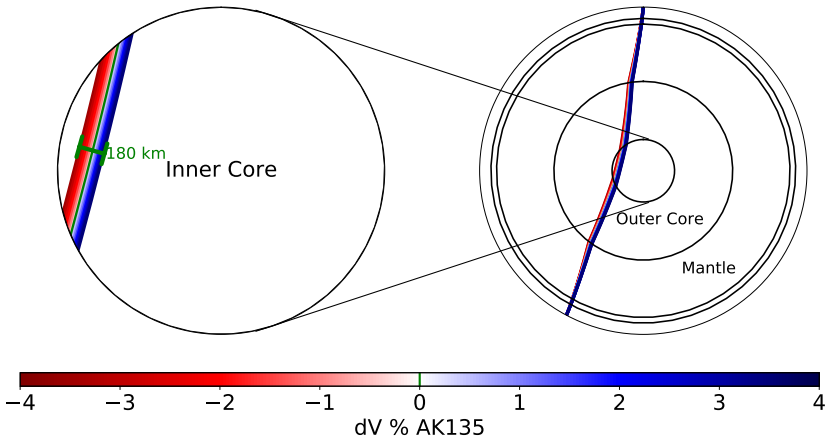

Figure 3.9 Different raypaths for a distance of 152° with the green path being the path modelled by AK135, the red paths are slower by up to -4% and the blue paths are faster by up to +4% of overall AK135 inner core velocity

from the SSI are more affected than other data because they have a large δt measurement and relatively small epicentral distance.

Another approach than the one described above is also possible where the velocity model and raypath are updated iteratively until convergence is reached, this produces identical results across all values of distance and δt as our methodology.

Sun and Song (2008a) also identified the problem that the raypath changes as a function of inner core velocity. They used the adaptive ray bending method from Koketsu and Sekine (1998) to incorporate the raypath changes in tomographic modelling, and requires significant numerical modelling. Our approach is very simple and can be easily and effectively applied to data measurements without requiring intensive computer modeling or raytracing.

The SSI data are accurate

There is an alternative explanation which should not be ruled out: that the SSI anomaly is a consequence of real inner core structure. There are some merits to this idea. Indeed, despite the possible mantle influence and raypath errors described previously, the differential travel time methodology is

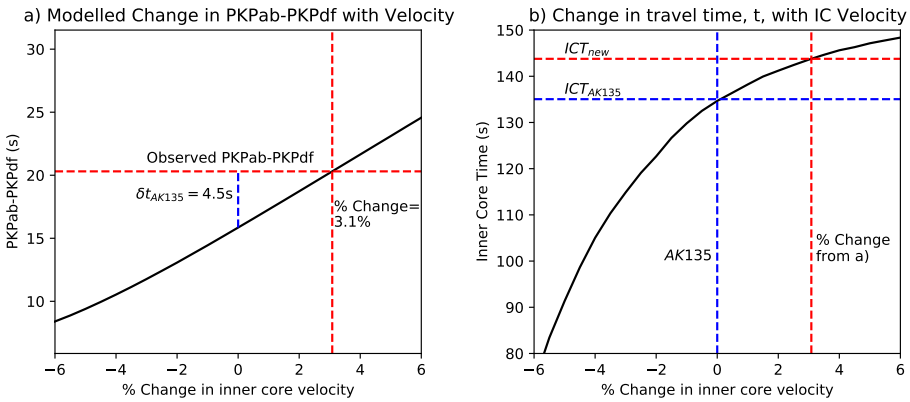

Figure 3.10 A visual explanation of the raypath corrections for an event originating in the South Sandwich Islands at 2016/07/31 and going to station COLD in the AK network with an epicentral distance of 152°. a) Predicted PKPab-PKPdf differential time, relative to AK135, as a function of increased or decreased inner core velocity (solid black line). The horizontal red dashed line shows the observed PKPab-PKPdf differential travel time. The vertical red dashed line indicates which percentage increase in inner core velocity best fits the observed PKPab-PKPdf. The vertical blue dashed line shows the δt that would be calculated using AK135 inner core velocities. b) Effect of increasing or decreasing inner core velocity on time time spent in the inner core (solid black line). For our example event and epicentral distance, the AK135 predicted inner core travel time is indicated by dashed blue lines, and the corrected inner core travel time value calculated by taking the 3.1% change found in a) is shown by the dashed red lines.

a tried and tested methodology in seismology for removing event mislocation effects and mantle and outer core structure. Furthermore it cannot be denied that the SSI anomaly is a robust observation; there is no polar path in the inner core better sampled than the SSI to Alaska raypaths. Furthermore, there have been multiple attempts to isolate and identify the root cause of the SSI anomaly outside of the inner core and while the analysis in recent years are improving (Frost *et al.* (2020); Long *et al.* (2018)) none (including this research), have yet been totally conclusive. The consequence of accepting the SSI anomaly as a product of inner core anisotropy is that it requires anisotropy in the inner core within a (relatively) small region to be 4% or greater and an increased level of heterogeneity.

3.4 Inner core structure

Having corrected for mantle velocity anomalies using UUP07 and raypath changes in the inner core (Figure 3.5 e,f), we investigate how our new data set constrains inner core structure. Our data shows large variations in anisotropy with longitude and depth. The analysis here is an initial estimate and the basis from which we will conduct more rigorous modelling in the following chapters.

3.4.1 Variations with longitude

A first order observation made by multiple other studies is the stronger anisotropy in the 'western' hemisphere than in the 'eastern' hemisphere at depths greater than approximately 200 km (Tanaka and Hamaguchi (1997); Creager (1999); Garcia and Souriau (2000); Garcia (2002); Niu and Wen (2001); Wen and Niu (2002); Oreshin and Vinnik (2004); Yu and Wen (2006); Deuss *et al.* (2010); Irving and Deuss (2011); Waszek and Deuss (2011); Lythgoe *et al.* (2014)). The hemispherical variation in anisotropy is also visible in our data with polar paths being faster than equatorial paths in the west while in the east there is a smaller difference in travel time between polar and equatorial paths (Figure 3.11).

To quantitatively define boundaries between regions of different anisotropy and test the resolution of the inner core that can be achieved with our data, we compute a value of anisotropy for overlapping windows of fixed longitude width (Figure 3.12). We fit Equation 3.3 to a subset of the data defined by a window of a fixed width centred around a specific longitude. For example, the anisotropy centred at longitude 0° with a window width of 180° is defined by determining the anisotropy for all the data between $90°W$ and $90°E$ defined by their turning point location. We then move this

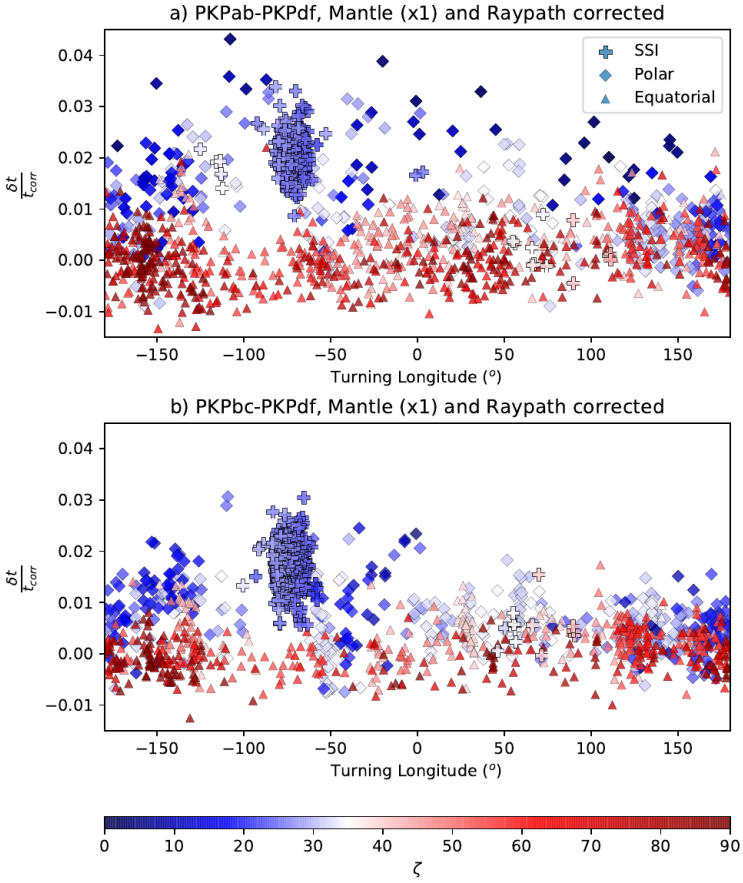

Figure 3.11 Values of $\frac{\delta t}{t_{corr}}$ plotted against the longitude of the inner core turning point for the mantle corrected (UUP07 amplitudes x1) and raypath corrected data for a) the PKPab-PKPdf data and b) the PKPbc-PKPdf data. Triangles are equatorial data, diamonds are polar data not including the South Sandwich Islands and crosses are the data from the South Sandwich Islands. The color shows the value of ζ for each data point where blue is polar and red is equatorial.

window by 1° across all the longitudes. This allows us to test for structures on different scales. Hemispheres, which are thought to split the inner core approximately in half, are investigated by using a width of 180° (Figure 3.12a). We confirm previous studies and find stronger anisotropy of 2-3% in the west and only 1-1.5% in the east. Even when we increase the mantle corrections to x2 or x3, or when we leave out the SSI data, still we find stronger anisotropy in the west than in the east. The mantle corrections do, however significantly reduce the magnitude of the western hemisphere's anisotropy from 3% to 2%, while not changing the anisotropy in the east. Figure 3.12a shows reductions in anisotropy around longitudes 60°W and 120°E representing the best locations for the hemisphere boundaries.

Decreasing the window width will lead to an increase in longitudinal resolution, but at the same time decreases the amount of data in each window and therefore increasing the uncertainty in the anisotropy calculation. We choose to limit our window widths so that no sub-set of data can have less than 50 polar data points, and find we require a minimum window width of 60° longitude. Decreasing the window width to 90° and 60° (Figure 3.12 b,c) results in changing from one highly anisotropic western region and one low anisotropic eastern region (Figure 3.12a) to three regions with distinct anisotropy (Figure 3.12c). We find a region with strong anisotropy of 3-4% between $110°W$ and $40°W$, moderate anisotropy of 2% between $30°W$ and $75°E$, and a broad region of low anisotropy of 0.5% between $100°E$ and $170°W$. Increasing the amplitude of the mantle corrections once again only affects the highly anisotropic region, further outlining how the mantle corrections preferentially affect the SSI data. Interestingly however, even when the SSI are not included in this analysis (the black line) there is still a recognisable increase in anisotropy around 100°W. This sharp peak cannot be seen in Figure 3.12a), where the window width is much larger masking this smaller feature. This shows that even without the SSI a region of higher anisotropy in the west is still required by the data. This analysis represents an increase in resolution when it comes to identifying inner core structure and is a direct result of an increase in polar and ultra polar data.

3.4.2 Variations with depth

It has been hypothesized that there is an innermost inner core with a distinct anisotropic structure (Ishii *et al.* (2002a); Beghein and Trampert (2003); Ishii and Dziewoński (2003); Sun and Song (2008a); Wang *et al.* (2015); Wang and Song (2018)), although this is an open question as some research also finds a lack of evidence for an innermost inner core (Cormier and Stroujkova (2005); Lythgoe *et al.* (2014); Frost and Romanowicz (2019)). An

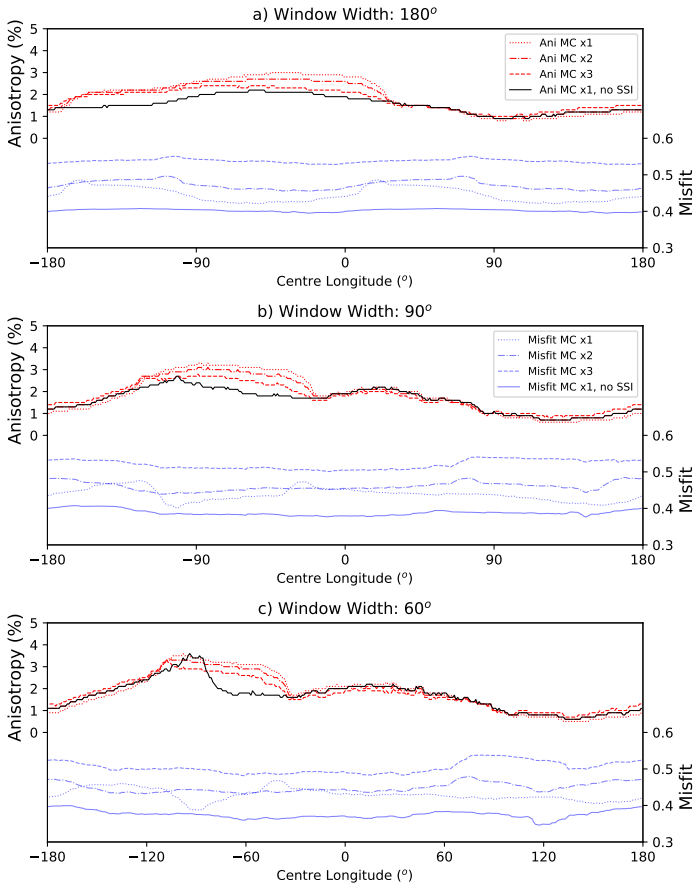

Figure 3.12 Anisotropy measured within a window of longitudes with window widths of a) 180° , b) 90 ° and c) 60°. Each window panel shows results from data with mantle corrections (MC) with 1x, 2x, 3x UUP07 amplitudes and 1x UUP07 amplitudes but no data from the South Sandwich Islands. The L2 misfit is shown in blue for data with mantle corrections (MC) with 1x, 2x, 3x UUP07 amplitudes and 1x UUP07 amplitudes but no data from the South Sandwich Islands. All raypaths have been corrected for faster inner core velocities.

innermost inner core was originally inferred by Ishii *et al.* (2002a) who proposed a region with 300 km radius and a slow axis with an angle of 45° to the fast direction. To investigate the potential evidence of an innermost inner core, we conduct a misfit analysis on our data set, splitting the data in two layers based on the radius of the turning point of each raypath and calculating anisotropy and misfit for both subsets of data. Figure 3.13 shows the results of this analysis including the South Sandwich Islands (SSI) data. Comparing the variation of misfit with layer radius (Figure 3.13b) and the histogram showing the numbers of data for each radius (Figure 3.13a) it can be seen that the lowest misfit comes from a layer with a radius of 947 km, which corresponds to the maximum depth extent of the SSI data which mostly travel the top 300 km of the inner core. This shows that the large anomalous SSI data set is masking deeper structure and misfit reductions. While most SSI data travel the upper 300 km, there are also some SSI data (shown in Figure 3.13c) which travel deeper in the inner core between a radius of 450 and 947 km.

To be able to see any further misfit reductions we repeat the analysis with the SSI data removed (Figure 3.14). The variation of misfit with layer radius for a data set with no SSI raypaths has a misfit minima at a radius of 690 km (or 530 km below the inner core boundary) (Figure 3.14b). We find that the innermost inner core is significantly more anisotropic (Figure 3.14c). In contrast to Ishii and Dziewoński (2002) the slow direction appears to be perpendicular to the direction of fastest velocity which is still aligned with Earth's axis of rotation and our innermost inner core is 690 km in radius, much larger than their 300 km, but in better agreement with values proposed from the recent study by Frost and Romanowicz (2019). The ultra polar data which travels through the innermost inner core spans a large range of longitudes and there appears to be no justification for hemispherical variations within the innermost inner core.

It is interesting to see that increasing the strength of the mantle corrections show the same pattern of misfit with layer radius but that stronger mantle corrections increase overall misfit (although not significantly, Figures 3.13b, 3.14b). This can be seen in Figure 3.8, where the overall trend of the mantle corrections is to decrease the $\frac{\delta t}{t}$ anomaly of the SSI data, but that some SSI paths are not affected creating a slightly larger overall misfit.

3.5 Conclusion

We present a new high quality differential arrival data set for inner core P-wave phases containing a large number of polar data not originating in

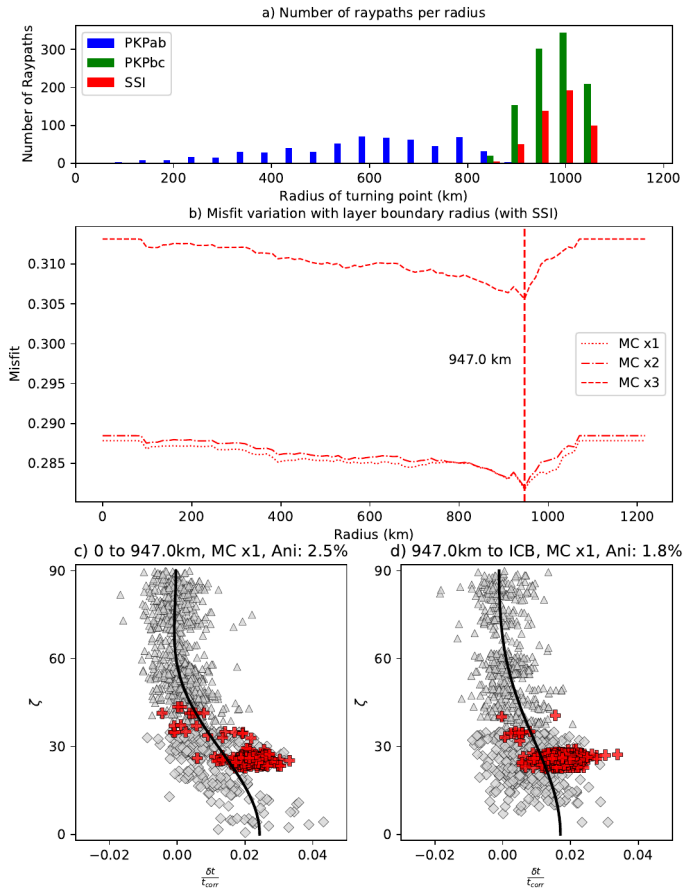

Figure 3.13 a) Histogram showing the numbers of data observed for each turning point radius. When both PKPbc and PKPab phases are observed only the PKPbc observation is used in misfit and anisotropy calculations. b) The variation of misfit with boundary radius used to separate data into two, for varying magnitude of the mantle corrections (x1,x2,x3). The vertical dashed line denotes the radius with the minimum misfit and (c,d) the corresponding plots of $\frac{\delta t}{t}$ against ζ for data with a turning point radius between 0 and 947 km and between 947 km (the minimum misfit boundary found by all data) and the inner core boundary respectively.

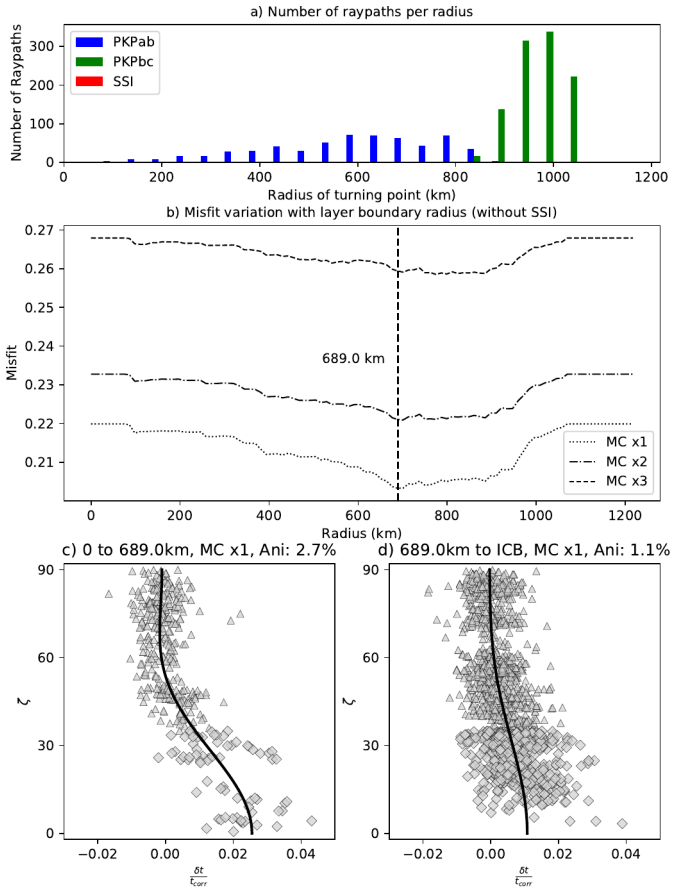

Figure 3.14 a) Histogram showing the numbers of data observed for each turning point radius. When both PKPbc and PKPab phases are observed in the same seismogram, then only the PKPbc observation is used in misfit and anisotropy calculations. This analysis does not include data from the South Sandwich Islands. b) The variation of misfit with boundary radius used to separate data into two, for varying magnitude of the mantle corrections (x1,x2,x3). The vertical dashed line denotes the radius with the minimum misfit and (c,d) the corresponding plots of $\frac{\delta t}{t}$ against ζ for data with a turning point radius between 0 and 690 km and between 690 km (the minimum misfit boundary found by all data) and the inner core boundary respectively.

the South Sandwich Islands (SSI) taking advantage of new stations in the Antarctic. The addition of ultra polar paths allows us to more reliably determine inner core anisotropy because extrapolation to small ζ is no longer required. We demonstrate that mantle structure and raypath changes have a larger effect on the anomalous SSI data than the other data, due to their short epicentral distances and large travel time anomalies. Our anisotropy values for the whole inner core including mantle and raypath correction range between 1.9% and 2.3%, which is significantly lower than previously published research.

4

3D Transdimensional seismic tomography of the inner core using body waves

Body wave observations of the Earth's inner core show that it contains strong seismic heterogeneity, both laterally and radially. Models of inner core structure generated using body wave data are often limited by their parameterization. Thus, it is difficult to determine whether features such as anisotropic hemispheres or an innermost inner core truly exist with their simple shapes, or result only from the chosen parameterization and are in fact more complex features. To overcome this limitation, we conduct seismic tomography using transdimensional Markov Chain Monte Carlo on a high quality dataset of 5296 differential and 2344 absolute P-wave travel times. In a transdimensional approach, the data defines the model space parameterization, providing us with both the mean value of each model parameter and its probability distribution, allowing us to identify well versus poorly constrained regions. We robustly recover many first order observations found in previous studies without the imposition of a priori fixed geometry including an isotropic top layer (with anisotropy less than 1%) which is between 60 and 170 km thick, and separated into hemispheres with a slow west and a faster east. Strong anisotropy (with a maximum of 7.2%) is found mainly in the west, with much weaker anisotropy in the east. We observe for the first time that the western anisotropic zone is largely confined to the northern hemisphere, a property which would not be recognised

The research in this chapter was published as: Brett, H., R. Hawkins, L. Waszek, K. Lythgoe, and A. Deuss (2022). "3D transdimensional seismic tomography of the inner core". In: *Earth and Planetary Science Letters* **Volume 593**, 117688.

in models assuming a simple hemispherical parameterization. We further find that the innermost inner core, in which the slowest anisotropic velocity direction is tilted relative to Earth's axis of rotation ($\zeta = 55° \pm 16°$), is offset by 400 km from the centre of the inner core and is restricted to the eastern hemisphere. We propose that this anomalous anisotropy might indicate the presence of a different phase of iron (either bcc or fcc) compared to the rest of the inner core (hcp).

4.1 Introduction

As global seismic data coverage increased, seismic investigations began to resolve 3D lateral variations and radial heterogeneity in the inner core. Hemispherical differences were first proposed by Tanaka and Hamaguchi (1997) and later confirmed by many other studies (Niu and Wen (2001); Waszek and Deuss (2011); Lythgoe *et al.* (2014); Burdick *et al.* (2019)). These hemispherical differences are characterized by a eastern hemisphere with weak anisotropy and fast isotropic velocity, and a western hemisphere with strong anisotropy and low isotropic velocity. The outermost layer of the inner core has been proposed as isotropic, both in the east and west (Wen and Niu, 2002; Waszek and Deuss, 2011). Furthermore, an innermost inner core (IMIC) with a different fast or slow symmetry axes may exist, although the details remain unconfirmed regarding the exact direciton of the slow axes, its regional distribution or its origins (Beghein and Trampert, 2003; Ishii and Dziewoński, 2003; Sun and Song, 2008b; Lythgoe *et al.*, 2014; Frost and Romanowicz, 2019). Sun and Song (2008b) produced an impressive early 3D tomographic model of the inner core using differential travel times. Their model recovered many of the main features in the inner core that we still see today, including isotropic quasi hemispheres, an innermost inner core and strong anisotropy in one quasi hemisphere.

One limitation in interpreting seismic body wave observations in terms of distinct regional features (like hemispheres) is that the resultant models strongly depend on the chosen parameterization. Furthermore, trade-offs exist between different structures depending on the model parameterization. Not accounting for lateral variations may explain why some studies find a sharp change in anisotropy at an apparent IMIC (Stephenson *et al.*, 2020; Frost and Romanowicz, 2019), while others find a gradual IMIC boundary, if it exists at all (Lythgoe *et al.*, 2014). In addition, hemispheres are often assumed to be defined by meridians and features such as the innermost inner core usually have a constant radius, which may be overly simplifying their shapes.

Another major challenge when imaging the inner core is removing the influence of mantle heterogeneity. A particular subset of raypaths, travelling from the South Sandwich Islands (SSI) to Alaska, have been noted to travel anomalously fast. It has been debated to what extent these travel times reflect inner core structure or mantle structure (Tkalčić (2010); Frost *et al.* (2020); Chapter 3 of this thesis). To address the issue of mantle heterogeneity, we use multiple tomographic mantle models to assess unaccounted for mantle structure, and we develop inner core models which both include and exclude the South Sandwich Islands data.

In this study, we apply a transdimensional Markov Chain Monte Carlo (MCMC) inversion technique (Bodin and Sambridge, 2009) to a large high-quality body wave data set to make a 3D model of inner core velocity and anisotropy. We consider our model to be the next step in inner core tomography, with the main difference that we use a transdimensional Monte Carlo approach and that we can now utilise significantly more data due to the increased coverage of seismic stations and events. The advantage of a transdimensional MCMC methodology over an inversion using a static paramaterization, is that the parameterization of the model space evolves with the Markov chain and is not predetermined. Thus, the model parameterization is driven by the data itself, with no prior assumptions on the parameterization, such as the existence of an IMIC or hemispheres. Previously, Burdick *et al.* (2019) and Pejić *et al.* (2019) used a transdimensional MCMC approach to image a single layer of inner core velocity and attenuation respectively. These previous studies were 2D spherical surface inversions and in this research we go further by conducting the first fully 3D transdimensional MCMC for the inner core, which allows us to resolve jointly for both lateral and radial variations in P-wave anisotropy, which is essential to answering questions on the mechanisms and causes of anisotropy in the inner core.

4.2 Data and pre-processing

We image the inner core using the phase PKPdf, which travels the mantle, outer core, and inner core as a compressional body wave. PKPdf is used either individually, or in combination with a reference phase (PKPcd, PKPbc, PKPab), which only traverses the mantle and outer core. We employ independent datasets from three previous studies consisting of 1603 PKPbc-PKPdf, 627 PKPab-PKPdf (Brett and Deuss (2020), or Chapter 3 of this thesis), and 3102 PKPcd-PKPdf (Waszek and Deuss, 2011) differential travel time measurements, and 2344 absolute PKPdf arrival times

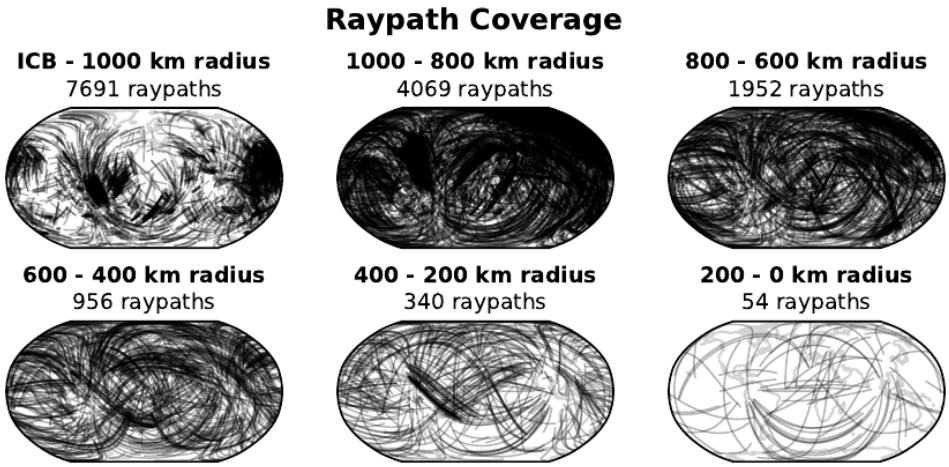

Figure 4.1 Raypath coverage of our entire dataset for different layers in the inner core. It shows all raypath segments through each given layer.

(Lythgoe *et al.*, 2014). The arrival times of Brett and Deuss (2020) and Lythgoe *et al.* (2014) are visual picks, while Waszek and Deuss (2011) used a combination of both visual inspection and cross correlation between the inner core and outer core phases. Combining these datasets provides good coverage of the inner core from its surface to 200 km radius (see Figure 4.1). We will need to consider the direction of travel of the PKPdf raypath through the inner core to image anisotropy. For cylindrical anisotropy, we describe the direction of travel by the angle ζ defined as the angle between the PKPdf raypath in the inner core and Earth's rotation axis. We have good raypath coverage for polar raypaths (defined as raypaths with $\zeta < 35°$), which is important for constraining inner core cylindrical anisotropy (Figure 4.2).

Following the methodology of Creager (1992), which is the same as in Chapter 3, we define the fractional differential travel time as:

$$\frac{\delta t}{t} = \frac{(\mathrm{t_{PKPref}} - \mathrm{t_{PKPdf}})_{\mathrm{data}} - (\mathrm{t_{PKPref}} - \mathrm{t_{PKPdf}})_{\mathrm{Model}}}{t} \tag{4.1}$$

where $(\mathrm{t_{PKPref}} - \mathrm{t_{PKPdf}})_{\mathrm{data}}$ is the observed difference in arrival time between a reference phase and the PKPdf phase, $(\mathrm{t_{PKPref}} - \mathrm{t_{PKPdf}})_{\mathrm{Model}}$ is the theoretical arrival time difference predicted by a model, and t is the inner core travel time of the PKPdf raypath as predicted by a reference model. We use the 1D reference model AK135 (Kennett *et al.*, 1995). For absolute

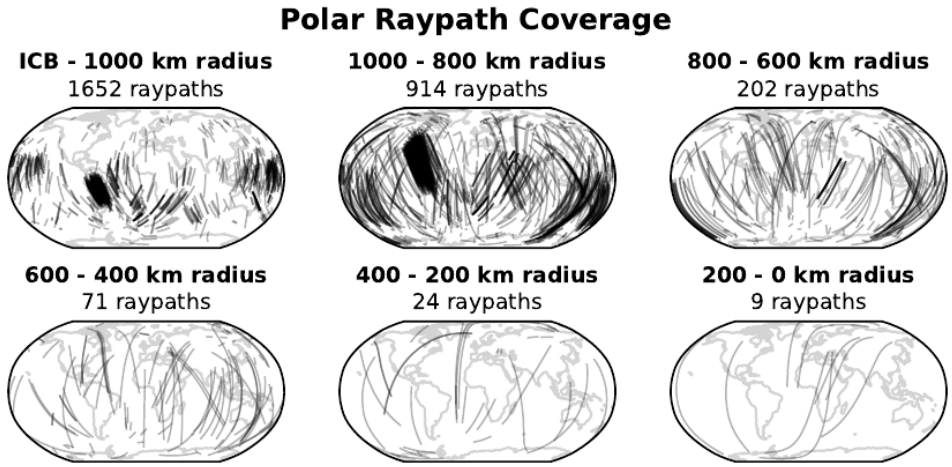

Figure 4.2 Data coverage of the polar raypaths in our data at different layers in the inner core

travel times, we remove the reference phase from the above equation.

Multiple studies have highlighted the significant influence of mantle structure on inner core travel times (Tkalčić (2010); Frost *et al.* (2020); Brett and Deuss (2020)). Mantle corrections will be especially large for absolute travel time measurements, but may also be important for differential travel time data. To correct for the influence of mantle structure and estimate any corresponding uncertainties introduced we calculate differential travel times using six different global P-wave models, integrated across the 1D raypaths from AK135. The global P-wave models used are: UUP07 (Amaru, 2007), MITP08 (Li *et al.*, 2008), GyPSuM, LLNL-G3Dv3 (Simmons *et al.*, 2012), SAW642AN (Panning and Romanowicz, 2006) and SPani (Tesoniero *et al.*, 2015). This results in six synthetic travel times for each PKPcd, PKPbc, PKPab and PKPdf travel time observation in our data set, from which we calculate six different values of δt (Figures 4.3-4.4). Inspection of Figures 4.3-4.4 reveals a significant uniform negative shift for the mantle-corrected absolute PKPdf travel times. We expect that this shift is due to 1D mantle structure that differs from the reference model used (AK135); we remove it by subtracting the mean of the mantle-corrected equatorial data from each measurement. Using the six $\frac{\delta t}{t}$ values for each data point for each model, we determine the mean and standard deviation, σ_{mantle}. The standard deviation σ_{mantle} is used as a starting estimate of the noise introduced into the data by the mantle structure which is then extended through hierarchical sampling (see Section 4.4.3).

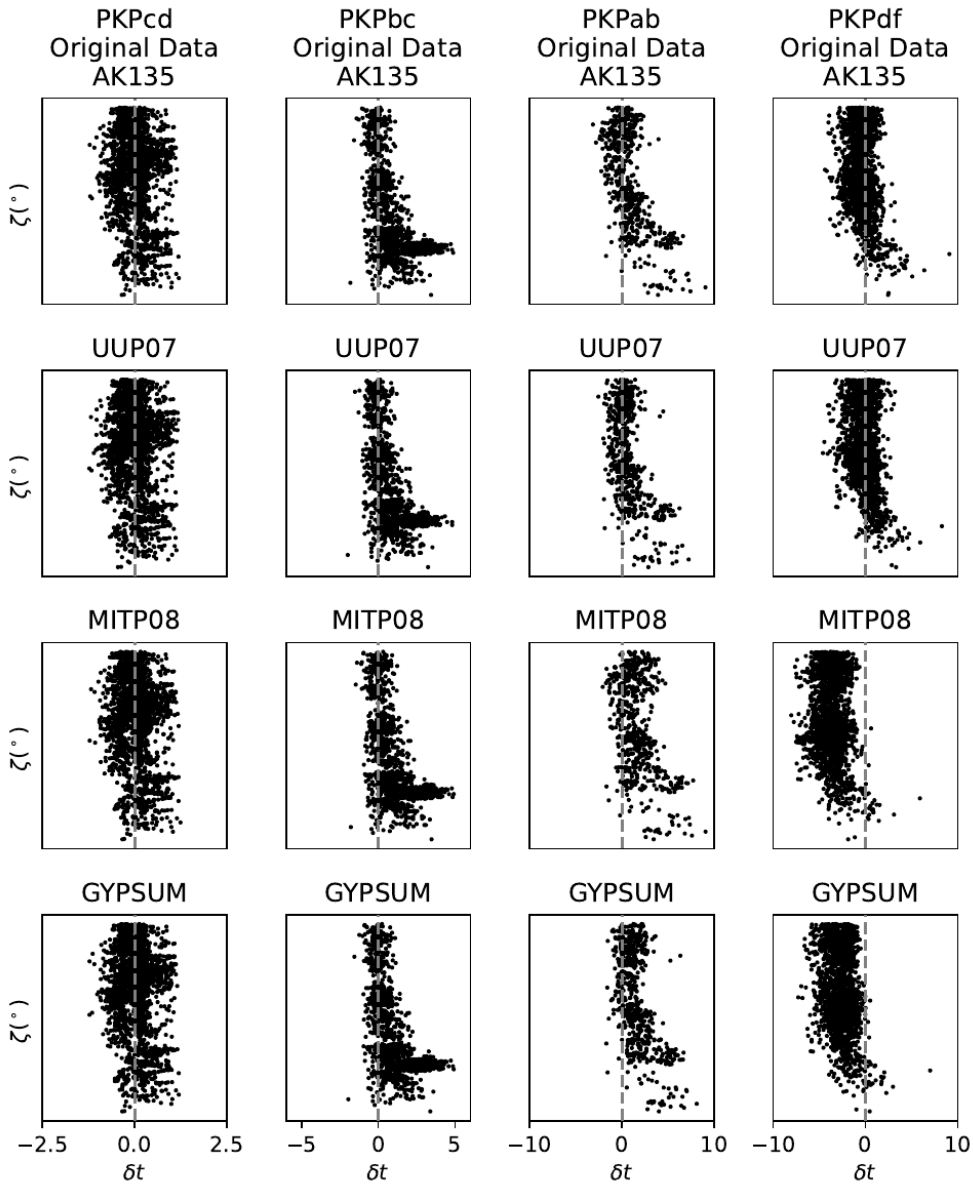

Figure 4.3 Residual travel times, δt, varying as a function of ζ, the angle between the PKPdf raypath and Earth's axis of rotation. The travel times use each of the following mantle P-wave models to correct for mantle structure: AK135 (Kennett *et al.*, 1995), UUP07 (Amaru, 2007), MITP08 (Li *et al.*, 2008), and GyPSuM (Simmons *et al.*, 2012).

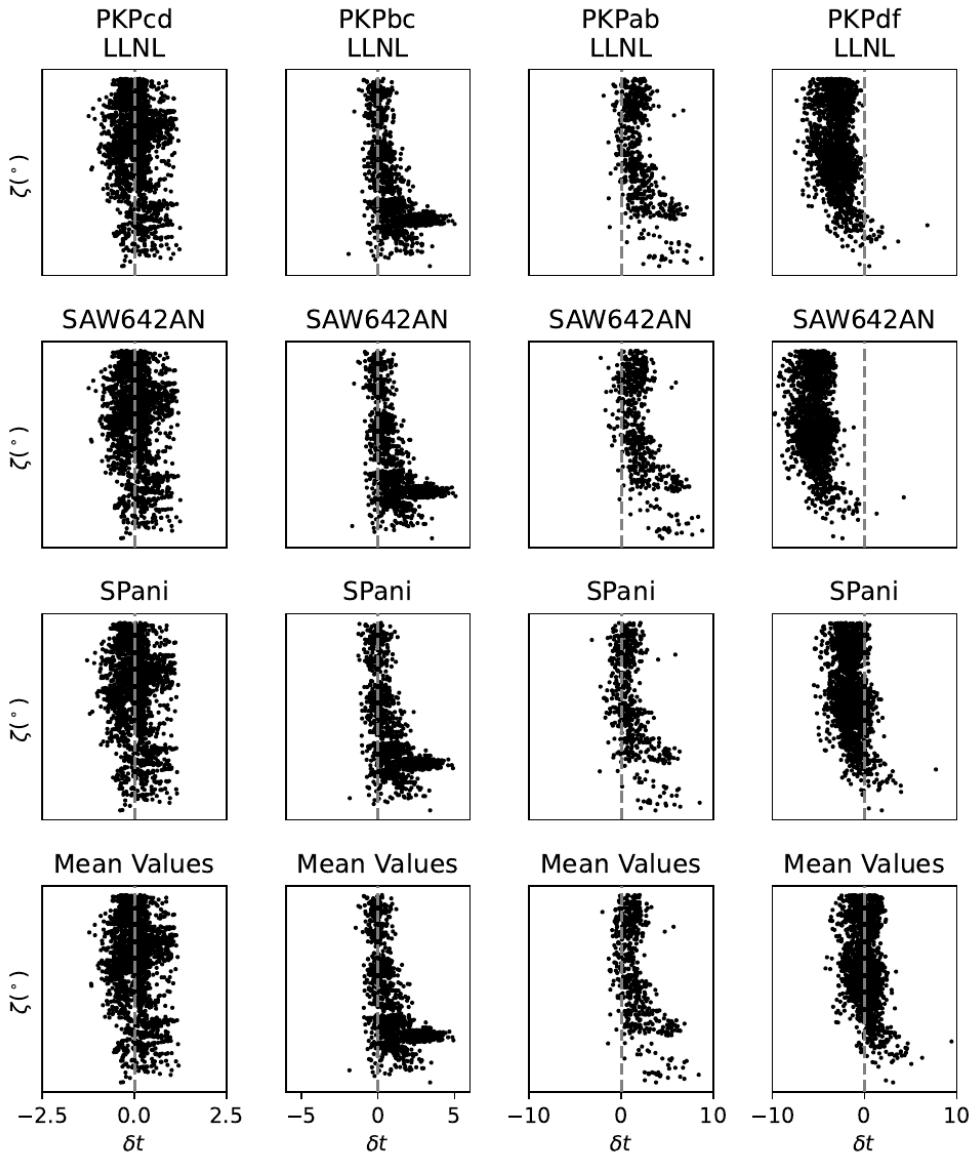

Figure 4.4 Residual travel times, δt, varying as a function of ζ, the angle between the PKPdf raypath and Earth's axis of rotation. The travel times use each of the following mantle P-wave models to correct for mantle structure: LLNL-G3Dv3 (Simmons *et al.*, 2012), SAW642AN (Panning and Romanowicz, 2006), and SPani (Tesoniero *et al.*, 2015). The bottom panel shows the mean of each of these differential travel times (also including the 3D models from Figure 4.3.

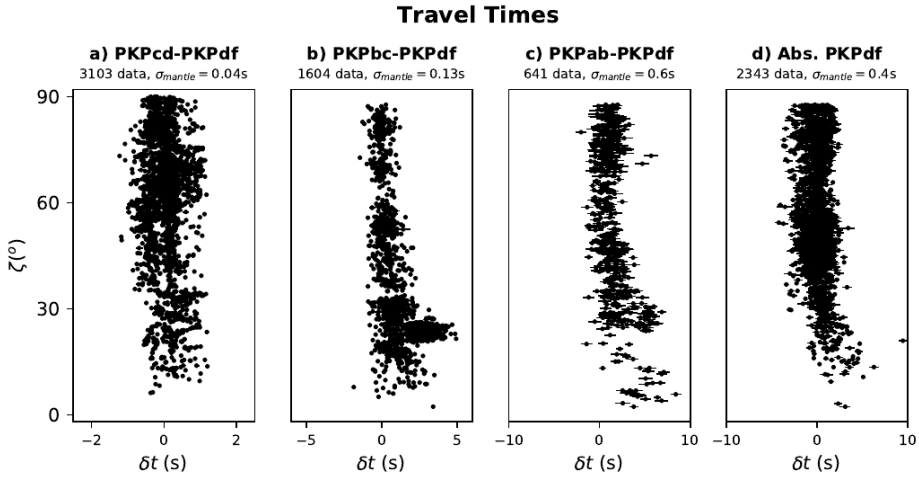

Figure 4.5 The variation of mean δt with the angle ζ for a) PKPcd-PKPdf, b) PKPbc-PKPdf, c) PKPab-PKPdf and d) absolute PKPdf differential travel times. The horizontal lines show the standard deviation σ_{mantle} of the δt due to 'mantle noise' from the 6 global P-wave mantle models used. The number of data points and the average of σ_{mantle} is shown in each subtitle. Plots showing the differential travel times for each mantle model, from which the means, are derived are shown in Figures 4.3-4.4.

While the mantle corrections will do a good job of correcting large scale lower mantle structure, strong velocity perturbations locally around events or seismic stations will not be as well resolved by these global tomographic models. However, we assume that such differences will be removed by the differential travel time methodology, because the primary and reference phases are most similar near the source and receiver. As expected, the PKPab-PKPdf and absolute PKPdf data are more affected by mantle structure than the PKPcd-PKPdf and PKPbc-PKPdf data (Figure 4.5). Regardless, the mantle corrections in all datasets are an order of magnitude less than the measurements themselves.

4.3 The forward problem

For a fast direction parallel to Earth's axis of rotation, cylindrical body wave anisotropy in the inner core is defined as follows (Creager, 1992) (see also Chapter 2)

$$\frac{\delta t}{t} = \frac{\delta v}{v} = a + b\cos^2(\zeta) + c\cos^4(\zeta) \tag{4.2}$$

where $\frac{\delta t}{t}$ is equivalent to the velocity anomaly $\frac{\delta v}{v}$ (assuming low attenuation in the inner core). The difference in the velocity of equatorial raypaths relative to the reference model (AK135), δV_{eq}, is given by a in Equation 4.2. (Equation 4.2 is derived in Section 2.1, Equation 2.9). The amount of anisotropy, δV_{ani}, is defined as the velocity difference between polar and equatorial raypaths, given by $b + c$. This measure of anisotropy is strictly for cylindrical anisotropy, and assumes that the slow and fast directions are perpendicular. The b and c parameters of Equation 4.2 are related to components of the elastic tensor, C_{ij}, which describes the anisotropy of a medium by $b = (-C_{11} + C_{44} + C_{13})/C_{11}$ and $c = (C_{11} + C_{33} - 4C_{44} - 2C_{13})/2C_{11}$ (Creager, 1992) . From the model parameters a, b and c we calculate the isotropic velocity, or Voigt average velocity (Lythgoe *et al.*, 2014) commonly interpreted by mineral physicists;

$$\delta V_{iso} = a + \frac{b}{3} + \frac{c}{5} \tag{4.3}$$

Equation 4.2 reveals that the slowest velocity direction is not restricted to an angle of $\zeta = 90°$, but depends on combinations of b and c, thus can be any angle between $0 - 90°$. The slowest angle is obtained by differentiating Equation (4.2) and calculating its maximum value, following Lythgoe *et al.* (2014), which results in the following:

$$\zeta_{slow} = \cos^{-1}\sqrt{\frac{-b}{2c}} \tag{4.4}$$

Some variations in ζ_{slow} are statistically insignificant: it is possible to have a large range of values of ζ_{slow} but with minimal absolute velocity differences between ζ_{slow} and $\zeta = 90°$. To only keep statistically significant values of ζ_{slow}, we use a tolerance condition, such that the difference between ζ_{slow} velocity and that at $\zeta = 90°$ must be greater than 0.5%. We will present our model showing variations in δV_{eq}, δV_{iso}, δV_{ani}, and ζ_{slow}. It is important to note that throughout this paper we define anisotropy to be the difference between the polar and the equatorial velocity (as is conventional for body wave studies of the inner core). However, in some regions of our model the difference between the polar and equatorial velocity is small ($\delta V_{ani} \sim 1.0\%$) while the difference between the ζ_{slow} direction and the $\zeta = 0°$ is stronger ($\sim$ 2.0%). These regions should still be thought of as anisotropic even though the value of δV_{ani} is small.

For a single raypath with ζ and set of coefficients (a, b, c) we predict the normalised differential travel time using Equation 4.2. However, this treats the inner core as a homogeneous volume, whereas we are interested in 3D variations. For an inner core with multiple sub-volumes, we split the ray into different portions for each model sub-volume travelled, resulting in the following linear forward problem:

$$\mathbf{Gm} = \mathbf{d}_{syn} \tag{4.5}$$

$$\mathbf{G} = \begin{pmatrix} A_{11}t_1 & A_{11}t_1\cos^2(\zeta) & A_{11}t_1\cos^4(\zeta) & A_{12}t_1\cdots \\ A_{21}t_2 & A_{21}t_2\cos^2(\zeta) & A_{21}t_2\cos^4(\zeta) & A_{22}t_2\cdots \\ A_{31}t_3 & A_{31}t_3\cos^2(\zeta) & A_{31}t_3\cos^4(\zeta) & A_{32}t_3\cdots \\ \vdots & \vdots & \ddots & \end{pmatrix} \tag{4.6}$$

$$\mathbf{m} = \begin{pmatrix} a_1 \\ b_1 \\ c_1 \\ a_2 \\ \vdots \end{pmatrix} \tag{4.7}$$

$$\mathbf{d} = \begin{pmatrix} \delta t_1 \\ \delta t_2 \\ \delta t_3 \\ \vdots \end{pmatrix} \tag{4.8}$$

where $\mathbf{G}$ is the sensitivity kernel matrix which has the same number of rows as the number of travel times in our dataset, and the same number of columns as the length of vector $\mathbf{m}$. A_{ij} within $\mathbf{G}$ is a value between 0 and 1 describing the fraction of raypath i which travels through volume j and $\sum_{j=1}^{N} A_{ij} = 1$ for a total of N volumes. The model vector, $\mathbf{m}$, contains the parameters a_j, b_j, c_j for each volume j. $\mathbf{d}$ is the data vector containing the differential travel time δt_i of each raypath i. Note that the inner core travel time t_i has been moved from the left hand side in Equation 4.2 to the right hand side, and is now part of matrix $\mathbf{G}$. In a static MCMC, the parameterization of the sensitivity kernel matrix $\mathbf{G}$ remains constant, forming a fixed forward problem. In the transdimensional MCMC, the sensitivity kernel matrix $\mathbf{G}$ changes at each step of every new model parameterization.

Calculating the A_{ij} terms is a function of the raypath discretization and the basis functions used. For this study, we use fixed raypaths as modelled by AK135 using the Taup Toolkit (Crotwell *et al.*, 1999) and assume the

inner core is spherical (note that we do correct our data for ellipticity using the methodology of Dziewonski and Gilbert (1976)). We do not adjust the raypaths in our model using 3D raytracing, the transdimensional inversion is already a computationally expensive non-linear inversion and tests incorporating 3D raytracing through an anisotropic model significantly increased the time taken to approximate the posterior making it unfeasible. Likewise, it would be more rigorous to incorporate finite frequency kernels rather than using a raypath approximation, as outlined by Calvet *et al.*, 2006a and Calvet *et al.*, 2006b, however due to the increased computational cost this would incur we decided that for this study it was sufficient to use fixed raypaths and assess the uncertainties in the travel times through hierarchical sampling.

The basis functions are 3D Voronoi cells, which provide a fast method of tessellating a domain with non-overlapping volumes. Appendix A describes in plain language simple algorithms to determine which Voronoi cell in a domain contains a given set of locations, from these algorithms it is then possible to conduct a raypath integration.

4.4 The inverse problem

4.4.1 Bayes' theorem

We solve the inverse problem using a Bayesian approach, where we do not consider one single solution but instead regard the solution to be a collection of models (an 'ensemble') from which uncertainties can be determined. In practise, the Bayesian approach combines prior information on a model space with data to produce a posterior probability distribution. Following Bodin and Sambridge (2009), the posterior probability $p(\mathbf{m}|\mathbf{d}_{obs})$ is given by

$$p(\mathbf{m}|\mathbf{d}_{obs}) \propto p(\mathbf{d}_{obs}|\mathbf{m})p(\mathbf{m}) \tag{4.9}$$

where the *likelihood* function $p(\mathbf{d}_{obs}|\mathbf{m})$ is the probability of observing a set of data given a set of model parameters. The *prior* function $p(\mathbf{m})$ describes our knowledge of the model space before considering the data. The posterior $p(\mathbf{m}|\mathbf{d}_{obs})$ represents how the data and our prior knowledge combine, providing us with the probability that a given set of model parameters are true.

4.4.2 Markov Chain Monte Carlo

We then use Markov Chain Monte Carlo (MCMC) to sample the posterior probability distribution of our data-model system (Cowles and Carlin,

1996). For a given prior probability and data, we evaluate the forward problem over many proposed models, with each proposed model related to the previous model with a small random perturbation (Section 4.5). After randomly perturbing an initial model, we use the Metropolis-Hastings algorithm (Hastings, 1970) to probabilistically accept or reject perturbations. The Metropolis-Hastings criteria ensures that accepted models are representative of the posterior probability distribution.

4.4.3 Likelihood and hierarchical noise

The likelihood function, $p(\mathbf{d}_{obs}|\mathbf{m})$, describes how well a set of model parameters reproduces the data:

$$p(\mathbf{d}_{obs}|\mathbf{m}) \propto \exp \frac{-\phi(\mathbf{m})}{2} \tag{4.10}$$

where ϕ is the least squares misfit of a model normalized by data noise. We use an L2 norm which is frequently used in seismic tomography:

$$\phi(\mathbf{m}) = \left|\left| \frac{\mathbf{d}_{syn} - \mathbf{d}_{obs}}{\lambda_d} \right|\right|^2 \tag{4.11}$$

where d_{syn} is the synthetic data predicted by the model $\mathbf{m}$ (calculated usine Equation (4.5)), λ_d is the hierarchical parameter and is the estimated data noise. λ_d has a profound influence on the MCMC because the algorithm will only fit the data to within this noise limit. Thus, λ_d is analogous to the damping parameter in a damped least squares inversion. However unlike the damping parameter, it is possible to assess the value of λ_d from the data itself using hierarchical methods. We separate λ_d into $\lambda_{DataType}$ for each data type, since the four data types (PKPcd, PKPbc, PKPab differential travel times and absolute PKPdf travel times) have different levels of noise. For each individual δt data point we use the mantle noise, σ_{mantle}, estimated from the six global tomographic models (see Section 4.2) as a minimum level of noise. From this, each measurement then has its own $\lambda_d = \sqrt{\lambda^2_{DataType} + \sigma^2_{mantle}}$. The misfit then becomes:

$$\phi(\mathbf{m}) = \sqrt{\sum_{n=1}^{N_{Data}} \left(\frac{(\mathbf{d}_{syn} - \mathbf{d}_{obs})_n}{\sqrt{\lambda^2_{DataType} + \sigma^2_{mantle,n}}} \right)^2} \tag{4.12}$$

The hierarchical parameter $\lambda_{DataType}$ is not a term that we choose, but is sampled as an additional perturbation step in the MCMC, which is also accepted following the Metropolis-Hastings algorithm. In this way,

$\lambda_{DataType}$ estimates the noise by examining contradictions within the data itself, and combining this with the prior estimate of the data noise from the tomographic models. For example, if two or more observations that sample the same region of the model are contradictory then they will be fit poorly and drive the hierarchical parameter to higher values indicating a greater level of uncertainty in the data. This approach handles data uncertainties thoroughly, using the estimates of σ_{mantle} from the tomographic models to provide a minimum misfit on individual data points, then using the $\lambda_{DataType}$ terms to maintain an overview of the noise of each subset of data. Substituting Equation (4.12) into Equation (4.10) provides us with the first term on the right hand side of Equation (4.9).

4.4.4 Prior

The prior, $p(\mathbf{m})$ (the second term on the right hand side of Equation 4.9), is a probability distribution function representing any knowledge on the physical system before data is considered. We use Gaussian probability distributions for model parameters, a, b and c with a mean of 0 and a standard deviation, σ, of 0.1 (or 10% velocity perturbations relative to AK135). That is, for the ith a parameter we have in our model we have:

$$p(a_i) = \frac{1}{\sigma\sqrt{2\pi}} \exp(-\frac{a_i^2}{2\sigma}) \tag{4.13}$$

with the same equation for b and c, giving a prior of the form:

$$p(\mathbf{m}) = \prod_i p(a_i)p(b_i)p(c_i). \tag{4.14}$$

This prior reflects current knowledge on inner core structure while not restricting the size of the model space prohibitively. For example, it has the capacity to incorporate anisotropy ($b + c$) of 10% in our model. We consider Gaussian priors to be more appropriate than uniform priors as uniform priors can overly restrict the size of the model space.

4.5 Model perturbations

In a traditional MCMC inversion the parameterization of the model space is static (i.e. the number and locations of the Voronoi cells remains the same across all iterations) and defined prior to the inversion. Thus, only the model parameters a, b and c within each Voronoi cell would be perturbed. However, in our transdimensional MCMC, the data defines how the model is

parameterized through perturbing the number and locations of the Voronoi cells. Thus, the transdimensional method samples models with different complexity (i.e. number of model parameters and volumes) resulting in an ensemble of varying dimensioned models that plausibly explain the observations. This is implemented as a 'reductionist' methodology, i.e. if the dataset can be fit equally well with 10 volumes instead of 11, then the final ensemble will include more models with 10 volumes than 11.

The velocity perturbations to the model parameters a, b and c are described in Section 4.5.1. The additional perturbations to the parameterization of the model space require three more perturbation types: *move* (moving cells), *birth* (generating new cells), and *death* (removing cells) and are described in detail in Sections 4.5.2-4.5.4.

4.5.1 Velocity perturbations and acceptance

In an MCMC, new model parameters are proposed based on a previous set of model parameters. For changes in a, b, or c (i.e. velocities of Voronoi cells) the proposal process is straightforward:

1. A volume, V, is randomly chosen in the current model m
2. It is randomly chosen whether to change the value of a, b, or c in volume V
3. A new value of a, b, or c is randomly drawn from a Gaussian distribution centred on the previous value and with a standard deviation, σ_{prop}

The Gaussian probability density of drawing a new value of a is defined thus:

$$q(a'|a) = \frac{1}{\sigma_{prop}\sqrt{2\pi}} \exp(-\frac{(a'-a)^2}{2\sigma_{prop}^2}) \tag{4.15}$$

where a' is the new value based on the previous model value a and σ_{prop} is the proposal standard deviation describing how large the deviation from model $\mathbf{m}$ will be. Following the conventions of many previous MCMC studies (Cowles and Carlin, 1996) we tune these values such that acceptance rates are $\sim$30%. This provides a balance between resolving small scale structures while also exploring the full model space in reasonable computational time. This process is analogous for perturbations of b and c.

We combine the prior $p(\mathbf{m})$, likelihood, and proposal probabilities of the current model $\mathbf{m}$, and of the proposed model $\mathbf{m'}$, to calculate the acceptance probability $\alpha(\mathbf{m}|\mathbf{m'})$, following the Metropolis-Hastings algorithm

(Hastings, 1970). The Markov chain will converge to the posterior distribution if proposals are accepted with a probability defined as:

$$\alpha(\mathbf{m'}|\mathbf{m}) = \text{Min}(1, \frac{p(\mathbf{m'})}{p(\mathbf{m})} \times \frac{p(\mathbf{d}_{obs}|\mathbf{m'})}{p(\mathbf{d}_{obs}|\mathbf{m})} \times \frac{q(\mathbf{m}|\mathbf{m'})}{q(\mathbf{m'}|\mathbf{m})}) \tag{4.16}$$

which shows that the acceptance probability is equal to the ratio of the priors multiplied by the ratio of the likelihoods multiplied by the ratio of the proposals. For a Gaussian proposal where the size of the model space has not changed, the probability $q(\mathbf{m}|\mathbf{m'})$ is equal to the probability of the reverse step $q(\mathbf{m'}|\mathbf{m})$ and thus the proposal ratio is equal to 1.

A random number r between 0 and 1 is drawn and if $r < \alpha$ then the model **m'** is kept and becomes model **m** for the next iteration. Otherwise, **m'** is discarded, model **m** is added another time to the chain and the next iteration again perturbs model **m**. Inspection of Equation (4.16) reveals that if the new model **m'** has a lower misfit (reflected in $p(\mathbf{d}_{obs}|\mathbf{m})$) and a higher prior probability (reflected in $p(\mathbf{m'})$, Equation (4.13)) than the initial model **m**, then $\alpha > 1$ and **m'** will always be accepted. However, if **m'** does not decrease misfit, it might be accepted with probability α.

4.5.2 Parameterization perturbations: Move

The *move* perturbation type involves selecting a random Voronoi cell in the current model **m**, then moving the nucleus of that cell to produce model **m'** (Figure 4.6). In 3D, the nucleus is perturbed according to a Gaussian distribution centred on its current position, with a standard deviation of 50 km, and the limitation that it cannot move outside of the inner core. The probability that a Voronoi nucleus moves from position **p** to **p'** is equal to the reverse step, i.e. the probability of the same Voronoi nucleus moving from **p'** to **p**. This means that the proposal ratio ($\frac{q(\mathbf{m}|\mathbf{m'})}{q(\mathbf{m'}|\mathbf{m})}$ from Equation 4.16) is 1 and Equation 4.16 simplifies to only the prior and likelihood ratios:

$$\alpha(\mathbf{m'}|\mathbf{m}) = \text{Min}(1, \frac{p(\mathbf{m'})}{p(\mathbf{m})} \times \frac{p(\mathbf{d}_{obs}|\mathbf{m'})}{p(\mathbf{d}_{obs}|\mathbf{m})}) \tag{4.17}$$

thus the acceptance criterion for a *move* perturbation is the same as for model parameter perturbations.

4.5.3 Parameterization perturbations: Birth

Creating a new Voronoi cell changes the size of the model space (Figure 4.7). This means that, unlike a move step, the proposal ratio, ($\frac{q(\mathbf{m}|\mathbf{m'})}{q(\mathbf{m'}|\mathbf{m})}$, is not equal to one, complicating the acceptance criteria calculation. When a

birth step is conducted, a new nucleus in the model space with a random location at point **p'** is added and the new Voronoi tessellation calculated. This new Voronoi cell will then have model parameters (a, b, c) equal to a Gaussian perturbation centred on the equivalent model parameters of the cell that occupied the point of the new nucleus in the previous model.

The acceptance term (alpha criterion) reduces to the following for the birth step:

$$\begin{aligned}\alpha_{Birth} = \sigma_{prop}\sqrt{2\pi}\mathbf{P}(a')\frac{1}{\exp(-\frac{1}{2}\frac{(a'-a)^2}{\sigma^2_{prop}})} \\ \times \sigma_{prop}\sqrt{2\pi}\mathbf{P}(b')\frac{1}{\exp(-\frac{1}{2}\frac{(b'-b)^2}{\sigma^2_{prop}})} \\ \times \sigma_{prop}\sqrt{2\pi}\mathbf{P}(c')\frac{1}{\exp(-\frac{1}{2}\frac{(c'-c)^2}{\sigma^2_{prop}})} \\ \times \frac{p(\mathbf{d}_{obs}|\mathbf{m'})}{p(\mathbf{d}_{obs}|\mathbf{m})}\end{aligned} \tag{4.18}$$

where a' and a are the values of a in the new volume and the volume which previously contained the new nucleus respectively, σ_{prop} is the same as in Equation (4.15) and represents the standard deviation of the Gaussian from which a new value of a, b, or c is drawn, and $\mathbf{P}(a')$ is the prior probability of the new value a being drawn. This is analogous for the terms b, b', $\mathbf{P}(b')$, c, c', and $\mathbf{P}(c')$. Thus, there is a trade off between the $(a'-a)^2$, $(b'-b)^2$, $(c'-c)^2$ terms inside the exponent, which dominate, and the misfit (contained within the likelihood ratio, $\frac{p(\mathbf{d}_{obs}|\mathbf{m'})}{p(\mathbf{d}_{obs}|\mathbf{m})}$), which determines whether the perturbation will be accepted. For example, the perturbation is more likely to be accepted if the $(a'-a)^2$, $(b'-b)^2$, $(c'-c)^2$ terms are large. However, this change in the model parameters is balanced by the likelihood ratio, which will be smaller if the misfit of the new model **m'** is greater than **m** resulting in a lower value of α (i.e. acceptance becomes less probable).

4.5.4 Parameterization perturbations: Death

When a Voronoi cell is removed from a model space, the surrounding Voronoi cells occupy the space left behind (Figure 4.8). This is one of the reasons why Voronoi cells are extremely useful for transdimensional methods: it is relatively simple to discretize quickly a domain when adding and removing volumes. This removal of a volume reduces the size of the model space

and, like the birth step, results in a proposal ratio not equal to one. The acceptance term reduces to the following for the death step:

$$\begin{aligned}\alpha_{Death} = & \frac{1}{\sigma_{prop}\sqrt{2\pi}\mathbf{P}(a')}\exp(-\frac{1}{2}\frac{(a-a')^2}{\sigma_{prop}^2}) \\ & \times \frac{1}{\sigma_{prop}\sqrt{2\pi}\mathbf{P}(b')}\exp(-\frac{1}{2}\frac{(b-b')^2}{\sigma_{prop}^2}) \\ & \times \frac{1}{\sigma_{prop}\sqrt{2\pi}\mathbf{P}(c')}\exp(-\frac{1}{2}\frac{(c-c')^2}{\sigma_{prop}^2}) \\ & \times \frac{p(\mathbf{d}_{obs}|\mathbf{m'})}{p(\mathbf{d}_{obs}|\mathbf{m})}\end{aligned} \tag{4.19}$$

which has a similar form to Equation (4.18) but taking the inverse and where a' and a are the values in the volume which occupies the old Voronoi node and the volume which is being removed respectively.

A analysis of the acceptance criterion can be made in a similar way to that of the birth acceptance criterion. The terms $(a-a')^2$, $(b-b')^2$, and $(c-c')^2$ inside the exponent dominate, if the misfit of the new model **m'** is greater than the misfit of the previous model **m** and then the likelihood ratio $\frac{p(\mathbf{d}_{obs}|\mathbf{m'})}{p(\mathbf{d}_{obs}|\mathbf{m})}$ is smaller resulting in the perturbation being less likely to be accepted. Equally, if the change in the model parameters ($(a-a')^2$, $(b-b')^2$, $(c-c')^2$) is large then the perturbation is also less likely to be accepted. Thus, the death step is effectively testing whether a model with fewer volumes (i.e. fewer degrees of freedom) can fit the data as well as the previous model, so it is more likely to be accepted if the volume which replaces the 'dying' Voronoi cell has similar velocity characteristics.

4.6 Ensemble analysis

We applied the transdimensional MCMC algorithm (Section 4.5) to our data (Section 4.2) and ran 20 chains for 4,000,000 iterations with an acceptance rate (the percentage of accepted perturbations) of 30.5%. Figure 4.9a shows how the misfit changes as a function of iteration in the inversion for all 20 chains. The misfit drops rapidly in the first 200,000 iterations before reaching a misfit minimum; the transdimensional algorithm then samples models around this minimum value.

Once the inversion has completed the desired number of iterations, the models are collected into an ensemble from which statistics are calculated. We remove the influence of the starting model by excluding the first third

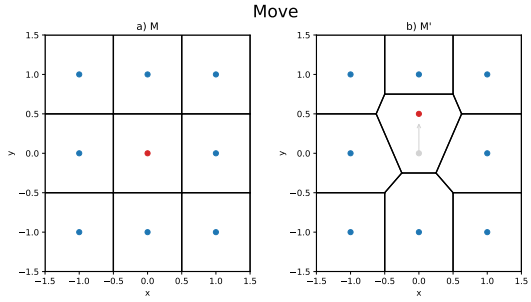

Figure 4.6 A 2D example of a *move* perturbation with a) the model space before the *move* perturbation and b) the model space after the move perturbation.

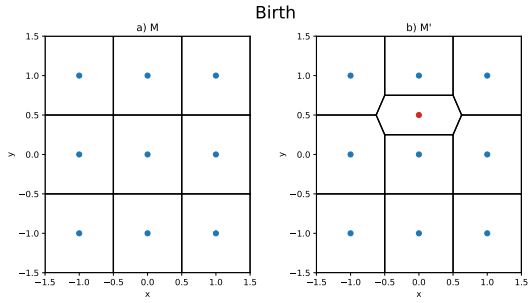

Figure 4.7 A 2D example of a *birth* perturbation with a) the model space before the *birth* perturbation and b) the model space after the *birth* perturbation.

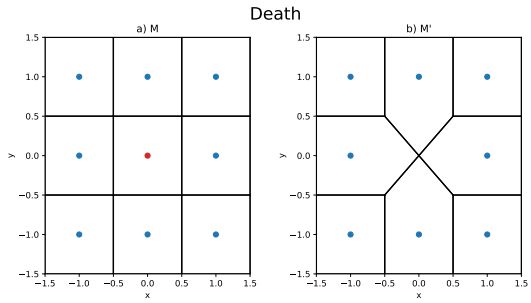

Figure 4.8 A 2D example of a *death* perturbation with a) the model space before the *death* perturbation and b) the model space after the *death* perturbation.

of all iterations in the ensemble of models; the so-called 'burn in'. It is also common practice to 'thin' the chain by only retaining every 100th model, which ensures that each model in an ensemble is independent. Following 'burn in' and 'thinning' leaves a final ensemble of 533,380 models. For further discussion regarding appropriate values for the 'burn in' and 'thinning' we refer the reader to Cowles and Carlin (1996).

For an MCMC investigation, it is important to ensure that the model sampling has converged, whereby the model space has been sufficiently explored and the models are no longer evolving substantially. To assess convergence, we examine the number of volumes in each chain as a function of iteration (Figure 4.9b). The number of volumes across all chains drops rapidly within the first 10,000 iterations, as the starting model is refined and Voronoi cells which do not reduce misfit are removed. After this initial reduction of volumes, the MCMC algorithm better assesses the noise level within the data, and the number of volumes across all chains starts to increase before flattening out after 1,000,000 iterations. For the next 3,000,000 iterations, the mean number of volumes across all chains does not change substantially, implying convergence. After convergence, the average model misfit has reduced from 1.0 to 0.55, and the models have between 23 and 38 volumes.

We also investigate the average hierarchical noise parameters for each data type (Section 4.4.3) from the 533,380 models in our final ensemble (Figure 4.9c). As expected, the PKPcd-PKPdf data has the lowest noise level with 0.29s on average of uncertainty in each measurement, followed by PKPbc-PKPdf data with a noise level of 0.63s. Finally, the PKPab-PKPdf data and absolute PKPdf data show the largest levels of noise with similar values of approximately 0.95s. Thus, the hierarchical sampling found the PKPcd-PKPdf data to have the lowest noise level, and will fit those observations more closely than the PKPab-PKPdf and absolute PKPdf data. From this analysis we expect that the top of the inner core is the best resolved region of our model due to the low noise level in the PKPcd-PKPdf data and the fact that we have more data sensitive to the top of the inner core than the centre of the inner core.

4.7 Results

Our final model was generated by calculating the mean and standard deviations of four different model parameters from the a, b and c values of the 533,380 models in our ensemble: the equatorial velocity (δV_{eq}), the isotropic or Voigt average velocity (δV_{iso}), the anisotropic velocity difference (δV_{ani}),

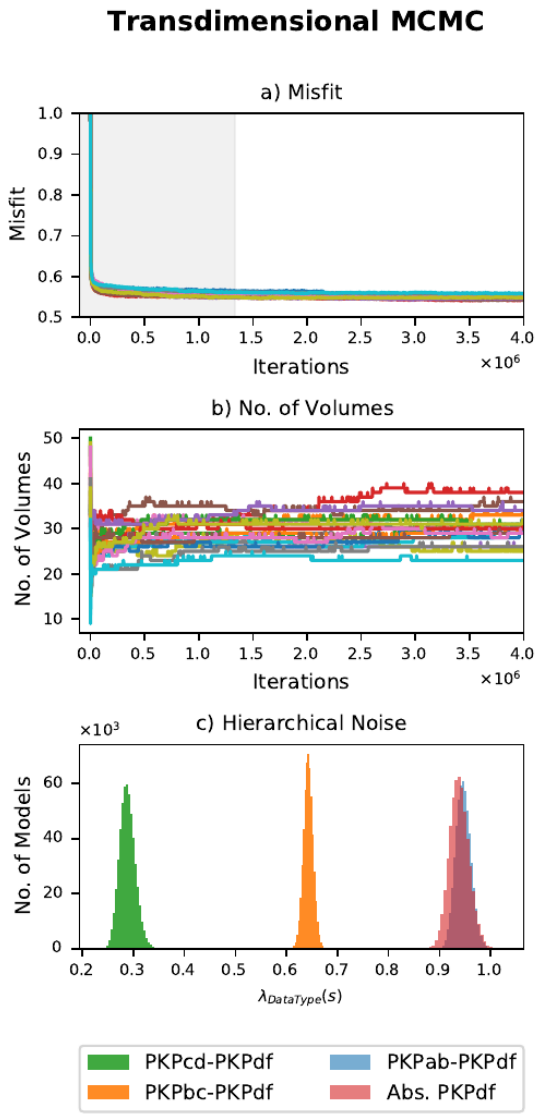

Figure 4.9 a) Variation of misfit with iteration in all 20 chains for our transdimensional model. b) Variation of no. of volumes with iteration in all 20 chains for our transdimensional model. The greyed out area in a) b) is the 'burn in'. c) The total hierarchical parameter of each of our data types, i.e. $\lambda^{total}_{DataType} = \sqrt{\lambda^2_{DataType} + mean(\sigma^{DataType}_{mantle})^2}$ calculated from the ensemble from our transdimensional model.

and the angle of slowest direction (ζ_{slow}) (see Section 4.3). Models in our ensemble will contain different numbers of Voronoi cells at different locations and these individual models will contain sharp boundaries. However when we average across all 533,380 models the boundaries will not be in exactly the same place in every model, meaning that the average model can contain smoothly varying and irregular shaped boundaries.

We will explore our results in terms of large-scale general observations that have been seen before, including the isotropic hemispheres (Section 4.7.1), the anisotropic zone (Section 4.7.2) and the innermost inner core (Section 4.7.3), but mainly focus on the finer-scale details which have become obvious because of our transdimensional approach.

4.7.1 Isotropic hemispheres

Our model confirms the previously found hemispherical pattern with seismic P-waves travelling anomalously fast in the 'eastern hemisphere' of the inner core and anomalously slow in the 'western hemisphere'. This is evident in maps of equatorial velocity throughout the inner core (Figure 4.10a-c), and at the top of the inner core in isotropic velocity (Figure 4.10g). The hemispherical pattern is also clearly visible in cross sections through the equatorial plane (Figure 4.11a,c) and meridional cross sections through the North and South pole (Figure 4.12a,c). This is in agreement with numerous previous studies (Tanaka and Hamaguchi (1997); Niu and Wen (2001); Waszek and Deuss (2011); Lythgoe *et al.* (2014); Burdick *et al.* (2019); Brett and Deuss (2020)). We avoid describing the hemisphere boundaries using single meridians because the hemisphere boundaries are not straight lines through the poles; this is most visible in the equatorial velocity at the ICB around southern Africa and Hawaii (Figure 4.10a.)

It is interesting to note that the hemispherical pattern in the equatorial velocity (Figure 4.11a and 4.12a) persists and the magnitude of the equatorial velocity increases with depth in the eastern hemisphere. The advantage of our use of the transdimensional approach, is that we are not limited to simple hemispherical shapes anymore and so are now able to identify regional heterogeneity within the hemispheres. Further complexity is particularly visible in the meridional cross section (Figure 4.12a), which reveals that the boundary separating the fast and slow equatorial velocities appears sharp and undulating. Some faster equatorial velocities associated with the eastern hemisphere encroach on the slower velocities of the western hemisphere. These new observations would be challenging to identify robustly without using a transdimensional methodology, as it would be difficult to know the extent to which the final model was influenced by the

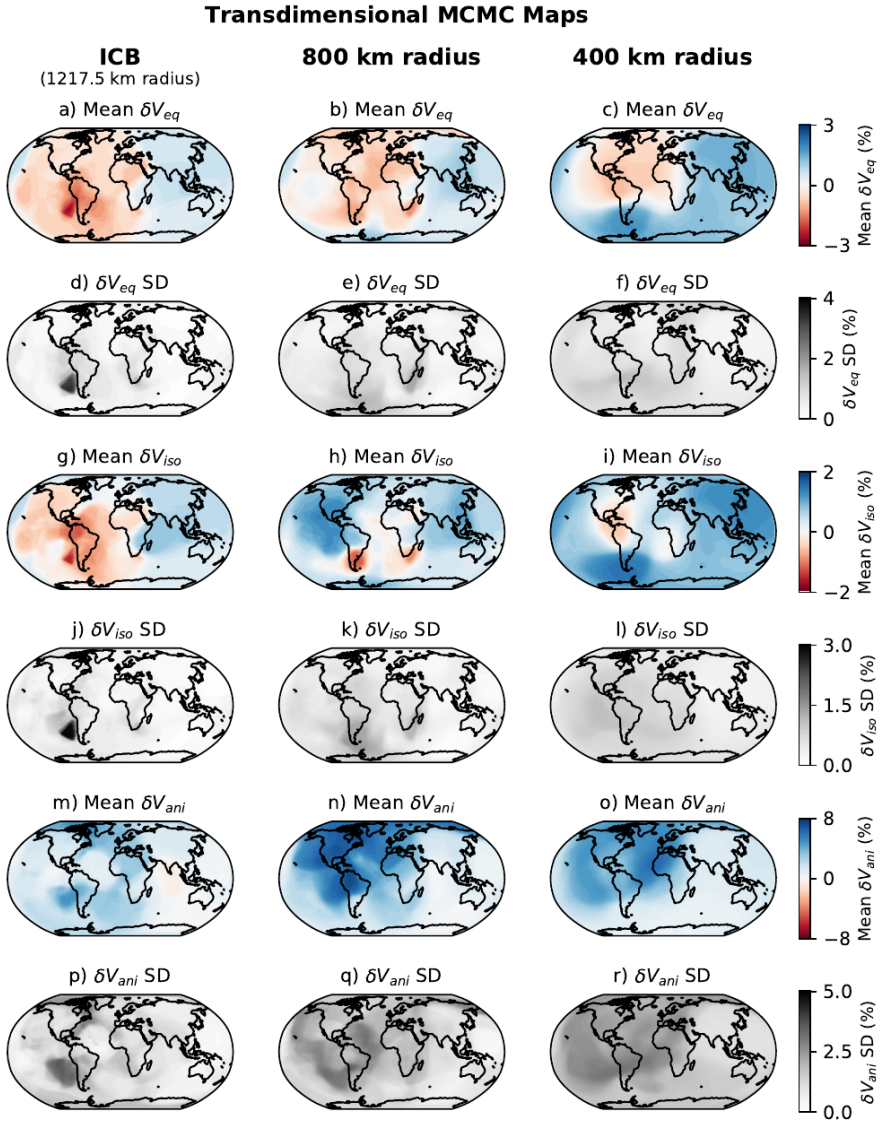

Figure 4.10 Maps of the mean and standard deviation (SD) of δV_{eq}, δV_{ani} and δV_{iso} at the ICB (1217.5 km radius), 800 km radius and 400 km radius throughout our model. The same plot showing a transdimensional inversion using the same model setup but excluding data originating from the South Sandwich Islands is shown on Figure 4.24.

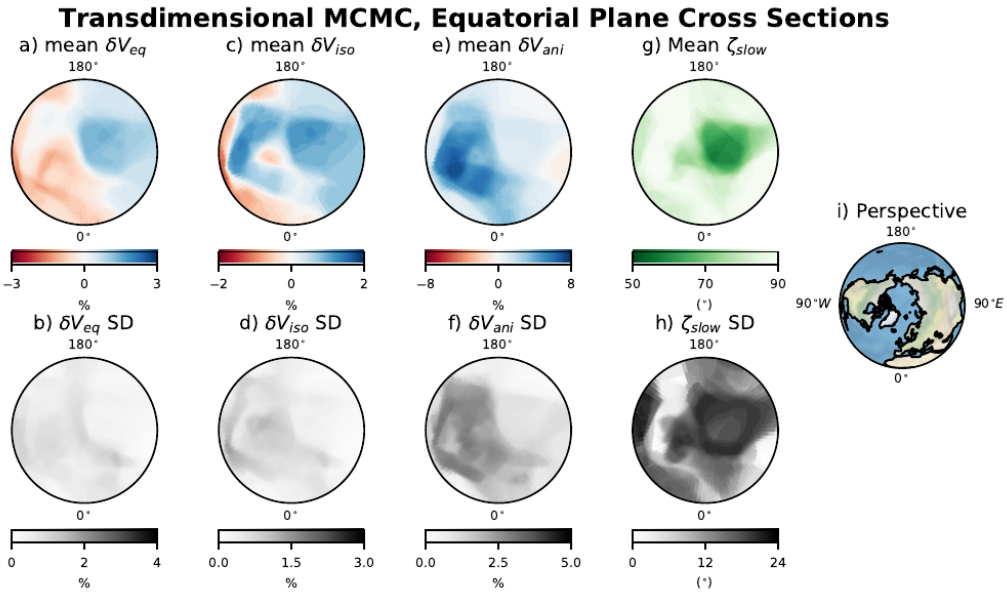

Figure 4.11 Cross sections showing the average and standard deviation (SD) of the δV_{eq}, δV_{ani}, δV_{iso} and ζ_{slow} variations throughout our model. The cross section is a horizontal slice through the equator with constant latitude. The view of the reader is shown in the perspective panel. The same plot showing a transdimensional inversion using the same model setup but excluding data originating from the South Sandwich Islands is shown on Figure 4.27

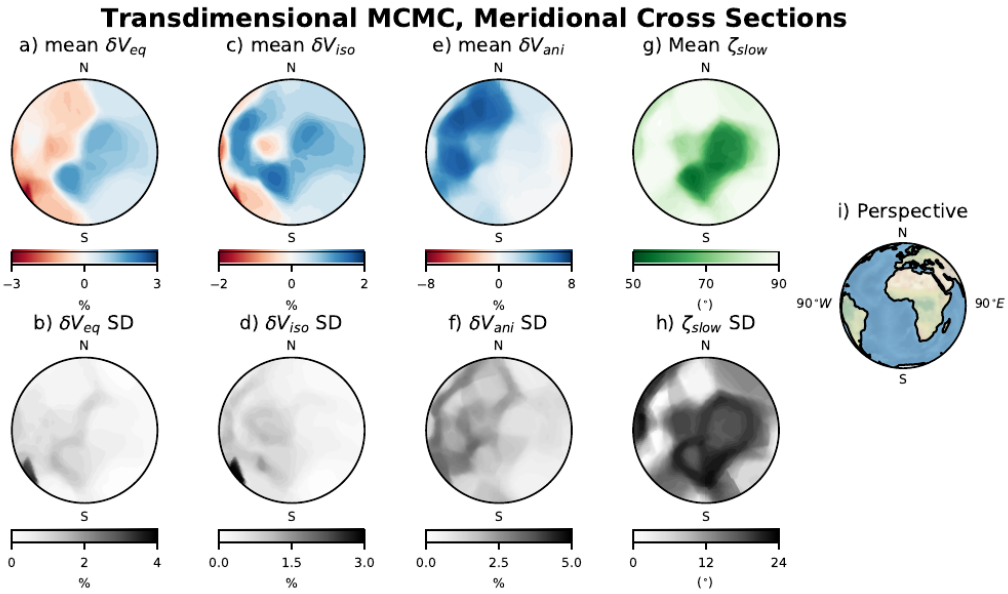

Figure 4.12 Cross sections showing the average and standard deviation (SD) of the δV_{eq}, δV_{ani}, δV_{iso} and ζ_{slow} variations throughout our model. The cross section is a vertical slice spanning all latitudes and going from 90°W to 90°E. The view of the reader is shown in the perspective panel. The same plot showing a transdimensional inversion using the same parameters but excluding data originating from the South Sandwich Islands is shown on Figure 4.26

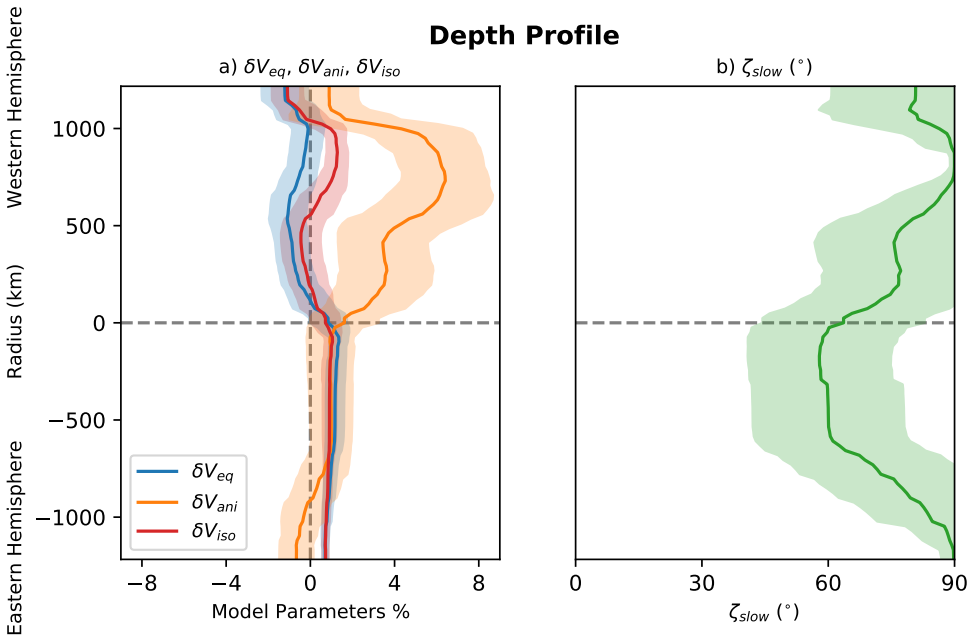

Figure 4.13 A profile through the inner core going from 90°W,0°N at the top to 90°E,0°N at the bottom. a) shows the mean and standard deviation (SD) of δV_{eq}, δV_{ani}, δV_{iso} while the profile on b) shows the variations in ζ_{slow} direction throughout our model.

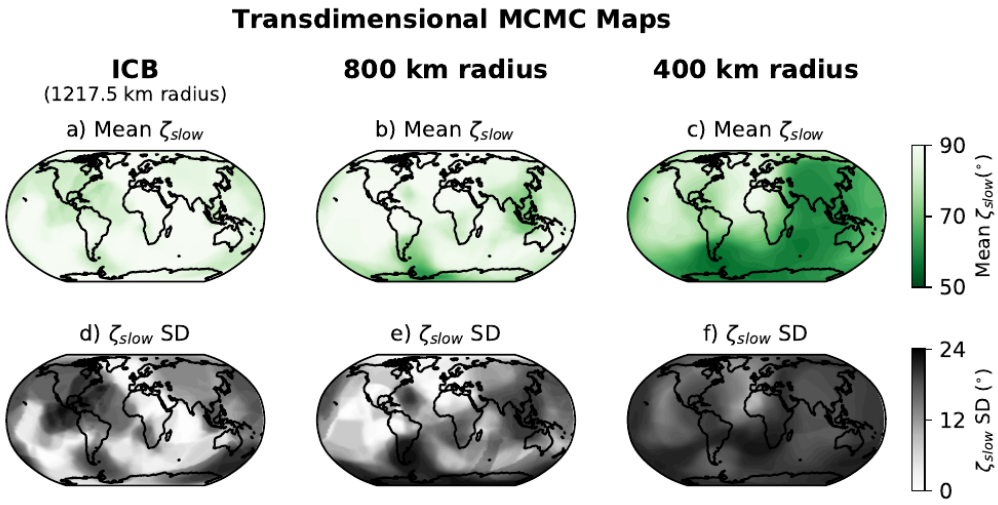

Figure 4.14 Maps of the mean and standard deviation (SD) of ζ_{slow} at the ICB, 800 km radius and 400 km radius throughout our model. The same plot showing a transdimensional inversion using the same model setup but excluding data originating from the South Sandwich Islands is shown on Figure 4.25.

initial fixed parameterization.

Comparing our model of the equatorial velocity to that of Burdick *et al.* (2019) we see good overall agreement in the location of the hemisphere boundaries, but with some extra complexity, this is due to the fact that we also solve for the 3D velocity structure and have more data both of which will influence the location of the boundaries at the ICB.

The hemispherical pattern in the isotropic velocity is present until about 60-170 km depth below the ICB (Figure 4.10g, 4.11c and 4.12c), with boundaries between slow 'west' and fast 'east' located approximately at 170°W and 30°E in broad agreement with previous studies (Tanaka and Hamaguchi (1997); Waszek and Deuss (2011); Burdick *et al.* (2019)). The reason that the isotropic velocity difference does not persist deeper in the inner core, is because the isotropic velocity is a Voigt average of the velocities in all directions. Although the hemispherical variations persist in the equatorial velocity with depth, the contribution of anisotropy (i.e. higher polar velocities) causes the isotropic velocity to lose its hemispherical pattern deeper than 60-170 km below the ICB (Figure 4.13a).

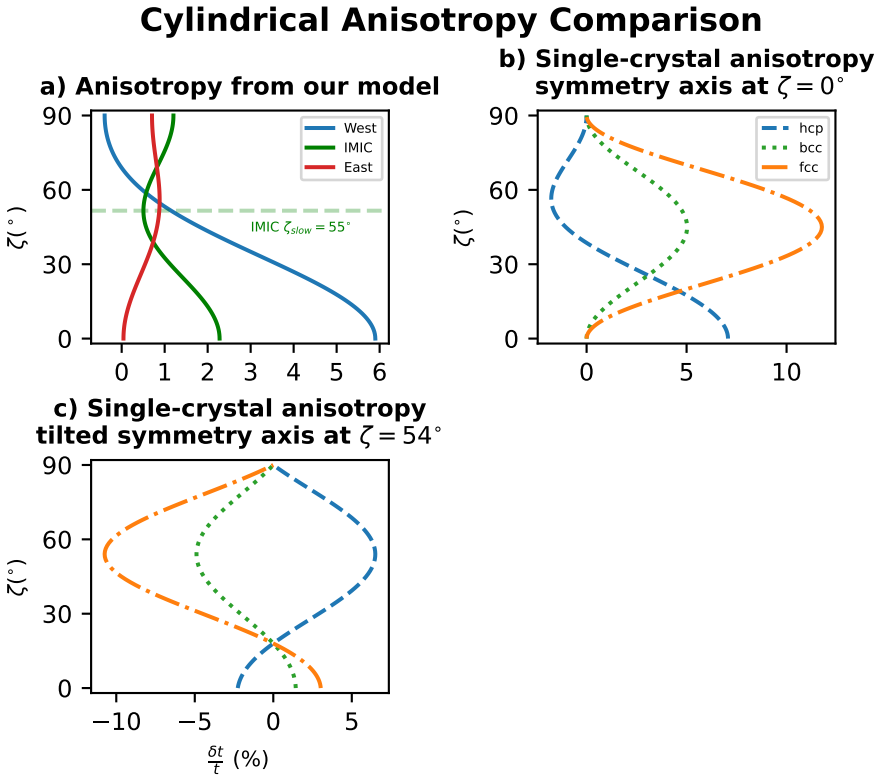

Figure 4.15 a) Cylindrical anisotropy curves from three characteristic locations in our model. The western region represents the velocity variations from location: 90°W, 0°N, 800 km radius. The IMIC curve is from the location: 90°E, 45°N, 100 km radius. The eastern hemisphere curve is from the location: 90°E, 0°N at the inner core boundary. The horizontal green dashed line highlights the ζ_{slow} direction for the IMIC location. b) show predicted single crystal anisotropy for three different iron crystal arrangements hcp, bcc, and fcc iron phases relative to velocity at $\zeta = 0°$ assuming the c-axis of the hcp crystal is at $\zeta = 0°$. c) shows the prediction if the azimuth of maximum velocity through a single bcc or fcc crystal is at $\zeta = 54°$. Values for the stiffness matrix for hcp and fcc iron are taken from Martorell *et al.* (2015) at 6600K and at 360GPa, while the values of the stiffness matrix for bcc iron was taken from Vočadlo (2007) at 6000K.

4.7.2 Anisotropic zone

In agreement with previous studies (i.e. Tanaka and Hamaguchi (1997); Niu and Wen (2001); Lythgoe *et al.* (2014); Brett and Deuss (2020)), our model also contains a strong anisotropic zone in the west where inner core seismic P-waves travelling in the north-south or polar direction travel faster than waves that travel in the east-west or equatorial direction. The lateral extent of the western anisotropic zone is clearly visible in maps of the anisotropic velocity difference (Figure 4.10n-o) at 400 and 800 km radius and also in cross-sections through our model (Figure 4.11e and 4.12e). The inner core displays very little anisotropy near the ICB (Figure 4.10m), with the exception of a strong patch with high uncertainty around South America, similar in location to a high uncertainty region found in Pejić *et al.* (2019).

A 1D profile through our model (Figure 4.13a) furthermore shows that indeed anisotropy is weak at the top of the inner core (0 to 1%) and confirms strong anisotropy to be located within the western hemisphere approximately between 50 and 1100 km radius, and only weak anisotropy ($< 0.5\%$) in the eastern hemisphere. The anisotropic strength increases rapidly with depth, reaching a maximum of 7.2% in the western hemisphere. The radius of the transition to strong anisotropy in this region occurs between 1170 km and 1050 km (Figure 4.13a). It is difficult to define more precisely this radius due to a lack of raypaths with turning points between 1110 km and 1060 km (Blom *et al.*, 2015), resulting in a partial null space. This lack of data is reflected in the standard deviation (Figure 4.11f), which shows a broad region of high uncertainty at the top of the anisotropic zone.

Tanaka and Hamaguchi (1997) described the anisotropic zone as being a 'quasi-hemisphere', i.e. it does not precisely span 180° of longitude. Indeed, we also observe that the anisotropic zone does not span 180° but runs between 170°W and 30°E (Figure 4.11e), spanning a width of 200° in broad agreement with previous models (Sun and Song (2008a); Irving and Deuss (2011); Lythgoe *et al.* (2014))

Most importantly, because of our transdimensional approach we do not prescribe simple hemispherical shapes; this enabled us to find that the anisotropic zone does not continue all the way to the south pole. Instead, we observe for the first time that the western anisotropic zone is largely confined to the northern hemisphere (Figure 4.12e). The anisotropy at the South pole of the inner core at 800 km radius is 2% with an uncertainty of 1.5%, while the anisotropy around North America is 8% with an uncertainty of 2% (Figure 4.12e) meaning that within the bounds of uncertainty in our model the South pole has significantly lower anisotropy than the the region around North America. This regional feature would have been

difficult to map using traditional seismic tomography employing fixed parameterizations, and has important implications for models of inner core growth (Section 4.8). Given that this region of strong anisotropy does not span half the inner core in either longitude or latitude, we use the descriptor of an 'anisotropic zone' (instead of hemisphere).

We conducted a resolution test, to ensure the concentration of anisotropy in the northern part of the western hemisphere was not an artefact of imperfect data coverage. To do this, we ran an inversion using synthetic data for a known synthetic model, containing simple hemispheres (with 8% anisotropy and 0% equatorial velocity in the west and 0% anisotropy and 2% equatorial velocity in the east) spanning all latitudes and a spherical IMIC (with 0.5% anisotropy and 1% equatorial velocity) located at the centre of the model (Figure 4.17-4.19). From this model we generated synthetic data using our real raypaths and added realistic Gaussian noise. The same transdimensional inversion was then conducted on the synthetic data as for the real data. We reproduced all major features from the synthetic model reliably (Figures 4.20-4.23), including an anisotropic hemisphere across all latitudes. This confirms that if the anisotropic region in the west of the inner core spanned all latitudes our data would be able to recover this feature.

We also ran a separate inversion excluding the particular subset of raypaths travelling from the South Sandwich Islands to Alaska (Figures 4.24-4.27). These raypaths appear to travel anomalously fast, and it has been debated to what extent these travel times reflect regional-scale inner core structure versus mantle contamination (Tkalčić (2010); Frost *et al.* (2020); Brett and Deuss (2020)). Our model excluding SSI data shows the same main features, in particular that the western anisotropic zone is still located primarily in the northern hemisphere. Thus, we conclude that the effect of the SSI data on our inversion is minimal and that the western anisotropic zone is indeed confined to the northern hemisphere.

4.7.3 Offset IMIC

The innermost inner core (IMIC) has been defined in previous studies as a anisotropic region where the slowest direction (i.e. ζ_{slow} of Equation 4.4) is at an angle less than 90 degrees from the fastest direction. ζ_{slow} is harder to constrain than δV_{eq} and δV_{ani} since variations in ζ_{slow} produce a more subtle effect on P-wave travel times. Despite this, we detect a clear region in which ζ_{slow} is $55^\circ \pm 16^\circ$; this is most notable in the cross-sections through our model (Figure 4.11g and 4.12g). Within this region, δV_{ani} (the difference between purely polar paths with $\zeta = 0^\circ$ and equatorial paths with

$\zeta = 90°$ is small ($\sim 1\%$). What matters here instead, is that the difference in velocity between polar paths with $\zeta = 0°$ and paths with ζ_{slow} is as large as 2% and therefore, despite having a small value of δV_{ani} this region should still be considered anisotropic.

Interestingly, it appears not to be a spherical feature at the centre of the inner core. In fact, the centre of the IMIC in our model is offset from the centre of the inner core by approximately 400 km, and our IMIC is contained within the eastern hemisphere (Figure 4.13b and Figure 4.14c). Our 'non-spherical' or offset IMIC appears to reconcile previous differing IMIC models (Ishii and Dziewoński, 2003; Beghein and Trampert, 2003; Sun and Song, 2008b; Lythgoe *et al.*, 2014; Frost and Romanowicz, 2019). The model of Sun and Song (2008b) was an early 3D inner core model which observed an IMIC, in their model the parameterization of the IMIC was fixed, with the IMIC in the central 600 km of the inner core. However, Sun and Song (2008b) also ran a model without a fixed IMIC. They concluded that their model with and without a fixed IMIC was approximately the same and that the IMIC was spherical. However, looking at their model again it seems possible that they were already seeing evidence of an offset IMIC but did not have the data at the time to be certain. Lythgoe *et al.* (2014) went further and proposed that the IMIC is in fact part of a larger hemispherical pattern which is in effect what we still see in our model today with more data and a more advanced technique.

We ensured that this offset is not an artefact of data coverage by running two synthetic tests. In one test we included a central spherical IMIC in our synthetic model (Figure 4.17-4.19) and produced synthetic data. After running a transdimensional inversion with this synthetic data we were able to resolve this regional feature (Figure 4.20-4.23), showing that if the IMIC was spherical our data would be able to resolve this. In the second synthetic test we used an offset IMIC which was only present in the eastern hemisphere (Figure 4.28-4.29) and we were also able to fully recover this synthetic model after running a transdimensional inversion (Figure 4.30-4.31).

4.7.4 Summary

Summarising the findings from our model, we identify three robust and particularly interesting features in our model:

1. Strong anisotropy is isolated to a zone within the western hemisphere. The anisotropy is strongest north of the equator and weakens to virtually no anisotropy near the south pole. The top of the inner core near

the ICB displays very little anisotropy, however, anisotropy increases sharply below 200 km depth in the west.

2. We interpret a region with $\zeta_{slow} = 55° \pm 16°$, located primarily in the eastern hemisphere at a radius less than 700 km as the IMIC, with the centre of the IMIC offset from the centre of the inner core by 400 km.

3. Equatorial and isotropic velocity anomalies are separated into two hemispheres, with a slow western hemisphere and a fast eastern hemisphere. The isotropic velocity difference between the hemispheres is present in the top 60-170 km of the inner core, and disappears at greater depth. The hemispherical pattern in equatorial velocity, on the other hand, persists to the centre of the inner core with the equatorial velocity increasing with depth in the eastern hemisphere.

4.8 Geodynamic implications

Relating our seismic observations to geodynamical processes in the inner core is challenging due to the multiple mechanisms proposed to explain the formation of anisotropy and the generation of hemispheres. It is now widely accepted that anisotropy is caused by the alignment of iron crystals, which occurs either during solidification or afterwards through texturing. However, the phase of iron which is stable at inner core conditions remains debated. At inner core temperatures and pressures iron takes the form of hcp (hexagonal close packed), bcc (body centred cubic), or fcc (face centred cubic) crystals. Each phase displays varying intrinsic anisotropy, although the magnitude of anisotropy observed seismically also depends on the degree of crystal alignment.

In order to test if our seismic observations would be able to constrain the phase of iron, we calculated the anisotropy of a single crystal of each phase of iron at inner conditions using values obtained by ab initio simulations from Vočadlo (2007) and Martorell *et al.* (2015). We calculate the velocity of a seismic wave travelling through a single crystal following the methodology of Stixrude and Cohen (1995) with the following equation:

$$\rho V^2 = \sum_{i,j,k,l=1}^{3} w_i n_j w_k n_l C_{ijkl} \tag{4.20}$$

where ρ is density, V is velocity, w is the polarization direction, n is the propagation direction, and C_{ijkl} is the stiffness matrix (obtained from Vočadlo

(2007) and Martorell *et al.* (2015)). We then calculate the P-wave velocity (where $w = n$) and plot the velocity as a function of the propagation direction for each phase of iron on polar plots (Figure 4.16a-c). On Figure 4.16a, the vertical direction through the hcp crystal is at the centre, and the edge of the plot represents different directions through the horizontal plane. The fastest velocities for hcp crystals are in a vertical direction (in the centre), while the slowest velocities are closer to the edge of the polar plot (58° from the vertical direction).

To facilitate the comparison between the single crystal anisotropy from the mineral physics and the anisotropy variations in our models, we used the mean a, b, and c parameters from our models for three different locations and plot the corresponding predicted fractional travel times (Figure 4.15a). We select locations from the western anisotropic zone (90°W, 0°N, 800 km radius), the IMIC (90°E, 0°N, 100 km radius), and the eastern hemisphere (90°E, 0°N, ICB). The western zone clearly exhibits strong cylindrical anisotropy, whereby polar raypaths are 5.9% faster than equatorial. There is negligible anisotropy in the eastern hemisphere ($< 0.5\%$), and rays which travel in a polar direction are slower than equatorial rays. In the IMIC, the equatorial and polar velocities are similar; the slowest direction is oriented at $\zeta = 55°$, with a velocity decrease of almost 2% relative to the polar velocity.

The anisotropy in the western zone (Figure 4.15a) appears most similar to the anisotropy predicted for a single hcp crystal with symmetry axis aligned N-S (Figure 4.15b), while anisotropy in the IMIC is more complex. Polar raypaths passing through the IMIC are only slightly faster than the equatorial raypaths; the largest travel time difference is instead between the slowest direction (at $\zeta = 55°$) and the equatorial and polar directions. This anomalous anisotropy could be caused by the dominance of the bcc or fcc iron phases with a tilted fast symmetry axis. For example, If we align the anisotropy symmetry axis with the fastest direction through a bcc or fcc crystal (which is at $\zeta = 54°$, see Figure 4.16b-c) then we get the predicted travel times shown in Figure 4.15c. The travel times for fcc and bcc (Figure 4.15c) bear a resemblance to the anisotropy we observe in the IMIC (Figure 4.15a). It is important to note, that this analysis is an approximation as we are assuming that the anisotropy of a large volume made of many crystals can be described by a single crystal with 100% alignment relative to Earth's axis of rotation. We are, however, making this comparison to encourage further research into the possibility that seismic anisotropy within different regions in the inner core could be explained by different phases of iron.

Anisotropic phases of iron, by themselves, do not account for the ob-

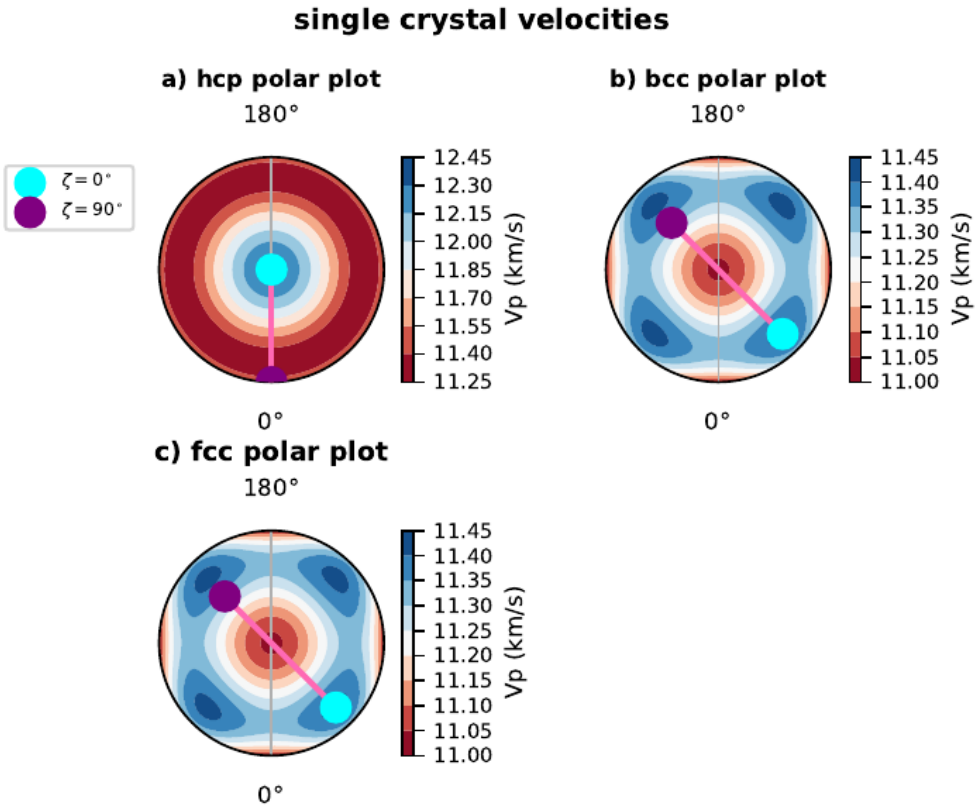

Figure 4.16 This shows the P-wave velocity through a single crystal as a function of propagation direction for a) hcp, b) bcc, and c) fcc crystals. This is a polar plot where the Z-direction is at the centre. The lines show a 90° arc from the fastest towards the slowest velocities across a crystal, where we assume the fastest direction is located at $\zeta = 0°$

served pattern of inner core anisotropy. The crystals must be aligned in a lattice preferred orientation (LPO) or alternatively in a shape preferred orientation (SPO), as a texture of randomly oriented anisotropic crystals would appear isotropic overall. Given a particular phase of iron, the question arises how this LPO is generated, and which mechanism(s) result in a heterogeneous distribution of this LPO. LPOs are commonly caused by post-solidification deformation, for the inner core one possible deformation mechanism would involve induced stresses causing axis symmetric flow, resulting in iron crystals aligning with this flow. A number of mechanisms have been proposed to create such texturing, including topographic relaxation (also known as equatorial growth, Yoshida *et al.* (1996)), whereby preferential growth at the equator of the inner core causes flow toward the poles due to geostatic forces. An alternative mechanism involves Maxwell stress or Lorentz forces induced by the magnetic field, causing deformation strongly influenced by outer core flow (Karato (1999); Buffett and Wenk (2001)). It is likely that a combination of these mechanisms is required to explain the observed seismic complexity. For example, models of topographic relaxation typically produce symmetric flow around the equator which would create seismic anisotropy at both poles. This is in contrast to our observation that anisotropy in the inner core does not extend from south pole to north pole. Given this new observation, it is important that future geodynamical models assess whether topographic relaxation mechanisms can produce asymmetric flow around the equator, resulting in stronger anisotropy at the north pole than the south pole.

Hemispherical structures in the inner core are equally complicated to account for, and must further be compatible with the processes to generate anisotropy. Proposed hemispherical models are separated broadly based on whether the density or thermal profile in the inner core is stable. If the inner core has an unstable density or thermal profile, then convection becomes probable (Lythgoe and Deuss, 2015). For specific conditions (large viscosity and low thermal conductivity), this convection will be in the form of inner core translation which can result in a hemispherical pattern (Alboussiere *et al.* (2010); Deguen *et al.* (2018)). An anisotropic fabric will be able to form if this translation is combined with a texturing mechanism such as topographical relaxation (Yoshida *et al.* (1996); Deguen *et al.* (2011)), deformation due to magnetic forces (Karato, 1999) or annealing during translation (Bergman *et al.*, 2010). For example, recent work by Frost *et al.* (2021) has shown that translation in the inner core is able to produce a region in the west with strong anisotropy. However, translation models require a high inner core viscosity ($> 10^{18}$ Pa s), which is not in agreement with current

viscosity estimates of $10^{13} - 10^{17}$ (Koot and Dumberry, 2011; Ritterbex and Tsuchiya, 2020).

Alternatively, variations in crystallization rate at the inner core boundary could result in hemispherical differences being 'frozen in' as the inner core grows (Aubert *et al.*, 2008). In this case, heat flux at the ICB would be influenced by flow in the outer core, the magnetic field, and potentially thermal anomalies at the core mantle boundary (Karato, 1993). This mechanism of hemisphere formation implies that structures at increasing depth within the inner core record older properties of ICB properties, outer core flow, and magnetic field strength. This opens the potential to use seismology to infer paleomagnetic properties, but it is also unclear if anomalies in the outer core could last long enough to maintain a consistent pattern of crystallisation in the inner core, and whether this pattern could truly be preserved for substantial periods of time.

4.9 Conclusion

Our transdimensional MCMC model of inner core seismic velocity shows that hemispherical structures and regional-scale variations in anisotropy are required to explain inner core body wave data. The observed features remain when removing anomalous data from earthquakes originating in the South Sandwich Islands, and also when using data corrected for 3D mantle structure. Our results reveal for the first time that the strong anisotropic region in the west is primarily located in the northern hemisphere, with implications for geodynamical models of inner core formation. This result is guided only by the data itself without any prior structure imposed in the parameterization, and is robust even when considering uncertainties in the data and model space. We propose to call this an anisotropic *zone* (rather than hemisphere) to better describe its shape. We also find robust evidence for a innermost inner core, in which the slowest velocity is at an angle of $55° \pm 16$. The IMIC is offset by 400 km from the centre of the inner core and is contained mainly within the eastern hemisphere. Its distinct anisotropy could indicate a different phase of iron (either bcc or fcc) than the rest of the inner core (hcp), and potentially result from multiple stages of inner core growth, while its offset is compatible with models of slow lateral translation.

4.10 Supplementary material

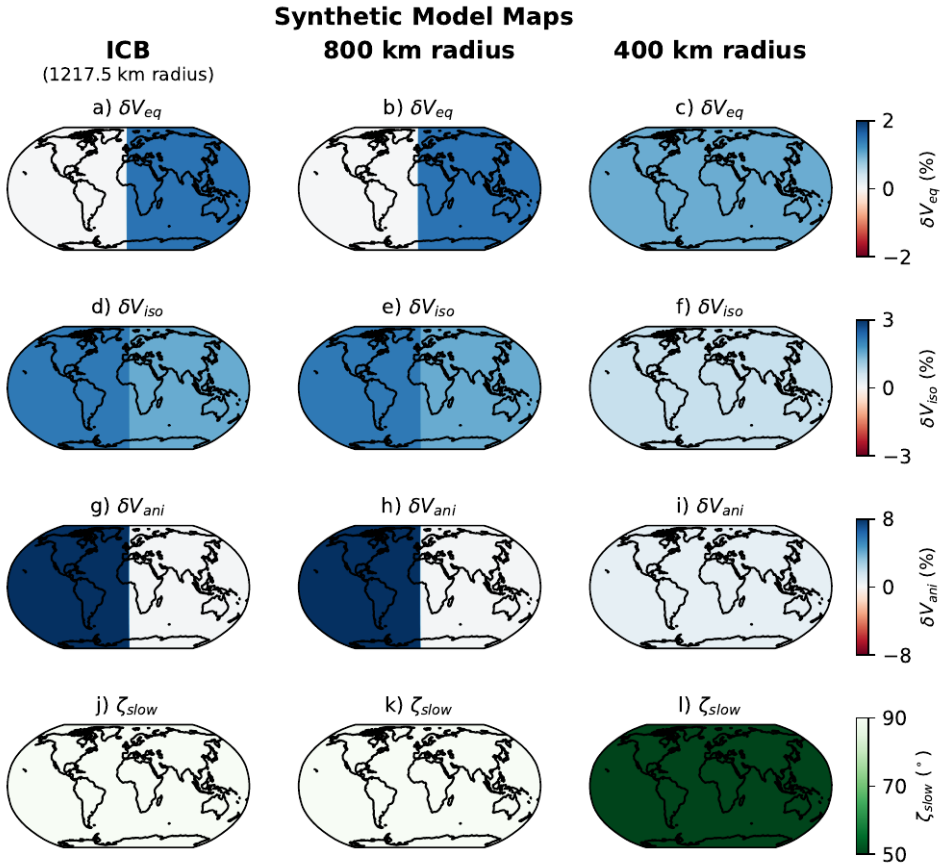

Figure 4.17 Maps of the variations of δV_{eq}, δV_{ani}, δV_{iso}, and ζ_{slow} at the ICB (1217.5 km radius), 800 km radius, and 400 km radius for our synthetic model, used to generate synthetic data

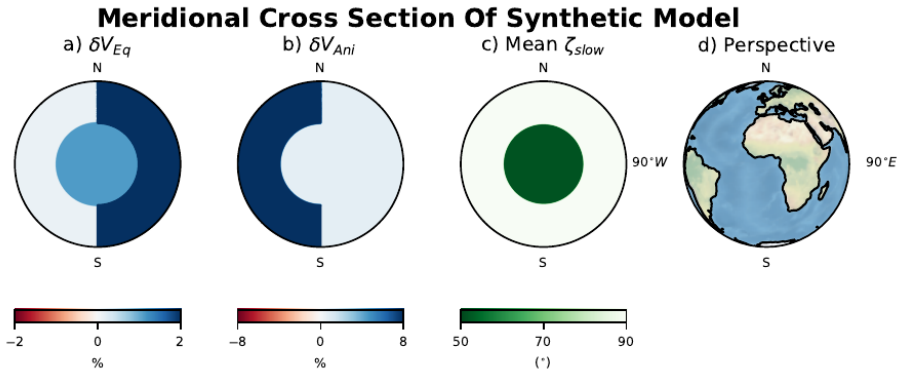

Figure 4.18 Cross sections showing V_{eq}, δV_{ani}, δV_{iso}, and ζ_{slow} variations throughout our synthetic model. The cross section is a vertical slice spanning all latitudes and traversing 90°W to 90°E. The view of the reader is shown in the perspective panel.

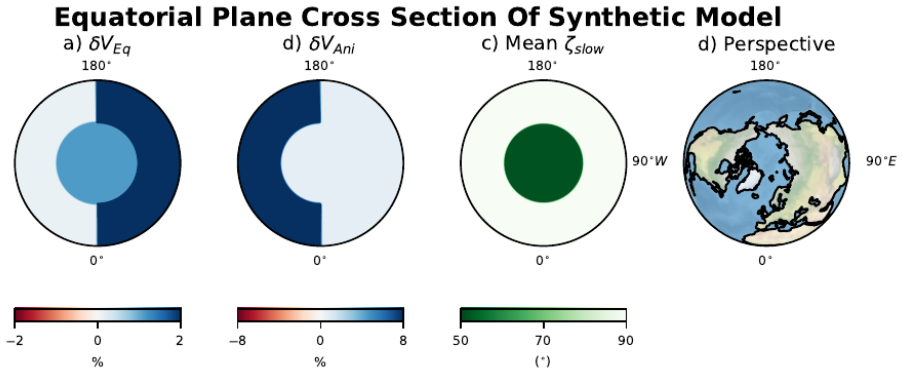

Figure 4.19 Cross sections showing the δV_{eq}, δV_{ani}, δV_{iso}, and ζ_{slow} variations throughout our synthetic model. The cross section is a horizontal slice through the equator with constant latitude. The view of the reader is shown in the perspective panel.

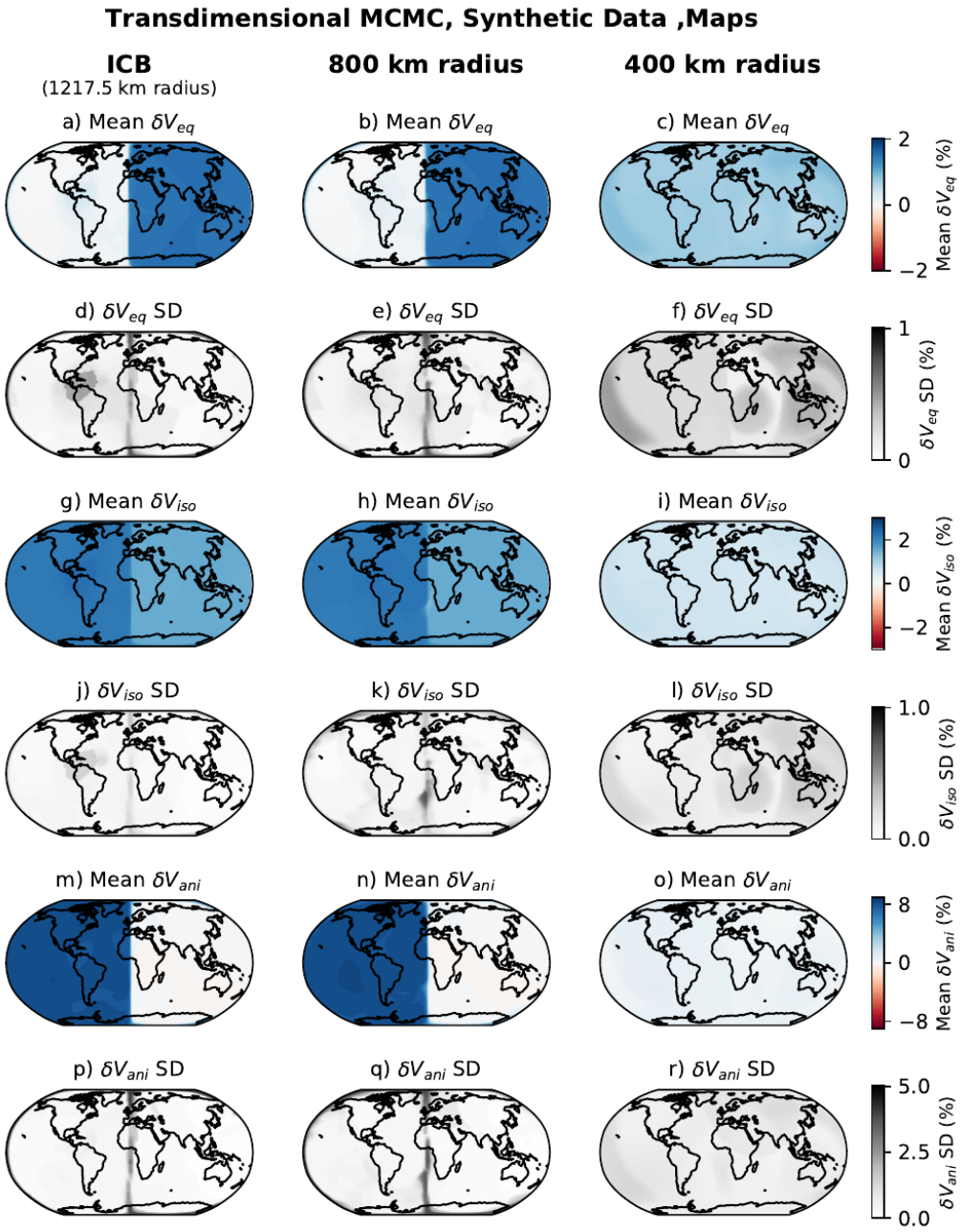

Figure 4.20 Maps of the mean and standard deviation of δV_{eq}, δV_{ani}, and δV_{iso} at the ICB (1217.5 km radius), 800 km radius, and 400 km radius for a transdimensional model run on synthetic data.

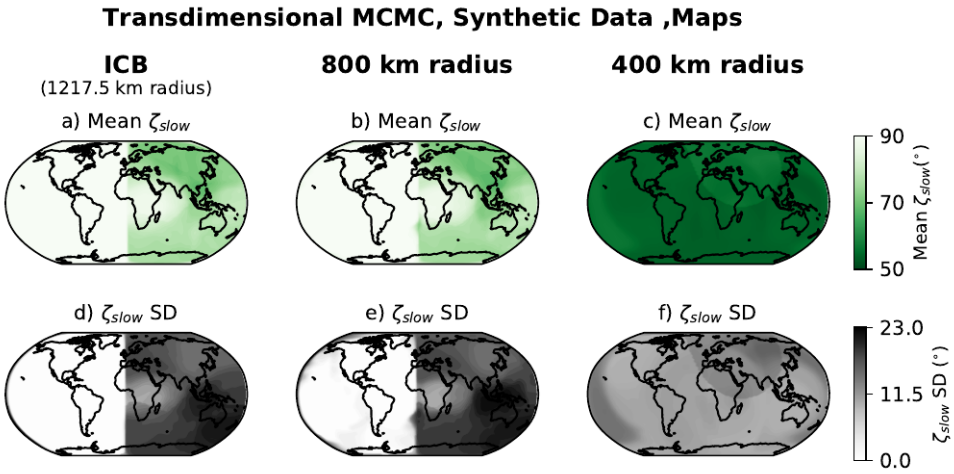

Figure 4.21 Maps of the mean and standard deviation of ζ_{slow} at the ICB, 800 km radius, and 400 km radius throughout for a transdimensional model run on synthetic data.

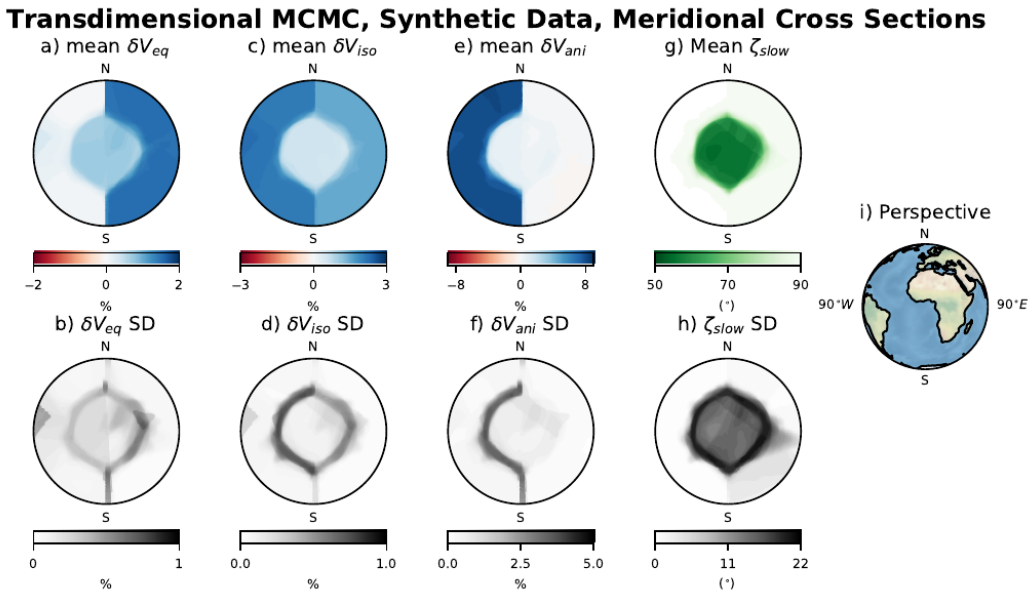

Figure 4.22 Cross sections showing the average and standard deviations of the δV_{eq}, δV_{ani}, δV_{iso}, and ζ_{slow} variation for a transdimensional model run on synthetic data. The cross section is a vertical slice spanning all latitudes and going from 90°W to 90°E. The view of the reader is shown in the perspective panel.

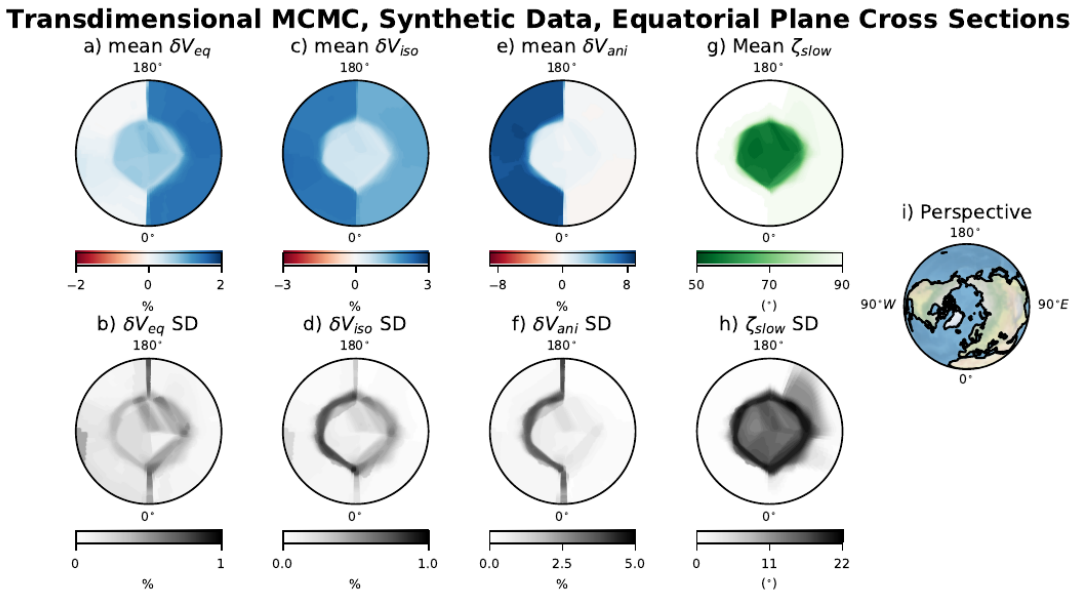

Figure 4.23 Cross sections showing the average and standard deviations of the δV_{eq}, δV_{ani}, δV_{iso} and ζ_{slow} variation for a transdimensional model run on synthetic data. The cross section is a horizontal slice through the equator with constant latitude. The view of the reader is shown in the perspective panel.

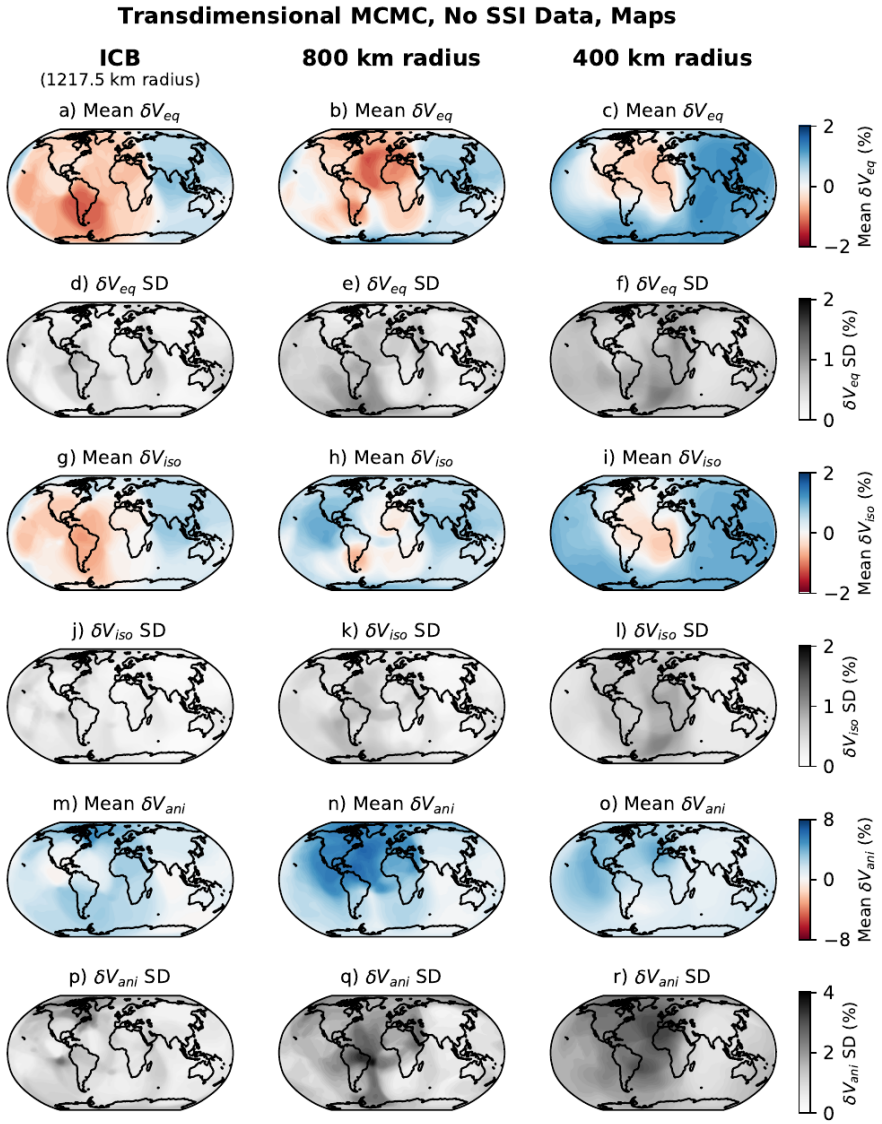

Figure 4.24 Maps of the mean and standard deviation of δV_{eq}, δV_{ani}, and δV_{iso} at the ICB, 800 km radius, and 400 km radius throughout our model

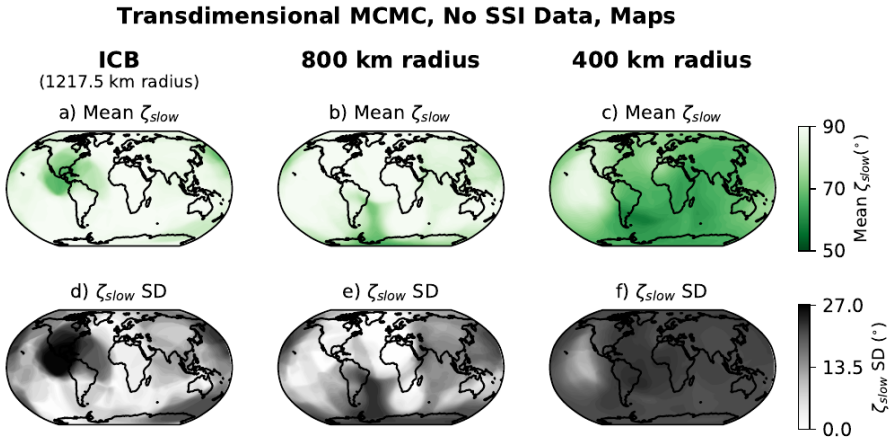

Figure 4.25 Maps of the mean and standard deviation of ζ_{slow} at the ICB, 800 km radius, and 400 km radius throughout our model

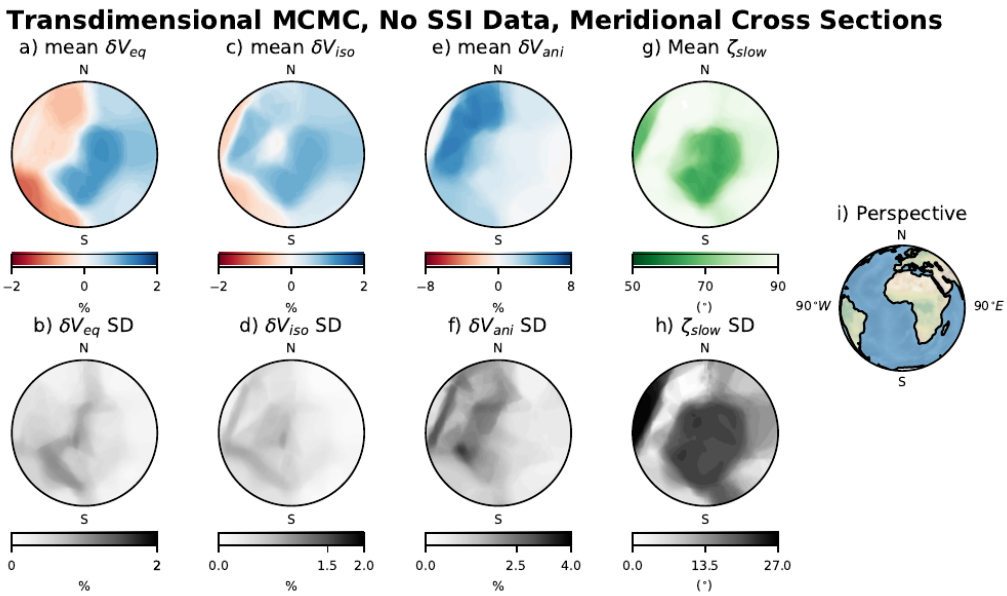

Figure 4.26 Cross sections showing the average and standard deviations ofδV_{eq}, δV_{ani}, δV_{iso}, and ζ_{slow} variations throughout for our model excluding SSI data. The cross section is a vertical slice spanning all latitudes and going from 90°W to 90°E. The view of the reader is shown in the perspective panel.

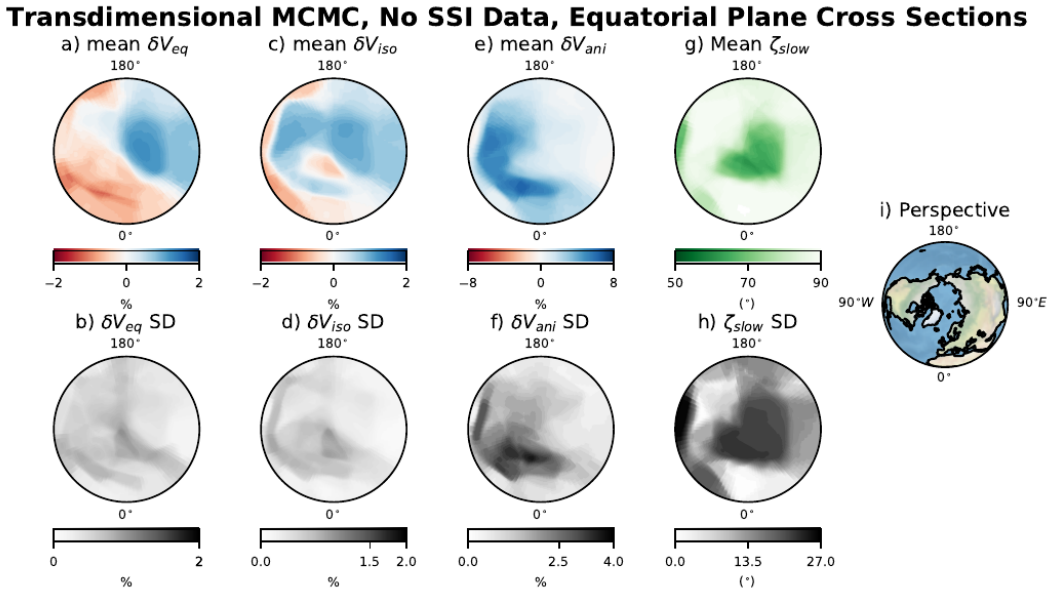

Figure 4.27 Cross sections showing the average and standard deviations of the a, $b + c$, δV_{iso}, and ζ_{slow} variation for our model excluding SSI data. The cross section is a horizontal slice through the equator with constant latitude. The view of the reader is shown in the perspective panel.

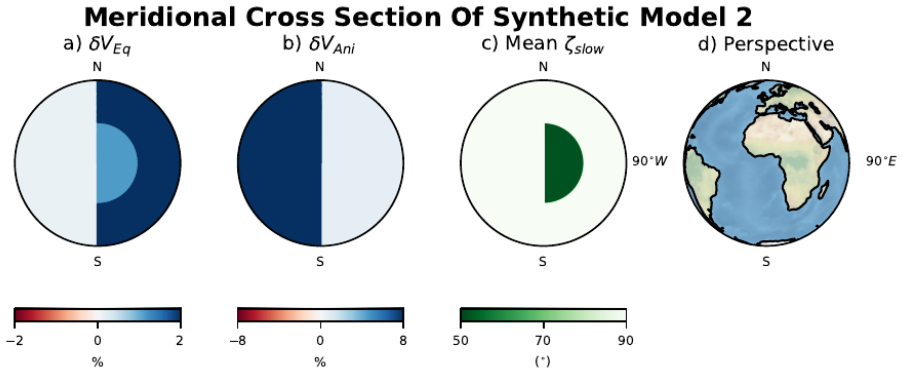

Figure 4.28 Cross sections showing V_{eq}, δV_{ani}, δV_{iso}, and ζ_{slow} variations throughout our second synthetic model with an offset IMIC. The cross section is a vertical slice spanning all latitudes and traversing 90°W to 90°E. The view of the reader is shown in the perspective panel.

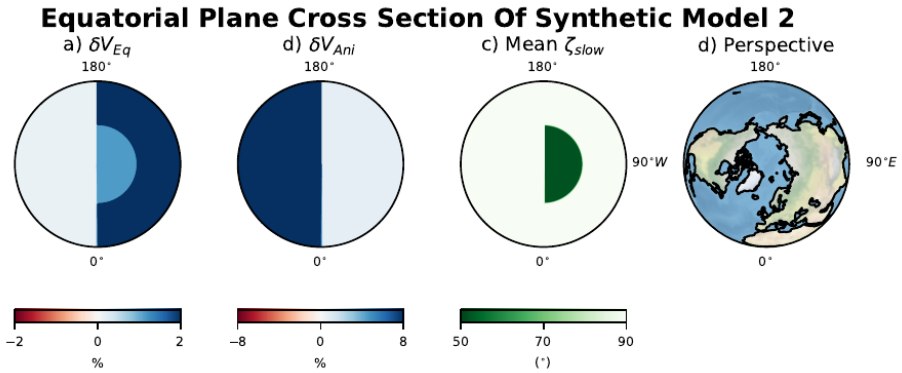

Figure 4.29 Cross sections showing the δV_{eq}, δV_{ani}, δV_{iso}, and ζ_{slow} variations throughout our second synthetic model with an offset IMIC. The cross section is a horizontal slice through the equator with constant latitude. The view of the reader is shown in the perspective panel.

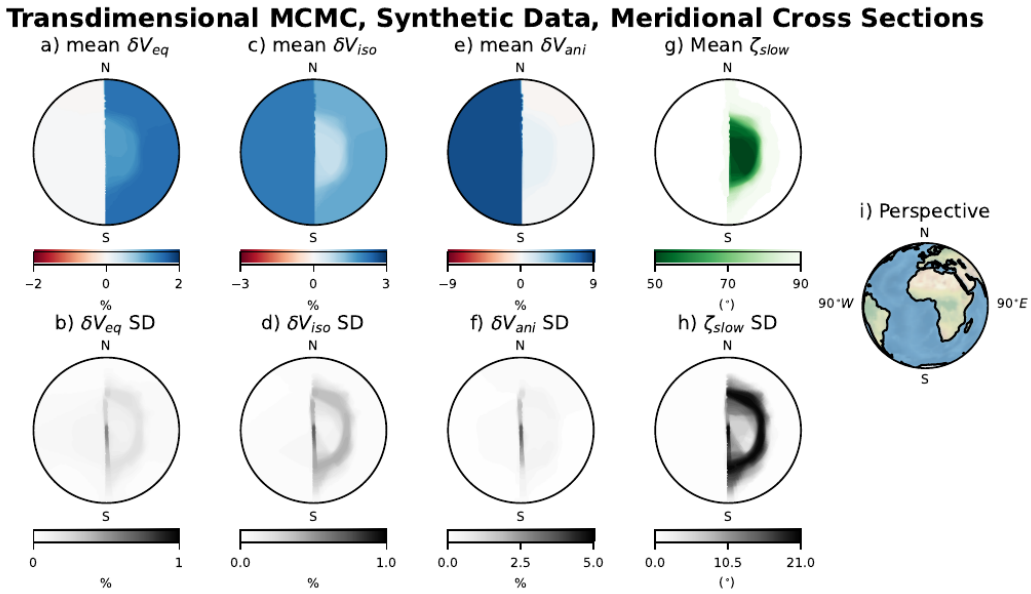

Figure 4.30 Cross sections showing the average and standard deviations of the δV_{eq}, δV_{ani}, δV_{iso}, and ζ_{slow} variation for a transdimensional model run on synthetic data produced with the synthetic model shown in Figures 4.28-4.29. The cross section is a vertical slice spanning all latitudes and going from 90°W to 90°E. The view of the reader is shown in the perspective panel.

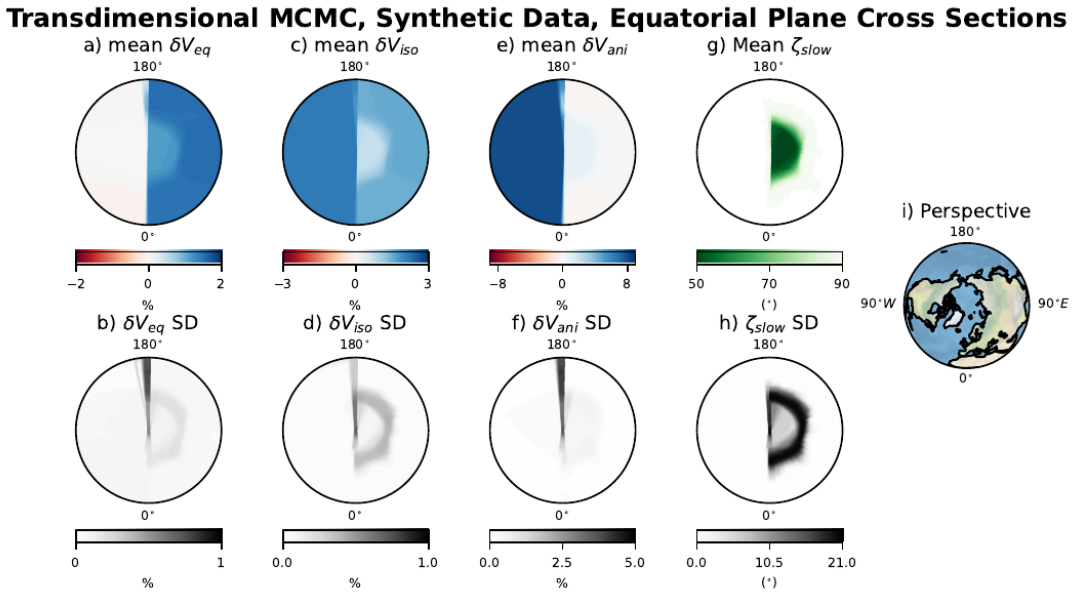

Figure 4.31 Cross sections showing the average and standard deviations of the δV_{eq}, δV_{ani}, δV_{iso} and ζ_{slow} variation for a transdimensional model run on synthetic data produced with the synthetic model shown in Figures 4.28-4.29. The cross section is a horizontal slice through the equator with constant latitude. The view of the reader is shown in the perspective panel.

5

Measuring splitting functions of inner core sensitive normal modes

Splitting function measurements of inner core sensitive normal modes typically have anomalously large absolute values of the zonal parameters c_{20} and c_{40}. These large values imply that there is strong anisotropy in the inner core with an approximately north-south direction, in general agreement with body wave observations of inner core anisotropy. The most common way to measure normal modes is using a splitting function methodology, which are obtained in an iterative least squares inversion using normal mode spectra as data. These splitting functions describe the lateral variation in frequency from the centre frequency of a given normal mode. Unfortunately, it has been found that the starting values of c_{20} and c_{40} in the splitting function inversion has a significant affect on the final measurement. To overcome this problem we conduct a grid search starting from thousands of combinations of c_{20} and c_{40} values for a range of damping parameters for 18 inner core sensitive self-coupled modes. From this grid search we robustly recover the best fitting measurement and the range of values for c_{20} and c_{40} which fit the data, allowing us to assess which modes are well determined from our data, and also provide us with measurement uncertainty.

5.1 Introduction

Corroborating the body wave studies, Woodhouse *et al.* (1986) first noticed anomalous zonal splitting in inner core sensitive normal modes and concluded that this could be explained by an anisotropic inner core. Normal modes are whole Earth oscillations which are excited after a large earthquake. They are independent measurements from body waves, observed only when looking at the frequency spectra of several days-long seismograms. They have long wavelength sensitivity which gives them uniform sampling within the deep Earth independent of event or station locations. This makes normal mode data valuable as a independent source of information from body waves on seismic parameters in the deep Earth. Normal modes are often included in tomographic models through a two-step inversion. In the first step we invert for splitting functions, where frequency deviations from a reference centre frequency for a specific mode are measured. Splitting functions are a depth-average of a how a mode sees the Earth. The splitting function technique was pioneered by Giardini *et al.* (1987) and has been applied to both mantle and core sensitive modes. In the second step, splitting functions are then inverted for 3D variations in mantle and core structure.

When measuring normal modes that are sensitive to the inner core, their splitting functions commonly have anomalously large absolute values of the zonal c_{20} and c_{40} parameters, as was first extensively studied by Woodhouse *et al.* (1986). This is significant as strong c_{20} and c_{40} parameters indicate that there is inner core anisotropy which is primarily aligned in a north-south direction, similar to observations of inner core anisotropy from body waves. Woodhouse *et al.* (1986) originally measured 7 inner core sensitive modes, but as the number of seismometers, recordings of large earthquakes and computational power increased more inner core sensitive normal modes were measured and with greater accuracy (Li *et al.* (1991); Widmer *et al.* (1992); He and Tromp (1996); Resovsky and Ritzwoller (1998); Durek and Romanowicz (1999); Deuss *et al.* (2013)).

Body waves suggest that the inner core is split broadly into two hemispheres with an anisotropic western hemisphere and a isotropic eastern hemisphere (Tanaka and Hamaguchi, 1997). Inner core sensitive modes are usually only measured with the self coupled approximation. Self-coupled modes are only sensitive to even-degree structure meaning they are not independently sensitive to odd-degree structure such as hemispheres. Odd-degree structure can only be observed using cross-coupled pairs of modes. Deuss *et al.* (2010) made the first measurements of pairs of inner core sensitive cross-coupled modes, using a splitting function approximation and

from this they were able to make the first normal mode observations of hemispherical structure in the inner core. Here we will ignore the cross-coupled modes and focus only on self-coupled modes in order to keep the problem simple and tractable in a grid search.

It is important to note that splitting functions are only a useful approximation and that in principle a one step inversion should be used. Durek and Romanowicz (1999) used a one-step direct spectra inversion to make a model of inner core anisotropy. In a direct spectra inversion you solve for structure in the Earth in a single step, without first measuring splitting functions. This has advantages as you apply regularisation only once and you fit all the modes simultaneously. However, it also comes at an increased computational cost, it is not feasible to use with sampling methods, such as Markov Chain Monte Carlo (MCMC) and it is more complex to combine with body waves than using splitting functions. Jagt and Deuss (2021) have been working on applying one-step inversions, but it only becomes feasible for the inner core once mantle velocity, density and anisotropy has been fully resolved.

Recently, Pachhai *et al.* (2020) used a nearest neighbour methodology to measure elastic and anelastic splitting functions jointly for 19 spheroidal inner core sensitive modes. They found that for modes which have strong shear-wave energy in the inner core it is important to also measure the anelastic part, such as was done by Mäkinen *et al.* (2014) for inner core sensitive modes. Again, for simplicity we will focus on the elastic splitting function only.

The main aim of this chapter is to deal with the problem that when measuring splitting functions for inner core sensitive normal modes, the final measurement strongly depends on the starting model used (Megnin and Romanowicz (1995); Durek and Romanowicz (1999)). To overcome this problem, we will perform a grid search over a large range of starting models for 18 inner core sensitive modes using a splitting function approximation. Through this grid search we are able to identify global and local misfit minima and use this information to make estimates of the uncertainty on our splitting function measurements.

5.2 Normal mode theory and method

Normal modes are whole Earth oscillations, or standing waves, which occur after a large earthquake. they exist for discrete frequencies in the Earth and can be split into two types: spheroidal modes and toroidal modes. Spheroidal modes consist of P-SV motion and are comparable to Rayleigh

surface waves, while toroidal modes consist of SH motion and so are comparable to Love waves. In this study we will only use spheroidal modes, ${}_nS_l$, which are specified by their overtone number n and angular order l. The overtone number roughly describes the complexity of the radial pattern while angular order is the number of nodal lines over the Earth's surface. Modes with $n = 0$ are called fundamental modes, while modes with $n > 0$ are overtones.

A mode with overtone number n and angular order l consists of $2l + 1$ singlets. The singlets of one mode together form a multiplet. Singlets are labeled by the azimuthal order m where $-l < m < l$. For a Spherical Non-Rotating Elastic and Isotropic Earth model (SNREI) the singlet frequencies of a mode are the same which is called degeneracy. However, deviations from SNREI removes the degeneracy which results in the singlets of modes deviating from each other. This is called splitting and can be caused by rotation, ellipticity and 3D variations in velocity, density, anisotropy, attenuation and boundary topography.

It is relatively simple to calculate the effect of rotation and ellipticity of the Earth for a given mode and then the challenge is to relate the remaining splitting to 3D Earth structure. Splitting can also be caused by the resonance of two or more modes with each other, which is called cross-coupling (Deuss *et al.*, 2010), however in this thesis we will focus on inner core sensitive self-coupled modes only. Within the self-coupling approximation modes are assumed to be isolated in frequency.

5.2.1 Splitting functions

We measure normal mode splitting functions using the methodology of Deuss *et al.* (2013). Splitting functions are a depth average of what a particular mode observes in the Earth and describe the splitting of a mode. It shows us where the frequency of a mode is locally higher or lower than its centre frequency and in that way describes 3D heterogeneity as a depth averaged perturbation from a reference model, for which we use PREM (Dziewonski and Anderson, 1981).

A significant advantage of using splitting functions is that they are linearly dependent on heterogeneous structure in the Earth (including velocity and density) and so can be efficiently incorporated into inversions with body waves and ensure that computationally expensive Markov Chain Monte Carlo (MCMC) methods are feasible.

Splitting function coefficients, c_{st}, are defined for each mode with a given

angular order l and overtone number n and can be computed thus;

$$c_{st} = \int_0^a \delta m_{st}(r) K(r) dr + \sum_d \delta h_{st} H_s^d \tag{5.1}$$

where δm_{st} and δh_{st} are coefficients describing Earth's heterogeneity (v_p, v_s and ρ) and discontinuity topography in terms of spherical harmonics and $K_s(r)$, H_s^d are known kernels (Woodhouse, 1980). s and t are the angular order and azimuthal order of the spherical harmonic used to describe the structure in the Earth while a is the radius of the Earth. I only measure self-coupled modes, in which s is an even integer and is maximum $2l$.

The c_{st} coefficients are defined following the conventions of Masters *et al.* (2000) and Resovsky and Ritzwoller (1998). $\mathrm{Re}(c_{00})$ and $\mathrm{Im}(c_{00})$ define the shift in centre frequency, f_c, and radial quality factor Q relative to the 1-D reference model, PREM (Dziewonski and Anderson, 1981), using the following relation:

$$f_c = f_0 + (4\pi)^{-\frac{1}{2}} \mathrm{Re}(c_{00}) \tag{5.2}$$

$$Q = \frac{f_c}{2(\frac{f_0}{2Q_0} + (4\pi)^{-\frac{1}{2}} \mathrm{Im}(c_{00}))} \tag{5.3}$$

where f_c is the centre frequency in Hz and f_0 and Q_0 are the frequency and quality factor of the reference model. We can represent splitting functions on maps to show local deviations in the frequency of a mode using the following relation:

$$F(\theta, \phi) = \sum_{s=0}^{2l} \sum_{t=-s}^{s} c_{st} Y_s^t(\theta, \phi) \tag{5.4}$$

where $Y_s^t(\theta, \phi)$ are the complex spherical harmonics (Edmonds, 1960), θ and ϕ are the latitude and colongitude of the spherical coordinate system.

5.2.2 Synthetic seismograms

The principle behind a splitting function measurement is to start from a 1D reference model. We then calculate the change to the degenerate centre frequency and how the mode singlets are split compared to the reference model and investiate how much splitting is required to fit a dataset of spectral segments. To calculate this fit we must be able to calculate synthetic seismograms. We use a methodology similar to Li *et al.* (1991) and used

extensively in previous research (Deuss and Woodhouse (2001); Deuss *et al.* (2013); Talavera-Soza and Deuss (2020); Talavera-Soza and Deuss (2021)).

A synthetic seismogram, $u(t)$, can be described as a harmonic function of time t:

$$u(t) = Re[\mathbf{r} \cdot \mathrm{e}^{i\sqrt{\mathbf{M}}t} \cdot \mathbf{s}] \tag{5.5}$$

where $\mathbf{s}$ is the source vector describing the moment tensor of the event, $\mathbf{r}$ is the receiver vector and describes instrument orientation and response. Both $\mathbf{r}$ and $\mathbf{s}$ are computed for PREM. $\mathbf{M}$ is the matrix which contains the splitting coefficients and also contributions from ellipticity and rotation. In a spherical non-rotating Earth model without aspherical heterogeneity, $\mathbf{M}$ would be a diagonal matrix which only contains the degenerate multiplet frequencies ω_0^2

When incorporating rotation, ellipticity and aspherical heterogeneity, then $\mathbf{M}$ is no longer diagonal. $\mathbf{M}$ is now a complex matrix containing the degenerate multiplet frequencies, ω_0^2 for PREM and the contributions of rotation, ellipticity and Earth's heterogeneity. When assuming self coupling for a mode with angular order l, $\mathbf{M}$ is a square matrix with $(2l+1)(2l+1)$ rows and columns. We can write $\mathbf{M}$ involving splitting function coefficients c_{st} for a pair of modes k and k' with degenerate frequencies ω_k and $\omega_{k'}$ as follows:

$$\mathbf{M}^{(kk')}_{m'm'} = \omega_0^2 \delta_{(kk')} + \omega_0 \mathbf{W}^{kk'}_{mm'} + \sum_{s=l-l'}^{l+l'} \sum_{t=-s}^{s} \gamma^{mm't}_{ll's} c_{st(kk')} \tag{5.6}$$

where $\omega_0 = (\omega_k + \omega_{k'})/2$ and $\delta_{kk'} = 0$ if $k \neq k'$ and 1 if $k = k'$, In the self-coupling approximation $k = k'$ however we have kept Equation 5.6 general for completeness. The coefficients $\gamma^{mm't}_{ll's}$ are given by:

$$\gamma^{mm't}_{ll's} = \int_0^{2\pi} \int_0^{\pi} Y_l^{m*}(\theta,\phi) Y_s^t(\theta,\phi) Y_l^{m'}(\theta,\phi) \sin\theta \mathrm{d}\theta \mathrm{d}\phi \tag{5.7}$$

where Y_l^m are the fully normalised complex spherical harmonics. Equations for evaluating this integral using Wigner 3-j symbols can be found in Woodhouse (1980) and Dahlen and Tromp (1998).

As we have to take its exponential when calculating synthetics (Equation 5.5) we first need to diagonalise $\mathbf{M}$. Eigenvalue decomposition results in $\mathbf{MU} = \mathbf{U}\Lambda$, where the matrix $\mathbf{U}$ contains the eigenvectors and λ is the diagonal matrix of non-degenerate eigenvalues ω^2. We can then rewrite Equation 5.5 as:

$$u(t) = Re[(\mathbf{r} \cdot \mathbf{U})\mathrm{e}^{i\sqrt{\Lambda}t}(\mathbf{U}^{-1} \cdot \mathbf{s})] \tag{5.8}$$

5.2.3 Partial derivatives

The synthetic seismograms depend non-linearly on the splitting function coefficients. We need to be able to calculate partial derivatives of the synthetic seismogram $u(t)$ with respect to the splitting function parameters c_{st}. The partial derivative is given by:

$$\begin{aligned}\frac{\partial u(t)}{\partial c_{st}} =& \mathrm{Re}[\mathrm{e}^{i\omega t}(\mathbf{r}\cdot\frac{\partial \mathbf{U}}{\partial c_{st}})(\mathbf{U}^{-1}\cdot\mathbf{s}) + (\mathbf{r}\cdot\mathbf{U})(\frac{\partial \mathbf{U}^{-1}}{\partial c_{st}}\cdot\mathbf{s}) \\ &+ (\mathbf{r}\cdot\mathbf{U})it\frac{\partial\omega}{\partial c_{st}}(\mathbf{U}^{-1}\cdot\mathbf{s})]\end{aligned} \tag{5.9}$$

where the diagonal matrix $\omega = \sqrt{\Lambda}$. A perturbation in δc_{st} causes a resulting perturbation in matrix $\mathbf{M}$. Using Rayleigh's principle we find the resulting perturbations in $\delta\mathbf{U}$ and $\delta\Lambda$ to the eigenvalues and eigenvectors see Deuss *et al.* (2013) for details. This leads to the eigenvalue perturbation:

$$\delta\omega_n^2 = \delta\Lambda = \mathbf{u}_n^{-1}\delta\mathbf{M}\mathbf{u}_n \tag{5.10}$$

where $\mathbf{u}_n$ is a column vector of $\mathbf{U}$ and $\mathbf{u}_n^{-1}$ is a row vector of $\mathbf{U}^{-1}$. The eigenvector perturbations are given by:

$$\delta\mathbf{u}_n = \sum_{l\neq n} = \frac{\mathbf{u}_l^{-1}\delta\mathbf{M}\mathbf{u}_n}{\omega_n^2-\omega_l^2}\mathbf{u}_l^{-1} \tag{5.11}$$

$$\delta\mathbf{u}_n^{-1} = \sum_{l\neq n} = \frac{\mathbf{u}_n^{-1}\delta\mathbf{M}\mathbf{u}_l}{\omega_n^2-\omega_l^2}\mathbf{u}_l^{-1} \tag{5.12}$$

where ω_n are the diagonal elements of ω. These eigenvector corrections are then substituted in Equation 5.9 for $\frac{\partial\omega}{\partial c_{st}}$, $\frac{\partial\mathbf{U}}{\partial c_{st}}$ and $\frac{\partial\mathbf{U}^{-1}}{\partial c_{st}}$ to compute the derivatives.

5.2.4 Inversion method

With the ability to calculate the derivatives of a c_{st} to a synthetic seismogram, we are now able to invert for the c_{st} values which best fit a dataset of spectral segments. As a seismogram $u(t)$ depends non-linearly on the splitting function coefficients c_{st}, we need to measure the coefficients using an iterated damped least squares inversion as outlined by Tarantola, Valette, *et al.* (1982). The recursive formula for a c_{st} measurement is then given by:

$$\begin{aligned}\mathbf{c}^{i+1} =& \mathbf{c}^i + (\mathbf{A}_i^T \mathbf{C}_d^{-1} \mathbf{A}_i + \mathbf{C}_m^{-1})^{-1} \\ & \times [\mathbf{A}_i^T \mathbf{C}_d^{-1} (\mathbf{d} - u(\mathbf{c}^i)) - \mathbf{C}_m^{-1} (\mathbf{c}^i - \mathbf{c}^0)]\end{aligned} \tag{5.13}$$

where $\mathbf{A}_i$ is the matrix of partial derivatives calculated from Equation 5.9, $\mathbf{c}^0$ is the starting model, $\mathbf{c}^i$ is the model parameter vector containing the splitting function coefficients at iteration i, $\mathbf{d}$ is the data vector containing the observed normal mode spectra, $u(\mathbf{c}^i)$ are the synthetic normal mode spectra calculated using Equation 5.8. $\mathbf{C}_d$ and $\mathbf{C}_m$ are the *a priori* data and model covariance matrices.

We assume that the data and model covariances $\mathbf{C}_d$ and $\mathbf{C}_m$ are the same for all data or model parameters. In this case Equation 5.13 can be rewritten so that it only depends on the ratio of $\mathbf{C}_d/\mathbf{C}_m$ and we apply damping by using one value of $\lambda = \mathbf{C}_d/\mathbf{C}_m$. The smaller the ratio λ, the less damping applied.

5.3 Data

Normal mode splitting function measurements require seismograms which are several days to weeks long records of large events (typically $M_w > 7.4$) with a high signal to noise ratio, in order to make the distinct frequencies of Earth's normal modes visible in the frequency spectrum (Figure 5.1). Events preceded or succeeded by another large event (within $M_w = 1.5$ of the original event's magnitude) by a week are excluded as this would distort and contaminate the spectra. The data needs to be Fourier transformed into the frequency domain, which requires processing of the time domain prior to transformation.

First, glitches or delta pulses were removed manually from the time domain of the seismograms along with the tidal signal. Secondly, the first few hours after the origin time of an event are removed. This removal has two desired affects; (i) to remove the influence of body waves which arrive within the first hour of an event and add noise to the frequency domain and (ii) to remove the signal of strongly attenuating mantle modes with similar frequencies to the inner core modes we are interested in. For most modes between 5-10 hours are excluded at the start, but in some specific cases with the longest period modes up to 30 hours were removed ($_2S_3$ and $_{13}S_3$). Finally prior to transformation, the time series is tapered and padded with zeros to the next power of 2. After transformation into the frequency domain, spectra are inspected by eye, with spectra with low signal to noise ratios excluded from the final dataset.

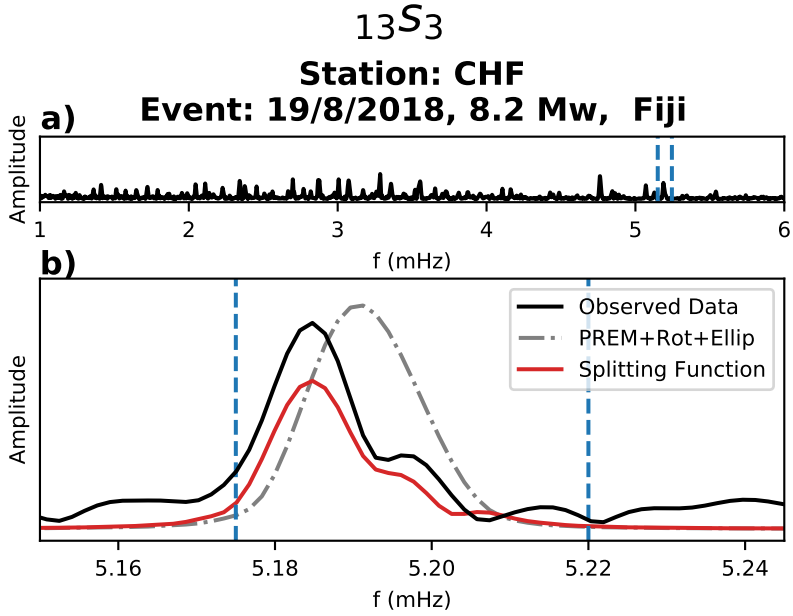

Figure 5.1 a) The observed spectra for an event with $M_w = 8.2$ which occurred on 19/8/2018 near Fiji at a depth of 555 km for station CHF. b) The same spectrum, zoomed in on mode $_{13}S_3$ showing the observed spectrum compared to the predicted spectra for PREM (including rotation and ellipticity) and the same spectrum predicted for our measured splitting function of this mode.

When picking segments for each mode we consider the Q-cycle of a mode, which defines the time window of the Fourier transform (Dahlen, 1982). The Q-cycle is defined as the quality factor, Q, of a mode divided by it's frequency in Hz. It is the time taken for a wave to decay to $e^{-\pi}$ of it's original amplitude, and Dahlen (1982) suggested that $1.1 \times Q$-cycle is the optimal time window to measure a given mode.

5.3.1 Event catalogue

We use an updated catalogue of events which combines the data used by Deuss *et al.* (2013) (events up to 2010), with data (from 2010-2018) previously used and processed by Talavera-Soza and Deuss (2021) and Schneider and Deuss (2021), and two new events from 2019 and 2021 were added in this study. The events used are listed in Table 5.1. Table 5.2 shows how many spectral segments we have per mode for the splitting function measurement.

It can be seen that some modes have more segments than others, this usually means that they generally have a high signal to noise ratio or that they are better isolated from other modes. For this research we focus solely on measuring inner core sensitive modes that are isolated from other modes, meaning we will use the self-coupled splitting function approximation. In reality, no mode is truly self coupled, all modes exchange some energy with other modes. For some modes the amount of energy which is exchanged is minimal and so it is valid to assume self-coupling. It is possible to measure cross-coupled modes in pairs or small groups including the exchange of energy across multiple modes, but this increases the computational cost and complexity preventing the grid search methodology we apply here. The same reason applies for measuring anelastic splitting functions as conducted by Mäkinen *et al.* (2014) and Pachhai *et al.* (2020); we would have too many parameters over which to perform a grid search (four instead of two).

When measuring splitting functions for each mode we set the maximum angular order s of the splitting function. A mode with angular order l is sensitive up to twice its angular order (so ${}_3S_2$ with angular order $l = 2$ is sensitive to structure up to $s = 4$). However, we incorporate a limit that there must be at least five times as many spectral data segments as there are unknown c_{st} model parameters in our measurement to prevent over parameterization. This means that for the three modes ${}_{13}S_6$, ${}_{15}S_4$ and ${}_{21}S_6$, we do not measure up to their maximum sensitivity, see table 5.2 for a list of modes and their maximum s in the c_{st} measurement.

Table 5.1 All the events we used in our normal mode splitting function measurements for inner core sensitive modes, as shown by their origin time, location, depth, magnitude and number of seismograms used during measurement. In bold are the two new events, while the other events are taken from Talavera-Soza and Deuss (2021), Schneider and Deuss (2021) and Deuss *et al.* (2013).

Event Time	Location	Depth (km)	M_w	N_s
29/07/2021	**Alaska Peninsula**	**29.6**	**8.2**	**19**
26/05/2019	**Northern Peru**	**126.6**	**8.0**	**26**
19/08/2018	Fiji Islands	555.0	8.2	29
08/09/2017	Chiapas, Mexico	50.2	8.2	14
29/07/2016	Mariana Islands	208.9	7.7	44
26/10/2015	Afghanistan	209.4	7.5	23
16/09/2015	Central Chile	17.4	8.3	32
30/05/2015	Bonin Islands Japan	680.7	7.9	36
24/05/2013	Sea of Okhotsk	611.0	8.3	79
31/08/2012	Philippine Island	45.2	7.6	1
14/08/2012	Sea of Okhotsk	598.2	7.7	16
11/03/2011	Tohoku, Japan	20.0	9.1	109
27/02/2010	Central Chile	23.2	8.8	84
05/07/2008	Sea of Okhotsk	610.8	7.7	64
12/05/2008	Sichuan, China	12.8	7.9	41
09/12/2007	South of Fiji Islands	149.9	7.8	44
14/11/2007	Northern Chile	37.6	7.7	3
28/09/2007	Volcano Islands	275.8	7.5	54
15/08/2007	Coast of Peru	33.8	8.0	34
08/08/2007	Java, Indonesia	304.8	7.5	49
01/04/2007	Solomon Islands	14.1	8.1	18
13/01/2007	Kuril Islands	12.0	8.1	54
15/11/2006	Kuril Islands	13.5	8.3	60
17/07/2006	South of Java	20.0	7.7	14
03/05/2006	Tonga Islands	67.8	8.0	43
20/04/2006	Eastern Siberia	12.0	7.6	9
27/01/2006	Banda Sea	397.4	7.6	73
08/10/2005	Pakistan	12.0	7.6	7
26/09/2005	Northern Peru	108.1	7.5	63
09/09/2005	New Ireland	83.6	7.6	59
28/03/2005	Northern Sumatra	25.8	8.6	86
26/12/2004	Northern Sumatra	28.6	9.0	77
23/12/2004	Macquarie Islands	27.5	8.1	49

Event Time	Location	Depth (km)	M_w	N_s
17/11/2003	Rat Islands	21.7	7.7	1
25/09/2003	Hokkaido, Japan	28.2	8.3	28
04/08/2003	Scotia Sea	15.0	7.6	1
15/07/2003	Carlsberg Ridge	15.0	7.5	5
03/11/2002	Central Alaska	15.0	7.8	25
08/09/2002	Papua New Guinea	19.5	7.6	1
19/08/2002	South of Fiji	699.3	7.7	51
14/11/2001	Qinghai China	15.0	7.8	24
07/07/2001	Coast of Peru	25.0	7.6	1
23/06/2001	Coast of Peru	29.6	8.4	82
26/01/2001	India	19.8	7.6	7
13/01/2001	El Salvador	56.0	7.7	18
18/06/2000	South Indian Ocean	15.0	7.9	25
04/06/2000	Southern Sumatra	43.9	7.8	32
28/03/2000	Volcano Islands	99.7	7.6	55
20/09/1999	Taiwan	21.2	7.6	1
17/08/1999	Turkey	17.0	7.6	2
29/11/1998	Ceram Sea	16.4	7.7	9
25/03/1998	Balleny Islands	28.8	8.1	50
04/01/1998	Loyalty Islands	114.3	7.4	31
05/12/1997	Kamchatka	33.6	7.8	21
08/11/1997	Tibet	16.4	7.5	4
14/10/1997	South of Fiji Islands	165.9	7.7	42
12/11/1996	Coast of Peru	37.4	7.7	21
17/06/1996	Flores Sea	584.2	7.8	53
10/06/1996	Andreanof Islands	29.0	7.9	7
17/02/1996	West Irian	15.0	8.2	19
01/01/1996	Minahassa	15.0	7.9	2
03/12/1995	Kuril Islands	25.9	7.9	8
09/10/1995	Jalisco, Mexico	15.0	8.0	23
30/07/1995	Northern Chile	28.7	8.0	44
28/12/1994	Coast of Honshu	27.7	7.7	24
04/10/1994	Kuril Islands	68.2	8.3	45
09/06/1994	Northern Bolivia	647.1	8.2	56

Event Time	Location	Depth (km)	M_w	N_s
02/06/1994	South of Java	15.0	7.8	1
09/03/1994	Fiji Islands	567.8	7.6	45
12/07/1993	Hokkaido, Japan	16.5	7.7	13
15/01/1993	Hokkaido, Japan	100.0	7.6	22
12/12/1992	Flores Island	20.4	7.7	8
11/10/1992	Vanuatu	141.1	7.4	30
02/09/1992	Nicaragua	15.0	7.6	4
22/12/1991	Kuril Islands	31.2	7.6	3
22/04/1991	Costa Rica	15.0	7.6	1
30/12/1990	New Britain, P.N.G.	204.8	7.4	10
16/07/1990	Luzon, Philippines	15.0	7.7	3
18/04/1990	Minahassa	33.2	7.6	3
03/03/1990	South of Fiji	25.3	7.6	4
23/05/1989	Macquarie Islands Region	15.0	8.0	14
06/03/1988	Gulf of Alaska	15.0	7.7	3
30/11/1987	Gulf of Alaska	15.0	7.8	7
20/10/1986	Kermadec Islands	50.4	7.7	5
07/05/1986	Andreanof Islands	31.3	7.9	2
03/03/1985	Central Chile	40.7	7.9	3
20/11/1984	Philippines	180.7	7.5	10
06/03/1984	Honshu Japan	446.0	7.4	3
24/11/1983	Banda Sea	157.1	7.4	9
04/10/1983	North Chile	38.7	7.6	2
26/05/1983	Honshu, Japan	12.6	7.7	6
18/03/1983	New Ireland	69.9	7.7	13
22/06/1982	Banda Sea	473.4	7.4	7
25/05/1981	South Island, N.Z.	33.3	7.6	1
17/07/1980	Sta. Cruz Islands	34.0	7.7	3
12/12/1979	Coast of Ecuador	19.7	8.1	4
06/12/1978	Kuril Islands	181.0	7.8	7
29/11/1978	Oaxaca, Mexico	16.1	7.7	1
19/08/1977	Sumbawa Island	23.3	8.3	4
22/06/1977	Tonga Islands	61.3	8.0	5
04/03/1977	Romania	83.6	7.5	1
30/11/1976	Chile-Bolivia	133.7	7.5	3
16/08/1976	Mindanao, Philippine Islands	33.0	8.0	1

mode	S_{max}	N_{ev}	N_s	PREM Misfit	Deuss Misfit	c_{st} Misfit
${}_2S_3$	6	69	558	1.22	0.36	0.36
${}_3S_2$	4	34	385	1.62	0.13	0.16
${}_9S_3$	6	67	522	1.38	0.40	0.36
${}_9S_4$	8	64	470	1.17	0.45	0.41
${}_{11}S_4$	8	59	772	2.00	0.29	0.39
${}_{11}S_5$	10	69	963	1.78	0.28	0.34
${}_{13}S_1$	2	35	521	2.94	0.31	0.28
${}_{13}S_2$	4	37	759	1.87	0.16	0.17
${}_{13}S_3$	6	41	455	1.87	0.34	0.35
${}_{13}S_6$	8	43	313	2.00	0.39	0.63
${}_{15}S_3$	6	58	554	1.81	0.35	0.51
${}_{15}S_4$	6	32	152	1.29	0.52	0.65
${}_{18}S_3$	6	43	390	2.99	0.45	0.49
${}_{18}S_4$	8	49	678	1.65	0.27	0.30
${}_{20}S_1$	2	19	147	1.00	0.34	0.33
${}_{21}S_6$	10	39	357	3.28	0.35	0.38
${}_{25}S_2$	4	39	392	1.34	0.50	0.50
${}_{27}S_2$	4	28	362	1.52	0.32	0.28

Table 5.2 A table which shows for each mode the maximum harmonic degree we measured to, the number of events we used for the measurement, the number of spectral segments were incorporated, the misfit of PREM to the spectral segments (relative to no mode modelled at all), the misfit of the c_{st} measurement from Deuss *et al.* (2013) and the misfit of our c_{st} measurement. Misfit is measured relative to the scenario where we didn't model the spectrum of that mode at all, and averaged across all spectral segments incorporated into that measurement.

5.4 Starting model grid searches

Previous studies have shown that for inner core sensitive modes, the assumed starting model (c^0 in Equation 5.13) can significantly affect the final measurement (Megnin and Romanowicz (1995); Durek and Romanowicz (1999); Deuss *et al.* (2013)). The problem is that inner core anisotropy causes large perturbations in the zonal parameters, c_{20} and c_{40} and the non-linear iterative nature of splitting function measurements makes it difficult to reach values that are significantly different from the starting model. The c_{20} and c_{40} parameters frequently have absolute values of 20 or greater, while the other c_{st} parameters typically have much smaller values ($< 5\mu$Hz), which means that if we start a splitting function measurement from PREM (all $c_{st} = 0.0$) it is likely that the the c_{st} measurement will not reach the global misfit minima. Here, we overcome this problem using a starting model grid search: we start many splitting function measurements with different combinations of c_{20} and c_{40} as starting model for a range of damping parameters and running each splitting function measurement for 10 iterations. Then for each mode we analyse the misfit for the collection of final models together.

Figure 5.2 shows an example of how c_{20} and c_{40} change in a splitting function grid search in each iteration for the mode ${}_{18}S_4$. For iteration 0, the c_{20} and c_{40} pairs are the starting model values which are organised in a grid from -30 to 30 with a step size of 1 in both c_{20} and c_{40} making a total of 3600 starting model c_{20} and c_{40} pairs. As the iteration progresses each individual measurement moves towards a nearby c_{st} with lower misfit. By iteration 10 the lowest misfit for mode ${}_{18}S_4$ is for $c_{20} = 20.2$ and $c_{40} = -0.2$, which started at: $c_{20} = 11$ and $c_{40} = -6$. In the final panel of Figure 5.2 we see the final misfit of each c_{20} and c_{40} splitting function measurement after ten iterations plotted at that measurement's starting location. This panel clearly shows that only a subset of our measurement starting locations (approximately between $10 < c_{20} < 30$ and $-10 < c_{40} < 15$) results in a measurement which comes close to the global misfit minima.

Performing an individual splitting function measurement is not computationally intensive, however doing thousands of measurements for multiple damping parameters for 18 modes and up to degree $s = 10$ results in a large computational problem. What we gain, however, is a more robust measurement whereby we obtain inversion results for a large range of starting c_{20} and c_{40} parameters so that we can clearly identify global and local misfit minima and gain information on the uncertainty of our measured c_{st} parameters.

After completion of the grid searches we analyse each mode individually.

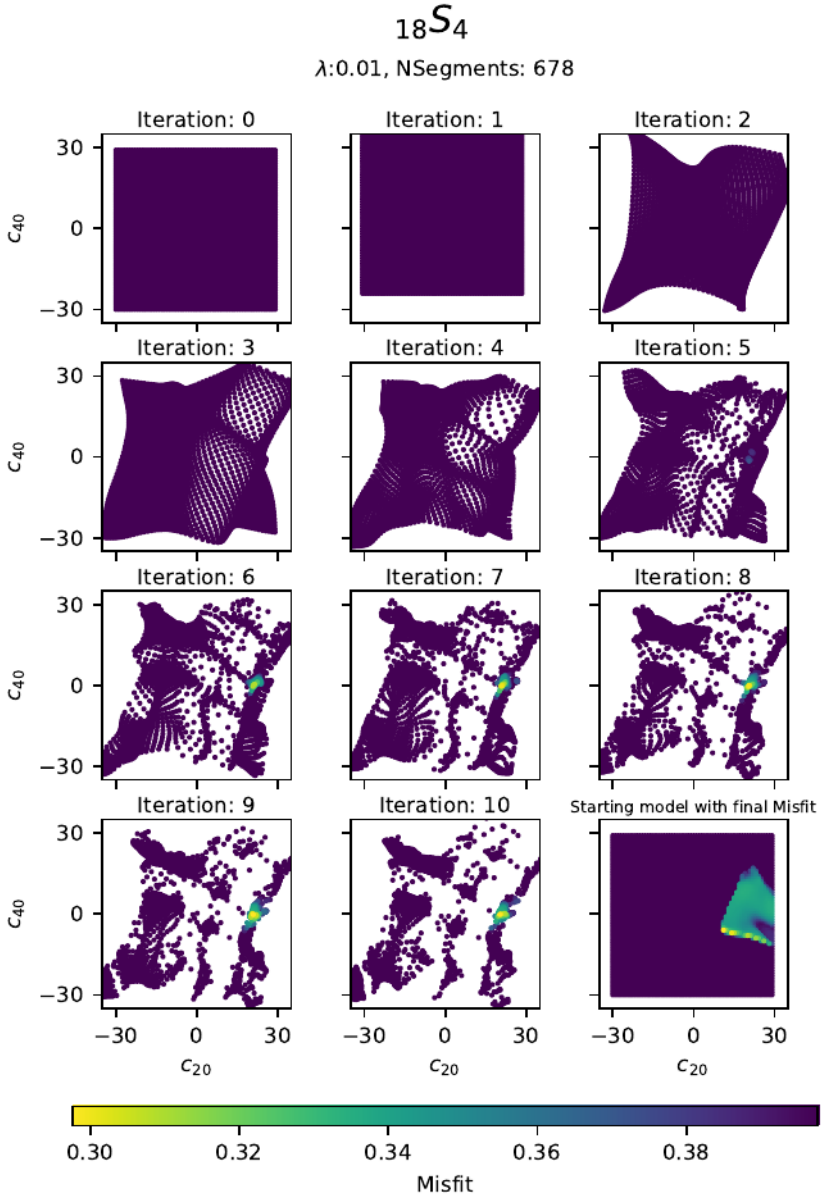

Figure 5.2 c_{20} and c_{40} values and their corresponding misfit for mode $_{18}S_4$ where each point is the c_{20} and c_{40} combination from a splitting function measurement for 10 iterations. The last panel shows the final misfit at iteration 10 as a function of the c_{20} and c_{40} starting values. The colour shows the misfit.

The main considerations are what the most appropriate damping is for each mode (we run each grid search for a range of damping parameters) and how well defined each mode is in the context of the grid search. Are there multiple measurements with a similar misfit but significantly different c_{20} and c_{40} values? Or is there a cluster of low misfit models around the same final values of c_{20} and c_{40}?

We will first outline the grid search analysis procedure using the mode ${}_{11}S_4$ (Section 5.4.1) as an example and discuss an interesting well determined mode; ${}_{13}S_2$ (Section 5.4.2). We will then look in detail at three modes which were more complicated to measure: ${}_{13}S_6$, ${}_{15}S_4$ and ${}_{15}S_3$ (Sections 5.4.3-5.4.4). Fortunately most of our grid searches resulted in an obvious minimum misfit location and we compare all our measurements with previous measurements and predictions from mantle and crustal models in Section 5.5. The grid search results for any mode not discussed in detail are shown in Figures 5.14-5.27 in the supplementary material at the end of the chapter for all measured modes.

5.4.1 ${}_{11}S_4$

Mode ${}_{11}S_4$ is a well defined mode with a clear misfit minimum. Figures 5.3-5.5 show the results of our grid searches for three different damping parameters, including $\lambda = 0.1$, $\lambda = 0.01$ and $\lambda = 0.001$. The first step when analysing the grid searches is to pick the optimal damping parameter which minimises misfit and model size. The choice is usually made by looking at L-curves (panels a-b, in Figures 5.3-5.5, which show for a given starting model the minimum misfit and model size as a function of damping parameter. Comparing the minimum misfit of the grid searches at $\lambda = 0.1$, $\lambda = 0.01$ it can be seen that $\lambda = 0.01$ results in the lowest misfit and smallest model size. Furthermore, the final c_{20} and c_{40} measurement of these two damping parameters are similar, suggesting that c_{20} and c_{40} are well constrained regardless of damping.

It is clear from Figure 5.5 that applying damping of $\lambda = 0.001$ results in an unstable inversion with none of the starting models achieving a misfit as low as the misfit minima of $\lambda = 0.1$ or $\lambda = 0.01$. In a linear inversion this would not occur as a smaller damping parameter would always result in a lower misfit until some misfit minimum was reached (restricted by the noise in the data and number of free parameters). However, spectra depend non-linearly on the splitting function, resulting in a non-linear inversion where there can be multiple local and global misfit minima. To navigate this complex misfit topography we calculate the gradient of the model to the data and iteratively move down the gradient towards a lower misfit

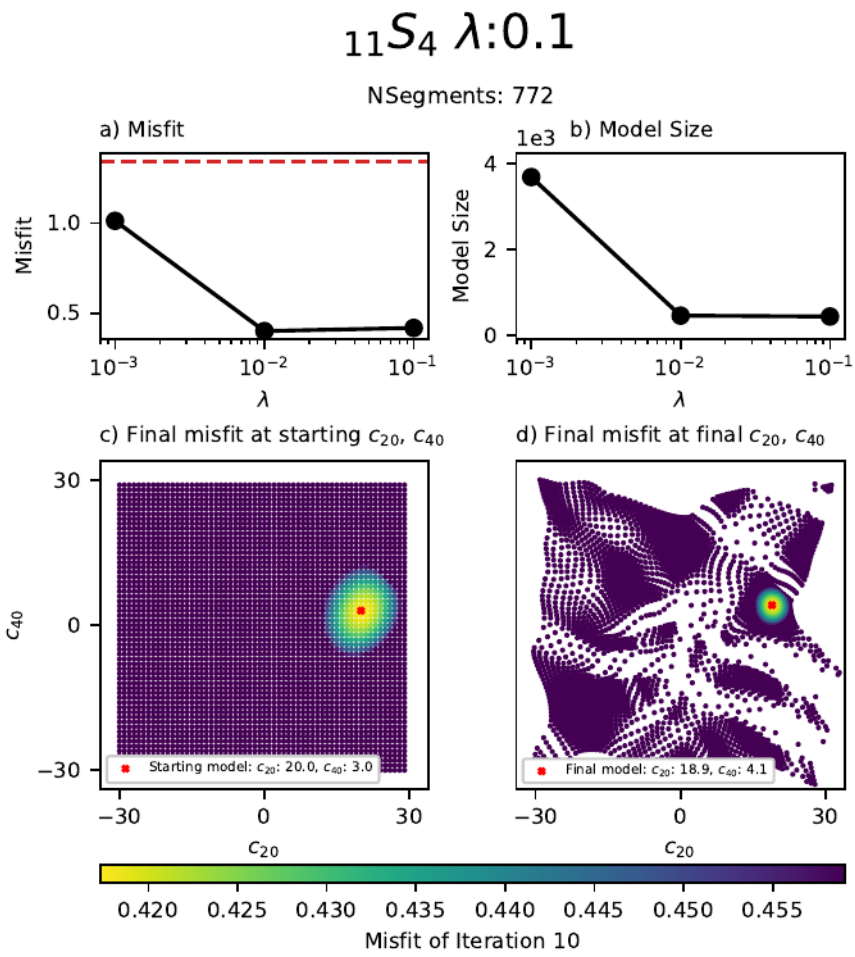

Figure 5.3 Grid search for mode $_{11}S_4$ with a damping of $\lambda = 0.1$. a-b) The variation of misfit and model size with damping for the same starting model which results in the minimum misfit for $\lambda = 0.1$. The red line on a) is the starting model misfit. c) final misfit as a function of the starting c_{20} and c_{40} values of each measurement, d) final misfit as a function of the c_{20} and c_{40} values of each measurement at the final iteration. The colour of each measurement displays the misfit, the red cross shows the measurement with the minimum misfit. Measurements are shown in grey when the singlets move outside of the frequency bounds of the spectral data.

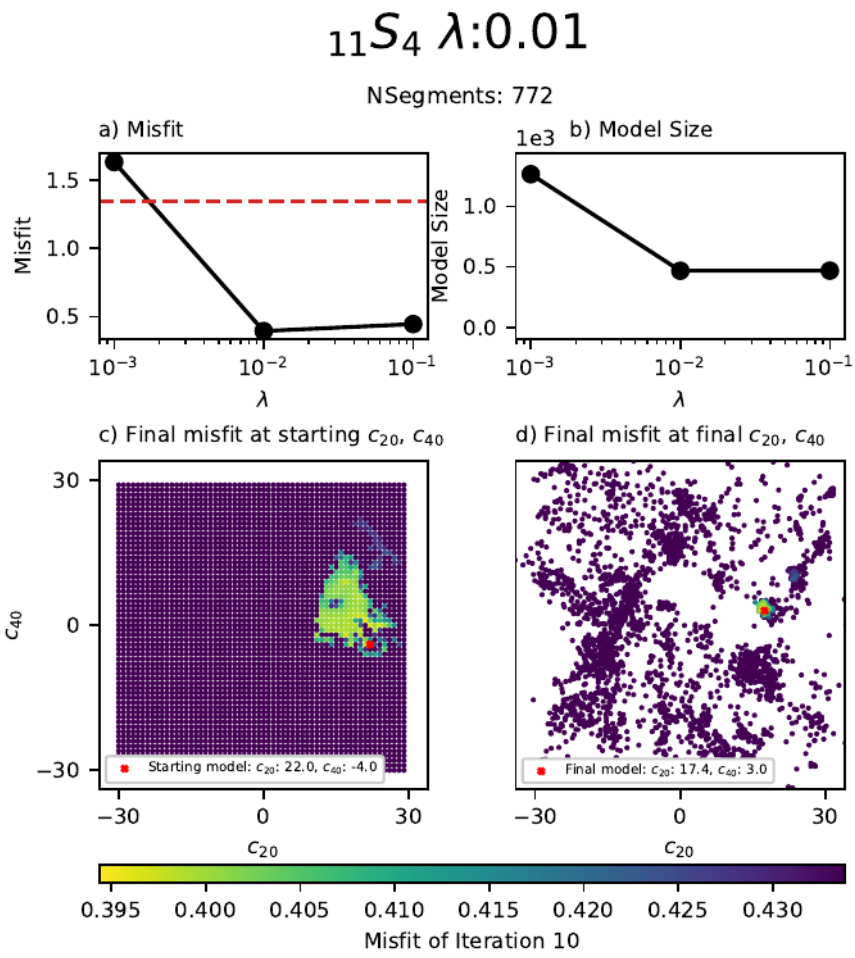

Figure 5.4 Grid search for mode $_{11}S_4$ with a damping of $\lambda = 0.01$. a-b) The variation of misfit and model size with damping for the same starting model which results in the minimum misfit for $\lambda = 0.01$. The red line on a) is the starting model misfit. c) final misfit as a function of the starting c_{20} and c_{40} values of each measurement, d) final misfit as a function of the c_{20} and c_{40} values of each measurement at the final iteration. The colour of each measurement displays the misfit, the red cross shows the measurement with the minimum misfit. Measurements are shown in grey when the singlets move outside of the frequency bounds of the spectral data.

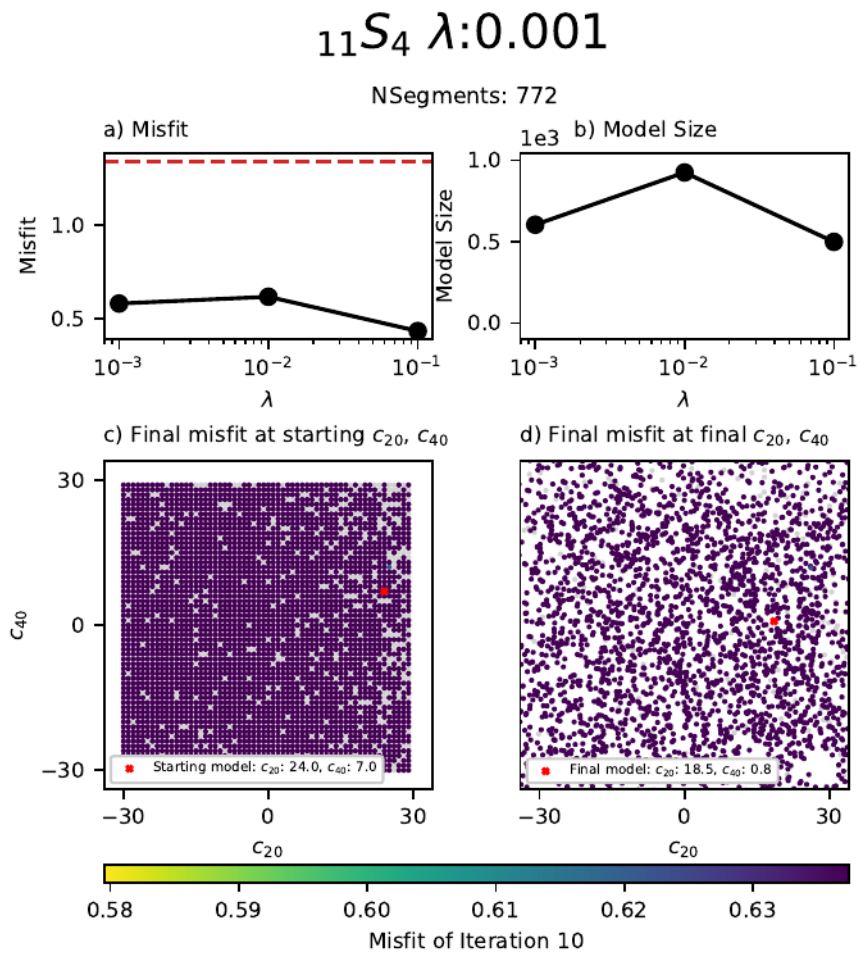

Figure 5.5 Grid search for mode $_{11}S_4$ with a damping of $\lambda = 0.001$. a-b) The variation of misfit and model size with damping for the same starting model which results in the minimum misfit for $\lambda = 0.001$. The red line on a) is the starting model misfit. c) final misfit as a function of the starting c_{20} and c_{40} values of each measurement, d) final misfit as a function of the c_{20} and c_{40} values of each measurement at the final iteration. The colour of each measurement displays the misfit, the red cross shows the measurement with the minimum misfit. Measurements are shown in grey when the singlets move outside of the frequency bounds of the spectral data.

(Equation 5.13). Being non-linear means that this gradient can change with each iteration. If the damping parameter is too small then this results in 'steps' which are too large, such that the c_{st} measurement 'overshoots' local and global misfit minima and results in an unstable inversion. For a single starting model this may even lead to a final measurement with greater misfit than the first iteration.

From our analysis above we choose a damping of $\lambda = 0.01$ for ${}_{11}S_4$; for this damping the lowest misfit measurements are all clustered around $c_{20} = 17.42 \pm 0.83$ and $c_{40} = 2.98 \pm 1.05$. Figure 5.4c) shows the range of starting models which approximately end up at this measurement and with similar small misfit.

We estimate the range of valid c_{20} and c_{40} values by assuming any measurement within 0.01 misfit difference from the lowest misfit measurement to be an equally valid result. When modelling inner core anisotropy with our normal mode measurements (Chapters 6-7) we will use the c_{20} and c_{40} values from our minimum misfit measurement as the centre of a Gaussian distribution and treat the range of values as the standard deviation of this Gaussian distribution. This uncertainty definition describes the measurement quite well for many of our grid searches (such as ${}_{11}S_4$) where there is a single obvious misfit minimum location. However for some of our grid searches this definition is less valid, such as ${}_{13}S_6$ and ${}_{15}S_4$ (see Section 5.4.3 for a more detailed discussion), where multiple distinct misfit minima exist. In future work we would like to better capture all the information these grid searches provide (going beyond simple Gaussian models of c_{20} and c_{40}) but for now we will use this simplification when estimating the uncertainty.

We repeat these steps for each mode and in the supplementary material show the grid search results for each mode not discussed in depth for their optimal damping parameter (Figures 5.14-5.27).

5.4.2 ${}_{13}S_2$

Mode ${}_{13}S_2$ is a inner core sensitive mode which was discussed at length in Durek and Romanowicz (1999), because it was a good example of a mode with multiple global misfit minima at the time. Durek and Romanowicz (1999) were more limited in computational resources than our current study and only measured ${}_{13}S_2$ starting from six different combinations of mantle and inner core models. That inversion resulted in six c_{st} measurements (at different damping parameters) and from these six starting models Durek and Romanowicz (1999) identified that ${}_{13}S_2$ had two different misfit minima and so two different c_{st} measurements. They then proceeded to rule out one model through inspection of the spectra themselves and found that one of

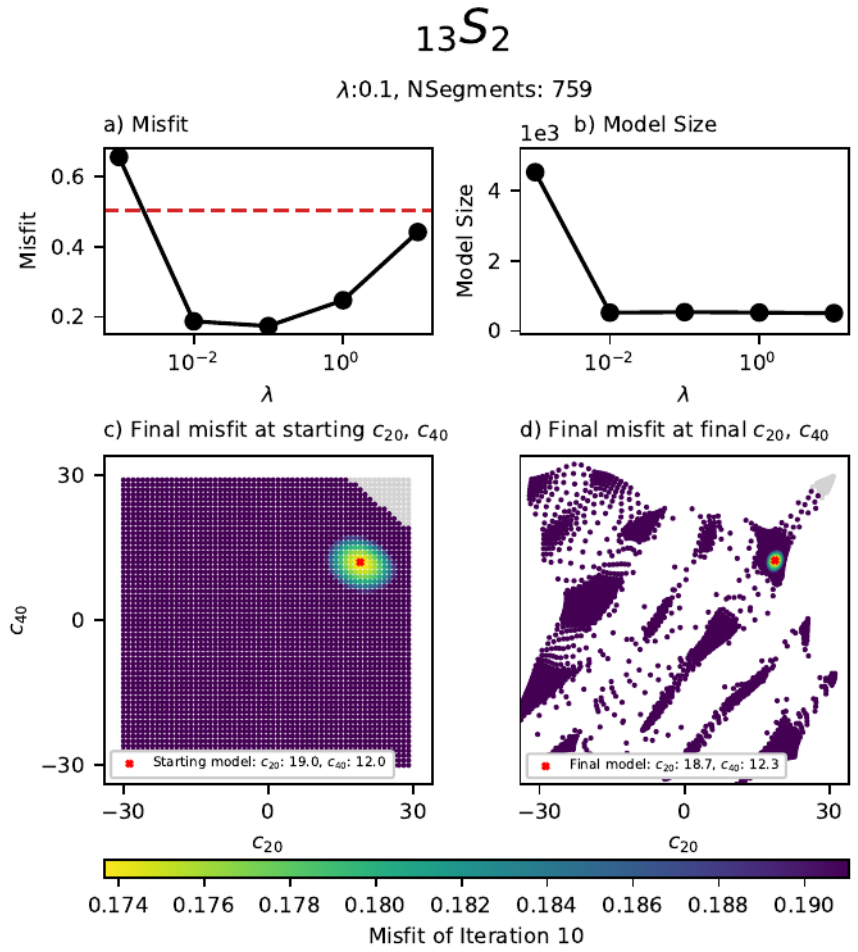

Figure 5.6 Grid search for mode $_{13}S_2$ with a damping of $\lambda = 0.1$. a-b) The variation of misfit and model size with damping for the same starting model which results in the minimum misfit for $\lambda = 0.1$. The red line on a) is the starting model misfit. c) final misfit as a function of the starting c_{20} and c_{40} values of each measurement, d) final misfit as a function of the c_{20} and c_{40} values of each measurement at the final iteration. The colour of each measurement displays the misfit, the red cross shows the measurement with the minimum misfit. Measurements are shown in grey when the singlets move outside of the frequency bounds of the spectral data.

the two better explained spectra for stations at high latitudes. Durek and Romanowicz (1999) only state their preferred measurement and they do not explicitly give the c_{st} values of their alternative measurement.

In our study, we are less restricted in computational resources and so are able to measure ${}_{13}S_2$ (and the other modes) not from 6 but many 1000's of starting models. Furthermore, we now have much more data due to increased global seismometer coverage and a larger catalogue of events than Durek and Romanowicz (1999), resulting in 759 spectral segments compared to their original 104. Inspection of Figure 5.6 shows that with our methodology and our increased data set, ${}_{13}S_2$ is now a well defined mode with one clear global misfit minimum instead of two minima. Interestingly, our measurement is close to the preferred measurement of Durek and Romanowicz (1999) confirming their previous analysis. The advantage of our method is that we can also use the grid search to estimate the noise in the splitting function measurements, and further rule out any other misfit minima.

5.4.3 ${}_{13}S_6$ & ${}_{15}S_4$

While most of our grid searches resulted in well defined misfit minima, ${}_{13}S_6$ and ${}_{15}S_4$ resulted in broad regions of low misfit (Figures 5.7-5.8). This means that for each mode the c_{20} and c_{40} values are poorly constrained by the data.

We believe this is due to not having enough data to fully constrain the splitting function measurement. Inspection of Table 5.2 reveals that ${}_{13}S_6$ and ${}_{15}S_4$ have the 2nd and 3rd least number of segments (313 and 152 respectively) of our dataset. The mode which has the least number of segments is ${}_{20}S_1$ which is well defined, however ${}_{20}S_1$ has a much lower spherical order l and therefore has fewer c_{st} values to constrain (i.e. there are more segments per free parameters for ${}_{20}S_1$ than either ${}_{13}S_6$ or ${}_{15}S_4$). We have decided to still incorporate ${}_{13}S_6$ and ${}_{15}S_4$ data into our inversions (Chapters 6-7) but always taking into account their significant uncertainty.

5.4.4 ${}_{15}S_3$

For ${}_{15}S_3$ we adjusted the measurement procedure. Previous measurements and predicted values from S20RTS show that ${}_{15}S_3$ has large real c_{22} and c_{42} values. Initially when measuring ${}_{15}S_3$ we found that we couldn't fit c_{20}, c_{40}, c_{22} and c_{42} with the same damping. Either we had to damp too much to fit c_{20} and c_{40} or damp too little to fit c_{22} and c_{42}. To overcome this problem, we set every c_{st} except c_{20}, c_{40} in our starting models to the predicted values from S20RTS (Ritsema *et al.*, 1999) plus the predicted values from CRUST

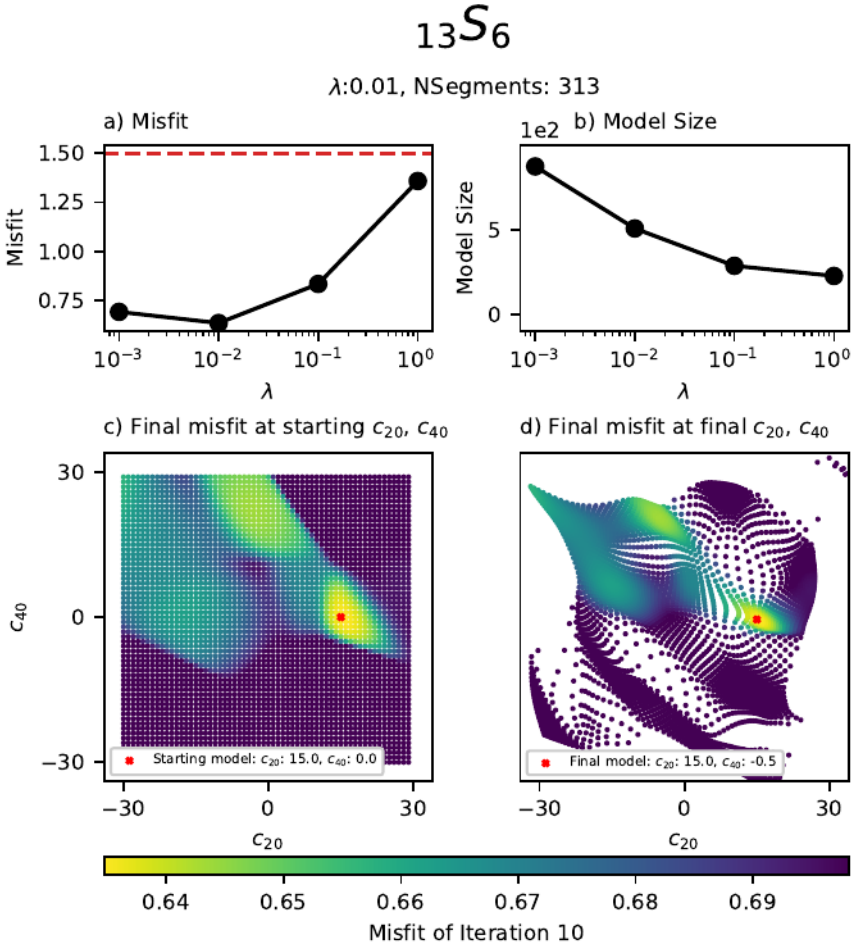

Figure 5.7 Grid search for mode $_{13}S_6$ with a damping of $\lambda = 0.01$. The variation of misfit and model size with damping for the same starting model which results in the minimum misfit for $\lambda = 0.01$. The red line on a) is the starting model misfit. c) final misfit as a function of the starting c_{20} and c_{40} values of each measurement, d) final misfit as a function of the c_{20} and c_{40} values of each measurement at the final iteration. The colour of each measurement displays the misfit, the red cross shows the measurement with the minimum misfit. Measurements are shown in grey when the singlets move outside of the frequency bounds of the spectral data.

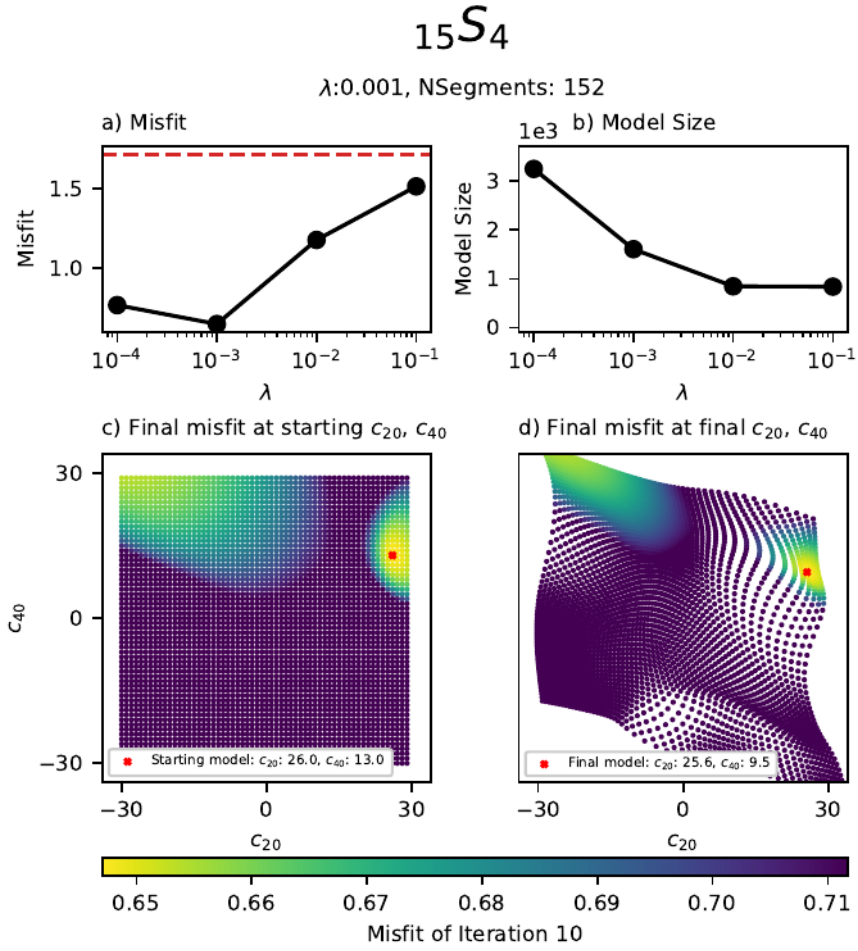

Figure 5.8 Grid search for mode $_{15}S_4$ with a damping of $\lambda = 0.001$. a-b) The variation of misfit and model size with damping for the same starting model which results in the minimum misfit for $\lambda = 0.001$. The red line on a) is the starting model misfit. c) final misfit as a function of the starting c_{20} and c_{40} values of each measurement, d) final misfit as a function of the c_{20} and c_{40} values of each measurement at the final iteration. The colour of each measurement displays the misfit, the red cross shows the measurement with the minimum misfit. Measurements are shown in grey when the singlets move outside of the frequency bounds of the spectral data.

5.1 Mooney *et al.* (1998). The c_{20} and c_{40} values varied normally like the other grid searches. In this way the c_{22} and c_{42} values were already close to their required values, as they are strongly influenced by the mantle and crust, aiding the measurement stability.

Mode	c_{20}	c_{40}	PREM f_c	c_{st} f_c	PREM Q	c_{st} Q
${}_2S_3$	8.15 ± 0.17	0.14 ± 0.29	1242.19	1242.82 ± 0.01	415.46	435.06 ±18.36
${}_3S_2$	16.3 ± 11.3	1.3 ± 14.95	1106.21	1106.36 ± 2.44	366.57	323.28 ±19.2
${}_9S_3$	2.18 ± 3.28	-7.32 ± 2.86	3554.98	3555.42 ± 0.42	777.6	748.72 ±52.55
${}_9S_4$	8.17 ± 5.97	-11.33 ± 5.03	3877.95	3877.37 ± 1.02	515.46	511.8 ±36.27
${}_{11}S_4$	17.42 ± 0.83	2.98 ± 1.05	4766.86	4765.76 ± 0.06	701.75	641.35 ±33.2
${}_{11}S_5$	8.52 ± 0.95	-0.37 ± 1.09	5074.41	5072.48 ± 0.08	665.34	608.78 ±18.58
${}_{13}S_1$	24.29 ± 1.6	-	4495.73	4494.59 ± 0.14	735.29	674.11 ±2.35
${}_{13}S_2$	18.72 ± 1.06	12.34 ± 1.36	4845.26	4844.5 ± 0.02	878.74	904.84 ±20.78
${}_{13}S_3$	16.7 ± 0.67	3.61 ± 0.82	5193.82	5193.68 ± 0.08	908.26	914.19 ±17.36
${}_{13}S_6$	14.96 ± 12.27	-0.47 ± 11.95	6161.19	6157.77 ± 0.91	648.93	555.68 ±14.19
${}_{15}S_3$	25.86 ± 1.85	20.26 ± 2.11	6035.22	6032.05 ± 0.12	805.8	703.01 ±11.15
${}_{15}S_4$	25.58 ± 28.81	9.52 ± 14.37	6332.35	6325.39 ± 1.79	398.88	363.76 ±60.08
${}_{18}S_3$	33.73 ± 0.0	19.73 ± 0.0	6891.93	6889.4 ± 0.0	851.79	735.2 ±0.0
${}_{18}S_4$	20.18 ± 0.17	-0.2 ± 0.08	7241.0	7238.68 ± 0.02	943.4	971.59 ±10.36
${}_{20}S_1$	23.37 ± 4.62	-	6954.04	6954.24 ± 0.47	876.42	778.76 ±5.68
${}_{21}S_6$	23.95 ± 1.58	-5.95 ± 2.29	8850.77	8848.28 ± 0.12	740.19	575.97 ±54.54
${}_{25}S_2$	19.87 ± 2.27	-7.66 ± 3.2	9022.91	9025.07 ± 0.15	788.02	749.76 ±8.77
${}_{27}S_2$	27.42 ± 10.23	4.14 ± 13.42	9865.33	9871.8 ± 1.32	789.89	788.49 ±11.31

Table 5.3 Our measured values of c_{20} and c_{40} for each of the self-coupled inner core modes along with their uncertainty estimate, the centre frequency and attenuation for each mode predicted by PREM and our measured centre frequency and attenuation

5.5 Discussion

Our splitting function measurements are broadly in agreement with previous studies (Figure 5.9) and have a consistent pattern where all modes exhibit a positive c_{20} while c_{40} can be either positive or negative. Most of our measurements of c_{20} and c_{40} are significantly different from predictions of the mantle and crust, for tomographic model S20RTS (Ritsema *et al.*, 1999) and crustal model CRUST 5.1 (Mooney *et al.*, 1998). This difference implies that our anomalous measurements of c_{20} and c_{40} are unlikely to be due to mantle or crustal structure.

Table 5.3 shows for each mode the best fitting c_{20} and c_{40} values, the uncertainties in these values, the predicted centre frequency and attenuation factor from PREM and our measured centre frequency and attenuation values. Our measured deviation in centre frequency and attenuation from PREM is shown in Figure 5.10 and it can be seen that our change in centre frequency relative to PREM is in very close agreement with Deuss *et al.* (2013) and in reasonable agreement with the corresponding measurements from Durek and Romanowicz (1999), He and Tromp (1996) and Resovsky and Ritzwoller (1998).

Our measured attenuation relative to PREM is more variable, with most modes requiring greater attenuation than PREM. This is in agreement with previous body wave and normal mode studies (Mäkinen *et al.* (2014); Pejić *et al.* (2019); Pachhai *et al.* (2020)) which conclude that the inner core has significant attenuation. Our estimates of δQ are mostly in good agreement with Deuss *et al.* (2013) but differ from the estimates of Durek and Romanowicz (1999) and He and Tromp (1996) for the higher frequency modes ($_{13}S_3$ and beyond). This can be attributed to the fact that we have incorporated significantly more spectral segments than Durek and Romanowicz (1999) and He and Tromp (1996) and that attenuation is a more difficult parameter to constrain than centre frequency, with greater uncertainty.

Modes $_9S_3$, $_9S_4$, $_{21}S_6$ and $_{25}S_2$ all stand out because they have a positive c_{20} and a negative c_{40}. With the exception of $_{21}S_6$ we see that our measurements of the zonal parameters of these modes is in good agreement with previous studies. Taking into account the uncertainties from the grid searches the negative c_{40} values seem robust. In Chapters 6-7 we see how the negative c_{40} parameters in these modes are well described by a positive S-wave anisotropy anomaly at the top of the inner core. This explanation can also be seen intuitively from inspection of the sensitivity kernels of these modes (Figure 6.2-6.3), where a positive S-wave anisotropy anomaly at the top of the inner core would result in positive c_{20} and negative c_{40}.

Comparing maps of our splitting function measurements with the same

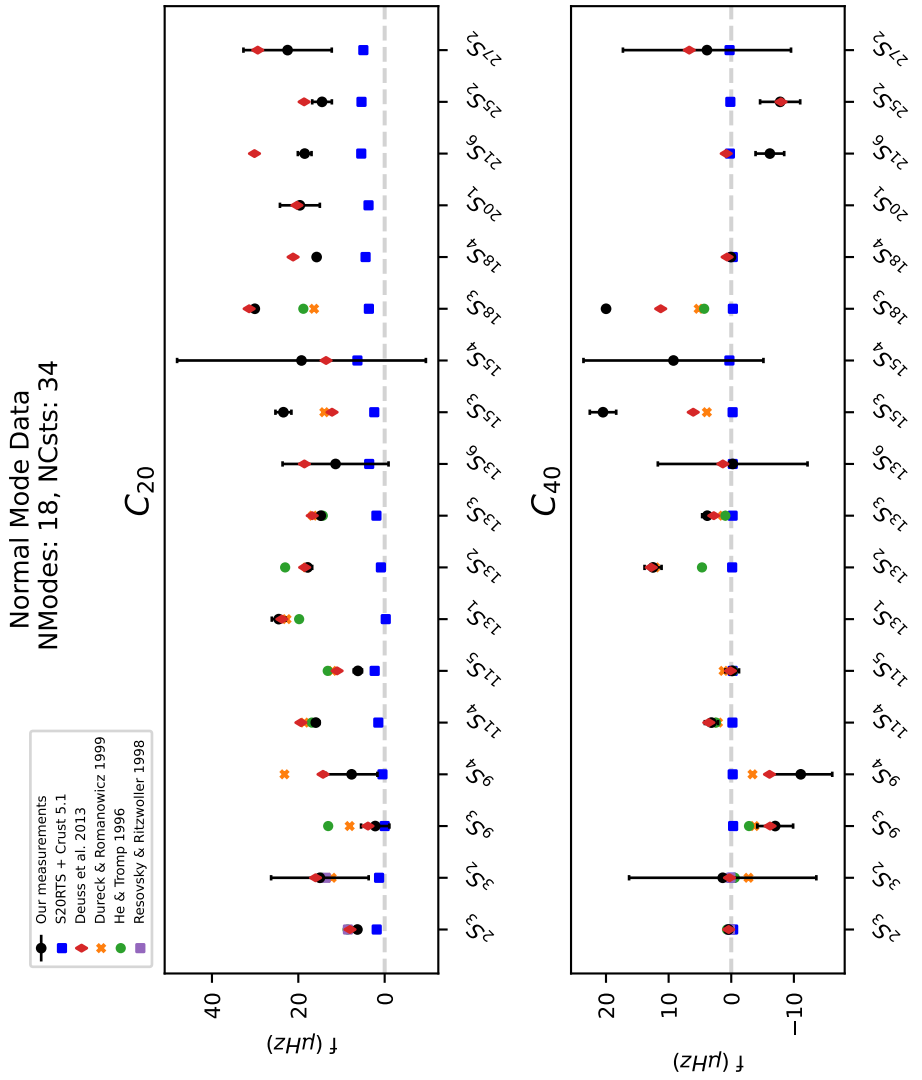

Figure 5.9 Our final dataset of c_{20} and c_{40} coefficients along with predicted values from S20RTS (Ritsema *et al.*, 1999) and Crust 5.1 (Mooney *et al.*, 1998) and previous measurements by Deuss *et al.* (2013), Durek and Romanowicz (1999), He and Tromp (1996) and Resovsky and Ritzwoller (1998)

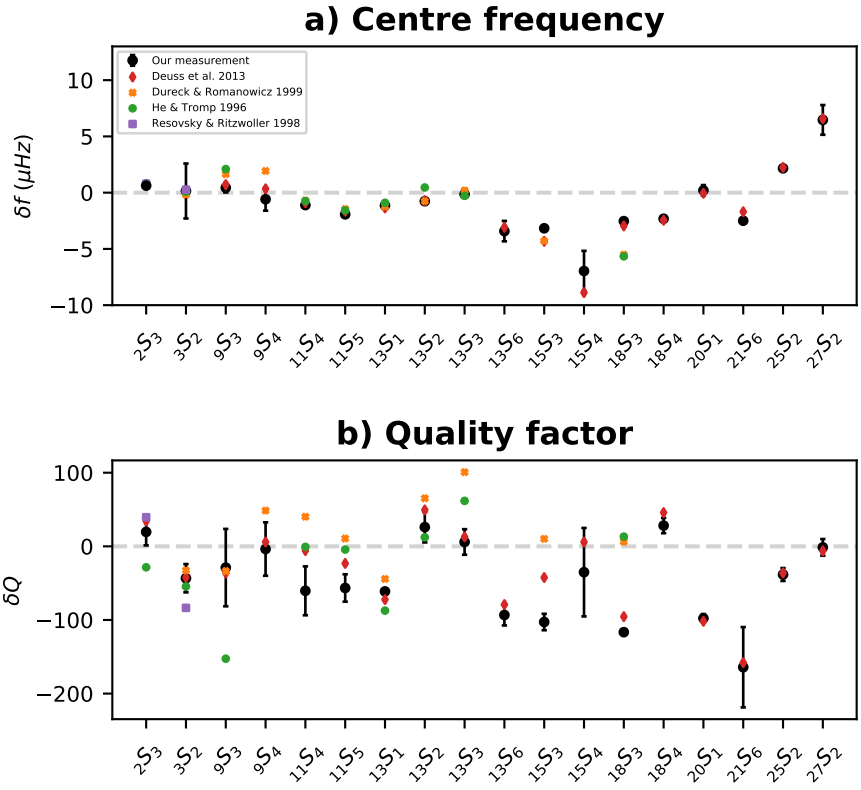

Figure 5.10 Our measured values of centre frequency and attenuation factor, Q, relative to our reference model PREM, and the equivalent measurements from Deuss *et al.* (2013), Durek and Romanowicz (1999), He and Tromp (1996) and Resovsky and Ritzwoller (1998).

splitting functions measured by Deuss *et al.*, 2013 and the predicted c_{st} maps from S20RTS and CRUST 5.1 (Figures 5.11-5.13) we see that for many modes our splitting function maps are similar to that of Deuss *et al.* (2013), which is not surprising because we have overlapping datasets. Most of our measurements show structures different in shape or magnitude from mantle and crustal predictions. Indeed, we see the typical anomalous 'zonal splitting' with strong positive anomalies near the poles and negative anomalies along the equator.

Our measured zonal values for ${}_{15}S_3$ and ${}_{18}S_3$ are significantly different from previous studies (Figure 5.9). We have increased the number of spectra for ${}_{15}S_3$ from 426 spectral segments in Deuss *et al.* (2013) to 554 and for ${}_{18}S_3$ from 285 to 390 through the inclusion of new events since Deuss *et al.* (2013) which we believe is the cause of this difference.

5.6 Conclusion

In this chapter we present new measurements of splitting functions for 18 inner core sensitive normal modes using an updated data set of normal mode spectra combining events and stations from Deuss *et al.* (2013), Talavera-Soza and Deuss (2021) and Schneider and Deuss (2021) and two previously unused events. It has been observed previously that the starting model (specifically the c_{20} and c_{40} values) of an inner core sensitive splitting function measurement has a significant effect on the final measurement. We conduct a systematic grid search over a large range of c_{20} and c_{40} starting models in our splitting function measurement, to resolve this starting model dependence. From our grid searches we are able to map out and identify local and global misfit minima and use it to determine the best fitting c_{20} and c_{40} values for each mode and their respective uncertainties.

We find a consistent pattern in the zonal parameters c_{20} and c_{40} in our measured splitting functions, where all the c_{20} values are positive while only some of the c_{40} are negative. When comparing our measurements to predictions from mantle and crustal models we find that the c_{20} and c_{40} values of our measured modes cannot be explained by mantle and crustal structure, and conclude that these anomalous measurements are due to inner core anisotropy. Our measurements are broadly consistent with previous studies but with higher uncertainties for some modes, including ${}_{15}S_4$ and ${}_{3}S_2$. We believe that our approach of performing a grid search over the starting values for c_{20} and c_{40} is essential to better constrain the measurement of inner core sensitive modes and to obtain realistic uncertainties.

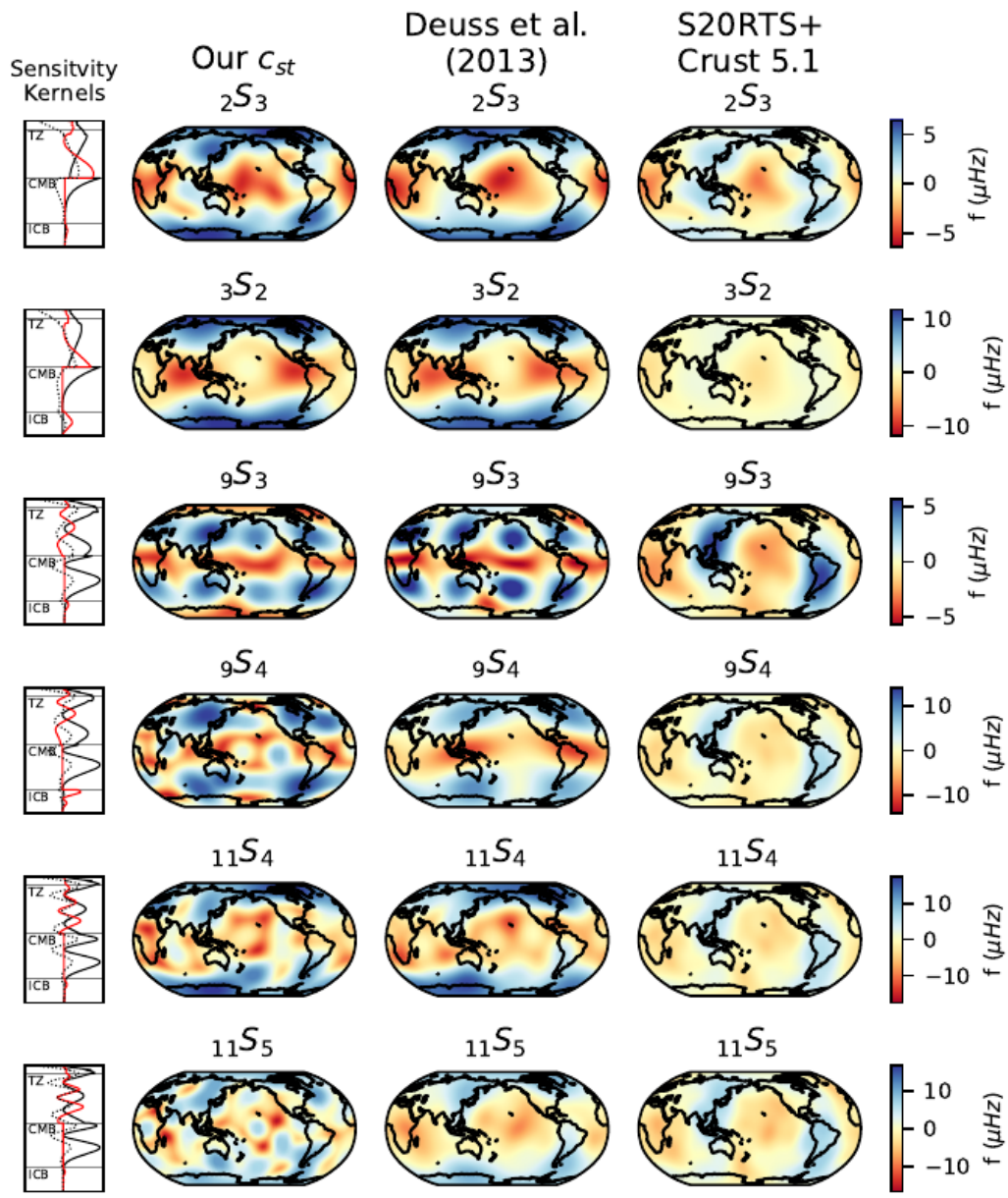

Figure 5.11 Maps of our measured splitting functions compared to the measurement by Deuss *et al.* (2013) and the predicted c_{st} from S20RTS (Ritsema *et al.*, 1999) and CRUST 5.1 (Mooney *et al.*, 1998), alongside the degree $s = 0$ sensitivity kernels where the solid black line is v_p, the solid red line is v_s and the black dotted line is ρ.

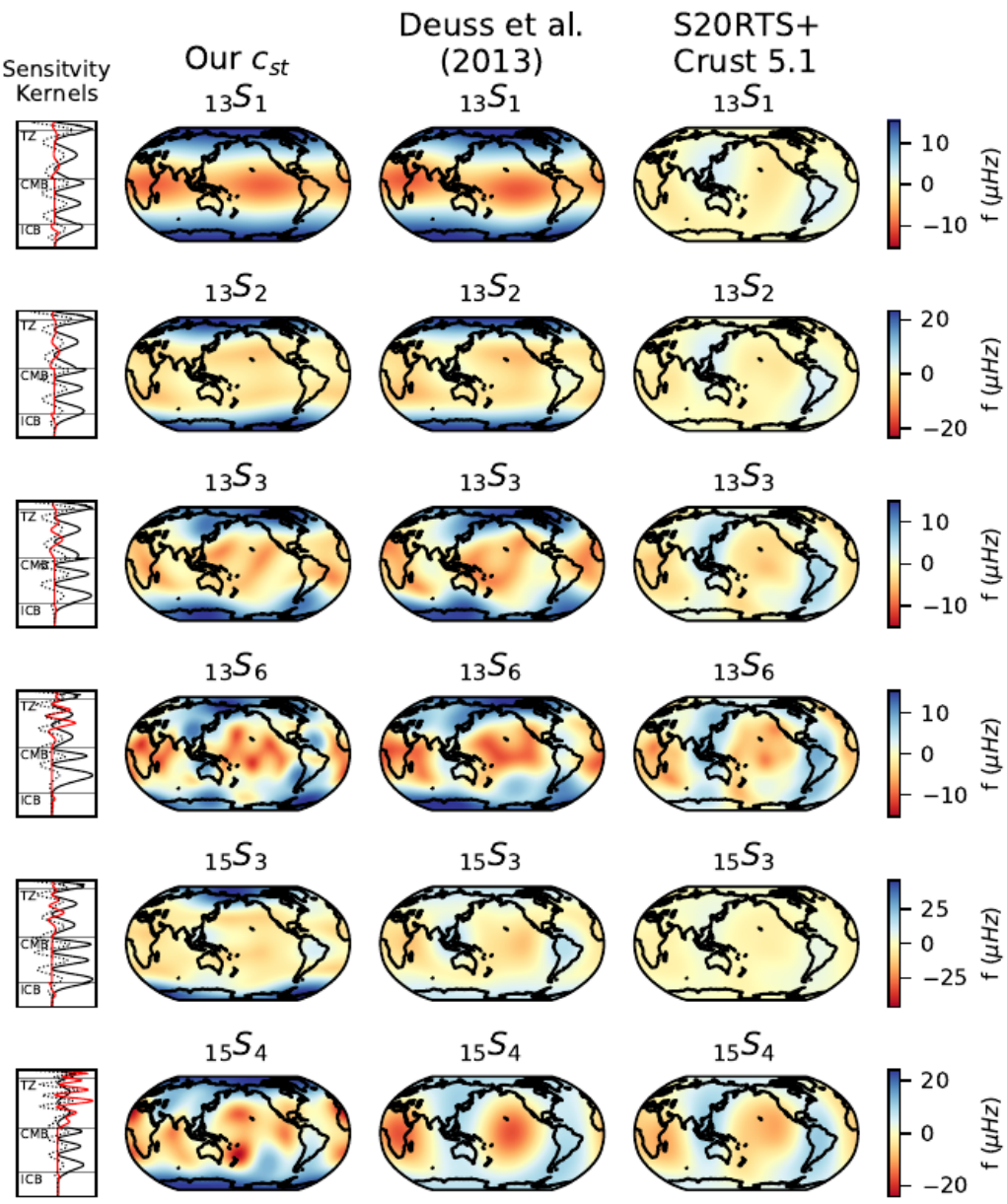

Figure 5.12 Maps of our measured splitting functions compared to the measurement by Deuss *et al.* (2013) and the predicted c_{st} from S20RTS (Ritsema *et al.*, 1999) and CRUST 5.1 (Mooney *et al.*, 1998), alongside the degree $s = 0$ sensitivity kernels where the solid black line is v_p, the solid red line is v_s and the black dotted line is ρ.

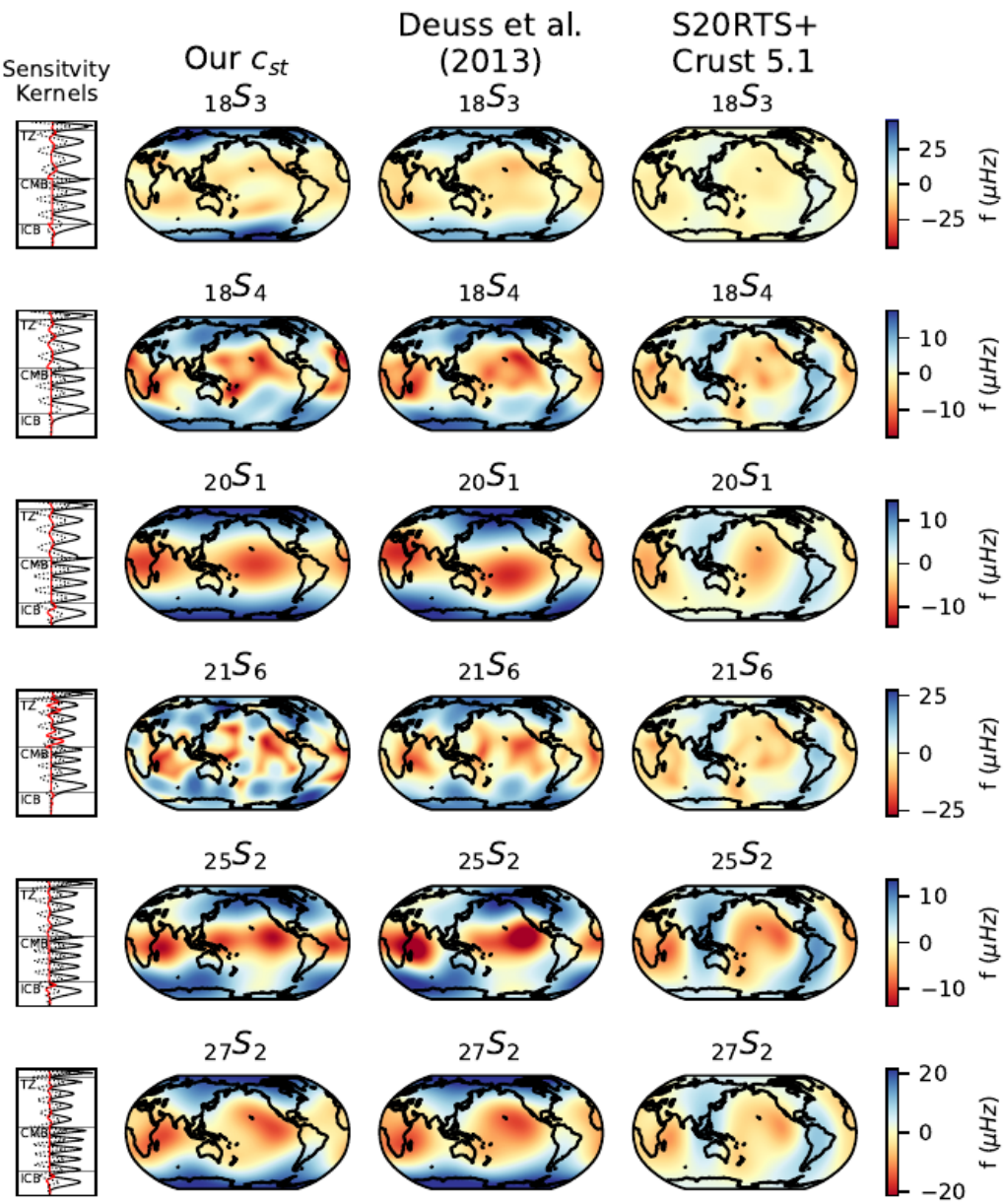

Figure 5.13 Maps of our measured splitting functions compared to the measurement by Deuss *et al.* (2013) and the predicted c_{st} from S20RTS (Ritsema *et al.*, 1999) and CRUST 5.1 (Mooney *et al.*, 1998), alongside the degree $s = 0$ sensitivity kernels where the solid black line is v_p, the solid red line is v_s and the black dotted line is ρ.

5.7 Supplementary material

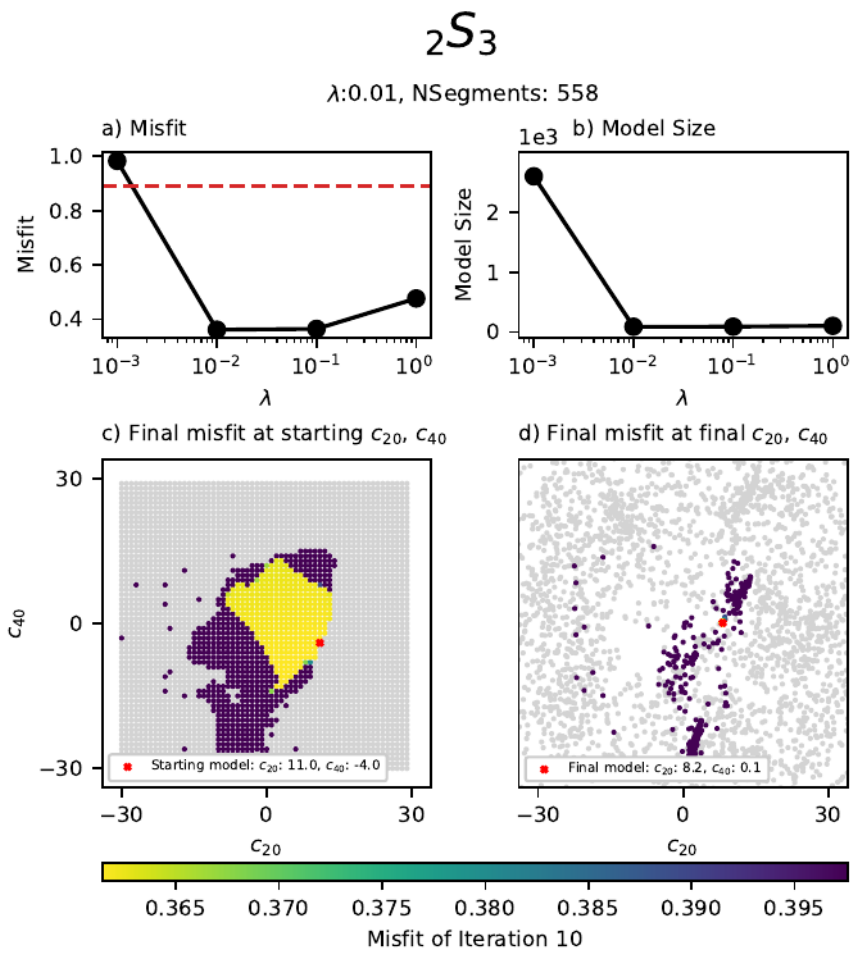

Figure 5.14 Grid search for mode $_2S_3$ at a damping of $\lambda = 0.01$. a-b) The variation of misfit and model size with damping for the same starting model which results in the minimum misfit for $\lambda = 0.01$. The red line on a) is the starting model misfit. c) final misfit as a function of the starting c_{20} and c_{40} values of each measurement, d) final misfit as a function of the c_{20} and c_{40} values of each measurement at the final iteration. The colour of each measurement displays the misfit, the red cross shows the measurement with the minimum misfit. Measurements are shown in grey when the singlets move outside of the frequency bounds of the spectral data.

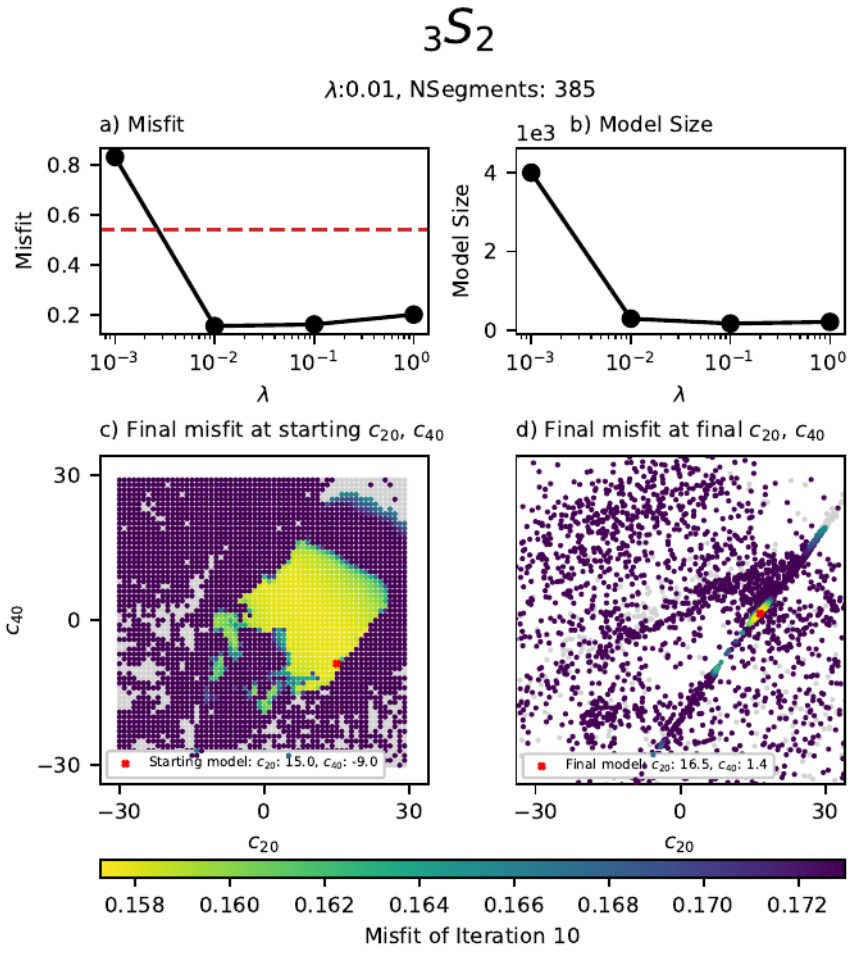

Figure 5.15 Grid search for mode $_3S_2$ at a damping of $\lambda = 0.01$. a-b) The variation of misfit and model size with damping for the same starting model which results in the minimum misfit for $\lambda = 0.01$. The red line on a) is the starting model misfit. c) final misfit as a function of the starting c_{20} and c_{40} values of each measurement, d) final misfit as a function of the c_{20} and c_{40} values of each measurement at the final iteration. The colour of each measurement displays the misfit, the red cross shows the measurement with the minimum misfit. Measurements are shown in grey when the singlets move outside of the frequency bounds of the spectral data.

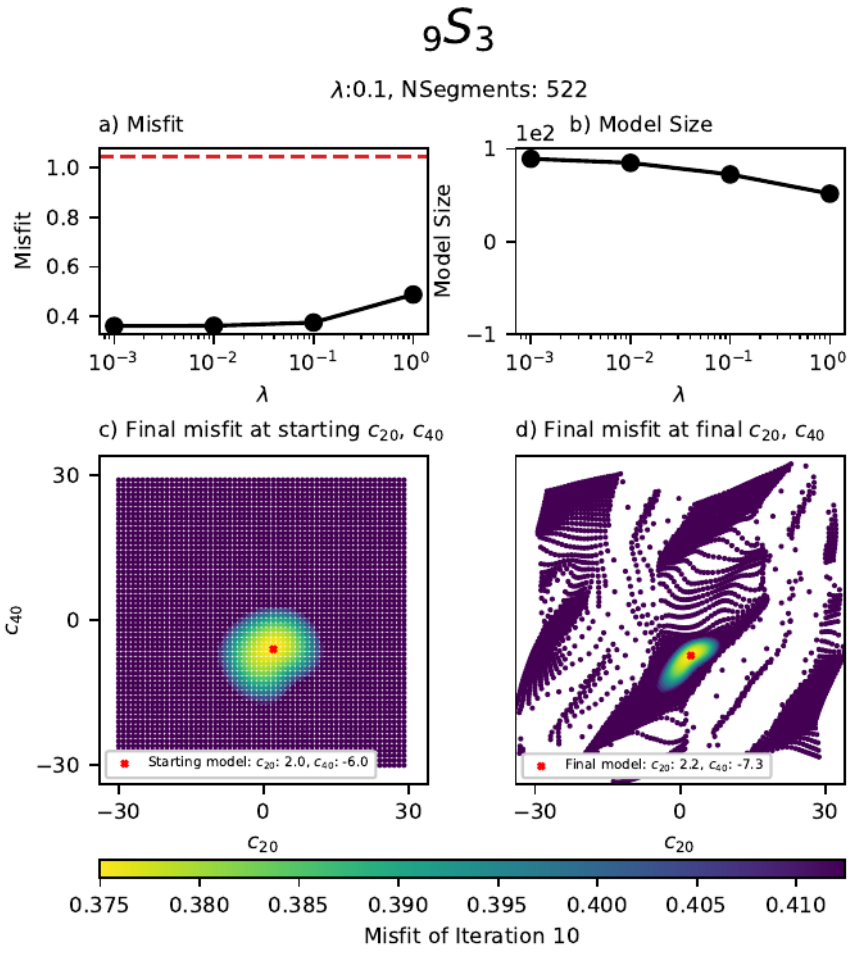

Figure 5.16 Grid search for mode $_9S_3$ at a damping of $\lambda = 0.1$. a-b) The variation of misfit and model size with damping for the same starting model which results in the minimum misfit for $\lambda = 0.1$. The red line on a) is the starting model misfit. c) final misfit as a function of the starting c_{20} and c_{40} values of each measurement, d) final misfit as a function of the c_{20} and c_{40} values of each measurement at the final iteration. The colour of each measurement displays the misfit, the red cross shows the measurement with the minimum misfit. Measurements are shown in grey when the singlets move outside of the frequency bounds of the spectral data.

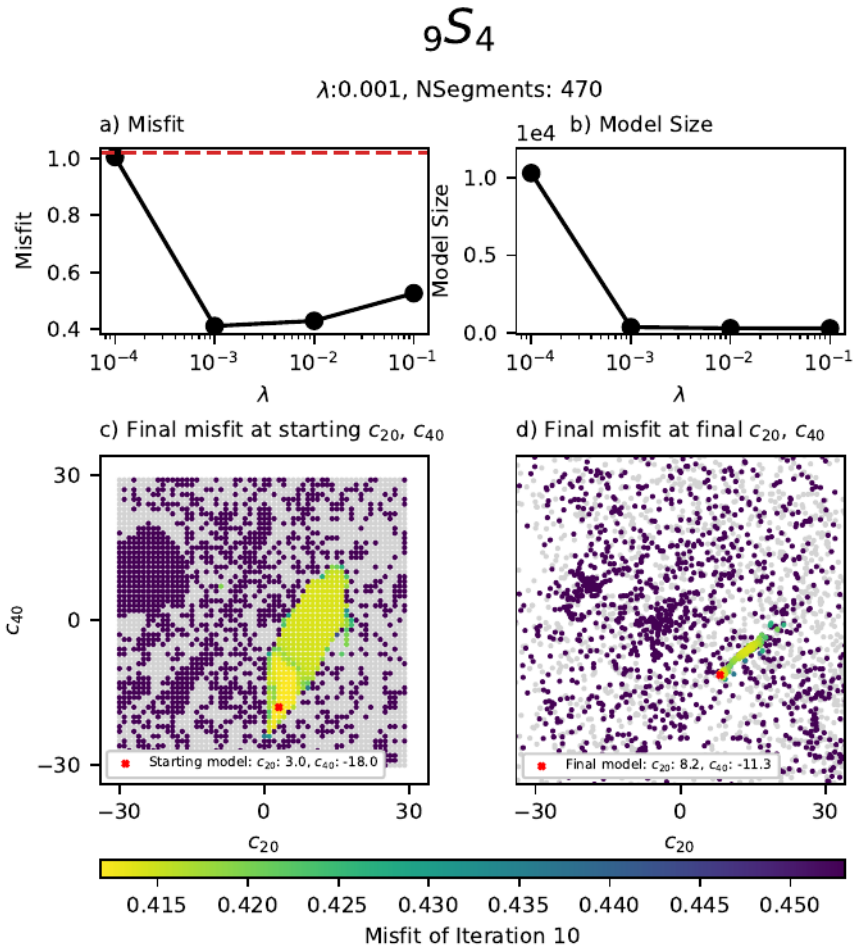

Figure 5.17 Grid search for mode $_9S_4$ at a damping of $\lambda = 0.001$. a-b) The variation of misfit and model size with damping for the same starting model which results in the minimum misfit for $\lambda = 0.001$. The red line on a) is the starting model misfit. c) final misfit as a function of the starting c_{20} and c_{40} values of each measurement, d) final misfit as a function of the c_{20} and c_{40} values of each measurement at the final iteration. The colour of each measurement displays the misfit, the red cross shows the measurement with the minimum misfit. Measurements are shown in grey when the singlets move outside of the frequency bounds of the spectral data.

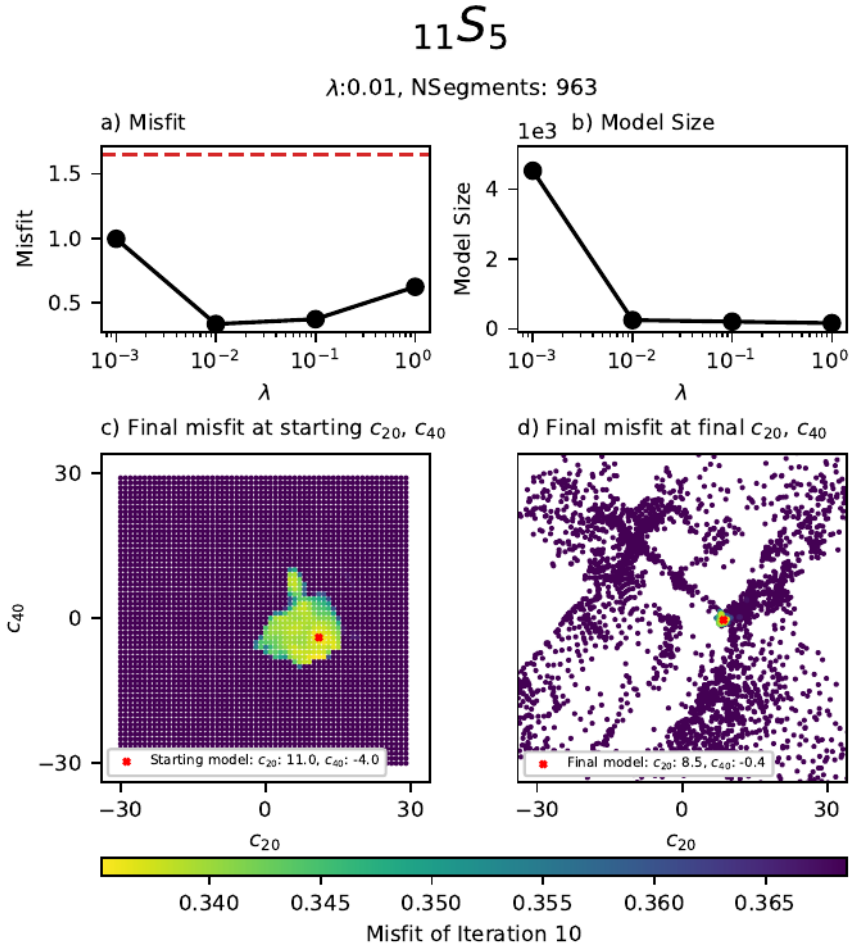

Figure 5.18 Grid search for mode $_{11}S_5$ at a damping of $\lambda = 0.01$. a-b) The variation of misfit and model size with damping for the same starting model which results in the minimum misfit for $\lambda = 0.01$. The red line on a) is the starting model misfit. c) final misfit as a function of the starting c_{20} and c_{40} values of each measurement, d) final misfit as a function of the c_{20} and c_{40} values of each measurement at the final iteration. The colour of each measurement displays the misfit, the red cross shows the measurement with the minimum misfit. Measurements are shown in grey when the singlets move outside of the frequency bounds of the spectral data.

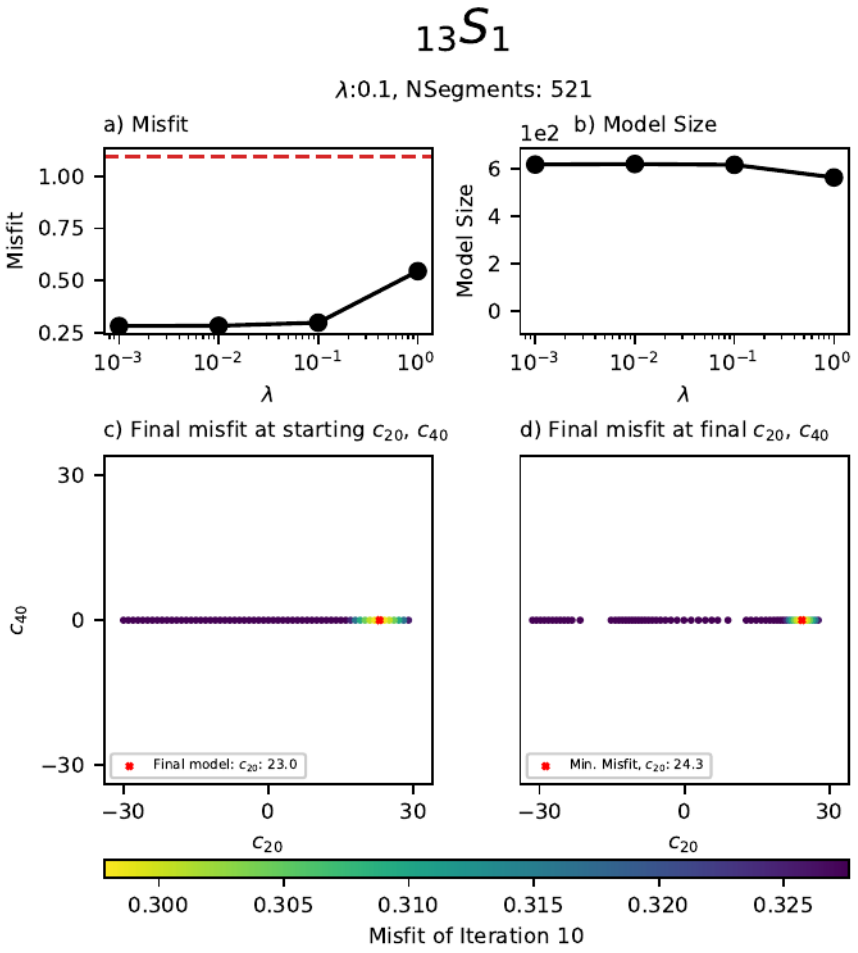

Figure 5.19 Grid search for mode $_{13}S_1$ at a damping of $\lambda = 0.1$. a-b) The variation of misfit and model size with damping for the same starting model which results in the minimum misfit for $\lambda = 0.1$. The red line on a) is the starting model misfit. c) final misfit as a function of the starting c_{20} and c_{40} values of each measurement, d) final misfit as a function of the c_{20} and c_{40} values of each measurement at the final iteration. The colour of each measurement displays the misfit, the red cross shows the measurement with the minimum misfit. Measurements are shown in grey when the singlets move outside of the frequency bounds of the spectral data.

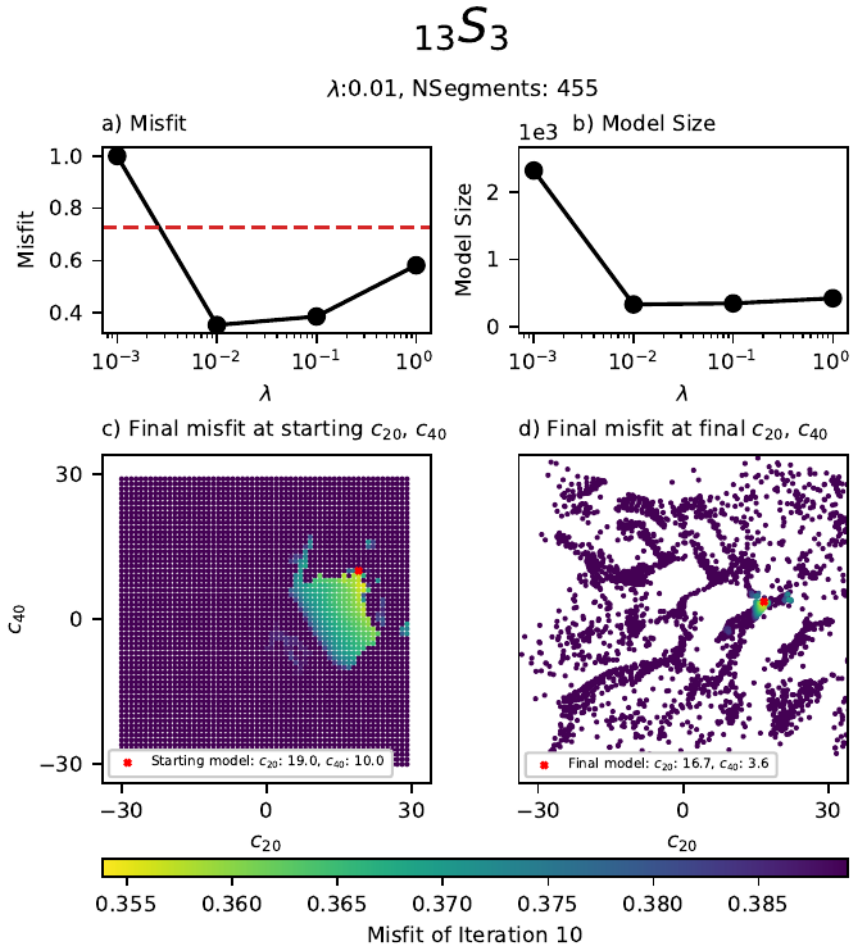

Figure 5.20 Grid search for mode $_{13}S_3$ at a damping of $\lambda = 0.1$. a-b) shows The variation of misfit and model size with damping for the same starting model which results in the minimum misfit for $\lambda = 0.1$. The red line is the starting model misfit and model size. c) is the starting c_{20} and c_{40} values of each measurement while d) Shows the c_{20} and c_{40} values of each measurement at the final iteration. The colour of each measurement in c) and d) displays the misfit. The red cross shows the measurement which results in the minimum misfit and measurements in grey occur when the singlets move outside of the frequency bounds.

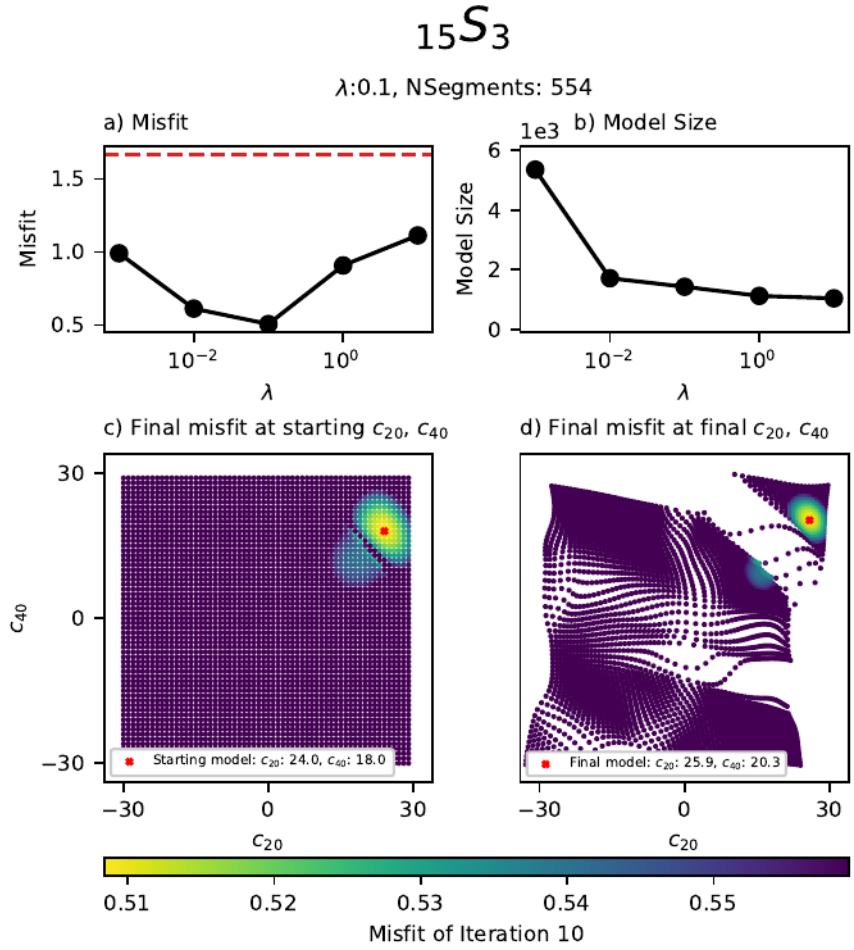

Figure 5.21 Grid search for mode $_{15}S_3$ at a damping of $\lambda = 0.1$. a-b) The variation of misfit and model size with damping for the same starting model which results in the minimum misfit for $\lambda = 0.1$. The red line on a) is the starting model misfit. c) final misfit as a function of the starting c_{20} and c_{40} values of each measurement, d) final misfit as a function of the c_{20} and c_{40} values of each measurement at the final iteration. The colour of each measurement displays the misfit, the red cross shows the measurement with the minimum misfit. Measurements are shown in grey when the singlets move outside of the frequency bounds of the spectral data.

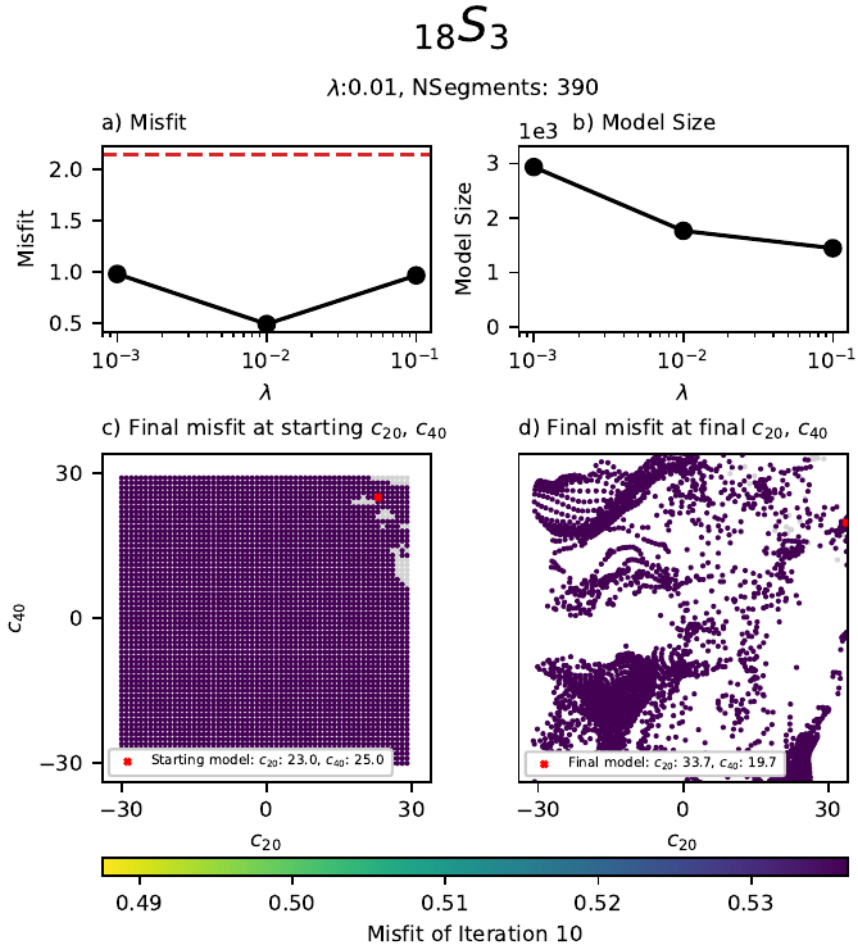

Figure 5.22 Grid search for mode $_{18}S_3$ at a damping of $\lambda = 0.01$. a-b) The variation of misfit and model size with damping for the same starting model which results in the minimum misfit for $\lambda = 0.01$. The red line on a) is the starting model misfit. c) final misfit as a function of the starting c_{20} and c_{40} values of each measurement, d) final misfit as a function of the c_{20} and c_{40} values of each measurement at the final iteration. The colour of each measurement displays the misfit, the red cross shows the measurement with the minimum misfit. Measurements are shown in grey when the singlets move outside of the frequency bounds of the spectral data.

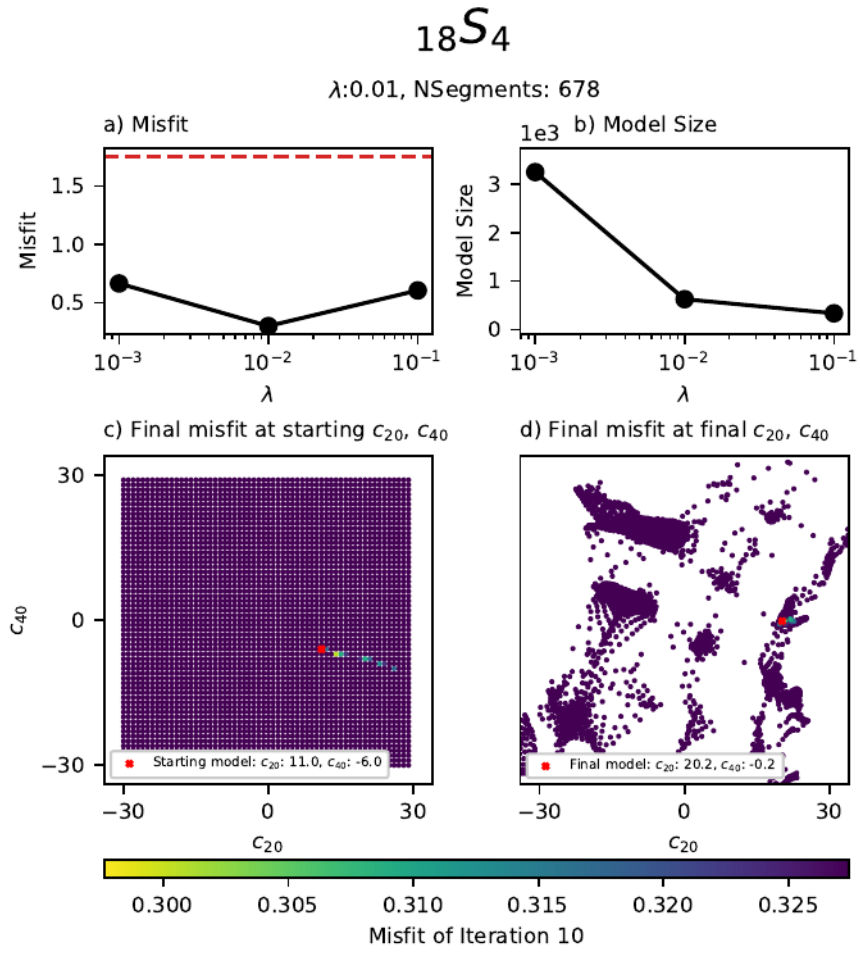

Figure 5.23 Grid search for mode ${}_{18}S_4$ at a damping of $\lambda = 0.01$. a-b) The variation of misfit and model size with damping for the same starting model which results in the minimum misfit for $\lambda = 0.01$. The red line on a) is the starting model misfit. c) final misfit as a function of the starting c_{20} and c_{40} values of each measurement, d) final misfit as a function of the c_{20} and c_{40} values of each measurement at the final iteration. The colour of each measurement displays the misfit, the red cross shows the measurement with the minimum misfit. Measurements are shown in grey when the singlets move outside of the frequency bounds of the spectral data.

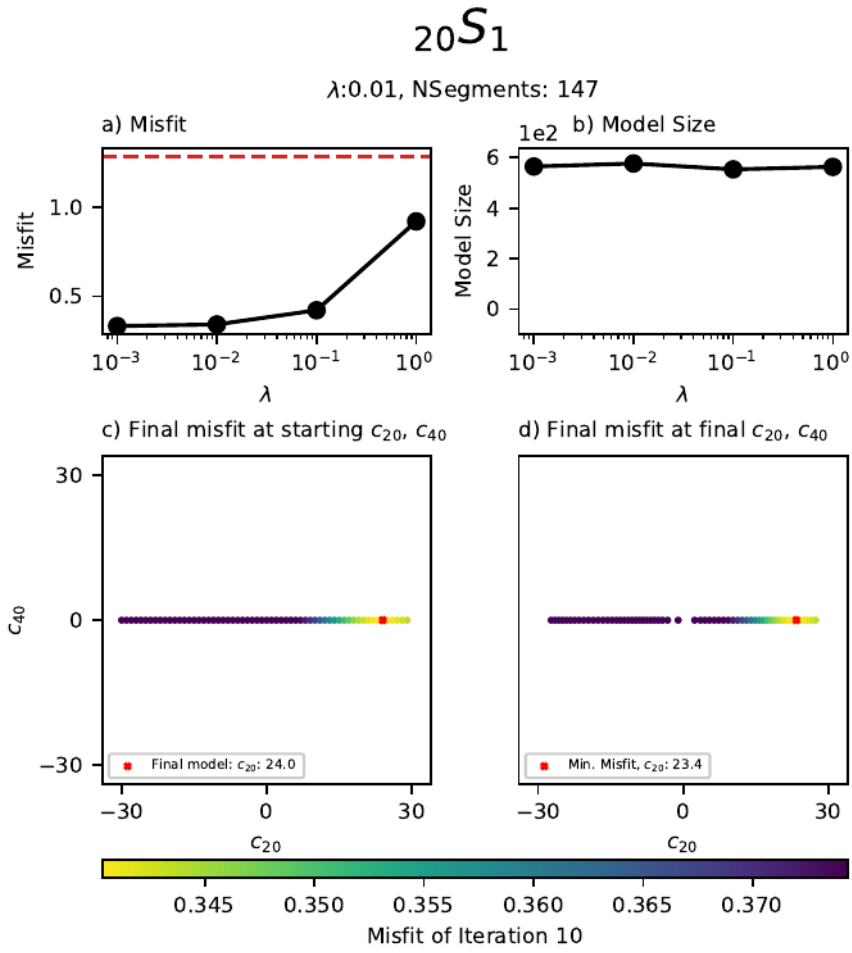

Figure 5.24 Grid search for mode $_{20}S_1$ at a damping of $\lambda = 0.01$. a-b) The variation of misfit and model size with damping for the same starting model which results in the minimum misfit for $\lambda = 0.01$. The red line on a) is the starting model misfit. c) final misfit as a function of the starting c_{20} and c_{40} values of each measurement, d) final misfit as a function of the c_{20} and c_{40} values of each measurement at the final iteration. The colour of each measurement displays the misfit, the red cross shows the measurement with the minimum misfit. Measurements are shown in grey when the singlets move outside of the frequency bounds of the spectral data.

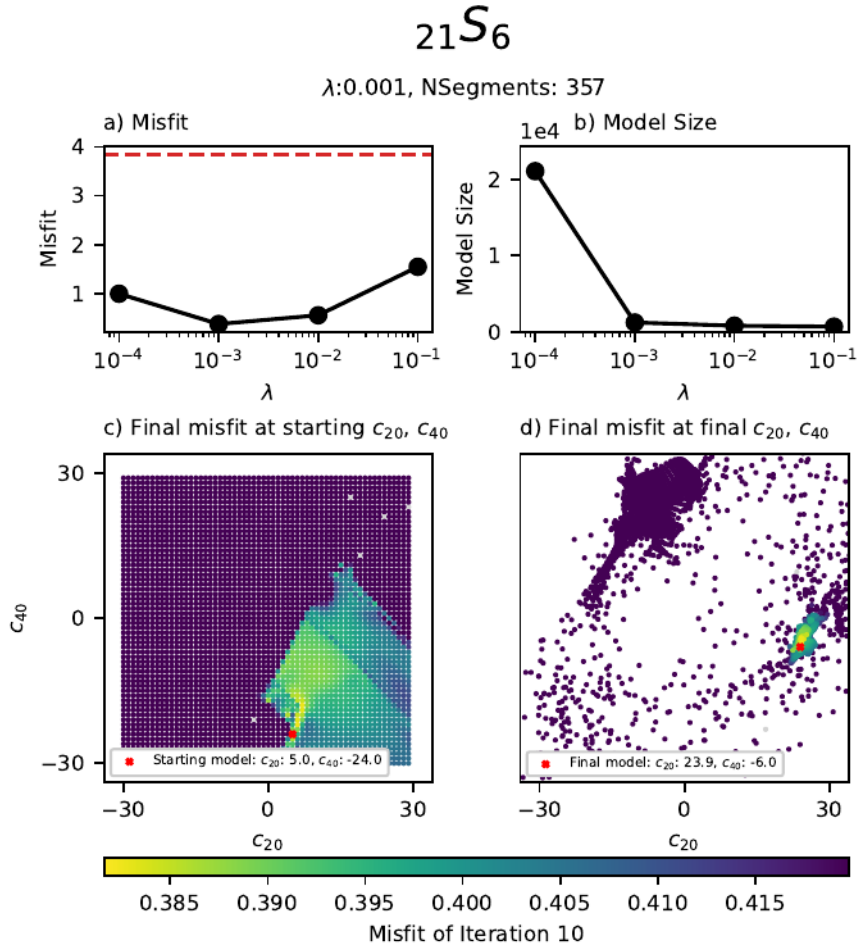

Figure 5.25 Grid search for mode $_{21}S_6$ at a damping of $\lambda = 0.001$. a-b) The variation of misfit and model size with damping for the same starting model which results in the minimum misfit for $\lambda = 0.001$. The red line on a) is the starting model misfit. c) final misfit as a function of the starting c_{20} and c_{40} values of each measurement, d) final misfit as a function of the c_{20} and c_{40} values of each measurement at the final iteration. The colour of each measurement displays the misfit, the red cross shows the measurement with the minimum misfit. Measurements are shown in grey when the singlets move outside of the frequency bounds of the spectral data.

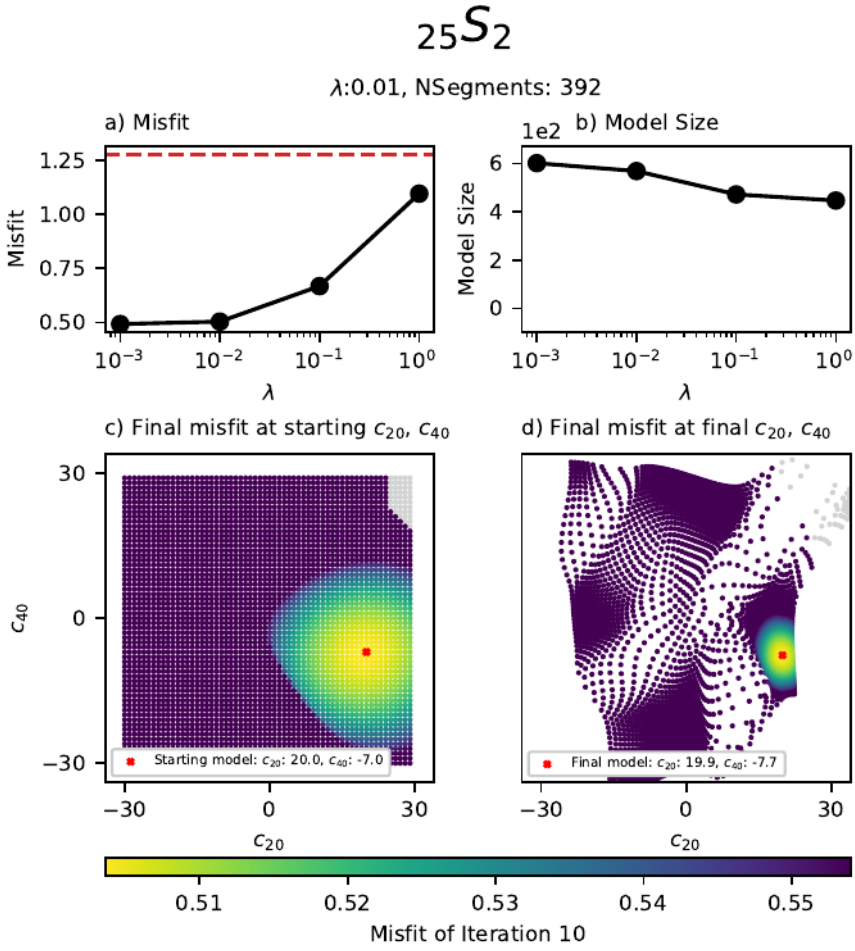

Figure 5.26 Grid search for mode $_{25}S_2$ at a damping of $\lambda = 0.01$. a-b) The variation of misfit and model size with damping for the same starting model which results in the minimum misfit for $\lambda = 0.01$. The red line on a) is the starting model misfit. c) final misfit as a function of the starting c_{20} and c_{40} values of each measurement, d) final misfit as a function of the c_{20} and c_{40} values of each measurement at the final iteration. The colour of each measurement displays the misfit, the red cross shows the measurement with the minimum misfit. Measurements are shown in grey when the singlets move outside of the frequency bounds of the spectral data.

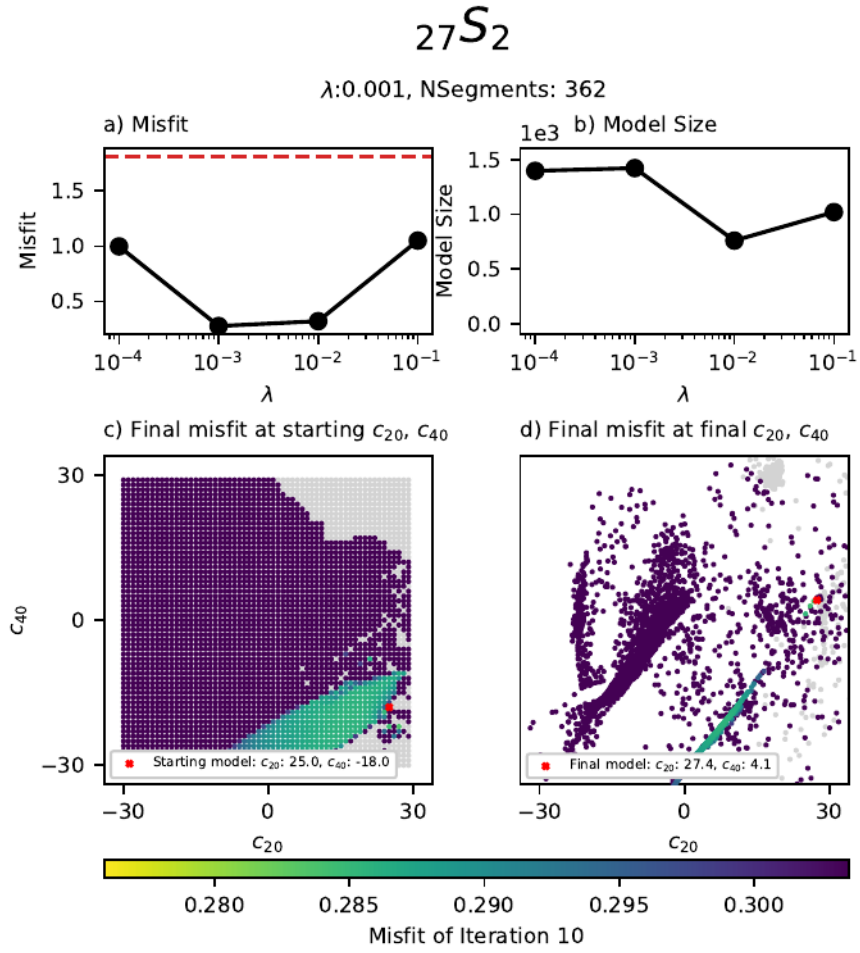

Figure 5.27 Grid search for mode $_{27}S_2$ at a damping of $\lambda = 0.01$. a-b) The variation of misfit and model size with damping for the same starting model which results in the minimum misfit for $\lambda = 0.01$. The red line on a) is the starting model misfit. c) final misfit as a function of the starting c_{20} and c_{40} values of each measurement, d) final misfit as a function of the c_{20} and c_{40} values of each measurement at the final iteration. The colour of each measurement displays the misfit, the red cross shows the measurement with the minimum misfit. Measurements are shown in grey when the singlets move outside of the frequency bounds of the spectral data.

6

1D Transdimensional seismic tomography of the inner core using normal modes (preliminary)

Inner core sensitive normal modes provide important constraints on inner core anisotropy. Here we use our new splitting function measurements to conduct a 1D transdimensional inversion of inner core anisotropy. Instead of Voronoi cells, which are particularly useful for body waves, we use polynomials as basis functions to parameterize inner core anisotropy as a function of depth. Our transdimensional 1D normal mode model finds 2.9% P-wave anisotropy in the middle of the inner core and 1.0% S-wave anisotropy at the Inner Core Boundary (ICB). We also see tentative evidence for an innermost Inner Core (IMIC). However, this result has to be considered alongside the relatively low sensitivity of the normal modes to the deepest 400 km of the inner core and also the corresponding large uncertainty for that depth range in our model. Comparing our normal mode model (this chapter) to the 1D average of our 3D body wave model (Chapter 4), we find that they agree on the magnitude of compressional anisotropy in the inner core.

6.1 Introduction

Inner core anisotropy was first measured using 7 normal mode splitting functions by Woodhouse *et al.* (1986); they found 3.35% P-wave anisotropy and 0.35% S-wave anisotropy on average through the inner core (Table 6.1 and Figure 6.1). Tromp (1993) extended the data to 18 splitting function measurements and allowed for depth variations. His model has 2.1% P-wave anisotropy decreasing from the ICB to the centre and 0.63% S-wave anisotropy on average in the inner core, peaking at 900 km radius (Figure 6.1).

Durek and Romanowicz (1999) represents a big step forward in normal mode models of inner core anisotropy, utilising more modes than either Woodhouse *et al.* (1986) or Tromp (1993) (25 in total). Furthermore, they conducted a direct spectra inversion, avoiding errors associated with the starting model when measuring inner core sensitive splitting functions (as discussed in Chapter 5). They also tested different model parameterizations that go beyond the 1D case, focusing on models with a central cylinder in the inner core representing strong anisotropy. Their models of inner core anisotropy have on average 2.5% P-wave anisotropy and 0.4% S-wave anisotropy. Interestingly, their P-wave anisotropy is 2% at the ICB decreasing at ∼1000 km radius, before increasing again. This feature is not observed by other inner core models (Figure 6.1), but appears at depths similar to the innermost inner core (IMIC).

The IMIC was first proposed by Ishii and Dziewoński (2003) as a region at the centre of the inner core with distinct anisotropy; primarily that the direction of the slowest velocity is not perpendicular to the symmetry axis. We have discussed the IMIC in detail in Chapter 4 (Section 4.7.3), but it is still an open question whether this anomalous anisotropy can be observed with normal modes. To investigate the inner most inner core we look at the ζ_{slow} angle, which is the angle of the slowest direction of inner core anisotropy relative to Earth's axis of rotation. The prediction for ζ_{slow} from previous models is shown on Figure 6.1d).

Beghein and Trampert (2003) used the neighbourhood algorithm (Sambridge, 1999) to search for the best fitting model using splitting functions. This model space search resulted in a model with 2.9% P-wave anisotropy and 0.85% S-wave anisotropy on average throughout the inner core but with significant radial variation. Through the neighbourhood algorithm they were able to provide uncertainty estimates on these model parameters. They propose that anomalies at the centre of their model can be explained by increasingly tilted hcp iron in the inner core, but found that a different phase of iron would be necessary at the centre of the inner core to explain

Table 6.1 Radial averages of α, β and γ (in %) for previous inner core models which used normal modes as data. [1]models which do not vary radially. [2]parameterized as $a + br^2$. *also included body wave data in a joint inversion.

Author(s)	α	β	γ
Woodhouse *et al.* (1986)[1]	6.70	0.70	2.70
Woodhouse *et al.* (1986)[2]	6.24	1.14	1.98
Tromp (1993)	4.21	1.27	2.33
Durek and Romanowicz (1999)	5.00	0.80	0.50
Ishii *et al.* (2002a)*	3.49	0.99	0.88
Beghein and Trampert (2003)	5.87	1.71	1.53
Mäkinen *et al.* (2014)[1]	2.99	0.72	0.15
Mäkinen *et al.* (2014)[2]	3.46	0.85	-0.54

their findings, possibly alluding to an IMIC.

The most recent inner core model is from Mäkinen *et al.* (2014), who produced a joint elastic and anelastic anisotropy model for the inner core by incorporating both anelastic and elastic splitting functions, finding 1.5% P-wave anisotropy and 0.35% S-wave anisotropy on average throughout the inner core. S-wave anisotropy stays almost constant throughout the inner core while P-wave anisotropy decreases from a maximum of 3% at the ICB to $\sim 0.0\%$ at the centre of the inner core. While, Mäkinen *et al.* (2014) does not explicitly discuss the IMIC in their paper (focusing more on the anelastic structure), we have calculated their predicted value of ζ_{slow} throughout the inner core (Figure 6.1d) and found a ζ_{slow} anomaly remarkably similar in depth and magnitude to what we would expect of the IMIC from body waves.

Since Woodhouse *et al.* (1986) inner core anisotropy models inferred from normal modes have varied in the amount of modes incorporated and also in the type of basis functions used to parameterize the depth dependence (polynomials or b-splines). Only one previous paper has used a Bayesian sampling methodology (Beghein and Trampert, 2003); all others utilised linear inverse methodologies. In this chapter we will use our new splitting function measurements (Chapter 4) for a 1D transdimensional inversion of inner core anisotropy. The transdimensional algorithm will allow the data to define how many model parameters are required to parameterize the depth dependence of the anisotropy and additionally allow us to recover uncertainties on these model parameters. We will also compare P-wave anisotropy and ζ_{slow} from our 1D normal mode model with the average of

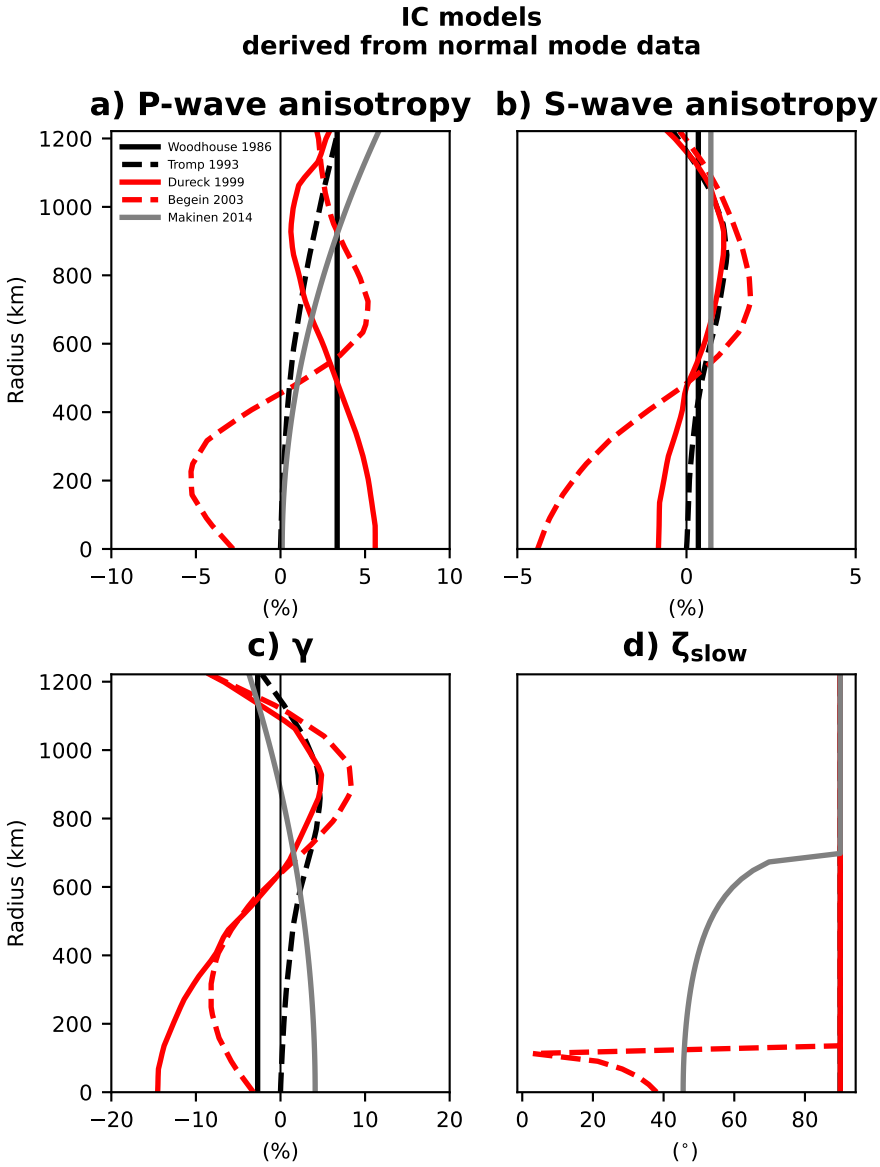

Figure 6.1 Variations of P-wave anisotropy ($\alpha/2$), S-wave anisotropy ($\beta/2$), γ (the velocity at intermediate angles) and ζ_{slow} from previous inner core models made with normal mode data, including Woodhouse *et al.* (1986), Tromp (1993), Durek and Romanowicz (1999), Beghein and Trampert (2003) and Mäkinen *et al.* (2014).

our 3D body wave model and we will show that the two are in reasonable agreement.

6.2 Methodology

6.2.1 Anisotropy parameterization

We model inner core anisotropy assuming transverse cylindrical isotropy with the symmetry axis parallel to Earth's axis of rotation. From normal mode theory (Woodhouse *et al.* (1986); Tromp (1995)) it follows that the zonal coefficients (c_{20} and c_{40}) are then linearly dependent on only three model parameters, α, β and γ which describe seismic anisotropy:

$$c_{s0} = \int_0^{ICB} \alpha(r)K_s^{\alpha} + \beta(r)K_s^{\beta} + \gamma(r)K_s^{\gamma}dr \tag{6.1}$$

where r is the radius, which we integrate from 0 to the ICB, s is the spherical harmonic degree, c_{s0} is our measured splitting function value of c_{20} or c_{40}. α, β and γ are three anisotropic parameters describing P-wave anisotropy, S-wave anisotropy and the velocity of waves not travelling parallel or perpendicular to the symmetry axis. K_s^{α} is the sensitivity kernel of the zonal parameter with spherical harmonic degree s to the model parameter α and which varies as a function of radius (and similarly for K_s^{β} K_s^{γ}). α, β and γ are related to the love parameters A, C, L, N and F (Love, 1927) in the following way:

$$\alpha = \frac{(C-A)}{A_0} \tag{6.2}$$

$$\beta = \frac{(N-L)}{A_0} \tag{6.3}$$

$$\gamma = \frac{(A-2N-F)}{A_0} \tag{6.4}$$

where A_0 is the value of the elastic parameter A at the centre of the Earth from the reference model.

The fractional velocity of a P-wave at a given angle of ζ (the angle the raypath makes with Earth's axs of rotation) as a function of α, β and γ can be calculated thus (derived in Section 2.2, Equation 2.18) :

$$\frac{\delta t}{t} = \delta V_p(\zeta) = (2\beta - \gamma)\cos^2(\zeta) + (\frac{1}{2}\alpha - 2\beta + \gamma)\cos^4(\zeta) \tag{6.5}$$

here we use the equation without δV_{eq} as the zonal parameters of the normal mode splitting functions are not sensitive to changes in the equatorial velocity.

The slow direction is calculated by taking the derivative of Equation 6.5, setting it to zero and solving for the angle ζ_{slow}:

$$\zeta_{slow} = \frac{1}{2}\cos^{-1}\left(\frac{\alpha}{\alpha - 4\beta + 2\gamma}\right) \tag{6.6}$$

As in Chapter 4 we set a threshold such that the magnitude of the velocity at ζ_{slow} must be 0.5% slower than the velocity at $\zeta = 90^\circ$ to ensure that the anomalous anisotropy is a robust observation, otherwise $\zeta_{slow} = 90^\circ$.

From normal mode perturbation theory we are able to calculate the sensitivity kernels K^{α}_{st}, K^{β}_{st} and K^{γ}_{st} (Tromp, 1995) of each c_{st} to α, β and γ. Figures 6.2-6.3 display sensitivity kernels for all modes used in this chapter; they show that our normal mode data has strong sensitivity to inner core anisotropy in the upper and middle inner core, with reduced sensitivity from 400 km radius and below. This is to be expected as normal modes have zero sensitivity at the centre of the Earth as it represents a nodal point.

We use our c_{20} and c_{40} measurements from Chapter 5 (see Table 5.3) and correct each measurement for crustal structure using CRUST 5.1 (Mooney *et al.*, 1998) and mantle structure using S20RTS (Ritsema *et al.*, 1999). We then apply a transdimensional inversion (see below) for α, β and γ as a function of depth.

6.2.2 Transdimensional polynomial models

Previous studies used polynomials (Woodhouse *et al.* (1986); Tromp (1993); Durek and Romanowicz (1999); Mäkinen *et al.* (2014)) or b-splines (Beghein and Trampert, 2003) for the depth dependence of α, β and γ. When modelling inner core anisotropy with the body wave data it is a good choice to use a basis function with sharp discrete boundaries such as Voronoi cells because the sensitivity of the body waves (when using ray theory) are themselves discrete, i.e. a raypath either passes through a volume or not. With normal modes the opposite is true, normal modes have broad sensitivity which varies smoothly as a function of radius. Thus, it is preferable to use smooth basis functions when using normal modes as the sensitivity kernels of normal modes to Earth structure are themselves smooth functions which are sensitive to the whole inner core.

Following previous studies we will use polynomial basis functions to model radial variations in α, β and γ. For each model parameter we define

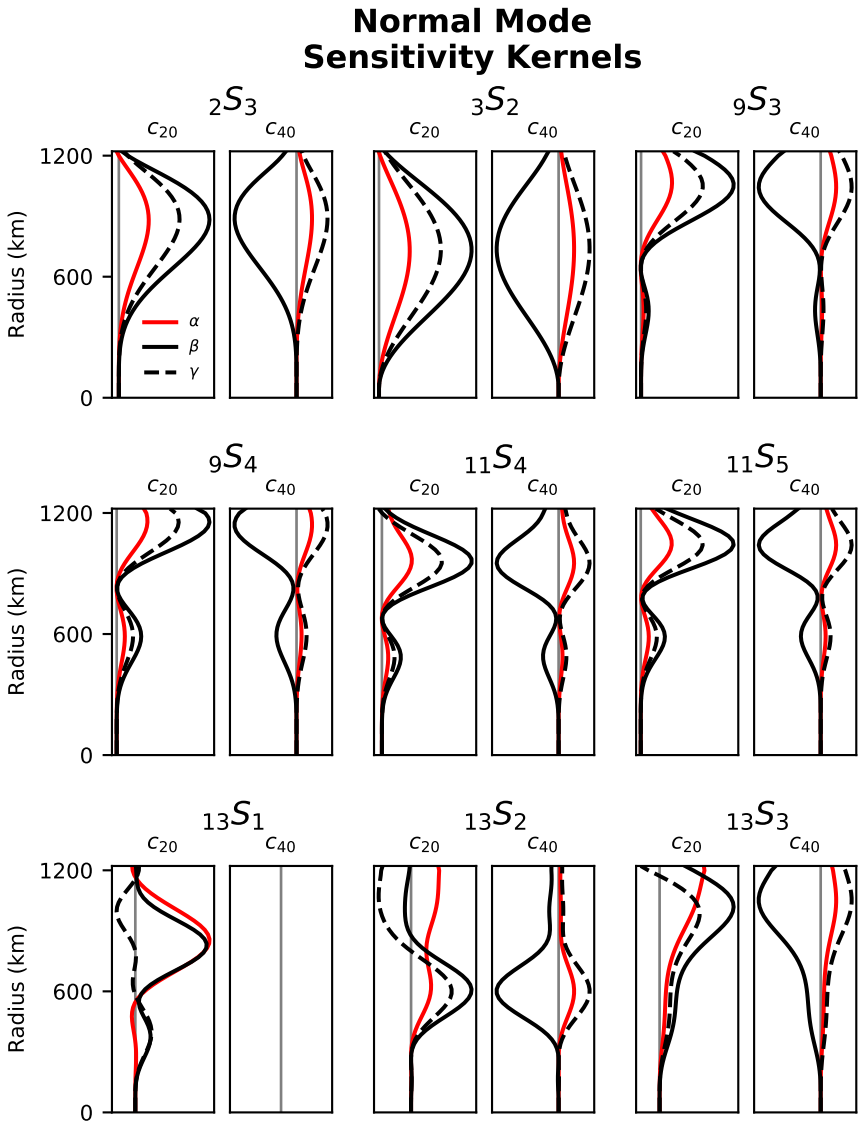

Figure 6.2 Sensitivity kernels of the zonal parameters of 9 inner core sensitive modes to α,β and γ.

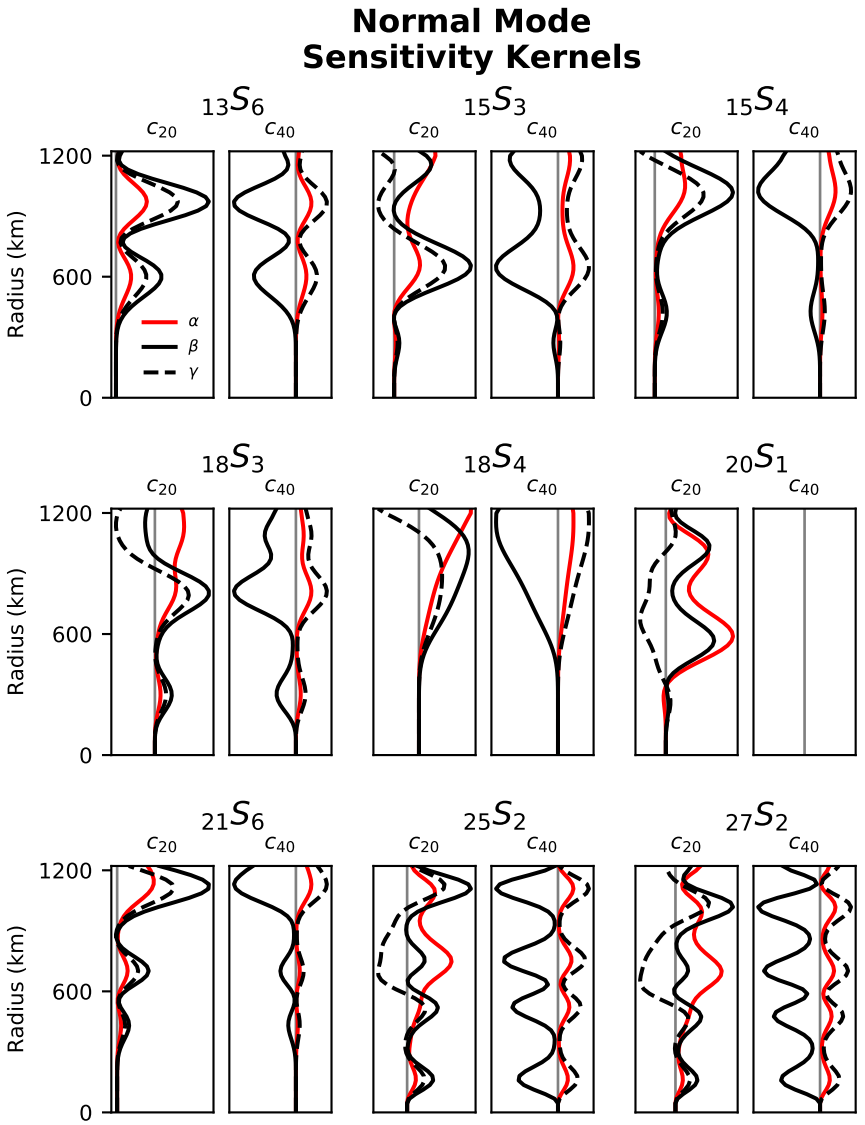

Figure 6.3 Sensitivity kernels of the zonal parameters of 9 inner core sensitive modes to α,β and γ.

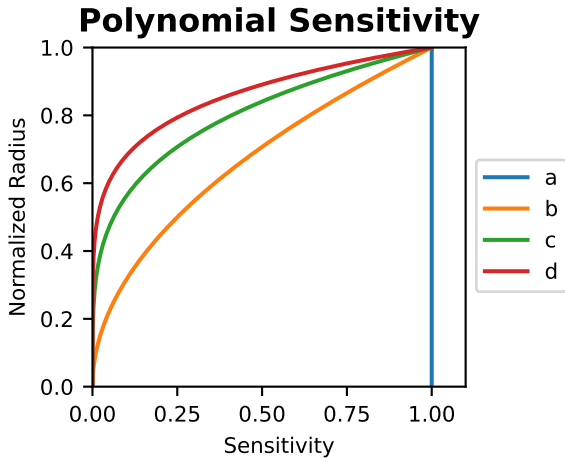

Figure 6.4 Sensitivity of each polynomial coefficient as a function of radius normalised between 0.0 and 1.0

our polynomials in increasing polynomial order;

$$\alpha(r) = a_\alpha + b_\alpha r^2 + c_\alpha r^4 + d_\alpha r^6 \dots \tag{6.7}$$

$$\beta(r) = a_\beta + b_\beta r^2 + c_\beta r^4 + d_\beta r^6 \dots \tag{6.8}$$

$$\gamma(r) = a_\gamma + b_\gamma r^2 + c_\gamma r^4 + d_\gamma r^6 \dots \tag{6.9}$$

where r is the radius of the inner core normalised between 0.0 and 1.0. The parameters in blue are the polynomial coefficients which we solve for. Figure 6.4 shows how the sensitivity of a, b, c and d vary as a function of radius. It can be seen that a is uniform throughout the inner core, while b has sensitivity which decreases with depth in the inner core and that each parameter after this has steadily stronger sensitivity to the top of the inner core.

Markov Chain Monte Carlo (MCMC) is a sampling methodology which utilises the Metropolis-Hastings (Hastings, 1970) algorithm alongside Bayes theorem (Bayes, 1763) to combine prior information on model space with data to approximate the posterior probability distributions of the data-model system. MCMC works by calculating many millions of models, each a small perturbation on the previous model forming a Markov-Chain. Model

perturbations will be accepted or rejected following the Metropolis-Hastings algorithm, with models that reduce the misfit to the data always being accepted and model perturbations which increase the misfit, sometimes being accepted. Once the MCMC algorithm has finished, an ensemble of models can be analysed deriving statistical measures such as the mean of each model parameter and the standard deviation at different locations in the ensemble.

Transdimensional MCMC goes further by incorporating the size of the model space into the inversion. Thus not only the magnitude of the polynomial coefficients (in blue in Equation 6.9) is perturbed but also the number of polynomial coefficients is allowed to change independently for each model parameter α, β and γ. To achieve this we have adapted our transdimensional algorithm from Chapter 4 to ensure that we do not over fit one model parameter or under fit another. More heterogeneity and a low noise level in the normal mode data will result in more polynomial coefficients and more complex radial structure, and vice versa.

The transdimensional inversion will produce an ensemble of models with varying numbers of polynomial coefficients for each model parameter. This is achieved by incorporating three types of model perturbations:

1. Velocity perturbations: a random model parameter from α, β or γ is chosen and a random polynomial coefficient from this parameter is then perturbed relative to a previous model (in the same way as outlined in Section 4.5.1).

2. *Birth* of a polynomial coefficient: a random parameter is chosen from α, β or γ and a polynomial coefficient is added. This coefficient will always be of the next order (i.e. if there are already 2 polynomial coefficients a and b and a *birth* step is accepted then the new coefficient will be c).

3. *Death* of a polynomial coefficient: a random parameter is chosen from α, β or γ and the last coefficient from their respective polynomial expansion is removed.

6.2.3 Hierarchical noise

We model the noise in our data using the uncertainty estimates from our grid searches and a hierarchical noise methodology. For each c_{st} the uncertainty from our grid searches from Chapter 5 is used as a minimum noise level. We then additionally add a hierarchical noise parameter which is solved for

iteratively in the MCMC. Thus, for a specific c_{st} the noise is calculated using:

$$\lambda_{st} = \sqrt{\sigma_{st}^2 + \lambda^2} \tag{6.10}$$

where λ_{st} is the total noise combining the hierarchical parameter and the estimated uncertainty from the grid searches, σ_{st} is the uncertainty derived from the grid searches for each c_{st} in Chapter 5 and λ is the hierarchical noise parameter. The hierarchical noise assesses agreement between data in the model-data system. Consider a simple example; If two c_{st} measurements have exactly the same sensitivity to anisotropy in the inner core, but it is not possible to fit both measurements simultaneously then the difference in the c_{st} measurements will be interpreted as noise and results in an increase in the hierarchical parameter. A larger hierarchical parameter therefore means that the transdimensional algorithm fits the data less well (as the noise is increased) and so results in fewer polynomial coefficients.

6.3 Results

Just like in Chapter 4 for the body waves, we run 20 Markov chains for 1 million iterations which after thinning (removing every 100th model) and burn in (disregarding the first third of models) results in an ensemble of 133380 models. We use Gaussian priors on our model parameters with a mean of 0.0 and a standard deviation of 0.2 (i.e. 20% perturbations relative to PREM, well within the expected range of anisotropy in the inner core). The misfit in each chain quickly drops to a mean misfit of 0.55, i.e. 45% reduction relative to PREM (Figure 6.5a). The number of polynomials varies across the models in our chains; we found that the majority of models requires between 1-3 coefficients for α. For β the most common number of coefficients is 2, while for γ it is 2-3, but in our ensemble there were also a significant number of models with 5-6 coefficients for β and γ. Overall, the majority of the variance in the data can be described by polynomial functions with 3 coefficients a, b and c in Equation 6.9. The mean noise in our data is 8.3μHz, which is the average of all the hierarchical noise parameters in our ensemble plus the mean noise in our c_{st} measurements. This noise level means that on average each c_{st} is fit to within 8.3μHz.

Our model fits the c_{20} data better with a 71% misfit reduction (relative to PREM) than the c_{40} data with only a 13% misfit reduction (Figure 6.6). This implies that there is more noise or disagreement in our c_{40} measurements than our c_{20} measurements. Alternatively the way in which we have parameterized the inner core, either in terms of polynomial basis functions

or in terms of cylindrical anisotropy, does not describe the c_{40} parameters well.

Figure 6.7 shows how $\delta \mathrm{Vp}_{ani}$ $(\frac{\alpha}{2})$, $\delta \mathrm{Vs}_{ani}$ $(\frac{\beta}{2})$, γ, and ζ_{slow} vary as a function of radius throughout our model. We see that our normal mode model predicts Vp_{ani} varying from 1.2% at the ICB to a maximum of 2.1% at 1000-950 km radius and then reducing to 1% at the centre of the inner core. Variations in $\delta \mathrm{Vs}_{ani}$ are less strong, with 0.7% anisotropy at the ICB, dropping to 0.17% between 800-850 km and increasing again towards the centre of the inner core reaching a maximum of 0.96%, but with increasing uncertainty. γ shows stronger variations with -9.9% at the ICB increasing to 3.7% at 800 km and reducing back to 0.3% at the centre of the inner core.

The combination of α, β and γ is then used to calculate the angle of slowest direction, ζ_{slow} (Equation 6.6). ζ_{slow} is interesting because it has been proposed that there in is an innermost inner core (IMIC) with anomalous ζ_{slow} and we indeed found the IMIC in our body wave transdimensional model in Chapter 4. Here, we use the same tolerance condition as defined in Section 4.3, such that the difference between the velocity at the slowest direction and the velocity at $\zeta = 90°$ has to be greater than 0.5%. Our normal mode model finds $\zeta_{slow} = 90°$ at the ICB, which decreases to $\zeta_{slow} = 75°$ at 730 km radius, before increasing back to $\zeta_{slow} = 85°$ at the centre (Figure 6.7d). This ζ_{slow} anomaly could potentially be the modes picking up some structure from the inner most inner core (IMIC), however, the anomaly is shallower than we would expect from our body wave model (Chapter 4), or from recent studies on the IMIC (Frost and Romanowicz (2019); Stephenson *et al.* (2020)) where the IMIC boundary is found to be between 600-700 km radius.

6.3.1 Comparison with body wave model

Before making a combined model for body waves and normal mode data (Chapter 7), it is useful to compare the models made with only the body wave data (Chapter 4) and only the normal mode data (this chapter) as this will help us identify elements of the different models that are likely to agree or disagree. Our body wave model uses AK135 as a reference model (Kennett *et al.*, 1995) while the normal mode model uses PREM (Dziewonski and Anderson, 1981). In the following figures we adjust the anisotropy from our body wave model to use PREM as a reference model. The affect is small given the similarities in compressional velocity between PREM and AK135 in the inner core. Furthermore, each model is parameterized differently. The body wave model uses a, b and c parameters and the nor-

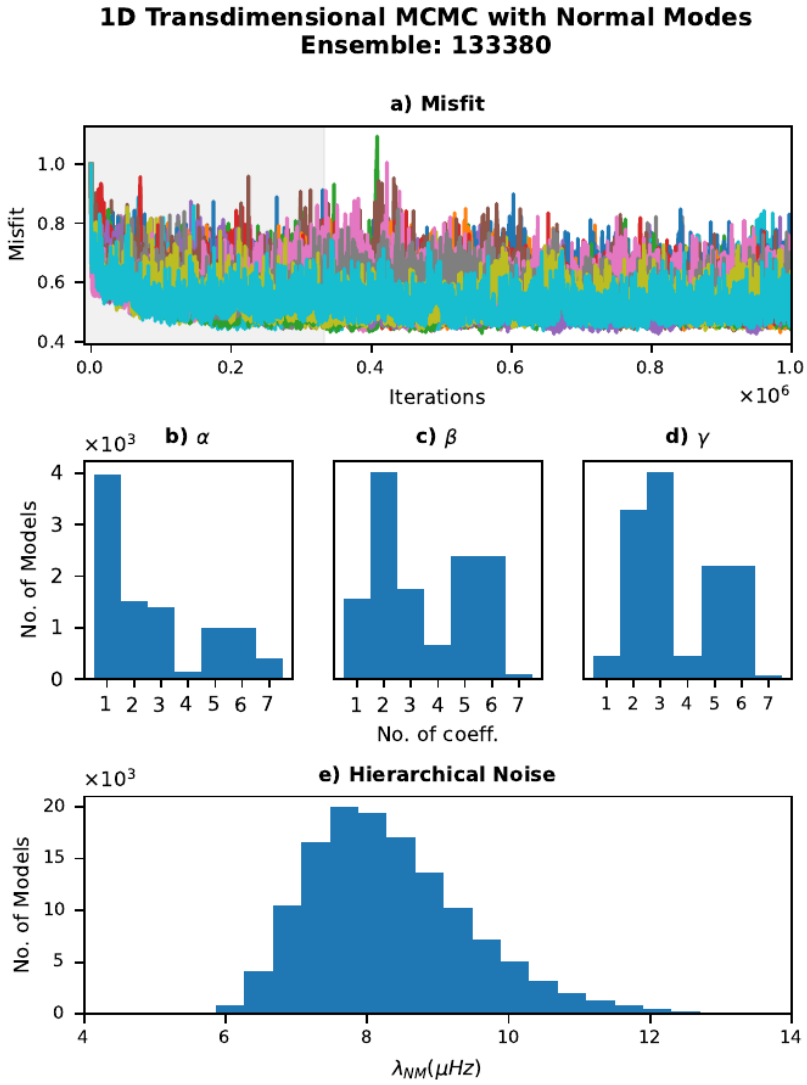

Figure 6.5 a) shows how misfit relative to PREM varies as a function of iteration across all our chains, b-d) shows the distributions of the number of polynomial coefficients required by our ensemble to describe α, β and γ. e) is a histogram showing the distribution of mean noise in our data across our ensemble, calculated: $\lambda_{NM}^{total} = \sqrt{\lambda_{NM}^2 + mean(\sigma_{st})^2}$ where λ_{NM} is the hierarchical parameter and σ_{st} is the noise in our data estimated from the grid searches.

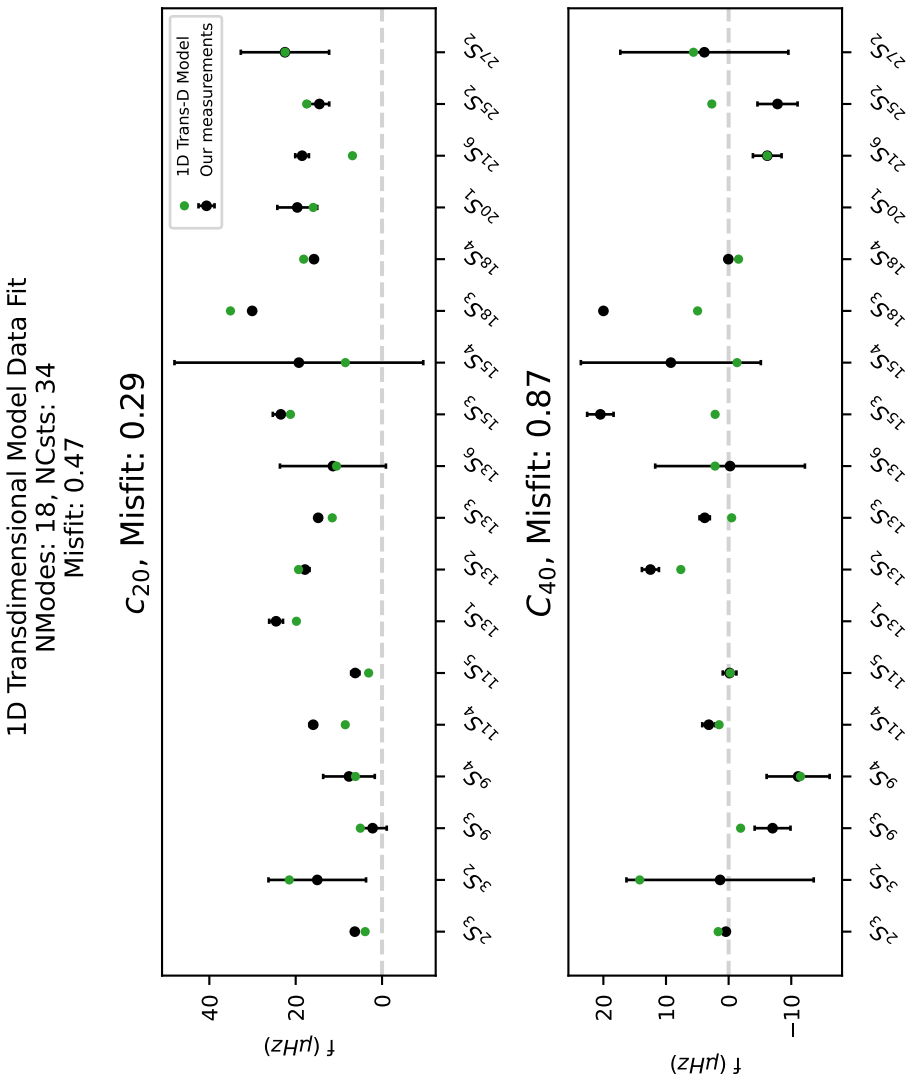

Figure 6.6 A comparison between our c_{20} and c_{40} measurements and the predicted values from our 1D transdimensional model shown in green.

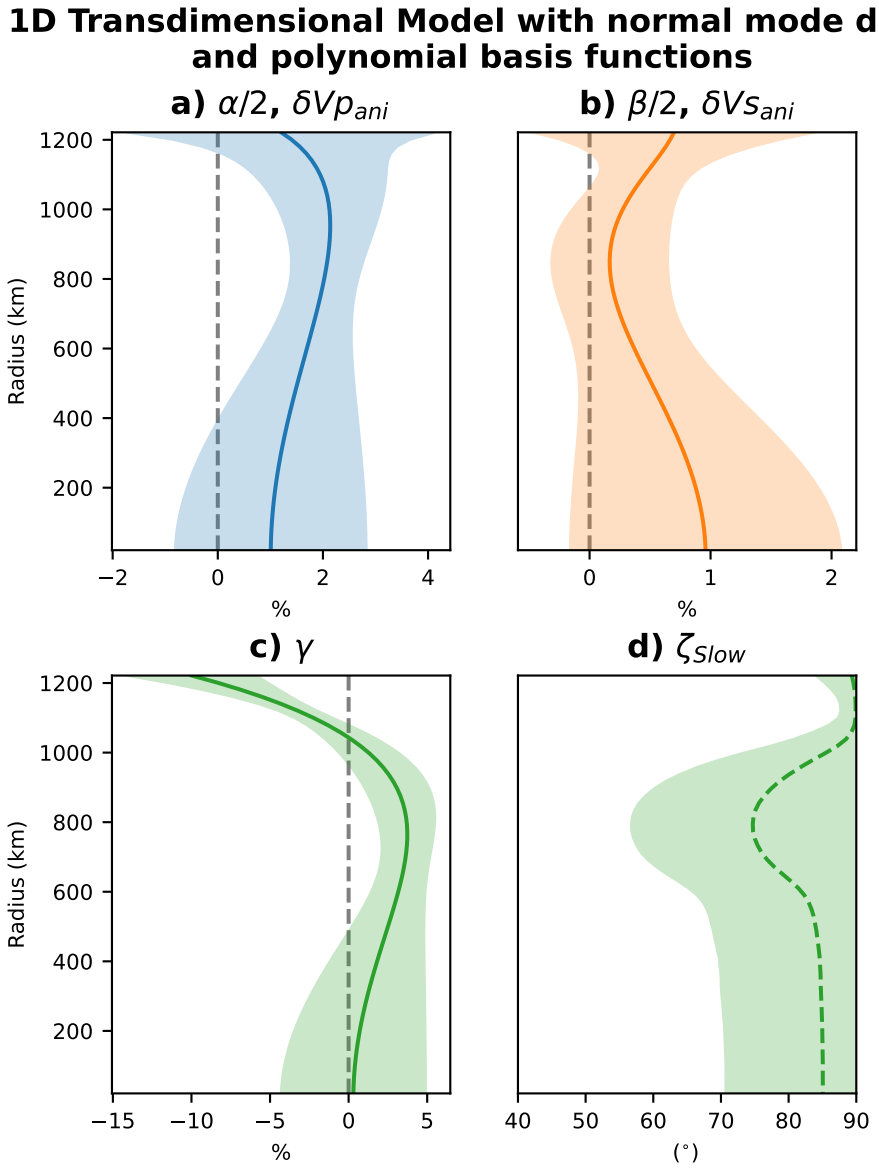

Figure 6.7 Variations throughout the inner core of δVp_{ani}, δVs_{ani}, γ and ζ_{slow} from our 1D Transdimensional model.

mal mode model uses α, β and γ (Chapter 2). There are two parameters which are common to both models that we can readily compare: the P-wave anisotropy, $\delta \mathrm{Vp}_{ani}$, ($\delta \mathrm{Vp}_{ani} = b + c = \frac{\alpha}{2}$) and ζ_{slow} between each model.

When looking at the models in cross section (Figure 6.8) it appears at first that the two models are very different. The maximum value of Vp_{ani} in the body wave model is 7.2% while it is only 2.1% in the normal mode model. However, if we compare the normal mode model with a spherical average of the body wave model (Figure 6.9a) we see there is good agreement for Vp_{ani} between the two models throughout the inner core. The average Vp_{ani} structure from the normal mode model is always within the uncertainty of the body wave model.

Both models find a deviation of ζ_{slow} away from 90°, however the body wave model finds the ζ_{slow} anomaly to be deeper and stronger than in the normal mode model (Figure 6.9b). This could be due to the differences in sensitivity between the normal modes and body waves, as inspection of Figures 6.2-6.3 reveals that the normal modes have minimal sensitivity below 400 km radius.

6.4 Discussion

An optimal 1D parameterization is difficult for normal modes in the inner core. We chose to use polynomials with a dependence of r^n where n is an even integer. This parameterization follows from similar models by Woodhouse *et al.* (1986) and Mäkinen *et al.* (2014). It has the advantage that the gradient of the model parameters at the centre of the inner core is always 0, which is a logical condition to meet as the centre of the inner core in our 1D model represents a single point. It is also the reason for the main difficulty of using other 1D parameterizations such as splines; as it is difficult to construct a spline parameterization with this zero gradient condition. The disadvantage of using the polynomial parameterization is that these basis functions are much less sensitive to the centre of the inner core than to the ICB. Furthermore, each polynomial coefficient has significant overlap in sensitivity with every other polynomial coefficient. Improving the choice of basis function and parameterization in our 1D models for the inner core is a step we wish to take in the future and the reason why this chapter is considered preliminary.

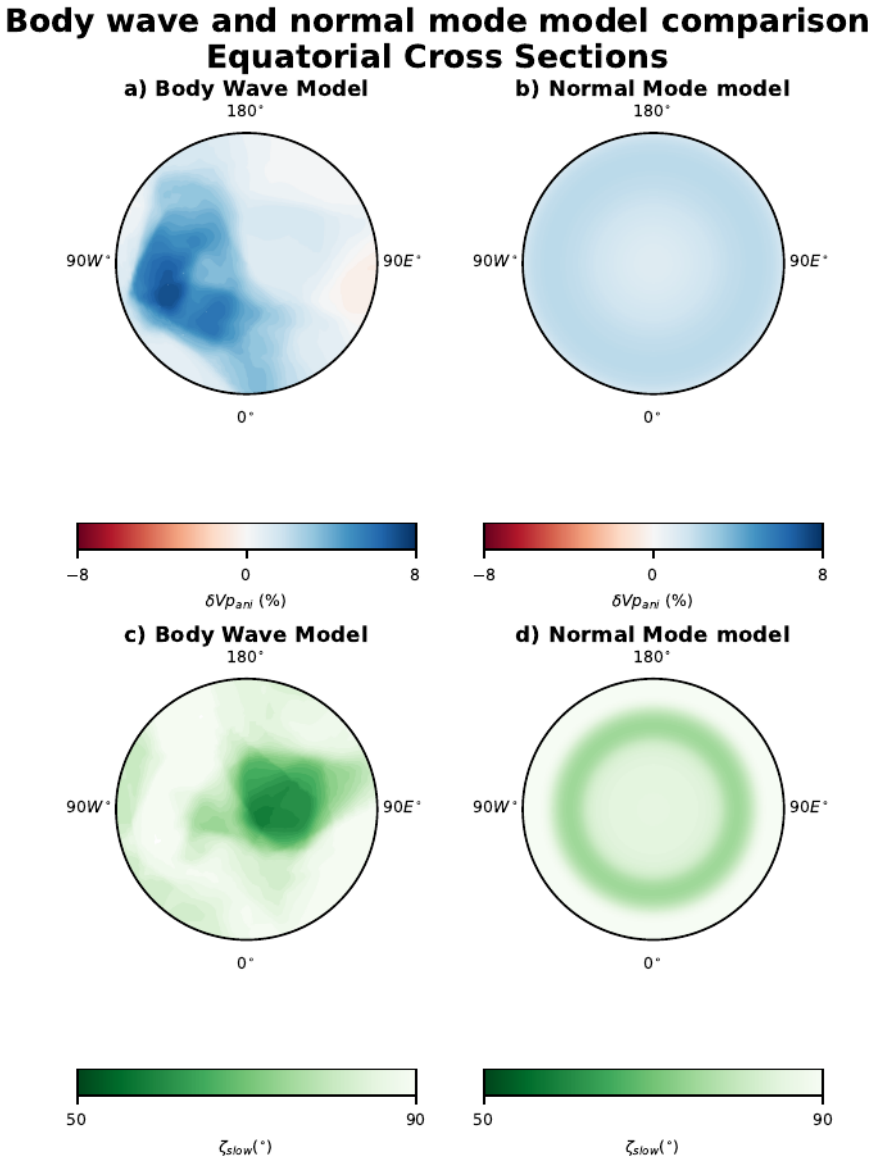

Figure 6.8 Equatorial cross sections showing δVp_{ani} and ζ_{slow} for the body wave and normal mode models.

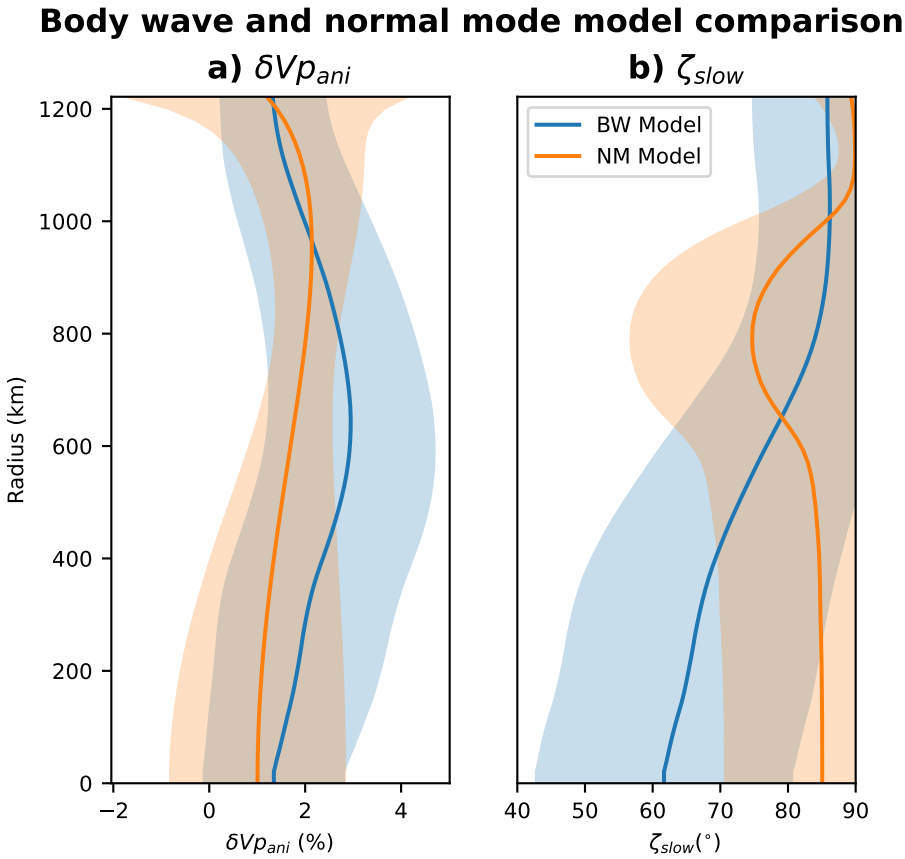

Figure 6.9 Radial variations δVp_{ani} and ζ_{slow} for the body wave and normal mode models. The body wave model was averaged to transform it to a 1D model.

6.5 Conclusion

In this chapter we use the splitting functions of 18 inner core sensitive normal modes which we measured in Chapter 5 and combine them with a transdimensional methodology utilising polynomial basis functions to construct a probabilistic 1D model of inner core P-wave and S-wave anisotropy. Our normal mode data can be fitted reasonably well by a model with 1.6% P-wave anisotropy and 0.5% S-wave anisotropy. Our normal mode model is also in good agreement with our body wave model from Chapter 4 especially for the magnitude of the 1D P-wave anisotropy structure and when considering that the normal mode model is 1D and the body wave model is 3D. The normal mode model also shows a change in ζ_{slow} with depth which may correspond to the IMIC, but this anomaly has a high uncertainty and its details have to be weighed against the low sensitivity of the modes to the centre of the inner core.

7

3D Transdimensional seismic tomography of the inner core using body waves and normal modes (preliminary)

In this chapter we outline a new methodology to incorporate normal modes and body waves in a joint 3D transdimensional tomographic model. This is the first time that transdimensional methods have been used jointly with normal mode and body wave data. The methodology to calculate the derivatives and sensitivity kernel for a normal mode splitting function coefficient to a Voronoi cell parameterization is described in full and can be adapted in future to calculate the sensitivity of other discrete basis functions. Fitting both types of data in a joint inversion requires compromises. To reduce trade offs, we only solve for compressional velocity anomalies in the inner core, assuming a constant background shear wave anisotropy model. We also exclude 5 modes from our normal mode dataset which we were unable to fit jointly with the body wave data. With these caveats, however it is possible to fit both our normal mode and body wave data with a single anisotropy model. Preliminary results show remarkably similar structures in compressional anisotropy for our body wave only model, including an isotropic layer at the top of the inner core, and an anisotropic zone isolated to the west and north of the inner core from 100 km depth and below. However, we now observe a more complex variations in slow direction, ζ_{slow}, which is the angle between the slowest velocity direction and Earth's axis of rotation and is often interpreted as indicative of an inner most inner core. This heterogeneous structure spread across both hemispheres, and also present at shallower depth, in contrast to our body wave model which

found a distinct homogeneous region with anomalous ζ_{slow} only near the centre of the inner core.

7.1 Introduction

In Chapter 3 we looked at increasing the quantity and quality of body wave travel time observations for constraining inner core anisotropy and in Chapter 4 we used these observations to create a 3D model of inner core anisotropy. In Chapter 5 we measured inner core sensitive normal modes using a grid search methodology to map out the splitting function model space and in Chapter 6 we produced a 1D model of inner core anisotropy using the normal mode data. In this chapter we are going to present preliminary results combining both normal mode and body wave data into a joint inversion model. This is an interesting challenge as each data type has overlapping yet different sensitivities; this is also why the approach of combining them could be valuable, where each data type makes up for the shortcomings of the other.

The last joint inversion for both body wave and normal mode data for inner core anisotropy was conducted by Ishii *et al.* (2002a). The fact that this study was published 20 years ago, is a testament to how difficult it is to reconcile the two types of data. Most normal mode studies invert for normal mode data only (Woodhouse *et al.* (1986); Tromp (1993); He and Tromp (1996); Deuss *et al.* (2010); Mäkinen *et al.* (2014)) and then make a prediction for body wave data to aid comparison, while most body wave studies don't compare their final models with normal mode data at all (Creager (1992); Tanaka and Hamaguchi (1997); Garcia (2002); Waszek and Deuss (2011); Frost *et al.* (2021)). Ishii *et al.* (2002a) was a pioneering study, combining PKPbc-PKPdf, PKPab-PKPdf, absolute PKPdf body wave travel times with 123 spheroidal and 42 toroidal modes measured by multiple groups. A majority of these modes are sensitive to the mantle, so Ishii *et al.* (2002a) also incorporated 1D mantle structure in their model. They found that radially varying anisotropy was able to fit the modes and absolute PKPdf body wave data simultaneously with 1.75% P-wave anisotropy and 0.44% S-wave anisotropy on average, and in general with anisotropy decreasing from the ICB to the centre of the inner core. Nevertheless, they also found that the differential travel time data and normal modes were difficult to reconcile with each other.

In a follow up paper, Ishii *et al.* (2002b) produce laterally varying models which fit the differential travel time data and do not contradict the normal modes. They found that an isotropic layer at the top of the inner core did

not fit their body wave data and that if there was an isotropic layer it would have to be less than 150 km thick to fit their normal mode measurements. They also argued that hemispherical variations in the body wave data could be an artefact of imperfect sampling of the inner core and pointed out that the hemispherical pattern could also be explained by a north-south divide instead of an east west divide. 20 years later and these findings remain robust; with more data we do see a western anisotropic zone with a north-south and east-west divide. Furthermore, an isotropic layer of less than 150 km thick at the top of the inner core is within current estimates from body wave models.

In our approach we will solve for inner core anisotropy in 3D using a Transdimensional MCMC methodology, utilising 13 splitting function measurements described in Chapter 5 and the body wave data used when conducting a transdimensional inversion in Chapter 4. The normal mode data is sensitive to long wavelength structure in the inner core, specifically to P-wave and S-wave anisotropy. If we assume that the anisotropy symmetry axis is Earth's axis of rotation, then only the zonal parameters are sensitive to this anisotropy. This means that normal modes will give us the variation in elastic parameters in the inner core as a function of radius but no regional variation. Body waves on the other hand are short wavelength (0.5 - 2 Hz) observations which are sensitive primarily to P-wave anisotropy in the inner core, and unlike the normal modes are able to provide us with regional variation of inner core anisotropy. In effect normal modes will constrain the average radial pattern in anisotropy and body waves will provide regional 3D information.

In this chapter, we will first describe our choice of data and justify our use of a constant background S-wave anisotropy model, then we will describe our inverse problem, and how we calculate the sensitivity of normal mode splitting function coefficients to Voronoi cells. Finally, we will show the preliminary results from our transdimensional inversion and discuss what can be improved in the future.

7.2 Data

We use the same body wave observations as in Chapter 4, but with a small alteration. Our combined model needs to use PREM (Dziewonski and Anderson, 1981) as a reference model instead of AK135 (Kennett *et al.*, 1995), because only PREM is able to fit the normal mode data while also fitting the body wave data. The drawback is that PREM only predicts PKPbc arrivals up to 152° epicentral distance, while AK135 predicts PKPbc up to

155.5° and our data set contains 541 PKPbc-PKPdf differential travel times with an epicentral distance between 152-155.5°. Thus, for these paths we do not get a prediction from PREM for the PKPbc arrival time. To solve this problem these raypaths are now included in the absolute PKPdf dataset instead. This results in a total dataset of 7668 raypaths, with 3103 PKPcd-PKPdf, 1060 PKPbc-PKPdf, 640 PKPab-PKPdf and 2865 absolute PKPdf raypaths. This is 11 raypaths less than in Chapter 5 because we found that 11 of the raypaths that were formerly measured relative to PKPbc contained strong mantle influence (See Section 4.2), which could not be accounted for without a reference phase.

We use 13 of our 18 normal mode measurements from Chapter 5 as our normal mode dataset. Through initial modelling and testing we found that we were not able to reconcile the body wave data with the splitting function coefficients for modes; ${}_3S_2$, ${}_9S_3$, ${}_9S_4$, ${}_{25}S_2$ and ${}_{27}S_2$. Figure 7.1 shows predictions for our normal mode data from our body wave model developed in Chapter 4. While most modes are well fit by our body wave model, the five modes ${}_3S_2$, ${}_9S_3$, ${}_9S_4$, ${}_{25}S_2$ and ${}_{27}S_2$ are not well fit, especially for c_{40} (Figure 7.1b), and account for 53% of all the misfit. As we cannot fit both the body waves and these 5 modes, the question then becomes whether the measurement of these modes is at fault or if there is structure in the inner core or elsewhere we are not correctly accounting for? This problem requires further study. Potentially the incorporation of more modes will inform us as to whether these modes are poorly measured or if their is some common structure they are sensitive to which we are not correctly accounting for, in or outside of the inner core. For simplicity we have chosen to simply remove these modes from our current preliminary model.

7.3 Methodology

7.3.1 Transdimensional Markov Chain Monte Carlo

As in Chapter 4 and Chapter 6 we will utilise a Transdimensional Markov Chain Monte Carlo (MCMC) methodology (Bodin and Sambridge, 2009). The details of this method can be found in Chapter 4, but in summary: transdimensional MCMC is a sampling methodology, which solves not only for the best fitting model parameters but also incorporates the parameterization of the model space into the inversion. This involves creating a Markov chain of models where each model is a small perturbation on the previous model, this perturbation can either be in the velocity characteristics of sub volumes, or by the addition, removal or movement of these sub volumes. Perturbations which decrease the misfit to the data will always

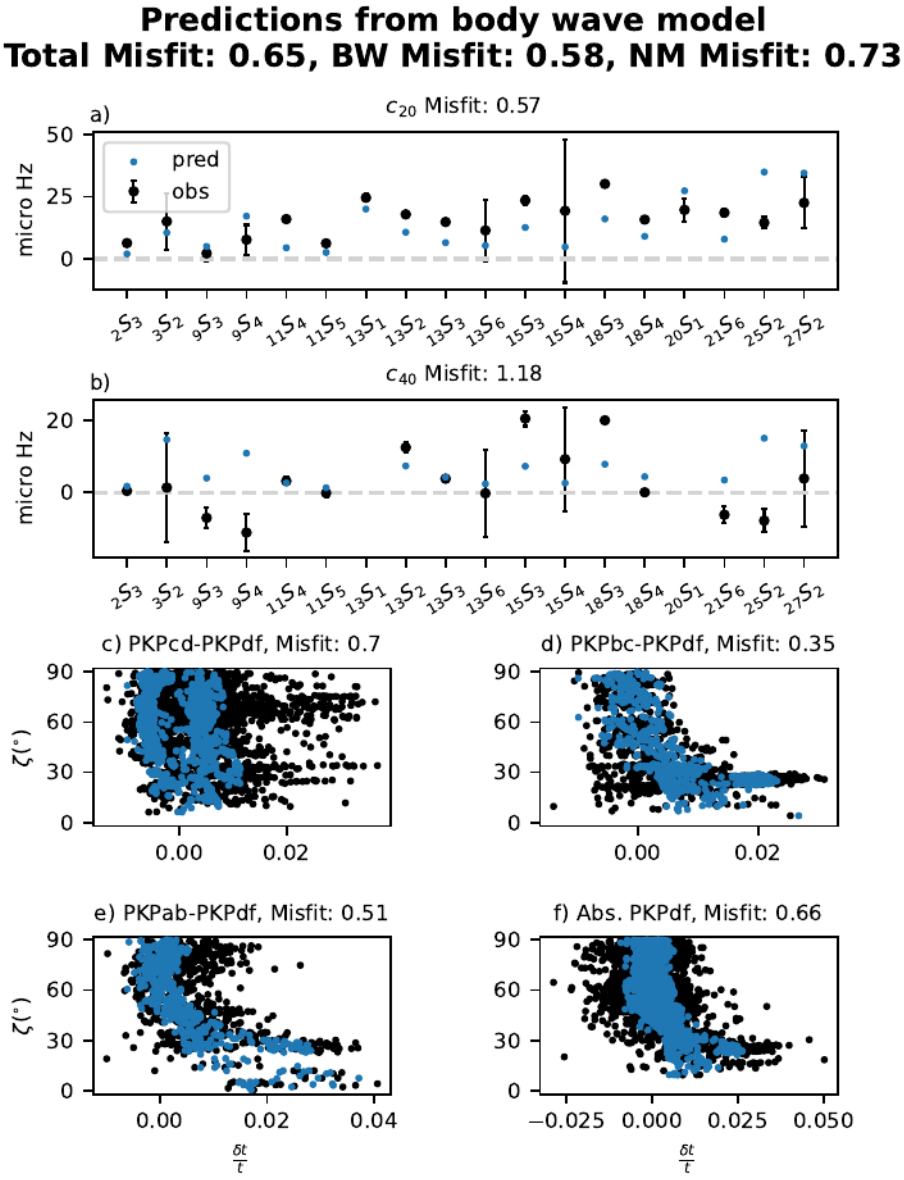

Figure 7.1 Predictions for our normal mode dataset (a-b) and (c-f) body wave dataset using our body wave model, made in Chapter 4.

be accepted, while perturbations which increase the misfit to the data will either be accepted or rejected following the Metropolis-Hastings algorithm (Hastings, 1970). In this way we explore the model space and sample the posterior probabilities of our model parameters and parameterization.

We also use hierarchical noise sampling (explained in detail in Section 4.4.3) which produces an estimate of the noise in our data by analysing the contradictions between groups of data with the same sensitivity. This can be most intuitively understood by imagining two differential travel times, whose PKPdf raypaths travel exactly the same path in the inner core and therefore have the same sensitivity. Any difference in the differential travel times between these two data points will then be interpreted as noise and increase the hierarchical parameter. We combine the hierarchical noise parameter with estimates of the noise from mantle structure for the body wave data (Section 4.2) and with estimates of uncertainty from the grid searches for the normal mode data (Section 5.4).

7.3.2 Combined inner core anisotropy from body waves and normal modes

Combining the body waves and the normal modes into a joint tomographic inversion is an interesting challenge. The body waves provide good constraints on regional variations in anisotropy while the normal modes provide valuable information on average structure to constrain the velocities in regions of the inner core without any body wave observations. Body waves are only sensitive to V_p while normal modes are sensitive to V_p and V_s. However, one of the problems is that once we start incorporating transverse isotropy, we also see that the fractional travel time of the P-wave observations are non-uniquely sensitive to S-wave anisotropy, which can be seen in the following equation (derived in Section 2.2, Equation 2.19):

$$\delta V_p = \delta V_{eq} + \frac{1}{2}\alpha\cos^4(\zeta) + 2\beta[\cos^2(\zeta) - \cos^4(\zeta)] + \gamma[\cos^4(\zeta) - \cos^2(\zeta)] \quad (7.1)$$

where δV_{eq} is the deviation of compressional equatorial velocity from a reference model. δV_{eq} was called a in Chapters 3-4; we have renamed it to δV_{eq} in this chapter to avoid confusion with α. α is the compressional wave anisotropy, β is the shear wave anisotropy and γ is the velocity of waves travelling at angles between the symmetry axis and the perpendicular plane.

It can be seen from Equation 7.1 and Figure 7.2 that the body wave sensitivity to β trades off with γ. This means that with only body wave information we do not separately resolve variations in β and γ. The normal

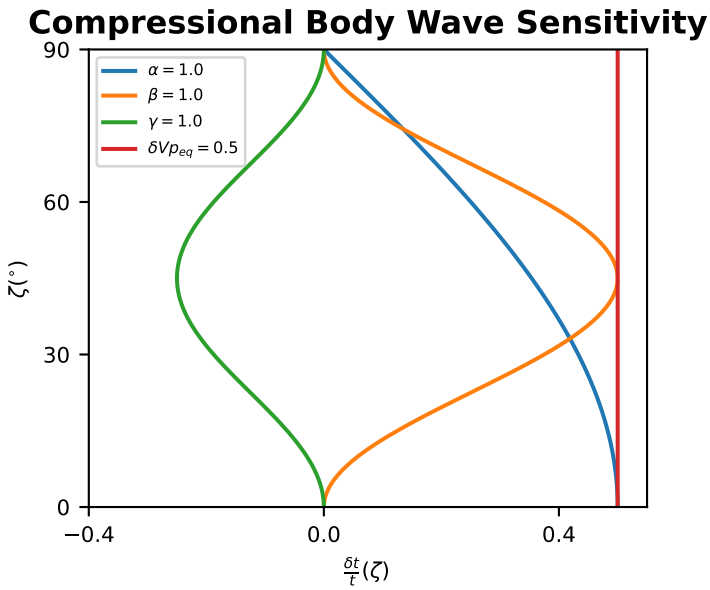

Figure 7.2 The change in $\frac{\delta t}{t}$ for compressional waves as a function of ζ due to the model parameters δV_{eq}, α, β and γ, if $\delta V_{eq} = +0.5$, $\alpha = 1.0$, $\beta = 1.0$ and $\gamma = 1.0$,

modes have independent sensitivity to β and γ, because the zonal coefficients, c_{20} and c_{40}, are related to α, β and γ:

$$c_{s0} = \int_0^{ICB} \alpha(r)K_s^{\alpha} + \beta(r)K_s^{\beta} + \gamma(r)K_s^{\gamma} dr \tag{7.2}$$

However, when only using the c_{20} and c_{40} coefficients the normal modes do not have sensitivity to 3D variations in α, β and γ and are only sensitive to the 1D average and may only provide depth (or radial) variations.

To avoid a trade off between γ and β we have decided to use the mean model of β from Chapter 6 in our joint inversion and only solve for δV_{eq}, α and γ. This means that for every iteration in the MCMC inversion our model of β is constant. In future work we will allow 1D β vary in the inversion but for now it was easiest to keep β constant. Ideally we would also have wide spread observations of S-wave body wave observations in the form of PKJKP arrivals from which we could constrain β on a regional basis and incorporate it as a fully 3D parameter in our model, but reliable observations of PKJKP arrivals are sparse (Deuss *et al.* (2000); Cao *et al.* (2005); Wookey and Helffrich (2008)). Perhaps coda-correlation methods in the future will help constrain some regional variations of S-wave anisotropy (Wang and Tkalčić, 2021). Likewise, incorporating measurements of cross-coupled inner core modes could also provide constraints on the 3D variations in α, β and γ.

Figure 7.3 shows predictions for our normal mode and body wave data, using only the values of β from our normal mode model, with $\alpha = 0.0$ and $\gamma = 0.0$. It can be seen that it mainly affects P-waves at intermediate angles around $\zeta = 45°$ and improves misfit to our data overall, but increases misfit with respect to the c_{40} values of our splitting function data. Interestingly, the negative c_{40} values are fit very well using only β. In our normal mode only model from Chapter 6 the fit to the positive c_{40} values was compensated for by α and γ.

7.3.3 The forward problem

We will solve for 3D variations in δV_{eq}, α and γ, with both normal mode and body wave data. We will use Voronoi cells as our basis functions as that will allow us to rapidly discretise a 3D domain and conduct a transdimensional inversion. In Section 7.3.4 we will explain how to calculate the sensitivity of a normal mode splitting function coefficient to a Voronoi cell parameterization.

To define the forward problem lets first consider a simple scenario, where we have one differential travel time, δt, and one c_{st} as our data and we want

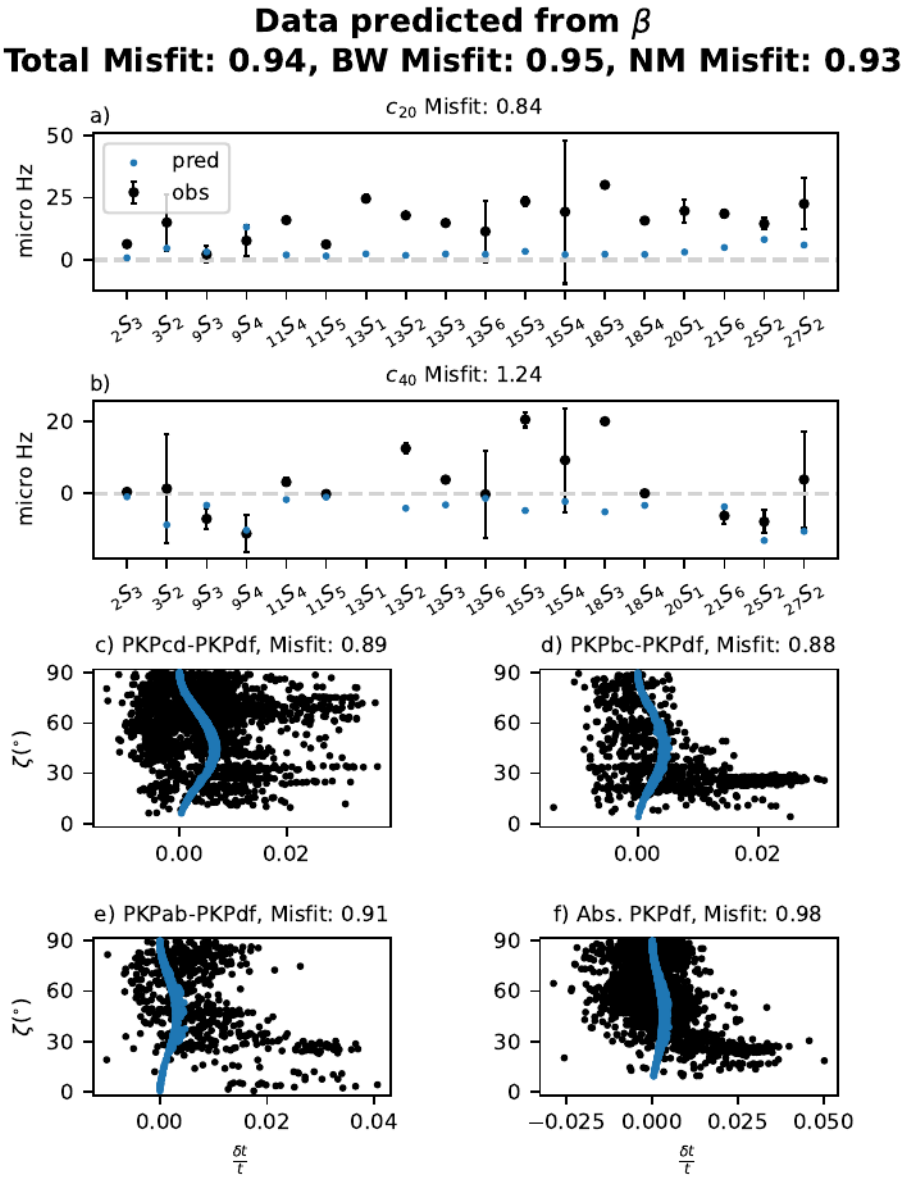

Figure 7.3 Our combined dataset compared to the predictions on each data point from β in the model derived in Chapter 6.

to construct a forward problem with one Voronoi cell of the form:

$$\mathbf{Gm} = \mathbf{d} \tag{7.3}$$

the data matrix is simple:

$$\mathbf{d} = \begin{pmatrix} \delta t \\ c_{st} \end{pmatrix} \tag{7.4}$$

and for one Voronoi cell the model matrix is thus;

$$\mathbf{m} = \begin{pmatrix} \delta V_{eq} \\ \alpha \\ \gamma \end{pmatrix} \tag{7.5}$$

The sensitivity kernel $\mathbf{G}$ can be separated into two parts, the body wave sensitivity, $\mathbf{G}_{bw}$ and the normal mode sensitivity, $\mathbf{G}_{nm}$. To calculate $\mathbf{G}_{bw}$ we separate the δV_{eq}, α and γ terms from Equation 7.1 and find the sensitivity of a raypath to each model parameter as a function of the raypaths' angle ζ;

$$\mathbf{G}_{bw} = \begin{pmatrix} A_{ij}t, & A_{ij}\frac{1}{2}\cos^4(\zeta)t, & A_{ij}[\cos^4(\zeta) - \cos^2(\zeta)]t \end{pmatrix} \tag{7.6}$$

such that the first, second and third columns correspond to the sensitivity of a raypath to the δV_{eq}, α and γ model parameters in the model matrix $\mathbf{m}$, A_{ij} is the fraction that raypath i spends in Voronoi cell j, in our scenario with one raypath and one Voronoi cell then $i = 1$ and $j = 1$ and $A_{ij} = 1.0$. As in Chapter 4 we move the reference inner core time, t from the left hand side of Equation 7.1 to the right hand side.

7.3.4 c_{st} sensitivity to Voronoi cells

Parameterizing spherical harmonic data using Voronoi cells is complicated, but we came up with an elegant solution. The sensitivity kernel of a spherical harmonic coefficient c_{st} to a Voronoi cell is denoted as $\mathbf{G}^{st}_{nm}$ where s and t is the angular order and azimuthal order of the c_{st} and nm denotes that it is a normal mode sensitivity (as opposed to $\mathbf{G}_{bw}$). The sensitivity kernel of a c_{st} varies as a function of radius. Calculating the sensitivity of a Voronoi cell to a c_{st} involves calculating the radial sensitivity of a Voronoi cell, R. The radial sensitivity R is how much a Voronoi cell occupies a particular radius or 'layer' of the inner core. The c_{st} sensitivity kernels are smooth functions (see Figures 6.2-6.3), which we discretise into N_k layers throughout the inner core. To calculate the radial sensitivity of a Voronoi cell to a c_{st} we have to calculate the fraction that a Voronoi cell makes up of a layer

k. We use a Fibonacci sphere (González, 2010) to define for each layer k, a mesh of N_p points which are equally spaced[1]. As the points are equally spaced they each represent the same $\frac{1}{N_p}$ proportion of the layer k. We can determine for each node on the mesh which Voronoi cell (denoted by j) contains that node and the number of nodes per Voronoi cell is proportional to its radial sensitivity R_{kj}.

This process is best understood graphically as outlined in Figure 7.4. Figure 7.4a shows for a single layer a Voronoi cell distribution, with each node location chosen at random. We then produce a mesh of (approximately) equally spaced points on this layer using a Fibonacci sphere algorithm and determine which nodes are contained in each Voronoi cell in this mesh, as shown on Figure 7.4b. We then count the number of nodes in each Voronoi cell, which is proportional to how much a Voronoi cell makes up a specific layer. This number then provides us with the fraction of each Voronoi cell, shown on Figure 7.4c, where it is clear that Voronoi cells which make up more of this layer in Figure 7.4a have a higher radial fraction. This process is then repeated for each layer, corresponding to the layers that we used to discretise K_s^α, K_s^β and K_s^γ (Equation 6.1).

We combine the radial sensitivity and the sensitivity kernel of a given c_{st} to α or γ in the following way:

$$K_\alpha^j = \sum_{k=1}^{N_k} R_{kj}\kappa_k^\alpha \tag{7.7}$$

$$K_\gamma^j = \sum_{k=1}^{N_k} R_{kj}\kappa_k^\gamma \tag{7.8}$$

where the index j stands for a individual Voronoi cell, k is the index for each layer that the sensitivity kernels are calculated. The sensitivity of one c_{st} to one Voronoi cell with δV_{eq}, α and γ model parameters is given by:

$$\mathbf{G}_{nm} = \begin{pmatrix} 0 & K_\alpha^j & K_\gamma^j \end{pmatrix} \tag{7.9}$$

We then combine both $\mathbf{G}_{bw}$ and $\mathbf{G}_{nm}$ to form a single forward problem

$$\mathbf{G} = \begin{pmatrix} A_{ij}t & A_{ij}\frac{1}{2}\cos^4(\zeta)t & A_{ij}[\cos^4(\zeta) - \cos^2(\zeta)]t \\ 0 & K_\alpha^j & K_\gamma^j \end{pmatrix} \tag{7.10}$$

[1]This is an approximation, the points are not perfectly equally spaced, but with increasing N_p the error becomes minimal relative to the number of Voronoi cells. In our algorithm we ensure that there are three orders of magnitude more points on the mesh than the number of Voronoi cells.

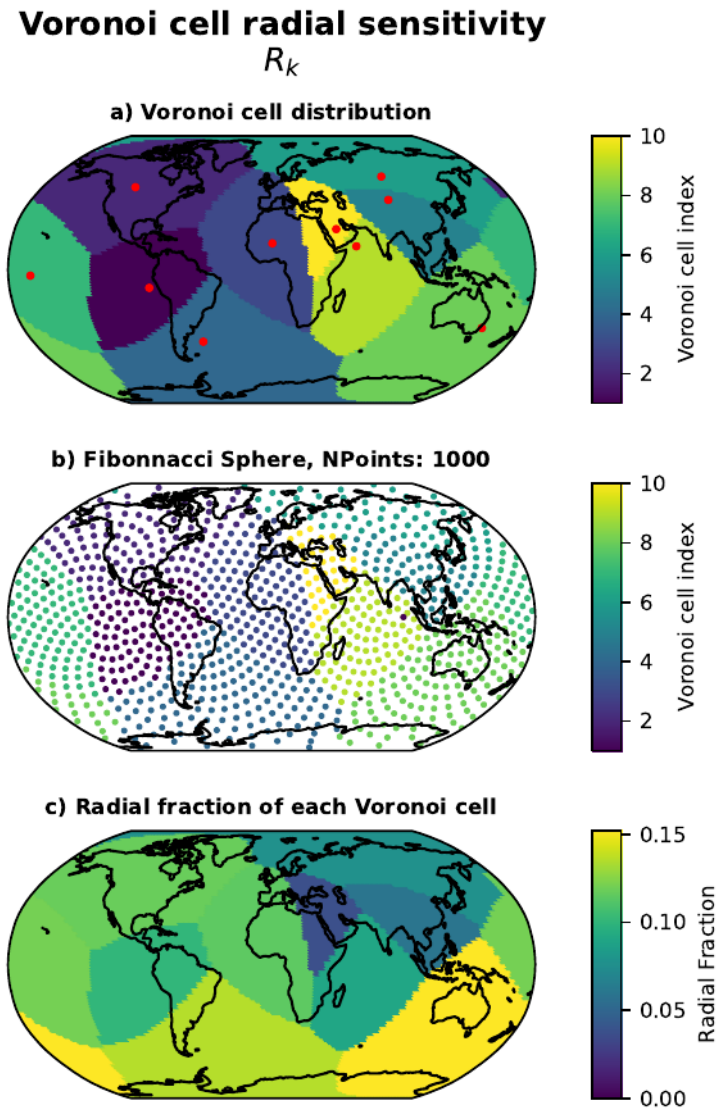

Figure 7.4 a) Explanation of the calculation of c_{st} sensitivity using Voronoi cells, showing for R_{kj} a single layer of a Voronoi cell distribution, b) a Fibonacci sphere mesh where colour indicates which Voronoi cell contains each node and c) the fraction that each Voronoi cell makes up of this layer.

$$\mathbf{m} = \begin{pmatrix} \delta V_{eqj} \\ \alpha_j \\ \gamma_j \end{pmatrix} \tag{7.11}$$

$$\mathbf{d} = \begin{pmatrix} \delta t \\ c_{st} \end{pmatrix} \tag{7.12}$$

This forward problem is easily expanded to more Voronoi cells or non zonal normal mode c_{st} data having longitudinal variation such as hemispheres from cross-coupled modes (Deuss *et al.*, 2010).

7.4 Results

We run 20 Markov chains for 1,000,000 iterations, which after burn in and thinning results in an ensemble of 133,380 models. The average misfit of the models in our ensemble is 0.54 (Figure 7.5a) which corresponds to a 46% misfit reduction compared to our reference model PREM. The number of Voronoi cells required to fit the data ranges from 15 to 28 volumes across all our chains. This number represents a range of differently dimensioned models from which we derive the mean and standard deviation of our model parameters throughout the inner core. As in Chapter 6 we use Gaussian priors on our model parameters, with a mean of 0.0 and a standard deviation of 0.2.

Inspection of Figures 7.5c-d and Table 7.1 reveals that the mean combined hierarchical noise estimate for the body waves is 0.23s for PKPcd-PKPdf, 0.55s for PKPbc-PKPdf, 1.21s for the PKPab-PKPdf and 0.97s for the absolute PKPdf data and 5.0μHz for the normal modes. In Table 7.1 we see that the noise in our combined model for the body waves is very similar to the noise from our body wave only model. Our combined model has a lower noise estimate for the PKPcd-PKPdf and PKPbc-PKPdf data and a higher noise for the PKPab-PKPdf and absolute PKPdf data. This difference can be attributed to two reasons. Firstly, a significant portion of the PKPbc-PKPdf data from Chapter 4 is now incorporated as absolute PKPdf data, which decreases the PKPbc-PKPdf noise estimate (as there is less disagreement between raypaths) and correspondingly increases, the noise estimate for the absolute PKPdf data. Secondly, the combined model is now also trying to fit the normal modes which will have a knock-on effect by making it more difficult to simultaneously fit the body wave data. The noise in the normal mode data is less in our combined model (4.8μHz) than in our normal mode only model (8.3μHz), but this is due to the fact that we

Data	Body wave model	Normal mode model	Combined model
PKPcd-PKPdf	0.29s	-	0.23s
PKPbc-PKPdf	0.63s	-	0.53s
PKPab-PKPdf	0.95s	-	1.21s
Abs. PKPdf	0.96s	-	0.97s
Normal Modes	-	8.3μHz	4.8μHz

Table 7.1 Comparison of the recovered hierarchical noise estimate for each type of data for our body wave only model (developed in Chapter 4), our normal mode only model (Chapter 6) and our combined model.

have removed five modes, meaning that there is less disagreement between the normal mode data.

The average model from our ensemble reduces the misfit for the normal mode data by 67% and for the body wave data by 45% (relative to PREM) with an overall misfit reduction of 54% (Figure 7.6). The lower noise in the normal mode data also means that the combined model fits the normal mode data 11% better than our normal mode only model from Chapter 6. This is most likely because we have five normal modes less in our combined model which reduces the misfit significantly. We fit the c_{20} measurements better than the c_{40} measurements for all our normal modes, similar to our normal mode only model (Chapter 6). For comparison we also include in Figure 7.6 the predictions for the five modes ${}_3S_2$, ${}_9S_3$, ${}_9S_4$, ${}_{25}S_2$ and ${}_{27}S_2$, which were excluded from the inversion and misfit calculation. The 45% misfit reduction for our body wave data is the same as in our body wave only model (Chapter 4), which is encouraging as it implies that we are recovering as much information from the body waves in the combined model as the body wave only model.

Looking at the model in cross section and in maps (Figures 7.7-7.10) reveals heterogeneity in δV_{eq} and $\delta \mathrm{Vp}_{ani}$ which is similar to the body wave only model of Chapter 4. It is encouraging that the observations of inner core anisotropy from normal mode and body waves are not contradictory. We find a fast eastern hemisphere and slow western hemisphere in the upper inner core, with an anisotropic zone isolated to the northern hemisphere in the west, starting at $\sim$100 km below the ICB. The maximum magnitude of the anisotropy for the combined model is 11% which is greater than 7.2% in the body wave only model. The maximum magnitude of the equatorial velocity is 1.8% in the combined model, which is the same as in the body wave only model. The overall pattern of the heterogeneity is very similar

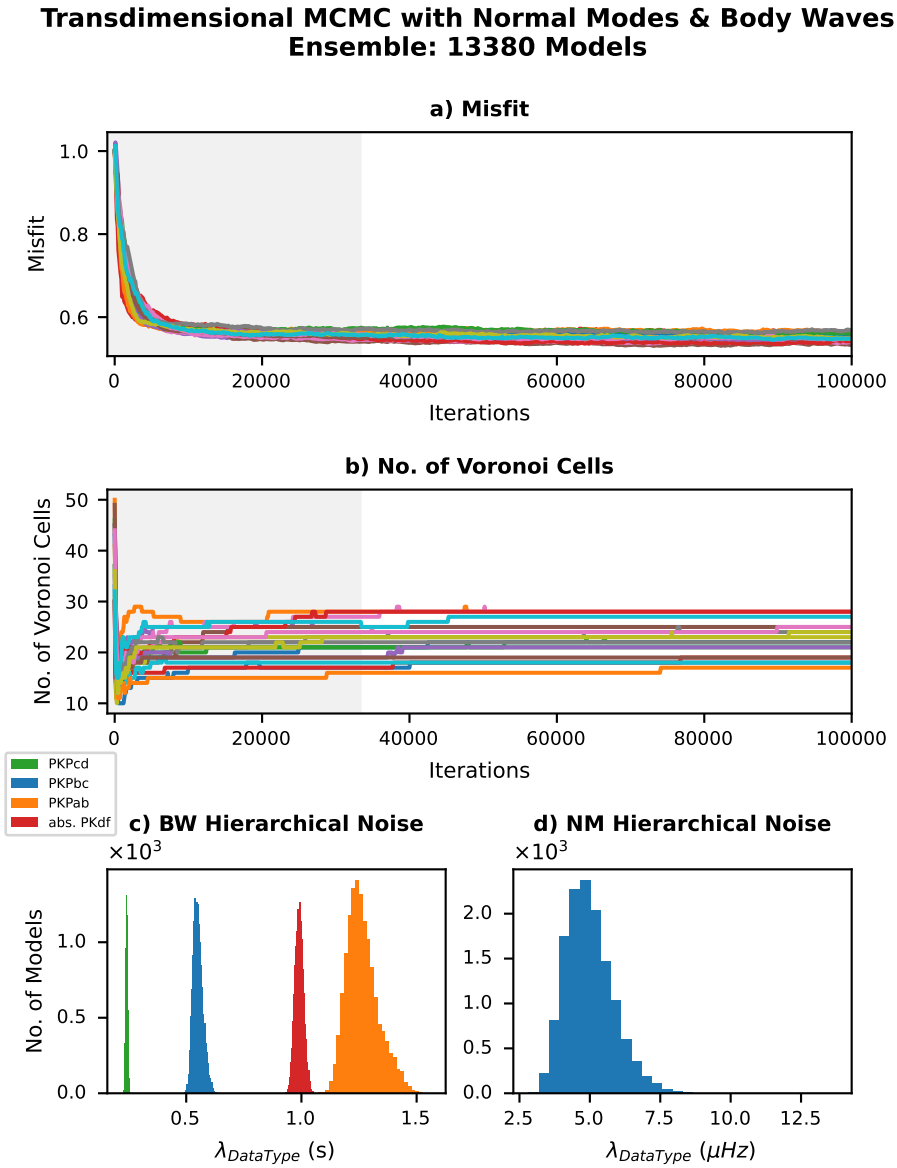

Figure 7.5 a) The variation of misfit with iteration in our Markov chains. b) The variation of the number of Voronoi cells in each chain with iteration. c) The total mean noise of our body wave data types across all models in our ensemble.

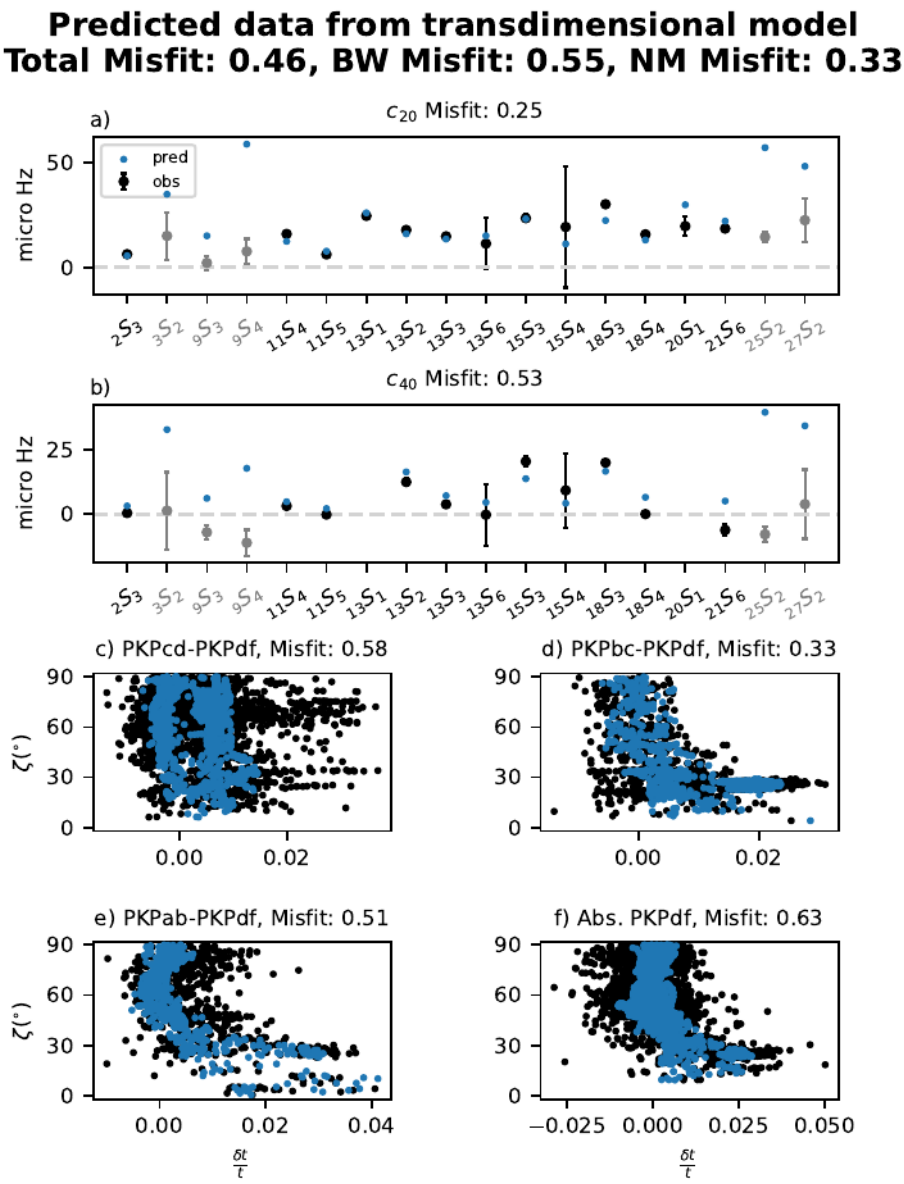

Figure 7.6 Predictions from our combined transdimensional model to our data, modes $_3S_2$, $_9S_3$, $_9S_4$, $_{25}S_2$, $_{27}S_2$ are shown but were not included in the inversion and are not used when calculating the misfit.

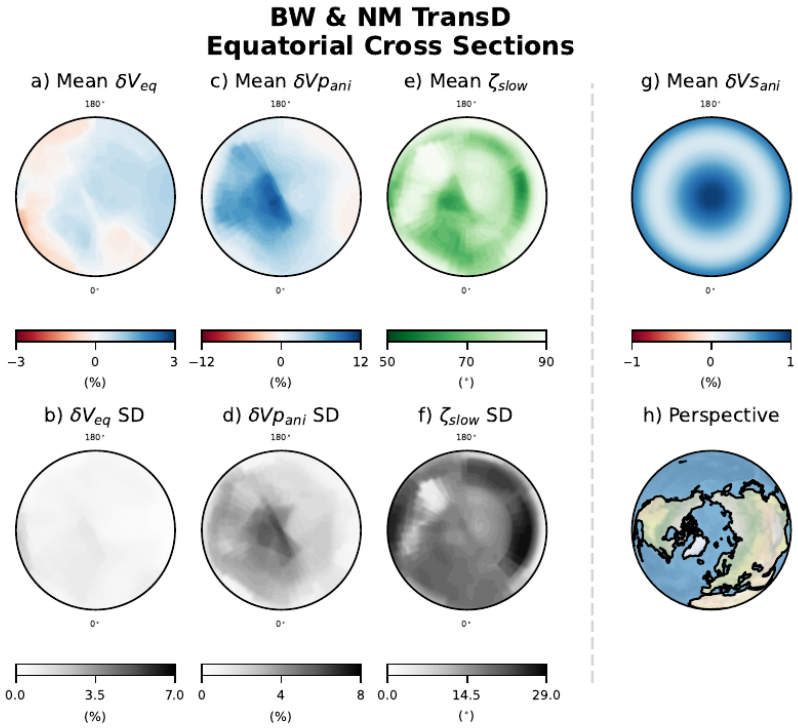

Figure 7.7 A cross section through our combined transdimensional model, going through the equator.

when comparing Figures 4.10-4.14 to Figures 7.7-7.10.

Our model for ζ_{slow} changes significantly with the inclusion of the normal mode data, with a more heterogeneous structure than in Chapter 4. There is still a region with a strong ζ_{slow} anomaly in the east of the inner core, but it is no longer only located near the centre of the inner core. ζ_{slow} is however, a difficult property to constrain and we believe that more research is needed to properly image and constrain this anomaly. Allowing 3D variations in the anisotropy symmetry axis away from Earth's axis of rotation might be the key to imaging this anomalous anisotropy region. Furthermore, we know that β influences the velocity of P-waves at intermediate angles and we have for simplicity used a constant background β model. However,we are certain that β varies throughout the inner core, and while it is not possible to constrain 3D β variations (Section 7.3.2), allowing the average 1D β model to vary as a part of the inversion will most likely improve our fit to these raypaths at intermediate angles and better constrain ζ_{slow}.

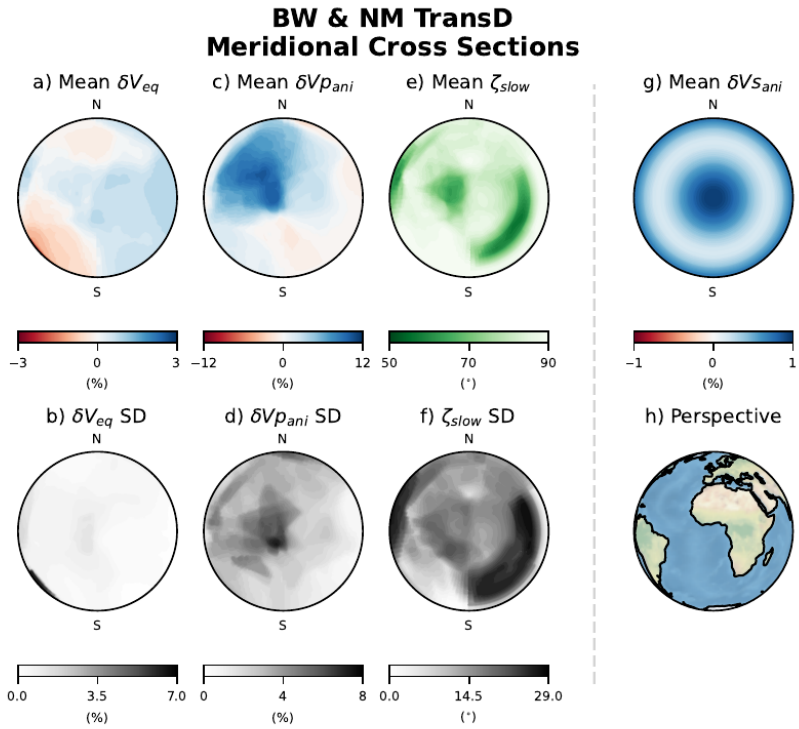

Figure 7.8 A cross section through our combined transdimensional model going through a meridian crossing between 90°W and 90°E and the poles.

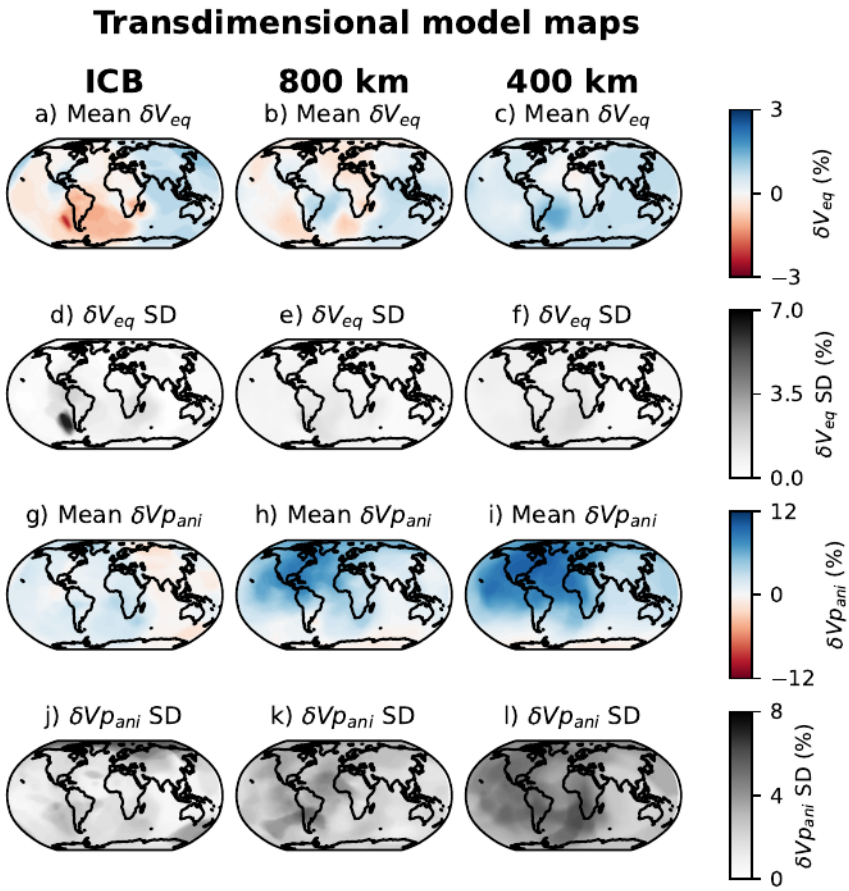

Figure 7.9 Maps showing variations in δV_{eq} and $\delta V p_{ani}$ throughout the inner core from our combined transdimensional model at the inner core boundary, 800 km radius and 400 km radius along with their uncertainties.

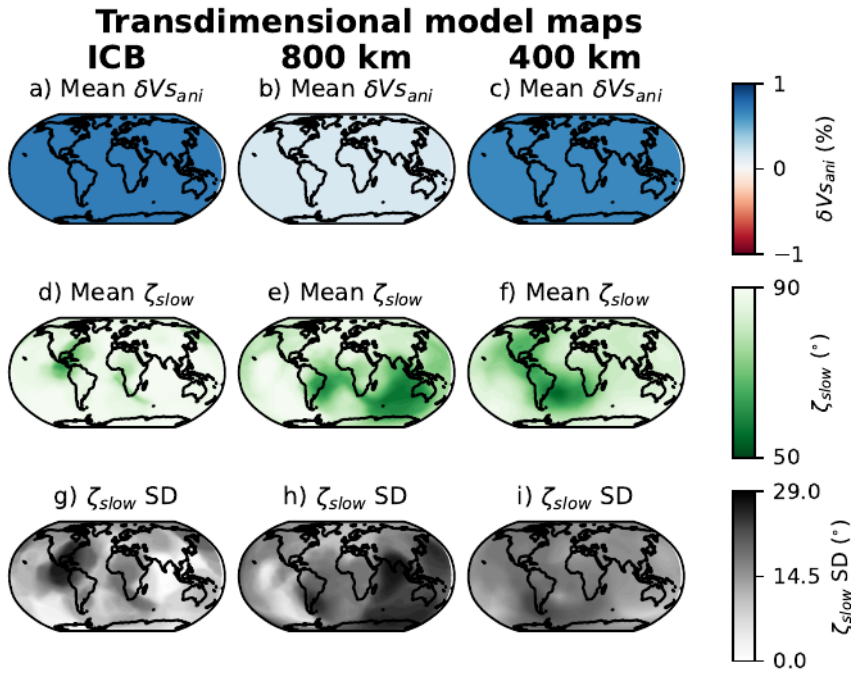

Figure 7.10 Maps showing variations in δVs_{ani} and ζ_{slow} throughout the inner core at the inner core boundary, 800 km radius and 400 km radius along with the uncertainty in ζ_{slow}.

7.5 Conclusion

We have conducted 3D transdimensional inversion of the inner core for a combined dataset of body wave and normal mode data and make a preliminary model of inner core anisotropy. Our methodology to calculate the splitting function sensitivity to a 3D Voronoi cell parameterization can easily be adapted to any discrete basis function and also be used to incorporate regional variations from normal mode data. We find that we are able to fit our body wave dataset and a subset of our splitting function zonal measurements providing we use a background β model to reduce trade offs.

Our preliminary model is similar to the body wave only model from Chapter 4 for the compressional equatorial velocity anomaly, (δV_{eq} or a in Chapter 4) and the compressional anisotropy (δV_{ani} in Chapter 4 or α in Chapter 6). We find a fast eastern hemisphere and slow western hemisphere in the upper inner core, with an anisotropic zone isolated in the northern hemisphere in the west, starting at $\sim$100 km below the ICB. There is also a region with a particularly strong ζ_{slow} anomaly in the east of the inner core, but it is no longer consistently located near the centre of the inner core. This anomaly previously called the IMIC requires further study. Our model is only preliminary, but we are confident that with the right approach it should be possible to reconcile the two ζ_{slow} anomalies as seen by the body wave and normal mode data.

8

Synthesis

The aim of this thesis was to better constrain the elastic structure of the inner core. To achieve this we first increased the number of observations of differential travel times, focusing especially on observations of paths which travel in ultra-polar directions (Chapter 3).

We then took these new observations and combined them with other travel time datasets to produce a 3D transdimensional model of inner core anisotropy (Chapter 4). This new approach allowed us to produce a high resolution 3D model along with the uncertainties in the model parameters. From this combination of novel methodology and new data we were able to robustly observe for the first time that the western anisotropic zone is in fact primarily located in the northern hemisphere. This result has important implications for our geodynamic understanding of the inner core. With the body wave data we also observe an inner most inner core (IMIC) which is primarily isolated in the eastern half of the inner core.

In Chapter 5 we then moved from short period body waves to long period normal modes and we started by improving the measurements of splitting functions of inner core sensitive modes. Especially the zonal coefficients c_{20} and c_{40} are strongly anomalous and their measurement heavily depends on starting values for c_{20} and c_{40} in the inversion. Thus, we conducted large grid searches systematically varying c_{20} and c_{40} for 18 modes using a self-coupled splitting function approximation. This method proved more complicated than we initially expected, yielding complex measurements with some modes having multiple misfit minima or large ranges of c_{20} and c_{40} values which fit the spectra equally well. We think these problems highlight something that has been seen before in the literature, that measuring inner core sensitive normal modes is far from simple.

Despite the complex nature of measuring these splitting functions, in Chapter 6 we used our new c_{20} and c_{40} measurements to produce a 1D transdimensional model of inner core anisotropy which significantly reduced

the misfit of our c_{st} measurements and agreed with the compressional anisotropy of the body wave model of Chapter 4.

In Chapter 7 we finally conducted 3D transdimensional inversion combining our body wave data with a subset of our normal mode data to produce a model which fits both data jointly. This model does come with some caveats however, for example we had to assume a 1D model of shear wave anisotropy because the body waves only provide 3D V_p variations and we had to remove 5 of our 18 measured normal modes to fit the normal modes and the body waves jointly. Because of these caveats we want to emphasise that the work in Chapter 7 is preliminary and we hope to explore this further in the future. But equally we feel it is still an achievement to produce a reasonable model of inner core anisotropy that significantly reduces the misfit of both the body wave and normal mode data. It has been said in previous studies that normal modes and body waves disagree on the magnitude of inner core anisotropy and while we don't pretend to have answered all the questions, we do think there is now reason to believe that is not the case. We find similar mean values of anisotropy in the inner core across both data types; previous studies argued that body waves see stronger anisotropy in the inner core than modes, but when we average our body wave model we find the anisotropy to be comparable to our normal mode model.

Bringing the major conclusions together, Figure 8.1 shows a simplified summary of the compressional velocity structure we observe in the inner core. We find the inner core is split broadly into 4 regions of distinctive compressional velocity properties. In the west we robustly find a isotropically slow western layer in the top 100 km of the inner core as indicated by the body waves, and not contradicted by the normal modes. From 100 km depth to the center we find an anisotropic western zone primarily isolated in the northern hemisphere. This zone is strongly indicated by the body waves (even when excluding data from the South Sandwich Islands to Alaska raypaths) and is able to fit the normal mode observations when balanced with weaker anisotropy in the eastern part of the inner core. The eastern part of the inner core is a large region with fast isotropic velocities extending to the centre of the inner core. This difference is seen with the body waves and is required by the normal modes to average out the strong compressional anisotropy in the west (i.e. given that there is strong anisotropy in the west of the inner core, the east of the inner core must be isotropic to reduce the spherical average anisotropy to fit the normal modes). Finally, in the central 600 km of the eastern 'hemisphere' we see some indication of anomalous anisotropy with a slow direction, ζ_{slow}, which is not equal to 90°, the previously called inner most inner core (IMIC). The

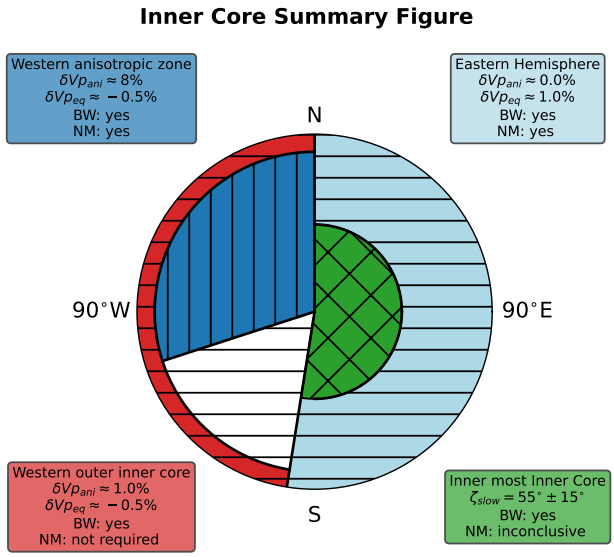

Figure 8.1 Simple schematic figure summarising the general findings of this thesis in terms of $\delta \mathrm{Vp}_{ani}$, δV_{eq}, ζ_{slow}, where BW means body wave data and NM normal mode data.

details of the IMIC in the east change when adding the normal mode data, but the normal mode data are inconclusive because we have assumed that β is constant and they only provide 1D and no 3D variations. There is some indication of a ζ_{slow} anomaly in the inner core from the modes, but the modes and the body waves do not agree on its location or form.

This thesis also highlights the benefit of applying transdimensional methods to improve imaging the deep Earth. While this is not the first study to apply this method to the inner core (Burdick *et al.* (2019); Pejić *et al.* (2019)) we have pushed the method further by combining different types of data and extend the transdimensional method from 2D to 3D. When it comes to parameterization of tomographic models, in general our philosophy has been whenever possible to allow the data to make choices for you; either through transdimensional methods to resolve uncertainties due to the parameterization or through hierarchical noise sampling to improve the modelling of noise in the data. However, of course, it is not possible to avoid all decisions. Choices such as the type of basis function, the physical parameterization and ultimately what data to incorporate into a model all have significant influence on the final model. When these choices are un-

avoidable we have tried to be clear why we prefer one option over another, and if possible test both options and investigate if there is any difference (such as whether to incorporate the South Sandwich Islands to Alaska data in our body wave model).

Ultimately interpretations and understanding will change as new data is acquired and new modelling methodologies are applied but what matters more in our opinion than one model or dataset is the insight that you gain. It seems that inner core seismology is at a turning point where we are now able to start to rigorously resolve 3D elastic structure in the inner core and begin to better understand what drives the dynamic processes in the inner core and reveal its dynamic past.

8.1 Future work

This research comes at an interesting time in inner core seismology. While at the moment it is computationally intractable to conduct Full Waveform Inversion (FWI) of the inner core it seems inevitable that it will be achieved in the coming years. This opens up new information as inner core seismologists will begin to fit not only the arrival times but the whole waveform with all of the complexity it entails. Similarly, when using normal modes a direct spectra inversion would reduce uncertainties from regularisation and fit the spectra of many modes simultaneously instead of using the intermediate step of measuring splitting functions (Jagt and Deuss, 2021). Durek and Romanowicz (1999) already conducted a direct spectra inversion for the inner core, but now we have significantly more data than Durek and Romanowicz (1999) and need to consider incorporating the body wave data simultaneously. At the same time, we believe that modelling using ray theory and splitting functions will still have an important role to play in future inner core studies. The reduced computational cost of these approximations allows more data to be incorporated, more starting models to be considered and a more rigorous statistical foundation on which to base the modelling than FWI or direct spectra methods. Indeed we see these two philosophies in inverse theory as complementary: more precise theory and minimal statistics versus approximate theory and rigorous statistics.

Other interesting developments in inner core seismology include the recent use of coda correlation methods (Phạm *et al.* (2018); Wang and Tkalčić (2021); Lima *et al.* (2022)) which makes use of a part of the seismic wavefield not yet fully exploited (between 5-50s period). Coda correlation might provide new information on the elastic parameters of the inner core separate from normal modes and body waves. Indeed it would be feasible to make

a model based on all three data types in the future (using ray theory and splitting function approximations).

Also worthwhile is the recent work combining seismology with geodynamics conducted by Frost *et al.* (2021) and which should be continued as new seismic data and observations become available, along with more regional array studies focused on inner core data (Frost and Romanowicz, 2019). Indeed, perhaps an array should be installed in the South Sandwich Islands to further explore whether the anomalous South Sandwich Islands to Alaska data is being influenced by the subduction zone close to the earthquake epicentres, as proposed in Chapter 3 and by Tkalčić (2010).

While these are all longer term suggestions for future work, there are also a number of intermediate steps that would logically follow from the work in this thesis and would be the kind of research to focus on in the near future:

- Measure attenuation splitting functions, d_{st}, for inner core sensitive normal modes and incorporating them into the grid searches, especially because the work of Mäkinen *et al.* (2014) and Pachhai *et al.* (2020) has shown the importance of measuring anelastic splitting functions alongside the elastic splitting functions,

- Measure cross-coupled inner core sensitive normal modes (Deuss *et al.*, 2010) in a grid search to further constrain 3D inner core tomography,

- Construct a better basis function to describe 1D variations in model parameters for the inner core without the drawbacks of either splines or polynomials.

- Investigate radial anisotropy at the top of the inner core from radial modes (Lythgoe and Deuss (2015); Talavera-Soza and Deuss (2020)),

- Incorporate raypath bending in our 3D transdimensional models, by allowing the raypaths through the inner core to vary as a function of the inner core velocity structure. We already showed the importance of this affect in Chapter 3, but for simplicity and computational tractability did not incorporate this into our models in Chapter 4 and Chapter 7,

- Use finite frequency kernels for our body wave data in the inner core, taking into account the broad Fresnel zones of these PKPdf paths,

- Investigate models with varying anisotropy symmetry axes,

- Increase the body wave dataset further, seeking to improve sensitivity to the very centre of the inner core, with the goal of improving the constraints on ζ_{slow}.

Appendix A
Voronoi cell algorithms

Voronoi cells are a useful way of quickly discretising a domain with non-overlapping volumes (Okabe *et al.*, 1994). They are defined by a set of nuclei, $\mathbf{c_i}$, where a point $\mathbf{p_q}$ exists within the Voronoi cell whose nucleus is closest to p_q. So taking a simple example, it can be seen on Figure A.1 that we have a domain discretised with 9 Voronoi cells each with a regularly spaced nucleus (producing a grid of cells).

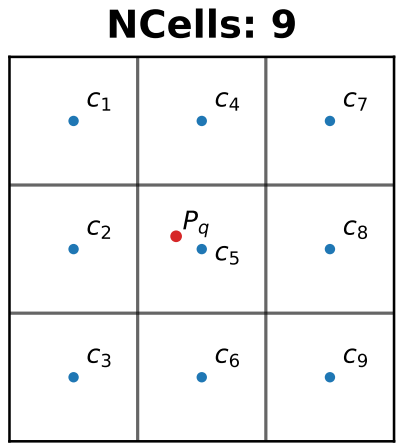

Figure A.1 A diagram of Voronoi cell boundaries, their corresponding nuclei ($\mathbf{c_i}$) and a query point $\mathbf{p_q}$.

We want to know which cell, $\mathbf{c_i}$, contains the point $\mathbf{p_q}$, from inspection of the diagram it is obvious to us that it is cell $\mathbf{c_5}$, computationally however we have to calculate the distances between $\mathbf{p_q}$ and each cell nuclei $\mathbf{c_i}$ and then the nuclei corresponding to the smallest distance is the correct answer (Figure A.2). This is the easiest way to implement Voronoi cells as a ba-

sis function for inversions, and I recommend to anyone who wishes to get started with Voronoi cells to implement this themselves.

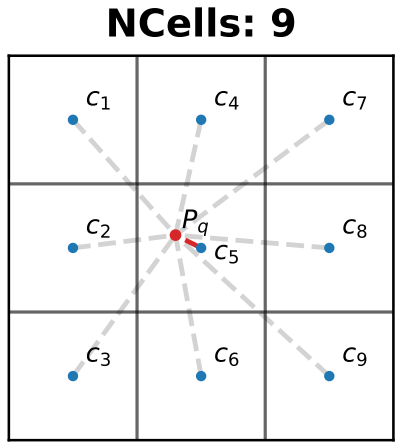

Figure A.2 A diagram of Voronoi cell boundaries, their corresponding nuclei ($\mathbf{c_i}$) and a query point $\mathbf{p_q}$.

The problem with this algorithm is that the number of calculations required to find the Voronoi cell which contains $\mathbf{p_q}$ increases linearly with N_c. This is not very cumbersome when you want to query a small number of points with a few Voronoi cells or if you only need to run the algorithm once (i.e. with non-transdimensional or 'static' inversions), however, when running transdimensional inversions you need to re-evaluate the sensitivity kernels with each transdimensional step. With body waves this means calculating how much of a given raypath travels through a Voronoi cell ($A_{i,j}$ in Equation 7.6) and with normal modes, re-evaluating the radial fraction of a Voronoi cell ($R^{st}_{i,j}$). Each of these calculations require the model space to be discretised into thousands of points and to evaluate which Voronoi cells contain each of these points. This is where more complex Voronoi cell algorithms can be introduced, if we know which Voronoi cells share a boundary (i.e. which cells are neighbours to each other) we can drastically reduce the number of distance calculations required to evaluate which Voronoi cell contains a point.

We use the software package *QHull* published by Barber *et al.* (1996) which can rapidly provide us with this 'neighbour' information (the compute time is insignificant up to ∼1000 Voronoi cells in 3 dimensions). This is invaluable as we can now define algorithms which make use of this neighbour

Algorithm 1 Which Voronoi Cell? (Simple)

```
1: procedure WHICH VORONOI CELL?
2:     c_i = list of Voronoi cell nuclei locations (Array)
3:     N_c = length of c_i (Integer)
4:     p_q = query point (Array)
5:     d_min = the minimum distance between p_q and c_i (Float)
6:     d_temp =a distance between p_q and a Voronoi nuclei (Float)
7:     i_q = the Voronoi cell index which contains point p_q (Integer)
8:
9:     for i = 1 : N_c do
10:        d_temp=distance(c_i,p_q)
11:        if i = 1 then
12:            d_min = d_temp
13:            i_q = i
14:        else
15:            if  d_temp < d_min then
16:                d_min = d_temp
17:                i_q = i
18:            end if
19:        end if
20: return i_q
21:
```

information to avoid having to compute all N_c distances.

Figure A.3 show's a new problem whereby we have more Voronoi cells, we still want to find the cell which contains $\mathbf{p_q}$, but this time we also have the neighbour information. For our new algorithm we will start off by (arbitrarily) guessing that cell $\mathbf{c_9}$ (shown with an orange nuclei on Figure A.3) contains $\mathbf{p_q}$, if this is the case, then the distance between $\mathbf{c_9}$ and $\mathbf{p_q}$ must be smaller than the distance between $\mathbf{p_q}$ and all of the neighbours of $\mathbf{c_9}$ (which are shown by green nuclei on Figure A.3).

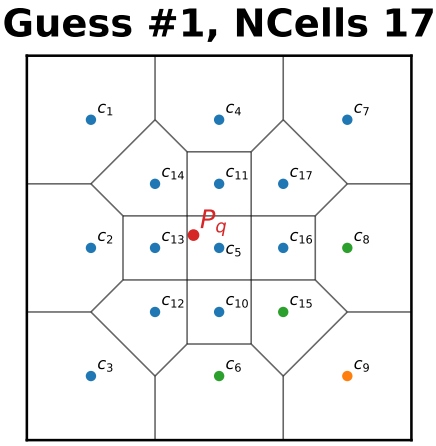

Figure A.3 A diagram of Voronoi cell boundaries, their corresponding nuclei ($\mathbf{c_i}$) and a query point $\mathbf{p_q}$. The initial guess cell is shown with an orange nuclei and it's neighbours are shown with green nuclei.

After calculating the distances between $\mathbf{c_9}$, $\mathbf{c_6}$, $\mathbf{c_{15}}$, $\mathbf{c_8}$ and $\mathbf{p_q}$, we find that $\mathbf{c_{15}}$ is closer to $\mathbf{p_q}$ than our initial guess of $\mathbf{c_9}$.

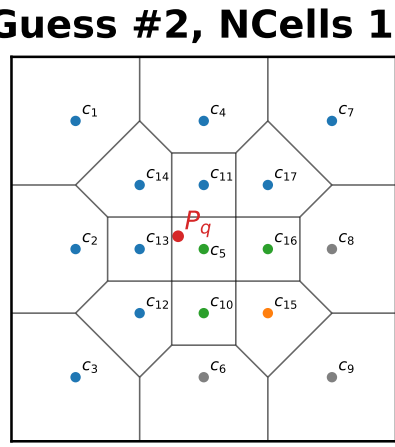

Figure A.4 A diagram of Voronoi cell boundaries, their corresponding nuclei ($\mathbf{c_i}$) and a query point $\mathbf{p_q}$. The initial guess cell is shown with an orange nuclei, its neighbours whose distances with $\mathbf{p_q}$ which still need to be calculated are shown with green nuclei and the cells for which this distance has already been calculated have grey nuclei.

We now repeat the algorithm calculating the distances between the neighbours of $\mathbf{c_{15}}$ and $\mathbf{p_q}$ (Figure A.4), to see if any of those Voronoi cell nuclei are closer (without repeating the distances between $\mathbf{c_9}$, $\mathbf{c_6}$, $\mathbf{c_8}$ and $\mathbf{p_q}$). From this next step we find that the distance between $\mathbf{c_5}$ and $\mathbf{p_q}$ is smaller than the distance between $\mathbf{c_{15}}$ and $\mathbf{p_q}$, now from inspection of Figure A.4 we can see that $\mathbf{c_5}$ is the Voronoi cell which contains $\mathbf{p_q}$, but we still have to calculate the distance between the neighbours of $\mathbf{c_5}$ and $\mathbf{p_q}$ to confirm that $\mathbf{c_5}$ is the correct Voronoi cell (Figure A.5). Through keeping track of which Voronoi cell distances have been calculated and knowing the neighbour information of the Voronoi cells we have reduced the number of distance calculations necessary to evaluate which cell contains $\mathbf{p_q}$ from 17 (the number of cells) down to 12, and this improvements scales significantly with the number of cells.

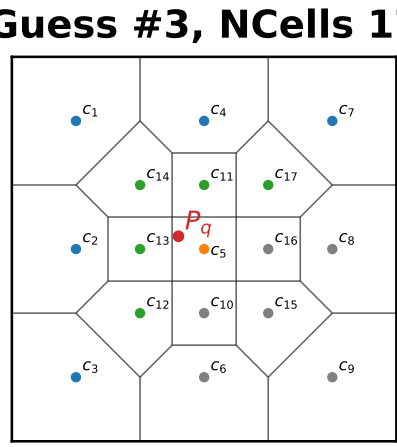

Figure A.5 A diagram of Voronoi cell boundaries, their corresponding nuclei ($\mathbf{c_i}$) and a query point $\mathbf{p_q}$. The initial guess cell is shown with an orange nuclei, its neighbours whose distances with $\mathbf{p_q}$ which still need to be calculated are shown with green nuclei and the cells for which this distance has already been calculated have grey nuclei.

Furthermore, in this scenario we were unlucky that our initial guess of cell $\mathbf{c_9}$ was far away from the actual Voronoi cell which contained $\mathbf{p_9}$, it can be seen that if we had guessed the correct cell, $\mathbf{c_5}$ straight away we would have only made 9 distance calculations. In the case of evaluating which Voronoi cells contains a series of points on a mesh or along a raypath you can utilise this optimisation by taking the Voronoi cell which contains the previous point along a raypath or in a mesh as your initial guess for the next point, assuming the raypath or mesh has been discretised finely enough they are likely to be close together and contained by the same Voronoi cell. This can be seen on Figure A.6 where a raypath crosses our model space discretised into Voronoi cells. To calculate $A_{i,j}$ we have discretised our raypath into points (shown in red) and we need to calculate which Voronoi cell contains which point, (and if we know the distance between the points on the raypath we can calculate $A_{i,j}$).

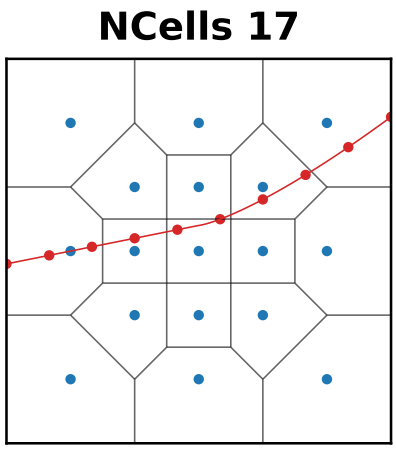

Figure A.6 A diagram of Voronoi cells, their corresponding nuclei ($\mathbf{c_i}$) and a raypath in red, with nodes along the path.

Algorithm 2 Which Voronoi Cell? (Neighbour)

procedure WHICH VORONOI CELL? (NEIGHBOUR)
    $\mathbf{c_i}$ = list of Voronoi cell nuclei locations (Array)
    N_c = length of $\mathbf{c_i}$ (Integer)
    $\mathbf{p_q}$ = query point (Array)
    dist = a list which is N_c long and initially is filled with Boolean 'False' but will be filled in with distances (Array)

    $\mathbf{Neighbour_i}$ = list of indexes which provide information on which Voronoi cells neighbour Voronoi cell i (Array)

    i_{guess} = the Voronoi cell index which we currently propose contains $\mathbf{p_q}$ (Integer)

    VCellFound = a parameter which is initially false but will stop the algorithm once the containing Voronoi cell has been determined (Boolean)

    dist[:]=False
    VCellFound=False
    while not *VCellFound* **do**
        dist[i_{guess}]=**distance**($\mathbf{c}_{i_{guess}}$,$\mathbf{p_q}$)
        for i in $\mathbf{Neighbour}_{i_{guess}}$ **do**
            if dist[i]=False **then**
                dist[i]=**distance**($\mathbf{c}_i$,$\mathbf{p_q}$)
            end if
        end for

        if any(**dist**[i] < **dist**[i_{guess}]) **then**
            i_{guess}=argmin(**dist**)
        else
            VCellFound=True
        end if
    end while
return i_{guess}

Acknowledgements

Along with all the usual challenges of doing a PhD (maintaining motivation, finding a direction with your research and enduring set backs) I didn't expect when I started that weathering a pandemic would be the hardest challenge of them all. I think anyone who has done a PhD would recognise that they couldn't do it alone and I am no exception.

I would like to start by thanking my promotor, **Arwen Deuss**. I want to thank you for your confidence in me back as a masters student. I had just started your course theoretical seismology and I was struggling with the mathematics within the course. I think a lesser teacher would have told me to switch to a different track and do something else, but instead you gave me a textbook showed me the chapters I had to read and told me that It would be hard, but I could catch up with everyone else. By the end of the course I was a much better physicist and seismologist and the experience stuck with me and really set the ball rolling, leading me to do a PhD with you. I thank you for your guidance over the last four years and sharing your passion for science with me. The freedom you gave me to test new concepts and go down different avenues of research even when they didn't seem so promising taught me a lot. Finally, I appreciate how open and accepting you are as a person.

Next, I would like to thank my co-promotor **Rhys Hawkins** you really helped to develop my understanding of inverse theory and transdimensional techniques and you are a great person to throw wacky ideas at to see how feasible they really are. Whats more, you were friendly and helpful at a time when we were all stuck at home trying to stay sane.

I would also like to thank the members of my examination committee; **Vernon Cormier**, **Peter Shearer**, **Christine Thomas**, **Jeannot Trampert** and **Jeroen Tromp** for taking the time to read my thesis and provide their insightful suggestions, comments and questions.

I would like to thank the staff in the department, especially; **Arie**, **Hanneke**, **Ivan**, **Jeannot**, **Laura** and **Theo** for their guidance, patience and friendly coffee chats. Also thanks to **Cedric** for sharing his enthusiasm

in music and geodynamics.

I would also like to thank many current and former PhD'ers in the department for great coffee chats, borrels and interesting discussions, including fellow *Arwenites*: **Su**, **Simon** and **Lisanne** who helped a great deal when it came to getting started with normal modes. Many thanks to Ivan's posse: **Haorui**, **Leon**, **David** and **Rens** (maybe one day I'll understand Marchenko imaging), and thanks to **Ashim**, **Wen**, **Thomas**, **Ronja**, **Bram**, **Eric**, **Suzanna** and **Eldert**. I have fond memories of our time together in San Francisco, Münster, Zürich, München and Toronto.

Outside of work I couldn't have asked for a better crew to have my back than the climbers; **Kasper**, **Mike**, **Sophie**, **Cami**, **Franco** and **Johannes**. You know you guys are the best, thanks for coming along and hanging off random bits of rock with me in our spare time, trying out new experiences, playing D&D and more than a few wild nights. You guys have always been there for me and I got pretty lucky when I met two random Dutch guys at the climbing gym in September 2016. Two PhD's down, three to go!

Thanks **Marj**, **Zeb** and **Lonneke**, you were some of the first friends I made when I moved to Utrecht and we've stayed good friends since and I don't doubt that we will remain so for many years to come.

There are a lot of people I wish I had seen more of in the last 4 years, not being able to easily travel home to Northern Ireland, or to England during the pandemic really hurt. I'm glad that we are starting to make up for lost time now and I'd like to thank some of the Belfast lads. Firstly, to the OG crew **John**, **Ryan**, **Bowen**, **Alec** and **Alex**. It felt like we started our journey into becoming massive nerds together and while I have lost touch with a lot of people from school, I'm always thankful to know that wherever we are we can get together and be immature like always. Seriously, for all your degrees you are still some of the dumbest people I have ever met and I love it. Also, I want to thank **Ben**, **Danny**, **Daniel** and **Andrew** for always being up for a pint, It really helps me to feel like I am going home when I come back to Belfast knowing that I still have good friends there.

Talking of people I haven't seen enough of, **Joe**, **Rob** and **Tom**. You guys introduced me to rock climbing and really started a huge passion for me, I miss the days when we could go fall off bits of wet rock in England on a weekly basis. Seeing you three has been harder than seeing any other friends of mine, its not easy to combine a trip home with visiting you guys and we're all a bit more spread out, but I still think about you three regularly and looking forward to more opportunities to go climbing with you.

Dankjewel **Marjon**, eerst was je mijn Nederlands docent en daarna ben je een goede vriend geworden. Ik ben veel over werkwoord conjuga-

tion vergeten, maar ik herinner nog veel biertjes en intressante filosofische gespreken. Je hebt me ook heel erg geholpen om me in dit vreemde land thuis te voelen, met wat ik van je heb geleerd maar ook door jou vriendschap.

I'd like to thank my Mum for teaching me the joy of learning, for all the letters, kindness and support over the years. Likewise, thanks Pa, for taking me out all these years to look at birds, walk in the mountains and teaching me to appreciate the natural world, which is ultimately the reason why I pursued my studies in Earth science. Thanks for all the support from my sisters **Elinor**, **Claire** and **Annie**. We really are scattered all over the place, (Dublin, London, Paris/Kyiv/South Sudan/Bangladesh...). Its a wonder we manage to meet up at all, but every time we do it feels really special. It's also been amazing to meet the latest member of the family, **Saorlaith**, and to get to know her the last two years.

I'd also like to thank, the Allers family, especially **Sjouk**, **Maarten**, **Annet**, **Frank** and **Hanneke** (along with the rest of the clan). You made me feel instantly welcome in the family and It helped me feel at home after I had moved to the Netherlands. All the support in the form of advice, beer and cake was very appreciated.

I couldn't possibly forget to thank my paranymphs and fellow members of FOCUS; **Rûna** and **Janneke**. The extensive coffee chats, therapy sessions, and support was frankly, essential. For real, I couldn't have done it without you two and I'm only sorry I won't be around to help you guys in your final months as you finish your own PhD's. I am curious what will happen once you've finished your PhD **Janneke**, and finally take over the world. Also, thanks as always **Rûna** for making sure het is nog gezzelig and being a **very** good listener. Also special thanks to **Annemijn**, you understand more than most how difficult a PhD can be and it was really great to have a friend to help keep everything in perspective.

Finally, I'd like to thank you **Esther**, you know how much you mean to me and being with you brings me such joy. I came to the Netherlands to study, but truly I stayed because of you. We have been together through all the difficulties of Covid, PhD life, an existential crisis and living in a tiny apartment and looking back I wouldn't change a thing. While it's uncertain what the future will bring I know that finding that out will be our greatest adventure yet.

References

Aki, K. and W. Lee (1976). "Determination of three-dimensional velocity anomalies under a seismic array using first P arrival times from local earthquakes: 1. A homogeneous initial model". In: *Journal of Geophysical research* 81.23, pp. 4381–4399.

Alboussiere, T. and R. Deguen (2012). "Asymmetric dynamics of the inner core and impact on the outer core". In: *Journal of Geodynamics* 61, pp. 172–182.

Alboussiere, T., R. Deguen, and M. Melzani (2010). "Melting-induced stratification above the Earth's inner core due to convective translation". In: *Nature* 466.7307, pp. 744–747.

Amaru, M. L. (2007). "Global travel time tomography with 3-D reference models". PhD thesis. http://www.igitur.nl/: Utrecht University.

Aubert, J., H. Amit, G. Hulot, and P. Olson (2008). "Thermochemical flows couple the Earth's inner core growth to mantle heterogeneity". In: *Nature* 454.7205, pp. 758–761.

Bamberger, A, G Chavent, C. Hemon, and P Lailly (1982). "Inversion of normal incidence seismograms". In: *Geophysics* 47.5, pp. 757–770.

Barber, C. B., D. P. Dobkin, and H. Huhdanpaa (1996). "The quickhull algorithm for convex hulls". In: *ACM Transactions on Mathematical Software (TOMS)* 22.4, pp. 469–483.

Bayes, T. (1763). "LII. An essay towards solving a problem in the doctrine of chances. By the late Rev. Mr. Bayes, first communicated by Mr. Price, in a letter to John Canton". In: *Philosophical transactions of the Royal Society of London* 53, pp. 370–418.

Beghein, C. and J. Trampert (2003). "Robust normal mode constraints on inner-core anisotropy from model space search". In: *Science* 299.5606, pp. 552–555.

Bergman, M. I. (1997). "Measurements of electric anisotropy due to solidification texturing and the implications for the Earth's inner core". In: *Nature* 389.6646, pp. 60–63.

Bergman, M. I., D. J. Lewis, I. H. Myint, L. Slivka, S.-i. Karato, and A. Abreu (2010). "Grain growth and loss of texture during annealing of alloys, and the translation of Earth's inner core". In: *Geophysical Research Letters* 37.22.

Blom, N. A., A. Deuss, H. Paulssen, and L. Waszek (2015). "Inner core structure behind the PKP core phase triplication". In: *Geophysical Journal International* 201.3, pp. 1657–1665.

Bodin, T. and M. Sambridge (2009). "Seismic tomography with the reversible jump algorithm". In: *Geophysical Journal International* 178.3, pp. 1411–1436.

Boehler, R. (1993). "Temperatures in the Earth's core from melting-point measurements of iron at high static pressures". In: *Nature* 363.6429, pp. 534–536.

Bozdağ, E., D. Peter, M. Lefebvre, D. Komatitsch, J. Tromp, J. Hill, N. Podhorszki, and D. Pugmire (2016). "Global adjoint tomography: first-generation model". In: *Geophysical Journal International* 207.3, pp. 1739–1766.

Brett, H. and A. Deuss (2020). "Inner core anisotropy measured using new ultra-polar PKIKP paths". In: *Geophysical Journal International* 223.2, pp. 1230–1246.

Buffett, B. and H.-R. Wenk (2001). "Texturing of the Earth's inner core by Maxwell stresses". In: *Nature* 413.6851, pp. 60–63.

Burdick, S., L. Waszek, and V. Lekić (2019). "Seismic tomography of the uppermost inner core". In: *Earth and Planetary Science Letters* 528, p. 115789.

Calvet, M., S. Chevrot, and A. Souriau (2006a). "P-wave propagation in transversely isotropic media: I. Finite-frequency theory". In: *Physics of the Earth and Planetary Interiors* 156.1-2, pp. 12–20.

— (2006b). "P-wave propagation in transversely isotropic media: II. Application to inner core anisotropy: Effects of data averaging, parametrization and a priori information". In: *Physics of the Earth and Planetary Interiors* 156.1-2, pp. 21–40.

Cao, A., B. Romanowicz, and N. Takeuchi (2005). "An observation of PKJKP: inferences on inner core shear properties". In: *Science* 308.5727, pp. 1453–1455.

Cormier, V. F. and A. Stroujkova (2005). "Waveform search for the innermost inner core". In: *Earth and Planetary Science Letters* 236.1-2, pp. 96–105.

Cowles, M. K. and B. P. Carlin (1996). "Markov chain Monte Carlo convergence diagnostics: a comparative review". In: *Journal of the American Statistical Association* 91.434, pp. 883–904.

Creager, K. C. (1992). "Anisotropy of the inner core from differential travel times of the phases PKP and PKIKP". In: *Nature* 356.6367, pp. 309–314.

— (1999). "Large-scale variations in inner core anisotropy". In: *Journal of Geophysical Research: Solid Earth* 104.B10, pp. 23127–23139.

Crotwell, H. P., T. J. Owens, and J. Ritsema (1999). "The TauP Toolkit: Flexible seismic travel-time and ray-path utilities". In: *Seismological Research Letters* 70, pp. 154–160.

Dahlen, F. (1982). "The effect of data windows on the estimation of free oscillation parameters". In: *Geophysical Journal International* 69.2, pp. 537–549.

Dahlen, F., S.-H. Hung, and G. Nolet (2000). "Fréchet kernels for finite-frequency traveltimes—I. Theory". In: *Geophysical Journal International* 141.1, pp. 157–174.

Dahlen, F. and J. Tromp (1998). "Theoretical global seismology". In: *Theoretical Global Seismology*. Princeton university press.

Deguen, R., T Alboussière, and S Labrosse (2018). "Double-diffusive translation of Earth's inner core". In: *Geophysical Journal International* 214.1, pp. 88–107.

Deguen, R., P. Cardin, S. Merkel, and R. A. Lebensohn (2011). "Texturing in Earth's inner core due to preferential growth in its equatorial belt". In: *Physics of the Earth and Planetary Interiors* 188.3-4, pp. 173–184.

Deuss, A., J. C. Irving, and J. H. Woodhouse (2010). "Regional variation of inner core anisotropy from seismic normal mode observations". In: *Science* 328.5981, pp. 1018–1020.

Deuss, A., J. Ritsema, and H. van Heijst (2013). "A new catalogue of normal-mode splitting function measurements up to 10 mHz". In: *Geophysical Journal International* 193.2, pp. 920–937.

Deuss, A. and J. H. Woodhouse (2001). "Theoretical free-oscillation spectra: the importance of wide band coupling". In: *Geophysical Journal International* 146.3, pp. 833–842.

Deuss, A., J. H. Woodhouse, H. Paulssen, and J. Trampert (2000). "The observation of inner core shear waves". In: *Geophysical Journal International* 142.1, pp. 67–73.

Durek, J. J. and B. Romanowicz (1999). "Inner core anisotropy inferred by direct inversion of normal mode spectra". In: *Geophysical Journal International* 139.3, pp. 599–622.

Dziewonski, A. M. (1984). "Mapping the lower mantle: determination of lateral heterogeneity in P velocity up to degree and order 6". In: *Journal of Geophysical Research: Solid Earth* 89.B7, pp. 5929–5952.

Dziewonski, A. M. and D. L. Anderson (1981). "Preliminary reference Earth model". In: *Physics of the earth and planetary interiors* 25.4, pp. 297–356.

Dziewonski, A. M. and F. Gilbert (1976). "The effect of small, aspherical perturbations on travel times and a re-examination of the corrections for ellipticity". In: *Geophysical Journal International* 44.1, pp. 7–17.

Dziewonski, A. M., B. H. Hager, and R. J. O'Connell (1977). "Large-scale heterogeneities in the lower mantle". In: *Journal of Geophysical Research* 82.2, pp. 239–255.

Edmonds, A. R. (1960). "Angular momentum in quantum mechanics". In: *Angular Momentum in Quantum Mechanics*. Princeton university press.

Frost, D. A., M. Lasbleis, B. Chandler, and B. Romanowicz (2021). "Dynamic history of the inner core constrained by seismic anisotropy". In: *Nature Geoscience* 14.7, pp. 531–535.

Frost, D. A. and B. Romanowicz (2019). "On the orientation of the fast and slow directions of anisotropy in the deep inner core". In: *Physics of the Earth and Planetary Interiors* 286, pp. 101–110.

Frost, D. A., B. Romanowicz, and S. Roecker (2020). "Upper mantle slab under Alaska: Contribution to anomalous core-phase observations on South-Sandwich to Alaska paths". In: *Physics of the Earth and Planetary Interiors*, p. 106427.

Garcia, R. (2002). "Seismological and mineralogical constraints on the inner core fabric". In: *Geophysical research letters* 29.20, pp. 19–1.

Garcia, R. and A. Souriau (2000). "Inner core anisotropy and heterogeneity level". In: *Geophysical research letters* 27.19, pp. 3121–3124.

Giardini, D., X.-D. Li, and J. H. Woodhouse (1987). "Three-dimensional structure of the Earth from splitting in free-oscillation spectra". In: *Nature* 325.6103, pp. 405–411.

González, Á. (2010). "Measurement of areas on a sphere using Fibonacci and latitude–longitude lattices". In: *Mathematical Geosciences* 42.1, pp. 49–64.

Hastings, W. K. (1970). "Monte Carlo sampling methods using Markov chains and their applications". In: *Biometrika* 57.1, pp. 97–109.

He, X. and J. Tromp (1996). "Normal-mode constraints on the structure of the Earth". In: *Journal of Geophysical Research: Solid Earth* 101.B9, pp. 20053–20082.

Hilst, R. D. Van der, S. Widiyantoro, and E. Engdahl (1997). "Evidence for deep mantle circulation from global tomography". In: *Nature* 386.6625, pp. 578–584.

Hirose, K., S. Labrosse, and J. Hernlund (2013). "Composition and state of the core". In: *Annu. Rev. Earth Planet. Sci* 41.1, pp. 657–691.

Hollerbach, R. and C. A. Jones (1995). "On the magnetically stabilizing role of the Earth's inner core". In: *Physics of the Earth and Planetary Interiors* 87.3-4, pp. 171–181.

Irving, J. C. E. and A Deuss (2011). "Hemispherical structure in inner core velocity anisotropy". In: *Journal of Geophysical Research: Solid Earth* 116.B4.

Ishii, M. and A. M. Dziewoński (2002). "The innermost inner core of the Earth: Evidence for a change in anisotropic behavior at the radius of about 300 km". In: *Proceedings of the National Academy of Sciences* 99.22, pp. 14026–14030.

— (2003). "Distinct seismic anisotropy at the centre of the Earth". In: *Physics of the Earth and Planetary Interiors* 140.1-3, pp. 203–217.

Ishii, M., A. M. Dziewoński, J. Tromp, and G. Ekström (2002b). "Joint inversion of normal mode and body wave data for inner core anisotropy 2. Possible complexities". In: *Journal of Geophysical Research: Solid Earth* 107.B12, p. 2380.

Ishii, M., J. Tromp, A. M. Dziewoński, and G. Ekström (2002a). "Joint inversion of normal mode and body wave data for inner core anisotropy 1. Laterally homogeneous anisotropy". In: *Journal of Geophysical Research: Solid Earth* 107.B12, p. 2379.

Isse, T. and I. Nakanishi (2002). "Inner-core anisotropy beneath Australia and differential rotation". In: *Geophysical Journal International* 151.1, pp. 255–263.

Jagt, L. and A. Deuss (2021). "Comparing one-step full-spectrum inversion with two-step splitting function inversion in normal mode tomography". In: *Geophysical Journal International* 227.1, pp. 559–575.

Jephcoat, A. and P. Olson (1987). "Is the inner core of the Earth pure iron?" In: *Nature* 325.6102, pp. 332–335.

Karato, S.-i. (1993). "Inner core anisotropy due to the magnetic field—induced preferred orientation of iron". In: *Science* 262.5140, pp. 1708–1711.

— (1999). "Seismic anisotropy of the Earth's inner core resulting from flow induced by Maxwell stresses". In: *Nature* 402.6764, pp. 871–873.

Kennett, B., E. Engdahl, and R Buland (1995). "Constraints on seismic velocities in the Earth from travel times". In: *Geophysical Journal International* 122.1, pp. 108–124.

Koketsu, K. and S. Sekine (1998). "Pseudo-bending method for three-dimensional seismic ray tracing in a spherical Earth with discontinuities". In: *Geophysical Journal International* 132.2, pp. 339–346.

Koot, L. and M. Dumberry (2011). "Viscosity of the Earth's inner core: Constraints from nutation observations". In: *Earth and Planetary Science Letters* 308.3-4, pp. 343–349.

Lehmann, I. (1936). "P', Publ". In: *Bur. Centr. Seism. Internat. Serie A* 14, pp. 87–115.

Lekić, V and B. Romanowicz (2011). "Inferring upper-mantle structure by full waveform tomography with the spectral element method". In: *Geophysical Journal International* 185.2, pp. 799–831.

Leykam, D., H. Tkalčić, and A. M. Reading (2010). "Core structure reexamined using new teleseismic data recorded in Antarctica: evidence for, at most, weak cylindrical seismic anisotropy in the inner core". In: *Geophysical Journal International* 180.3, pp. 1329–1343.

Li, C., R. D. van der Hilst, E. R. Engdahl, and S. Burdick (2008). "A new global model for P wave speed variations in Earth's mantle". In: *Geochemistry, Geophysics, Geosystems* 9.5.

Li, X.-D., D. Giardini, and J. H. Woodhouses (1991). "Large-scale three-dimensional even-degree structure of the Earth from splitting of long-period normal modes". In: *Journal of Geophysical Research: Solid Earth* 96.B1, pp. 551–577.

Li, X.-D. and B. Romanowicz (1996). "Global mantle shear velocity model developed using nonlinear asymptotic coupling theory". In: *Journal of Geophysical Research: Solid Earth* 101.B10, pp. 22245–22272.

Lima, T. Costa de, H. Tkalčić, and L. Waszek (2022). "A new probe into the innermost inner core anisotropy via the global coda-correlation wavefield". In: *Journal of Geophysical Research: Solid Earth* 127.4, e2021JB023540.

Long, X., H. Kawakatsu, and N. Takeuchi (2018). "A sharp structural boundary in lowermost mantle beneath Alaska detected by core phase differential travel times for the anomalous South Sandwich Islands to Alaska Path". In: *Geophysical Research Letters* 45.1, pp. 176–184.

Love, A. (1927). *The mathematical theory of elasticity.*

Lythgoe, K. H. and A. Deuss (2015). "The existence of radial anisotropy in Earth's upper inner core revealed from seismic normal mode observations". In: *Geophysical Research Letters* 42.12, pp. 4841–4848.

Lythgoe, K., A Deuss, J. Rudge, and J. Neufeld (2014). "Earth's inner core: Innermost inner core or hemispherical variations?" In: *Earth and Planetary Science Letters* 385, pp. 181–189.

Mäkinen, A. M., A. Deuss, and S. A. Redfern (2014). "Anisotropy of Earth's inner core intrinsic attenuation from seismic normal mode models". In: *Earth and Planetary Science Letters* 404, pp. 354–364.

Martorell, B., J. Brodholt, I. G. Wood, and L. Vočadlo (2015). "The elastic properties and stability of fcc-Fe and fcc-FeNi alloys at inner-core conditions". In: *Geophysical Journal International* 202.1, pp. 94–101.

Masters, G., G. Laske, and F. Gilbert (2000). "Matrix autoregressive analysis of free-oscillation coupling and splitting". In: *Geophysical Journal International* 143.2, pp. 478–489.

Meer, D. G. Van der, D. J. Van Hinsbergen, and W. Spakman (2018). "Atlas of the underworld: Slab remnants in the mantle, their sinking history, and a new outlook on lower mantle viscosity". In: *Tectonophysics* 723, pp. 309–448.

Megnin, C and B Romanowicz (1995). "Estimation of inner core mode splitting functions combining a genetic algorithm with a direct iterative inversion scheme". In: *EOS, Trans. Am. geophys. Un.* 76, p. 355.

Mooney, W. D., G. Laske, and T. G. Masters (1998). "CRUST 5.1: A global crustal model at 5× 5". In: *Journal of Geophysical Research: Solid Earth* 103.B1, pp. 727–747.

Morelli, A., A. M. Dziewonski, and J. H. Woodhouse (1986). "Anisotropy of the inner core inferred from PKIKP travel times". In: *Geophysical Research Letters* 13.13, pp. 1545–1548.

Nataf, H.-C., I. Nakanishi, and D. L. Anderson (1986). "Measurements of mantle wave velocities and inversion for lateral heterogeneities and anisotropy: 3. Inversion". In: *Journal of Geophysical Research: Solid Earth* 91.B7, pp. 7261–7307.

Niu, F. and L. Wen (2001). "Hemispherical variations in seismic velocity at the top of the Earth's inner core". In: *Nature* 410.6832, pp. 1081–1084.

Nolet, G. and F. Dahlen (2000). "Wave front healing and the evolution of seismic delay times". In: *Journal of Geophysical Research: Solid Earth* 105.B8, pp. 19043–19054.

Okabe, A., B. Boots, and K. Sugihara (1994). "Nearest neighbourhood operations with generalized Voronoi diagrams: a review". In: *International Journal of Geographical Information Systems* 8.1, pp. 43–71.

Oldham, R. D. (1906). "The constitution of the interior of the Earth, as revealed by earthquakes". In: *Quarterly Journal of the Geological Society* 62.1-4, pp. 456–475.

Olson, P., U. Christensen, and G. A. Glatzmaier (1999). "Numerical modeling of the geodynamo: mechanisms of field generation and equilibration".

In: *Journal of Geophysical Research: Solid Earth* 104.B5, pp. 10383–10404.

Oreshin, S. and L. Vinnik (2004). "Heterogeneity and anisotropy of seismic attenuation in the inner core". In: *Geophysical research letters* 31.2.

Pachhai, S, G Masters, and G Laske (2020). "Probabilistic estimation of structure coefficients and their uncertainties, for inner-core sensitive modes, using matrix autoregression". In: *Geophysical Journal International* 221.2, pp. 1366–1383.

Panning, M. and B. Romanowicz (2006). "A three-dimensional radially anisotropic model of shear velocity in the whole mantle". In: *Geophysical Journal International* 167.1, pp. 361–379.

Pejić, T., R. Hawkins, M. Sambridge, and H. Tkalčić (2019). "Transdimensional Bayesian attenuation tomography of the upper inner core". In: *Journal of Geophysical Research: Solid Earth* 124.2, pp. 1929–1943.

Phạm, T.-S., H. Tkalčić, M. Sambridge, and B. L. Kennett (2018). "Earth's correlation wavefield: Late coda correlation". In: *Geophysical Research Letters* 45.7, pp. 3035–3042.

Poupinet, G, R. Pillet, and A Souriau (1983). "Possible heterogeneity of the Earth's core deduced from PKIKP travel times". In: *Nature* 305.5931, pp. 204–206.

Resovsky, J. S. and M. H. Ritzwoller (1998). "New and refined constraints on three-dimensional Earth structure from normal modes below 3 mHz". In: *Journal of Geophysical Research: Solid Earth* 103.B1, pp. 783–810.

Ritsema, J., H. J. v. Heijst, and J. H. Woodhouse (1999). "Complex shear wave velocity structure imaged beneath Africa and Iceland". In: *Science* 286.5446, pp. 1925–1928.

Ritterbex, S. and T. Tsuchiya (2020). "Viscosity of hcp iron at Earth's inner core conditions from density functional theory". In: *Scientific reports* 10.1, pp. 1–9.

Romanowicz, B., H. Tkalcic, L. Breger, *et al.* (2003). "On the origin of complexity in PKP travel time data". In: *Earth's core: Dynamics, structure, rotation* 31, pp. 31–44.

Sambridge, M. (1999). "Geophysical inversion with a neighbourhood algorithm—I. Searching a parameter space". In: *Geophysical journal international* 138.2, pp. 479–494.

Schneider, S. and A. Deuss (2021). "A new catalogue of toroidal-mode overtone splitting function measurements". In: *Geophysical Journal International* 225.1, pp. 329–341.

Shearer, P. M. and K. M. Toy (1991). "PKP (BC) versus PKP (DF) differential travel times and aspherical structure in the Earth's inner core". In: *Journal of Geophysical Research: Solid Earth* 96.B2, pp. 2233–2247.

Simmons, N. A., S. C. Myers, G. Johannesson, and E. Matzel (2012). "LLNL-G3Dv3: Global P wave tomography model for improved regional and teleseismic travel time prediction". In: *Journal of Geophysical Research: Solid Earth* 117.B10.

Song, X. (1996). "Anisotropy in central part of inner core". In: *Journal of Geophysical Research: Solid Earth* 101.B7, pp. 16089–16097.

— (1997). "Anisotropy of the Earth's inner core". In: *Reviews of geophysics* 35.3, pp. 297–313.

Spakman, W, M. Wortel, and N. Vlaar (1988). "The Hellenic subduction zone: a tomographic image and its geodynamic implications". In: *Geophysical research letters* 15.1, pp. 60–63.

Stephenson, J, H Tkalčić, and M Sambridge (2020). "Evidence for the innermost inner core: Robust parameter search for radially varying anisotropy using the neighbourhood algorithm". In: *Journal of Geophysical Research: Solid Earth*, e2020JB020545.

Stixrude, L. (2012). "Structure of Iron to 1 Gbar and 40 000 K". In: *Physical Review Letters* 108.5, p. 055505.

Stixrude, L. and R. Cohen (1995). "High-pressure elasticity of iron and anisotropy of Earth's inner core". In: *Science* 267.5206, pp. 1972–1975.

Stixrude, L., E. Wasserman, and R. E. Cohen (1997). "Composition and temperature of Earth's inner core". In: *Journal of Geophysical Research: Solid Earth* 102.B11, pp. 24729–24739.

Su, W.-j. and A. M. Dziewonski (1995). "Inner core anisotropy in three dimensions". In: *Journal of Geophysical Research: Solid Earth* 100.B6, pp. 9831–9852.

Sumita, I. and P. Olson (1999). "A laboratory model for convection in Earth's core driven by a thermally heterogeneous mantle". In: *Science* 286.5444, pp. 1547–1549.

Sun, X. and X. Song (2008a). "The inner inner core of the Earth: Texturing of iron crystals from three-dimensional seismic anisotropy". In: *Earth and Planetary Science Letters* 269.1-2, pp. 56–65.

— (2008b). "Tomographic inversion for three-dimensional anisotropy of Earth's inner core". In: *Physics of the Earth and Planetary Interiors* 167.1-2, pp. 53–70.

Talavera-Soza, S and A Deuss (2021). "New measurements of long-period radial modes using large earthquakes". In: *Geophysical Journal International* 224.2, pp. 1211–1224.

Talavera-Soza, S. and A. Deuss (2020). “Constraining 1-D inner core attenuation through measurements of strongly coupled normal mode pairs”. In: *Geophysical Journal International* 223.1, pp. 612–621.

Tanaka, S. and H. Hamaguchi (1997). “Degree one heterogeneity and hemispherical variation of anisotropy in the inner core from PKP (BC)-PKP (DF) times”. In: *Journal of Geophysical Research: Solid Earth* 102.B2, pp. 2925–2938.

Tarantola, A., B. Valette, *et al.* (1982). “Inverse problems= quest for information”. In: *Journal of geophysics* 50.1, pp. 159–170.

Tateno, S., K. Hirose, Y. Ohishi, and Y. Tatsumi (2010). “The structure of iron in Earth’s inner core”. In: *Science* 330.6002, pp. 359–361.

Tesoniero, A., L. Auer, L. Boschi, and F. Cammarano (2015). “SPani, a whole-mantle Vp and Vs model: Implications on thermo-chemical structure.” In: *EGUGA*, p. 10514.

Thrastarson, S., D.-P. Van Herwaarden, L. Krischer, C. Boehm, M. van Driel, M. Afanasiev, and A. Fichtner (2022). “Data-adaptive global full-waveform inversion”. In: *Geophysical Journal International* 230.2, pp. 1374–1393.

Tkalčić, H. (2010). “Large variations in travel times of mantle-sensitive seismic waves from the South Sandwich Islands: Is the Earth’s inner core a conglomerate of anisotropic domains?” In: *Geophysical research letters* 37.14.

— (2015). “Complex inner core of the Earth: The last frontier of global seismology”. In: *Reviews of Geophysics* 53.1, pp. 59–94.

Tromp, J. (1993). “Support for anisotropy of the Earth’s inner core from free oscillations”. In: *Nature* 366.6456, pp. 678–681.

— (1995). “Normal-mode splitting due to inner-core anisotropy”. In: *Geophysical Journal International* 121.3, pp. 963–968.

Vocadlo, L and G Price (2007). “Mineralogy of the Earth—The Earth’s core: Iron and iron alloys”. In: *Mineral Physics*, pp. 91–120.

Vočadlo, L. (2007). “Ab initio calculations of the elasticity of iron and iron alloys at inner core conditions: evidence for a partially molten inner core?” In: *Earth and Planetary Science Letters* 254.1-2, pp. 227–232.

Vočadlo, L., J. Brodholt, D. Alfè, M. J. Gillan, and G. D. Price (2000). “Ab initio free energy calculations on the polymorphs of iron at core conditions”. In: *Physics of the Earth and Planetary Interiors* 117.1-4, pp. 123–137.

Wang, S. and H. Tkalčić (2021). “Shear-wave Anisotropy in the Earth’s Inner Core”. In: *Geophysical Research Letters* 48.19, e2021GL094784.

Wang, T. and X. Song (2018). "Support for equatorial anisotropy of Earth's inner-inner core from seismic interferometry at low latitudes". In: *Physics of the Earth and Planetary Interiors* 276, pp. 247–257.

Wang, T., X. Song, and H. H. Xia (2015). "Equatorial anisotropy in the inner part of Earth's inner core from autocorrelation of earthquake coda". In: *Nature Geoscience* 8.3, pp. 224–227.

Waszek, L. and A. Deuss (2011). "Distinct layering in the hemispherical seismic velocity structure of Earth's upper inner core". In: *Journal of Geophysical Research: Solid Earth* 116.B12.

Wen, L. and F. Niu (2002). "Seismic velocity and attenuation structures in the top of the Earth's inner core". In: *Journal of Geophysical Research: Solid Earth* 107.B11, ESE–2.

Widmer, R., G. Masters, and F. Gilbert (1992). "Observably split multiplets—data analysis and interpretation in terms of large-scale aspherical structure". In: *Geophysical Journal International* 111.3, pp. 559–576.

Woodhouse, J. (1980). "The coupling and attenuation of nearly resonant multiplets in the Earth's free oscillation spectrum". In: *Geophysical Journal International* 61.2, pp. 261–283.

Woodhouse, J. H. and A. M. Dziewonski (1984). "Mapping the upper mantle: Three-dimensional modeling of Earth structure by inversion of seismic waveforms". In: *Journal of Geophysical Research: Solid Earth* 89.B7, pp. 5953–5986.

Woodhouse, J. H., D. Giardini, and X.-D. Li (1986). "Evidence for inner core anisotropy from free oscillations". In: *Geophysical Research Letters* 13.13, pp. 1549–1552.

Wookey, J. and G. Helffrich (2008). "Inner-core shear-wave anisotropy and texture from an observation of PKJKP waves". In: *Nature* 454.7206, pp. 873–876.

Yoshida, S., I. Sumita, and M. Kumazawa (1996). "Growth model of the inner core coupled with the outer core dynamics and the resulting elastic anisotropy". In: *Journal of Geophysical Research: Solid Earth* 101.B12, pp. 28085–28103.

Yu, W.-c. and L. Wen (2006). "Seismic velocity and attenuation structures in the top 400 km of the Earth's inner core along equatorial paths". In: *Journal of Geophysical Research: Solid Earth* 111.B7.

Zhao, L., T. H. Jordan, and C. H. Chapman (2000). "Three-dimensional Fréchet differential kernels for seismic delay times". In: *Geophysical Journal International* 141.3, pp. 558–576.